

**Connecting  
the micro to  
macrophysics  
in black hole  
accretion**

J.R.J. Davelaar



# **Connecting the micro to macrophysics in black hole accretion**

J.R.J. Davelaar



# Connecting the micro to macrophysics in black hole accretion

## Proefschrift

ter verkrijging van de graad van doctor  
aan de Radboud Universiteit Nijmegen  
op gezag van de rector magnificus prof. dr. J.H.J.M. van Krieken,  
volgens besluit van het college van decanen  
in het openbaar te verdedigen op  
maandag 24 augustus 2020  
om 14.30 uur precies

door

**Jordy Ruben Jan Davelaar**

geboren op 18 september 1991  
te Wageningen

PROMOTOR: Prof. dr. H.D.E. Falcke

COPROMOTOR: Dr. M.A. Mościbrodzka

MANUSCRIPTCOMMISSIE: Prof. dr. N.P. Landsman  
Prof. dr. P.J. Armitage Stony Brook University, Verenigde Staten  
Prof. dr. P.G. Jonker  
Prof. dr. A.J. Levan  
Prof. dr. S.B. Markoff Universiteit van Amsterdam



© 2020, J.R.J. Davelaar

Connecting the micro to macrophysics in black hole accretion

Thesis, Radboud University Nijmegen

Illustrated; Daphne Davelaar (design cover)

with bibliographic information and Dutch summary

ISBN: 978-94-028-2102-4

*To my family and friends,  
who were with me at every step I made during this journey.*



# CONTENTS

<b>1</b>	<b>Introduction</b>	<b>1</b>
1.1	Black holes . . . . .	1
1.1.1	Schwarzschild black holes . . . . .	2
1.1.2	Kerr black holes . . . . .	3
1.1.3	Black hole shadows . . . . .	4
1.2	Astrophysical black holes . . . . .	7
1.3	Accretion flows . . . . .	11
1.3.1	Inflows . . . . .	11
1.3.2	Outflows . . . . .	13
1.4	General relativistic magnetohydrodynamics . . . . .	15
1.5	Radiation transport . . . . .	18
1.5.1	General relativistic ray tracing . . . . .	18
1.5.2	Electron temperature models . . . . .	20
1.6	Approaching the event horizon . . . . .	22
1.6.1	GRAVITY . . . . .	22
1.6.2	The Event Horizon Telescope . . . . .	22
1.7	Kinetic plasma physics . . . . .	26
1.7.1	Particle-in-Cell methods . . . . .	27
1.7.2	Reconnection . . . . .	30
1.7.3	Kink instability . . . . .	32
1.8	In this thesis . . . . .	34
<b>2</b>	<b>GRMHD <math>\kappa</math>-jet models for Sgr A</b>	<b>37</b>
2.1	Introduction . . . . .	38
2.2	Methods . . . . .	40
2.2.1	GRMHD simulation . . . . .	40
2.2.2	Numerical grid for simulating disks and jets . . . . .	42
2.2.3	Radiative transfer model and electron distribution functions . . . . .	42

CONTENTS

2.3	Results . . . . .	44
2.3.1	GRMHD jet structure . . . . .	44
2.3.2	SEDs and synchrotron maps of $\kappa$ -jet models . . . . .	46
2.3.3	Fitting the particle distribution function of Sgr A* . . . . .	49
2.4	Discussion . . . . .	49
2.4.1	SEDs of the jet launching zone as a function of electron distribution functions	49
2.4.2	Intrinsic size of the $\kappa$ -jet model as a function of $\lambda$ . . . . .	53
2.5	Conclusion . . . . .	54
2.A	Polar logarithmic camera . . . . .	54
2.B	The size of a synchrotron photosphere as a function of $\kappa$ and wavelength . . . . .	55
2.C	Particle acceleration efficiency . . . . .	60
<b>3</b>	<b>Modeling non-thermal emission from the jet-launching region of M 87 with AMR</b>	<b>63</b>
3.1	Introduction . . . . .	64
3.2	Methods . . . . .	67
3.2.1	GRMHD simulations . . . . .	68
3.2.2	AMR grid in Cartesian-Kerr-Schild coordinates . . . . .	68
3.2.3	Ray tracing in AMR CKS grid . . . . .	69
3.2.4	Electron model and radiative-transfer model parameters . . . . .	71
3.2.5	SED cut-off . . . . .	73
3.3	Results . . . . .	74
3.3.1	Structure of the accretion disk and jet in the AMR simulation . . . . .	74
3.3.2	Spectra and synchrotron images: dependency on electron distribution function	78
3.4	Discussion . . . . .	83
3.4.1	CKS GRMHD simulations . . . . .	83
3.4.2	The effect of electron acceleration on the SED . . . . .	83
3.4.3	The effect of electron acceleration on synchrotron maps . . . . .	84
3.4.4	Core size, shift, and jet-opening angle . . . . .	85
3.4.5	Reconnection as the source of particle acceleration . . . . .	85
3.4.6	The Event Horizon Telescope results . . . . .	85
3.5	Conclusion . . . . .	86
3.A	Phenomenological model explaining the dominance of the counter-jet . . . . .	87
3.B	Comparison with spherical grids . . . . .	91
<b>4</b>	<b>Particle acceleration in kink-unstable jets</b>	<b>93</b>
4.1	Introduction . . . . .	93
4.2	Numerical setup . . . . .	95
4.3	Results . . . . .	96
4.4	Discussion and conclusion . . . . .	101
4.A	Comparison with MHD . . . . .	103

<b>5 Observing Supermassive Black Holes In Virtual Reality</b>	<b>105</b>
5.1 Introduction . . . . .	106
5.2 Methods . . . . .	108
5.2.1 Black holes and gravitational lensing . . . . .	109
5.2.2 Camera trajectories . . . . .	112
5.2.3 Radiative-transfer calculations and background images . . . . .	117
5.2.4 Plasma and radiation models . . . . .	119
5.3 VR movie . . . . .	120
5.4 Discussion and conclusion . . . . .	127
<b>Bibliography</b>	<b>129</b>
<b>Summary</b>	<b>141</b>
<b>Samenvatting</b>	<b>143</b>
<b>Curriculum vitæ</b>	<b>145</b>
<b>Publication list</b>	<b>147</b>
<b>Acknowledgments</b>	<b>151</b>



# CHAPTER 1

## INTRODUCTION

*“The black holes of nature are the most perfect macroscopic objects there are in the universe: the only elements in their construction are our concepts of space and time.”*

— S. Chandrasekhar

### 1.1 Black holes

Black holes are objects that are so massive that even light cannot escape. Michell and Laplace (Michell, 1784; Laplace, 1796) were the first to hypothesize the existence of such an object, which they called dark stars. In Newtonian gravity, the escape velocity at the surface of a star is given by  $v_{\text{esc}} = \sqrt{2GM_*/R_*}$ , where  $G$  is Newton's constant,  $M_*$  the mass of the star, and  $R_*$  the radius of the star. Michell and Laplace argued that if a star is compact enough,  $M_*/R_* = c^2/(2G)$ , where  $c$  the speed of light, the escape velocity would exceed the speed of light. In the late 18th century, light was considered a particle with mass, and therefore subject to Newtonian gravity. In this reasoning, light would not be able to escape from this star and would, therefore, be invisible for an observer on Earth. When it became generally accepted that light is a (massless) electromagnetic wave (Clerk Maxwell, 1865), the theory of a dark star was rejected.

In the early 20th century, the hypothesis of the dark stars was revived by a new theory of gravity. This revival started in 1905 when Albert Einstein published his theory of Special Relativity (SR) (Einstein et al., 1905). SR was built around the notion that physical laws should hold independently of the observers' frame of reference. For electromagnetism, this results in a constant speed of light, which is the maximum velocity at which information is exchanged. Newtonian gravity does not incorporate this since the force is acting on a distance without any time delay. In 1915 Albert Einstein published his gravitational theory called; the theory of general relativity (GR) (Einstein, 1915). One of the anchor points of GR is the notion that the laws of physics should be the same in any free-falling reference frame. The underlying mathematical theory is that of differential geometry, spacetime is curved and is described by a manifold. The properties of this manifold are represented by the metric  $g_{\mu\nu}$ , which is a rank two tensor that

defines distances and angles on the manifold. In this thesis, the following sign convention for the diagonal of the metric is used;  $(-, +, +, +)$ . The metric can be written by using the line element  $ds$  which is the infinitesimal displacement defined by

$$ds^2 = g_{\mu\nu} dx^\mu dx^\nu, \quad (1.1)$$

where  $dx^\nu$  is an infinitesimal coordinate displacement. Here I used the Einstein summation convention; this means that summation of repeating upper and lower greek indices is implied and run from zero to three,  $A^\mu A_\mu = \sum_{\mu=0}^3 A^\mu A_\mu$ . By integrating the line element, the separation  $s$ , or spacetime interval, between two events can be computed. An event is called space-like separated when  $s^2 > 0$ , light-like separated when  $s^2 = 0$ , and time-like separated when  $s^2 < 0$ . The exact form of the metric is dictated by the Einstein equation,

$$R_{\mu\nu} - \frac{1}{2} R g_{\mu\nu} + \Lambda g_{\mu\nu} = \frac{8\pi G}{c^4} T_{\mu\nu}, \quad (1.2)$$

where  $R_{\mu\nu}$  is the Ricci curvature tensor,  $R$  is the Ricci scalar,  $\Lambda$  the vacuum constant, and  $T_{\mu\nu}$  the stress-energy tensor. The left-hand side of this equation holds geometrical objects that describe the curvature of spacetime, while the right-hand side contains stresses and energy densities. This equation shows that there is a one-on-one relation between the curvature of spacetime and the presence of energy. A source of energy generates curvature, and the presence of curvature affects the flow of energy. So far GR has stood every test, it showed agreement with, for example, observations of; the perihelion motion of Mercury, Venus, and Earth around the Sun, the perihelion motion observed in stellar binary systems (Clemence, 1947; Einstein, 1916; Weisberg & Huang, 2016), the apparent shift of the position of stars visible at a solar eclipse (Dyson et al., 1920), measurement of the Shapiro time delay (Shapiro et al., 1968), gravitational waves from the double pulsar PSR B1913+16 (Weisberg & Huang, 2016), from binary black hole mergers (LIGO Scientific Collaboration & Virgo Collaboration, 2016), and neutron star mergers (Abbott et al., 2017), tests of the equivalence principle in 3-body systems (Archibald et al., 2018), the first image of a black hole (Event Horizon Telescope Collaboration et al., 2019a), and Schwarzschild precession of the S2 star around Sagittarius A\* (GRAVITY Collaboration et al., 2020).

### 1.1.1 Schwarzschild black holes

Karl Schwarzschild obtained in 1916 the first analytical solution of the Einstein equation (translation Schwarzschild (1999)). The solution describes a non-rotating black hole. The line element of this solution is in spherical Boyer-Lindquist coordinates  $(t, r, \theta, \phi)$  given by

$$ds^2 = - \left(1 - \frac{2}{r}\right) dt^2 + \left(1 - \frac{2}{r}\right)^{-1} dr^2 + r^2(d\theta^2 + \sin^2 \theta d\phi^2), \quad (1.3)$$

here I used geometrical units  $G = M = c = 1$ , where  $M$  is the mass of the black hole. The solution contains two important radial points, at  $r = 2 = r_h$  and  $r = 0$ . At  $r_h$ , the radial component of the metric has a singularity, and the temporal and radial component changes sign. Crossing this surface has dire consequences for an observer, allowing it to only move inwards and unable to escape. This surface is known as the event horizon of a black hole, which marks the boundary of a causally disconnected region in spacetime. The choice of coordinates causes the singular behavior

of this hypersurface. The singularity can be lifted by shifting to horizon penetrating coordinates such as Kruskal-Szekeres coordinates. The second singularity at  $r = 0$ , however, is a physical singularity, this singularity points towards a shortcoming of GR, which can potentially be solved with quantum gravity theories. The horizon and singularity can be seen in the left panel of Figure 1.1.

### 1.1.2 Kerr black holes

The rotating analog of the Schwarzschild solution was found by Kerr (1963). The line element of this solution is in spherical Boyer-Lindquist coordinates given by,

$$ds^2 = - \left( 1 - \frac{2r}{\Sigma} \right) dt^2 + \frac{\Sigma}{\Delta} dr^2 + \Sigma d\theta^2 + \left( r^2 + a^2 + \frac{2ra^2}{\Sigma} \sin^2 \theta \right) \sin^2 \theta d\phi^2 - \frac{4ra \sin^2 \theta}{\Sigma} dt d\phi, \quad (1.4)$$

where  $a$  is the dimensionless spin parameter which correspond to the angular momentum  $J$  in c.g.s. units via  $a = J/(Mc)$ ,  $\Sigma = r^2 + a^2 \cos^2 \theta$ , and  $\Delta = r^2 - 2r + a^2$ . In the limit of  $a \rightarrow 0$  the Kerr metric recovers the Schwarzschild metric. The angular velocity of spacetime of a Kerr black hole is given by

$$\Omega = - \frac{g_{t\phi}}{g_{\phi\phi}} = \frac{2ra}{\Sigma(r^2 + a^2) + 2ra^2 \sin^2 \theta}. \quad (1.5)$$

The dependence on  $g_{t\phi}$  shows that the time and  $\phi$  coordinates are coupled. This means that the inertial frames are non-static and will be rotating along  $\phi$ . This rotation is known as frame dragging, and happens close to the horizon. This rotation is often referred to as Lense-Thirring precession which can be approximated by  $\Omega_{LT} \approx 2a/r^3$  (Lense & Thirring, 1918; Bardeen & Petterson, 1975). When  $a = 0$ ,  $g_{t\phi}$  vanishes as is the case in the Schwarzschild metric.

Similar to the Schwarzschild metric, the Kerr metric contains hypersurfaces where the metric is singular. The first surface that an infalling observer encounters is called the outer ergosphere at  $r = r_{E+} = 1 + \sqrt{1 - a^2 \cos^2 \theta}$ . This surface changes the sign of the temporal component of the metric,  $g_{tt}$ . The consequence of this is that for a stationary observer with  $u^\mu = dx^\mu/dt = (1, 0, 0, 0)$ , should have a timelike trajectory, but within the ergosphere  $u^\mu u^\nu g_{\mu\nu} = g_{tt} > 0$  which makes it spacelike separated, the consequence of this is that an observer crossing this radius has to co-rotate with the spacetime. The second surface is the outer event horizon at  $r = r_{H+} = 1 + \sqrt{1 - a^2}$  and the inner event horizon at  $r = r_{H-} = 1 - \sqrt{1 - a^2}$ . At the inner and outer horizon, the radial component of the metric,  $g_{rr}$ , is singular. The outer horizon is physically identical to the horizon in the Schwarzschild case. When crossing the horizon, the only allowed trajectories are pointed inwards, meaning an observer cannot escape from the black hole.

The inner horizon, also called the Cauchy horizon, marks the region where timelike loops are possible, which are curves that start and end at the same time coordinate. Within this surface, the concept of causality breaks down. However, the region within the inner horizon is known to be unstable, which makes the actual existence of the inner region highly doubtful (Poisson & Israel, 1989, 1990). Within the inner horizon, there are two more surfaces. The first one is the inner ergosphere at  $r = r_{E-} = 1 - \sqrt{1 - a^2 \cos^2 \theta}$ , within this radius the enforced co-rotation of spacetime that started at  $r = r_{E+}$  stops, since  $g_{tt}$  changes sign once more. Further in we find the ring singularity which lays in the equatorial plane at  $r = a$ ,  $\theta = \pi/2$ .

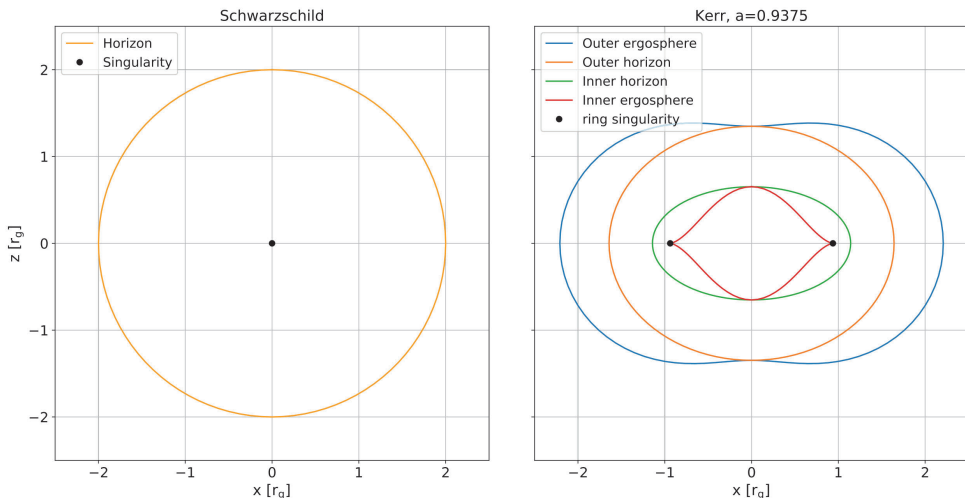


FIGURE 1.1: Important surfaces in the Schwarzschild geometry (left), and the Kerr geometry (right) for a black hole spin parameter of  $a = 0.9375$ .

The singular behavior of the metric in BL coordinates, except for the ring singularity, is caused, similarly to the Schwarzschild case, due to the choice of coordinates. They can be resolved when performing a coordinate transformation on the metric, for example, shifting to Kerr-Schild coordinates, which are horizon penetrating. The ring singularity is a curvature singularity and points toward a shortcoming of GR that can potentially be resolved by quantum gravity theories. The Kerr surfaces for a black hole with a spin parameter of  $a = 0.9375$  can be seen in the right panel of Figure 1.1.

### 1.1.3 Black hole shadows

In the early 1970s, the first numerical calculations of the appearance of a black hole by a distant observer were performed by Bardeen (1973); Cunningham & Bardeen (1973); Luminet (1979); Viergutz (1993). These early works showed that the event horizon is gravitationally lensed since the gravitational cross-section of the black hole is larger than the actual size of the horizon, see Figure 1.2 for the first computation performed by Bardeen (1973). For a non-rotating black hole, the apparent size of the black hole is given by  $r_{\text{app}} \approx 5 GM/c^2$ . For a rotating black hole, the size is asymmetric for viewing angles larger than zero, with respect to the rotation axis of the black hole. When spacetime rotation is present, the geodesics are either dragged towards the horizon when they move against the rotation of spacetime and accelerate away when they move along the rotation. Bardeen (1973) computed the apparent shape of the hole by using a faraway light source. The disadvantage of his is that the apparent size is larger compared to an emission source surrounding the black hole. Luminet (1979) showed that when a geometrically thin, optically thick accretion disk surrounds the black hole, the event horizon is also visible as a lensed darkening in the emission arising from the accretion flow, see Figure 1.3, Luminet (1979) also mentions that this is potentially observable for the supermassive black hole in Messier 87 but did not specify

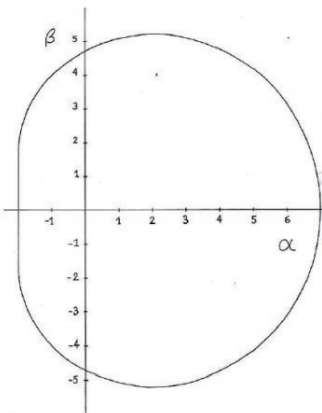


FIGURE 1.2: The apparent shape of a rapid spinning Kerr black hole, as seen side-on for a faraway observer. The shape is highly asymmetric with a flattening on the left side, caused by the rotation of spacetime. Figure from Bardeen (1973).

how. A note here is that the disk does not reach the actual horizon, and therefore, the apparent size is affected by the value for the inner radius of the disk.

In 1973 Bardeen wrote that “*It is conceptually interesting, if not astrophysically very important, to calculate the precise apparent shape of a black hole... Unfortunately, there seems to be no hope of observing this effect.*”. The reason behind this quote is that the apparent size on the sky of the black hole is  $\theta_{\text{size}} = 50 (M_{\text{bh}}/4 \times 10^6 M_{\odot})(8 \text{ kpc}/D) \mu\text{as}$ , which was unresolvable with any telescope.

With the technological advancements related to Very Long Baseline Interferometry (for a review on the history of VLBI see, for example Kellermann & Moran (2001); Clark (2003)), these resolutions came into reach. VLBI is an interferometric technique that combines signals collected at multiple telescopes to create a virtual telescope. The resulting resolution in VLBI is then set by distances between the individual telescopes. Falcke et al. (2000b) performed ray-tracing simulations of an optically thin plasma surrounding the black hole completely and computed synthetic observations for a VLBI array that spans the Earth, see Figure 1.4. The first set of simulations was performed around a rapidly rotating black hole with  $a = 0.998$  and  $M = 2 \times 10^6 M_{\odot}$ . The radiating plasma is free-falling with a density profile following  $r^{-2}$ ; the results of this can be seen in the top row of figure 1.4. The first column shows the ray-traced image, the second column shows the model as seen at 0.6 mm with scattering included, and the third column shows the same as the second column but now at 1.3 mm. The green lines correspond to the emission profile along  $y=0.5$  as a function of  $x$ . The bottom row of figure 1.4 shows a uniform density model where the plasma is in Keplerian orbit around a non-rotating black hole, where the three columns are the same as the top row. The models result in optically thin emission originating from the region close to the event horizon. In both models, a dark patch in the center can be distinguished, which was dubbed the black hole *shadow*. Falcke et al. (2000b) argued that if a VLBI observation is conducted with an array of telescopes separated approximately 8000 km



FIGURE 1.3: Black hole shadow as computed by Luminet. A radiating thin accretion disk surrounds the black hole. There is a clear asymmetric darkening of the flow visible that is a lensed image of the event horizon. Figure from Luminet (1979).

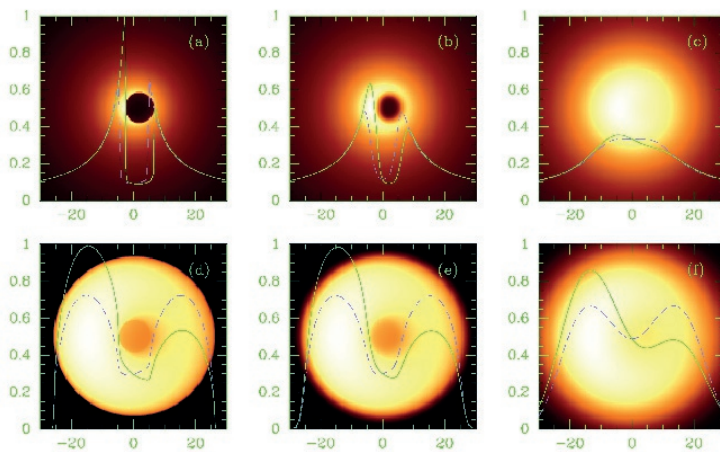


FIGURE 1.4: Top row shows a rapidly rotating black hole ( $a = 0.998$ ), bottom row non-rotating, both black holes have a mass of  $M = 2 \times 10^6 M_{\odot}$ . The emission is optically thin and based on either; free-falling gas where the emission coefficient is proportional to  $r^{-2}$  (top row), and uniform but on Keplerian velocities (bottom row). The first column shows ray-traced images, second column models seen by a VLBI array at 0.6 mm with scattering included, the third column the same as second but for 1.3 mm. Image from Falcke et al. (2000b).

apart, the shadow of Sagittarius A\*, the supermassive black hole in the center of our galaxy, is resolvable. An experiment like this could provide the first direct evidence for the existence of the black hole event horizon. Falcke et al. (2000a) also considered a jet model, which also shows a similar shadow at the jet base. The paper concludes that the exact distribution of emission over the emission ring depends strongly on the emissivity profiles, but a persistent asymmetric dark feature is present in all models. The asymmetry is due to the rotation of spacetime and the accretion disk.

More recently, black holes shadows from non-Kerr spacetime geometries are also computed, see, for example, Chirenti & Rezzolla (2007); Bambi et al. (2009); Johannsen & Psaltis (2010); Johannsen (2013); Abdujabbarov et al. (2015); Younsi et al. (2016); Olivares et al. (2018), comparing the shape and size of black hole shadows of different theories to observations opens a new test for GR in the most extreme gravitational environments in the Universe.

## 1.2 Astrophysical black holes

Since the theoretical prediction of the existence of black holes in the early 20th century, it took half a century before the first connection with astrophysical sources was made. For an excellent review of the history of AGN, see Shields (1999). 3C 405 (also known as Cygnus A) was the first source proposed as a supermassive black hole. The source was first discovered by Reber (1944); Hey et al. (1946), soon after the discovery Smith (1951) showed that the source was of extragalactic origin and Jennison & Das Gupta (1953) found that it consists out of multiple radio components. The connection with black holes was made during the 1960s when multiple high energetic extragalactic radio sources called Quasars were discovered (Schmidt, 1963; Greenstein, 1963; Oke, 1963; Hazard et al., 1963; Schmitt, 1968). Quasars were shown to have total luminosities up to  $10^{14}L_{\odot}$ , and they are of extragalactic origin. The first theoretical models by Hoyle & Fowler (1963b,a) for these sources assumed supermassive stars with masses up to  $10^8M_{\odot}$  as the main engine behind the observed radiation. These models predicted the right energetics and included the idea that toroidally wound magnetic fields could power the observed relativistic jets. However, the question of how to form such massive stars that would remain gravitationally stable throughout their lives was unanswered. Models that included accretion onto black holes were first proposed by Zeldovich (1964); Salpeter (1964); Hoyle (1966); Woltjer (1966). The hypothesis that accreting black holes are the main engines behind AGN became even more accepted after the paper by Lynden-Bell (1969) where they argued that potentially every galaxy contains an accreting supermassive black hole in their core.

The closest supermassive black hole candidate is located in the center of our galaxy. The first indications of this go back to the early 1970s when the existence was suggested by Lynden-Bell & Rees (1971). In 1974 it was detected by Balick & Brown (1974) in Sagittarius A, and soon after, dubbed Sagittarius A\* (Sgr A\*) (Brown, 1982). Due to its proximity to Earth, it is one of the most intensively studied supermassive black hole candidates. It is subject to extensive observational campaigns all over the electromagnetic spectrum, from radio to  $\gamma$ -ray wavelengths (Rogers et al., 1995; Zylka et al., 1995; Falcke et al., 1998; Melia & Falcke, 2001; Zhao et al., 2001; Bower et al., 2004; Shen et al., 2005; Doeleman et al., 2008; Bower et al., 2014, 2015; Rauch et al.,

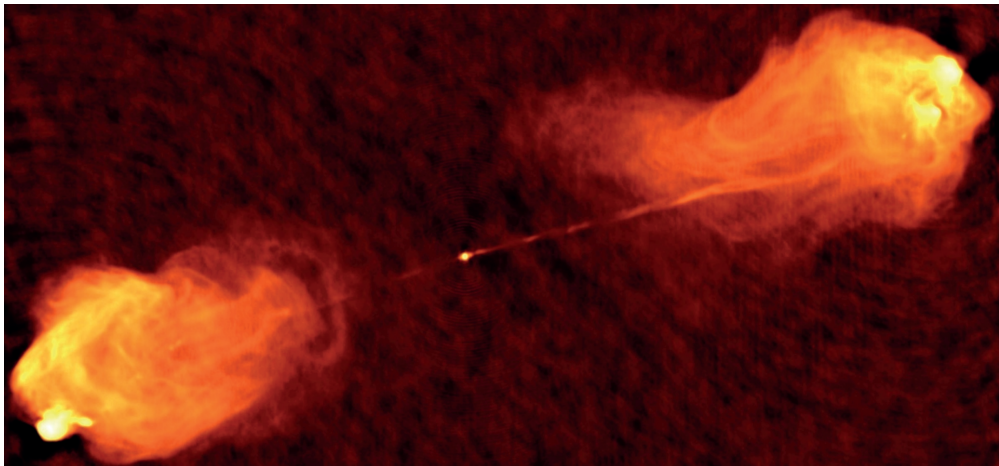


FIGURE 1.5: The radio jet in Cygnus A. Large radio lobes are visible originating from the deceleration of a relativistic jet seen a bright thin line. The jet starts in the central bright blob that is a giant elliptical galaxy. Image credit: NRAO/AUI

2016; Brinkerink et al., 2016; Capellupo et al., 2017; Issaoun et al., 2019), NIR (Genzel et al., 2003; Dodds-Eden et al., 2009; Gravity Collaboration et al., 2018; Do et al., 2019), X-ray (Baganoff et al., 2003; Eckart et al., 2004; Ponti et al., 2017), and gamma-rays (Mayer-Hasselwander et al., 1998; Tsuchiya et al., 2004; Aharonian et al., 2004; Albert et al., 2006). The spectrum shows an almost flat radio spectrum which peaks around mm wavelengths. In the NIR bands, variability is detected, which follows a red noise spectrum (Do et al., 2009). The full spectrum of Sgr A\* can be seen in Figure 1.6. The variability in NIR shows timescales of minutes (Dodds-Eden et al., 2009), which suggests that the emission is produced in a region smaller than the predicted size of the black hole.

Sgr A\* is considered a low luminosity AGN since its luminosity is low compared to the Eddington luminosity. The Eddington luminosity is defined as the luminosity that is strong enough to counterbalance the gravitational force. If the radiation force exceeds the gravitational force, the matter cannot accrete towards the black hole. This balance is achieved when the luminosity of the flow is equal to

$$L_{\text{Edd}} = \frac{4\pi GMm_p c}{\sigma_T}, \quad (1.6)$$

where  $M$  is the mass of the black hole,  $m_p$  is the proton mass, and  $\sigma_T$  the Thompson cross-section.

Due to its relatively close distance (compared to other supermassive black holes) and low Eddington luminosity, it is possible to measure stellar motions close to Sgr A\*. The central stars show eccentric orbits around a common center of mass and are called the S-stars, which were discovered by Eckart & Genzel (1997); Ghez et al. (1998), and have been extensively monitored over the past decades (Ghez et al., 2008; Gillessen et al., 2009b; Gravity Collaboration et al., 2018; Do et al., 2019). The latest passage of the star S2, which has a short orbital period of 16 years, was recently in 2018, based on this passage, see Fig. 1.7 a mass estimate of Sgr A\* was made of  $(4.148 \pm 0.014) \times 10^6 M_\odot$  at a distance of  $8.175 \pm 0.013$  kpc (Gravity Collaboration et al.,

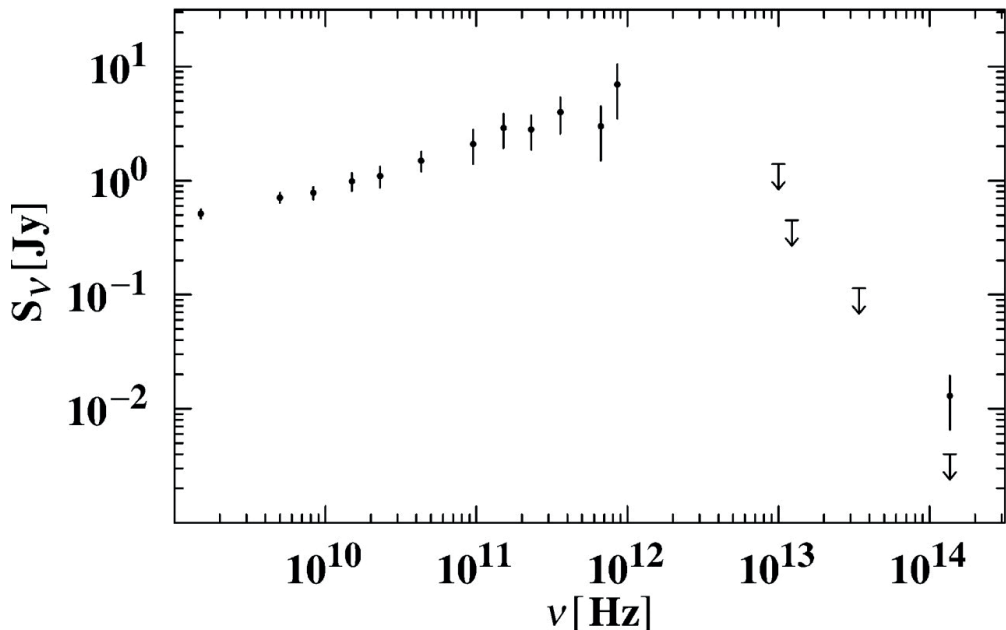


FIGURE 1.6: The spectral energy distribution of Sgr A\*. The spectrum shows a slightly inverted slope until 1 THz. Figure from Melia & Falcke (2001).

2019). Combining both the size and mass estimates, this suggests a compact object that powers emission over the full electromagnetic spectrum, the only viable object for this is a black hole. Measurements of the Schwarzschild precession (perihelion motion) of S2 around Sgr A\* put upper limits on the potential existence of a secondary intermediate-mass black hole (black holes with masses in the range of  $10^2$ - $10^5 M_\odot$ ) within the orbit of S2 to be smaller than  $10^3 M_\odot$  (GRAVITY Collaboration et al., 2020). Given the predicted shadow size of  $\theta_{\text{shadow}} = 50 \mu\text{as}$  Sgr A\* is one of the primary candidates of the Event Horizon Telescope Collaboration (EHTC). The goal of the EHTC is to image black holes on event horizon scales by using a global mm-VLBI array (for more details, see section 1.6.2).

The second primary candidate of the EHTC can be found in the elliptical galaxy Messier 87. The object was first discovered in the optical waveband by Heber Curtis in 1918, he described it as “*peculiar thin bright stream of matter originating from a compact source*” (Curtis, 1918). In the 1950s this feature was dubbed a ‘jet’ (Baade & Minkowski, 1954), which now is understood as a magnetized collimated outflow that is powered by accretion onto a compact object. The jet power of M87 is measured to be between  $10^{42}$  to  $10^{45} \text{ erg s}^{-1}$  (de Gasperin et al., 2012; Broderick et al., 2015). The jet radiates over the entire electromagnetic spectrum from radio (Bolton et al., 1949; Mills, 1952; Baade & Minkowski, 1954; Turland, 1975; Owen et al., 2000; Nagar et al., 2001; de Gasperin et al., 2012), to sub-mm (Junor et al., 1999; Ly et al., 2004; Krichbaum et al., 2006; Walker et al., 2008; Hada et al., 2011, 2013, 2016; Walker et al., 2018; Kim et al., 2018), to mm (Doeleman et al., 2012; Event Horizon Telescope Collaboration et al., 2019a), NIR (Perlman et al.,

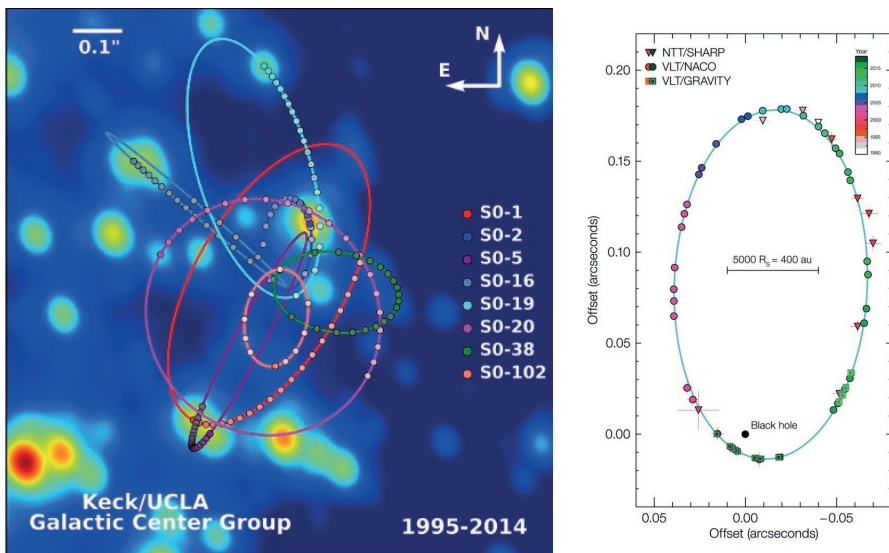


FIGURE 1.7: Left figure: the S star cluster around Sgr A\* as measured by Ghez et al. (2008). Image credit: the Keck/UCLA galactic center group. Right figure: the orbit of S2 as measured over 25 years of observations. The total period of the orbit is 16 years and the latest closest approach was in May 2018. Image credit: Gravity Collaboration et al. (2018)

2001; Prieto et al., 2016), optical (Perlman et al., 2011), X-ray (Wilson & Yang, 2001; Marshall et al., 2002; Perlman & Wilson, 2005) and gamma-rays (Albert et al., 2008; Abdo et al., 2009; Abramowski et al., 2012). The source shows X-ray variability on time scales of days (Harris et al., 2009). When observed in the radio regime, the jet size is inversely proportional to the observed frequency that flattens around 100 GHz, which suggest a compact source at its base (Hada et al., 2011). Previously indirect mass estimates based on gas dynamics and stellar motion suggests a compact mass of either  $3.5_{-0.3}^{+0.9} \times 10^9 M_{\odot}$  (Gebhardt et al., 2011) or  $6.1_{-0.6}^{+1.1} \times 10^9 M_{\odot}$  (Walsh et al., 2013). Based on these mass measurements, M87 has the second-largest angular size on the sky,  $\theta_{\text{shadow}} = 20 - 40 \mu\text{as}$ . In April 2019, the EHTC published the first image of the shadow of this supermassive black hole, providing evidence for the existence of a black hole at the center of M87\* that powers the observed jet (Event Horizon Telescope Collaboration et al., 2019a,b,c,d,e,f). Based on the measured shadow size of  $\theta_{\text{shadow}} = 42 \pm 3 \mu\text{as}$  the current mass estimate of M87\* is  $(6.5 \pm 0.7) \times 10^9 M_{\odot}$  (Event Horizon Telescope Collaboration et al., 2019a).

The first observational potential stellar-mass black hole is the bright X-ray source Cyg X-1. The X-ray Aerobee suborbital rocket (Bowyer et al., 1965) discovered Cyg X-1. The detection was later confirmed by two independent observations by Braes & Miley (1971); Hjellming & Wade (1971). In optical, it was found that this X-ray source is part of a binary system. The velocity measurement of the companion made it possible to make the first mass estimates of the central object (Bolton, 1972; Webster & Murrin, 1972). Based on the observed velocities, the current mass estimate of Cyg X-1 is  $14.8 \pm 1.0 M_{\odot}$  (Orosz et al., 2011). Given the high mass, it is unlikely

that this object is an accreting neutron star, which makes it a potential stellar-mass black hole.

A majority of the stars are part of a binary system. When these stars at the end of their lives become stellar-mass black holes, they start radiating gravitational waves (GW), resulting in the dissipation of orbital angular momentum, which results in binary black hole mergers. The LIGO collaboration measured the first GW event in 2015 (Abbott et al., 2016). The measured waveform is the best fit with a black hole binary with masses of  $36_{-4}^{+5} M_{\odot}$  and  $29_{-4}^{+4} M_{\odot}$ . This first direct measurement of gravitational waves provides evidence for the existence of black hole binaries. The first two completed science runs of LIGO/VIRGO contain ten black hole binary mergers (Abbott et al., 2019).

## 1.3 Accretion flows

### 1.3.1 Inflows

Astrophysical black holes are surrounded by accretion flows. These flows consist of ionized matter (plasma) originating from, for example, stellar winds, gas clouds, and tidal disruption events (tidally disrupted stars). Due to angular momentum conservation, a disk forms which rotates around the black hole. To transport plasma towards the horizon, it needs to liberate itself from angular momentum. The material can only fall towards the hole when it decreases its angular momentum. Based on the conservation of the angular momentum of the system as a whole, there should be a gain of angular momentum at larger radii leading to a flux of angular momentum outwards. Besides angular momentum, the accretion flow also releases gravitational energy. If a point particle of mass  $m$  free falls towards the event horizon of a black hole, it gains kinetic energy. The amount of energy gained, by using Newtonian gravity, is

$$E = \frac{GMm}{R_{\text{schw}}} = \frac{1}{2}mc^2 = \eta mc^2, \quad (1.7)$$

where we substituted the Schwarzschild radius, and  $\eta$  is the accretion efficiency (in this case  $\eta = 0.5$ ).

The first models for spherical accretion were developed by Hoyle & Lyttleton (1941); Bondi (1952), and for accretion disks by Weizsäcker (1943, 1948); Lüst (1952). The influential paper by Bondi (1952) assumed a spherically symmetric accretion flow onto a black hole. This model predicted a mass accretion rate of

$$\dot{M} = \frac{4\pi G^2 M^2 \rho_{\infty}}{(c_{s\infty}^2 + v_{\infty}^2)^{3/2}}, \quad (1.8)$$

where  $M$  is the mass of the accreting object,  $\rho_{\infty}$  is the density of the accreted material far away from the accretor,  $c_{s\infty}$  is the sound speed far away from the accreting object, and  $v_{\infty}$  is the velocity far away from the accretor. The initial studies by Hoyle & Lyttleton (1941); Bondi (1952) were Newtonian, later their results were, for the first time, generalized to relativistic solutions by Petrich et al. (1989).

Shakura & Sunyaev (1973) published a class of accretion disk models for geometrically thin and optically thick accretion flows called  $\alpha$ -disk model, this model was generalized to a relativistic version by Novikov & Thorne (1973). In these models, the turbulence of the gas introduces a

viscosity that is the source of angular momentum transport. The viscosity of the flow is set by  $\nu = \alpha c_s H$ , where  $H$  is the scale height of the disk. This model is a thin disk solution, where the accretion disk is relatively cold compared to the virial temperature ( $T_{\text{virial}} \approx 10^{12} K$ ). The disk consists of optically thick plasma that radiates as a black body. The  $\alpha$ -disk model is applicable to sources close to the Eddington Luminosity.

The actual mechanism causing the angular momentum transport remained unknown for almost three decades. In the early 1990s, Balbus & Hawley (1991) found that weak magnetic fields in a differentially rotating plasma give rise to an instability, called the magnetorotational instability. Shearing box simulations by Hawley et al. (1995); Balbus & Hawley (1998) showed that this instability in the non-linear phase triggers turbulence in accretion disks. These developments led to the generally accepted theory that the dissipation of angular momentum in accretion flows is mediated by turbulence that is generated by the MRI. The MRI instability arises when a magnetized flow undergoes differential rotation where the rotational velocity decreases as a function of increasing radius. When two plasma parcels at slightly different orbits are connected with a magnetic field line, they will undergo magnetic stresses. The parcel at the smaller radius will have a larger rotational velocity, it will try to outrun the second parcel, but the magnetic field line will act as a weak spring that will decrease the velocity of the parcel. To be able to conserve its angular momentum, the parcel will move inwards. The parcel at the larger radius accelerated by the magnetic field line and, based on angular momentum conservation, move outwards. However, when the rotational velocity of the flow as a whole decreases as a function of increasing radius, a new stable state is never reached. The rate of deceleration and acceleration keeps increasing as the parcels move away from each other and encounter larger differences in their velocities, which shows that this results in an unstable system. Since this effect happens at every radius for all fluid parcels, the fluid is mixed, leading to eddies that start turbulence.

In the case of advection dominated discs, the temperature of the accreting gas is close to the virial temperature of the flow. These disks are geometrically thick and optically thin and are modeled with Advection Dominated Accretion Flows (ADAF) (Narayan & Yi, 1994). In this regime, the accretion energy is viscously dissipated and heats the plasma flow instead of being radiated. A special class of the ADAF models is the Radiative Inefficient Accretion Flows (RIAF), which are accretion states with luminosities much lower than Eddington and have low surface densities (Ichimaru, 1977; Rees et al., 1982; Narayan & Yi, 1994, 1995b; Abramowicz et al., 1995). These models also intrinsically introduce a temperature difference between the electron and ion populations. The reason for the difference in temperature is because the electrons undergo radiation cooling, which is efficient, while protons cool via Coulomb interactions, which is inefficient due to the low densities, which makes the plasma collisionless. The RIAF model is successfully applied to low-luminosity AGN such as the black hole in the center of our galaxy or the one in Messier 87.

The second class of ADAF models applies to accretion flows, which are in an Eddington or super Eddington accretion state, and are called Slim disks (Begelman, 1979; Abramowicz et al., 1988). The accretion flow of a Slim disk is optically thick, and the mean free path of the photons becomes small compared to the system size. In this situation, radiation is trapped inside the flow and advected towards the black hole. The photons undergo interactions via collisions with the

plasma, enabling energy exchange. This results in additional radiation pressure force that puffs up the disk. This high-accretion state of the disk is optically thick and geometrically thick and is successfully applied to AGNs and X-ray binaries.

In the late 1970s pioneering work was done by Wilson (1977) and in the early 1980s by Hawley et al. (1984). They developed the first numerical tools to study accretion flows around compact objects, these codes solved the general relativistic magnetohydrodynamics equations (see section 1.4 for more details). Due to the low availability of computational resources, the field was not yet ready to grow. In the 1990s, with the increased availability of computational resources, a revival was led by work of Yokosawa (1993); Balbus & Hawley (1998); De Villiers & Hawley (2003). Currently many codes that use a large variety of numerical schemes are available to study accretion related problems, these are, among others, *Athena++* (White et al., 2016), *BHAC* (Porth et al., 2017) *Cosmos++*, *ECHO* (Del Zanna et al., 2007), *HAMR* (Liska et al., 2018), *HARM* (Gammie et al., 2003), *PLUTO* (Mignone et al., 2007), *KORAL* (Sądowski et al., 2013, 2017) and *RAISHIN* (Mizuno et al., 2006). In section 1.4, I will explain the formalisms used in these codes.

### 1.3.2 Outflows

Besides, an inflow of material accretion disks can also launch in some cases outflows, a mildly relativistic disk wind, and a relativistic jet. The disk wind is launched by magneto centrifugal forces acting on the edge of the accretion flow. Closer to the black hole where the differential rotation of both the disk and spacetime is largest, a relativistic jet is launched. Due to the differential rotation of the plasma, the initially poloidal magnetic field,  $B_p$  (pointing upwards along the black hole axis) is sheared. The shearing generates a toroidal magnetic field  $B_\phi$ , and induces an electric field in the  $\hat{\theta}$  direction,  $E_\theta$ , via  $\vec{E} = -(\vec{v} \times \vec{B})$ , where  $\vec{v} = R\Omega\hat{\phi}$ , where  $R$  is the radius,  $\Omega$  the orbital frequency, and  $B$  the magnetic field. The resulting in an  $E_\theta$  and  $B_\phi$  field generate a Poynting flux outflow  $\vec{S} = \frac{c}{4\pi}\vec{E} \times \vec{B}$ , which propagates outwards on radial curves supported by a pressure agent (e.g., a hot cocoon, or the pressure provided by the disk wind).

These Poynting flux dominated flows are observed as jets, see Figure 1.8 for the jet launched in the core of Messier 87. In the case of AGN, these jets can extend up to several Mpc and are responsible for emission over the entire electromagnetic spectrum, see the bottom part of Figure 1.8 for the spectral energy distribution of M87\*. The primary emission mechanism is synchrotron emission, which originates from the relativistic electron population that gyrates around the magnetic field lines.

Within the community, the most influential papers on jet launching models are the Blandford & Znajek (1977) (BZ) and Blandford & Payne (1982) (BP) models. Both models assume different origins of the rotation that is responsible for the jet launching. In the case of the BZ model, the rotation is provided by the black hole. While in the BP model, the rotation is provided by the accretion disk. In the BZ case, the total power of the outflow is given by

$$P_{\text{jet}} = \frac{\kappa}{4\pi c}\Phi\Omega_{\text{h}}, \quad (1.9)$$

where  $\kappa$  is a numerical factor,  $\Phi$  is the magnetic flux penetrating through the horizon, and  $\Omega_{\text{h}}$  the rotation of the horizon. The BZ model launches a relativistic outflow, jet, while the BP model can apply both to disk winds and jets. In realistic accretion flows, both processes are at play,

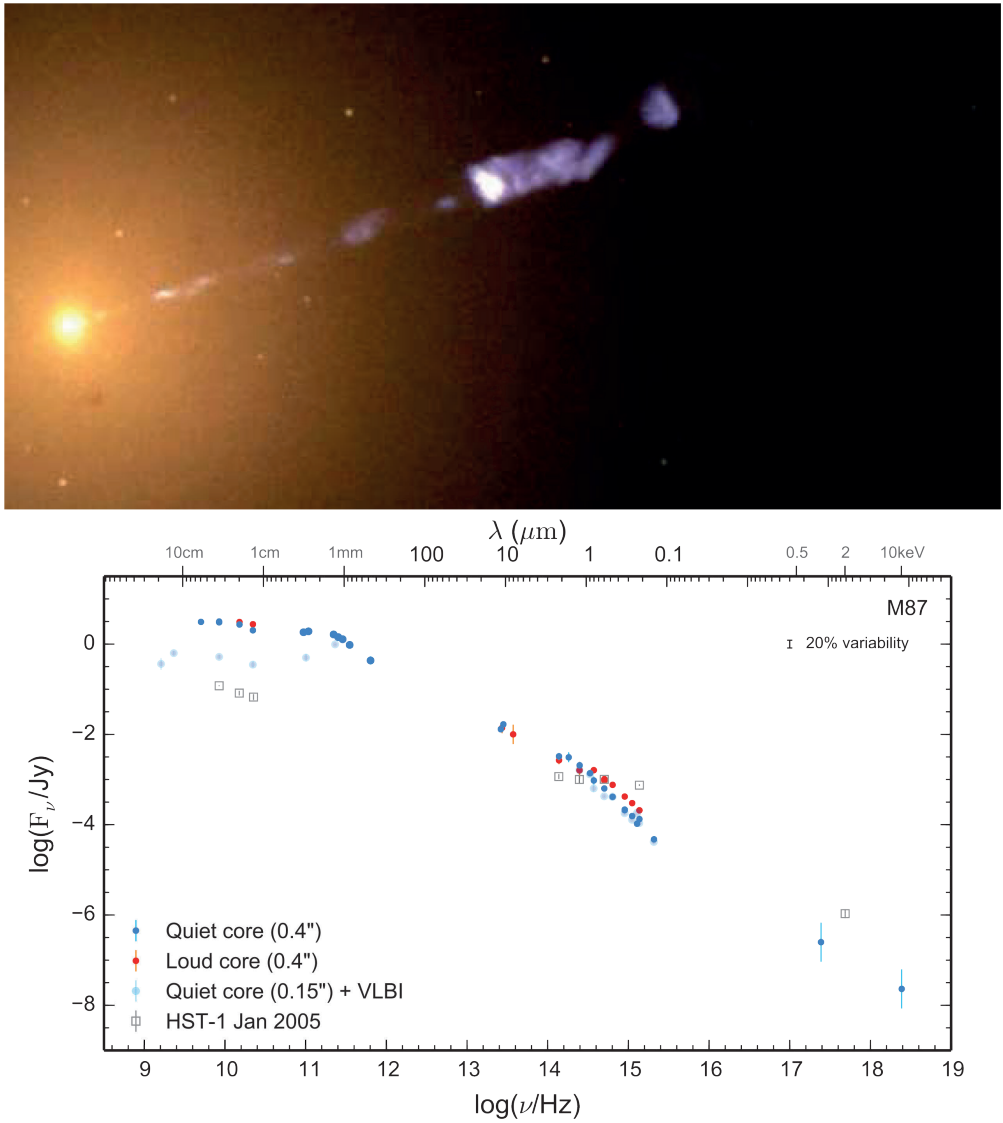


FIGURE 1.8: Top: The jet in M87 as measured with the Hubble Space Telescope. Image credit Biretta et al. (1999). Bottom: the spectral energy distribution of M87 as measured by Prieto et al. (2016).

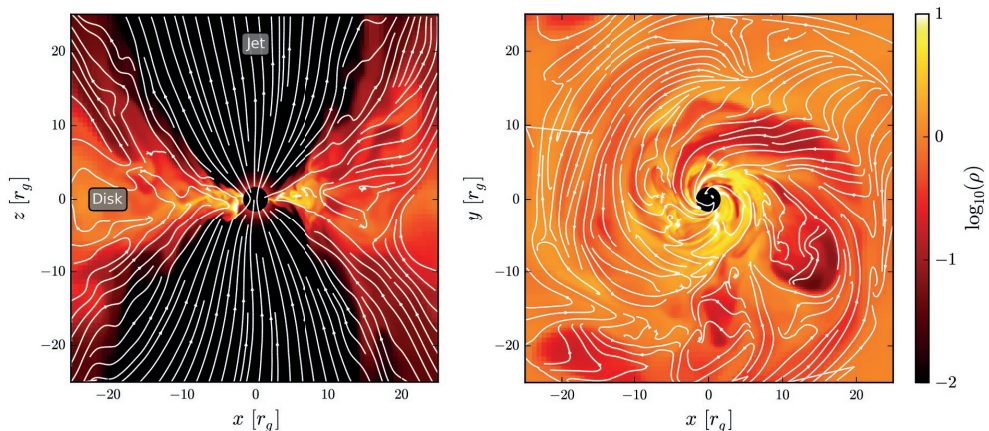


FIGURE 1.9: Simulation of black hole accretion with the code BHAC (Porth et al., 2017). Left panel: slice along the black hole spin axis, colormap is logarithm of density, white lines show magnetic field line. The jet and disk components are clearly visible. Left plot, shows same quantities but now sliced in the equatorial plane.

the relativistic jet interfaces with the disk wind resulting in a shear boundary where plasma is injected into the jet. After the jet is launched, it propagates outwards with a conical shape (Porth et al., 2011). Large-scale 2D simulations of jet launching were studied by Chatterjee et al. (2019) where they simulated the jet up to parsec scales and studied the interaction between the ambient medium and the highly relativistic jet. Accretion flows are numerically studied with general relativistic magnetohydrodynamics simulations (see next section for more details), an example simulation showing the accretion disk and jet is shown in Figure 1.9.

Blandford & Königl (1979) studied the radiative properties of jets. This model was extended by Falcke & Biermann (1995), where a connection between the disk and the jet was made. The number density in the jet scales as  $n \propto r^{-2}$ , the magnetic field strength with  $B \propto r^{-1}$ . From equipartition between magnetic energy and internal energy, it follows that the jet should be isothermal. The connection between the jet and the disk is then set by  $\dot{M} \propto Q_{\text{jet}}$ , where  $Q_{\text{jet}}$  is the jet power. The resulting jet spectra show a flat radio spectrum up to a break frequency where the emission becomes optically thin and follows a  $F_\nu \propto \nu^{-(p-1)/2}$  behavior when the electrons distribution function is a power-law distribution with power-law index  $p$ . The core position of the jet as a function of frequency in the flat part of the radio spectra follows a  $z \propto 1/\nu$  relation. These models successfully explain the flat radio spectra and core frequency dependence, as seen in (LL)AGN or in the low-state of X-ray binaries.

## 1.4 General relativistic magnetohydrodynamics

To model the full dynamics of the accretion flow the plasma can be approximated by a fluid. The system can then be evolved by using the general relativistic magnetohydrodynamics (GRMHD) equations (see e.g. Londrillo & Del Zanna (2000); Gammie et al. (2003); Porth et al. (2017);

White et al. (2016); Sądowski et al. (2013); Porth et al. (2019) among others). Which are given by,

$$\nabla_{\mu}(\rho u^{\mu}) = 0, \quad (1.10)$$

$$\nabla_{\mu} T^{\mu\nu} = 0, \quad (1.11)$$

$$\nabla_{\mu} {}^*F^{\mu\nu} = 0, \quad (1.12)$$

where  $\rho$  is the density,  $T^{\mu\nu}$  the stress-energy tensor, and  $F^{\mu\nu}$  the electromagnetic tensor which contains all electric and magnetic fields. The first equation is the conservation of mass, the second the conservation of energy and momentum, and the third equation the Maxwell equations. The tensor  $T^{\mu\nu}$  in the case of a plasma can be split in a fluid and electromagnetic part,

$$T_{fluid}^{\mu\nu} = (\rho + U + P)u^{\mu}u^{\nu} + pg^{\mu\nu}, \quad (1.13)$$

$$T_{EM}^{\mu\nu} = F^{\mu\alpha}F_{\alpha}^{\nu} - \frac{1}{4}g^{\mu\nu}F^{\rho\sigma}F_{\rho\sigma}, \quad (1.14)$$

where  $p$  is the fluid pressure,  $U$  the internal energy. The latter can be rewritten by defining an electromagnetic four-vector

$$b^{\mu} = \frac{1}{2}\epsilon^{\mu\nu\sigma\rho}u_{\nu}F_{\sigma\rho}, \quad (1.15)$$

where  $\epsilon^{\mu\nu\sigma\rho}$  is the Levi - Civita tensor which is antisymmetric under interchanging the indices. Using this in equation 1.14 gives

$$T_{EM}^{\mu\nu} = b^2u^{\mu}u^{\nu} + \frac{1}{2}b^2g^{\mu\nu} - b^{\mu}b^{\nu}. \quad (1.16)$$

Combining this with the fluid part this results in,

$$T^{\mu\nu} = (\rho + U + P + b^2)u^{\mu}u^{\nu} + \left(P + \frac{1}{2}b^2\right)g^{\mu\nu} - b^{\mu}b^{\nu}. \quad (1.17)$$

The GRMHD equation are then closed by the ideal MHD approximation,

$$u_{\mu}F^{\mu\nu} = 0, \quad (1.18)$$

which dictates that there are no electric fields in the comoving plasma frame, and the equation of state,

$$h(\rho, P) = 1 + \frac{\hat{\gamma}}{\hat{\gamma} - 1} \frac{p}{\rho}, \quad (1.19)$$

where  $h$  is the specific enthalpy, and  $\hat{\gamma}$  is the adiabatic index.

To solve these equations I used the GRMHD codes **BHAC** (Porth et al., 2017; Olivares et al., 2019) and **HARM** (Gammie et al., 2003). The **BHAC** code is a GR framework that builds upon the **AMRVAC** code (Porth et al., 2014; Xia et al., 2018). **BHAC** solves GRMHD equations in conservation form by using a finite volume method. Both codes are thoroughly tested in Porth et al. (2019).

The initial conditions of accretion onto a rotating black hole with spin  $a$ , are divided into two classes, Standard And Normal Evolution (SANE) or Magnetically Arrested Disks (MAD) (Narayan et al., 2003; Tchekhovskoy et al., 2011; Tchekhovskoy et al., 2012; McKinney et al., 2012), see Figure 1.10 for the initial conditions, shown is logarithm of density overplotted with

magnetic field lines, left SANE, right MAD. Both setups are initialized with a Fishbone-Moncrief torus (Fishbone & Moncrief, 1976), which is a hydro equilibrium solution for a disk in sub-Keplerian orbit around a rotating black hole. The difference between MAD and SANE is the initial configuration of the magnetic field. In the SANE case, the magnetic field is initialized via the vector potential given by

$$A_\phi \propto \max(\rho/\rho_{\max} - 0.2, 0), \quad (1.20)$$

while in the MAD case this is

$$A_\phi \propto \max(\rho/\rho_{\max} \left(\frac{r}{r_{\text{in}}}\right)^3 \sin^3 \theta \exp\left(-\frac{r}{400}\right) - 0.2, 0). \quad (1.21)$$

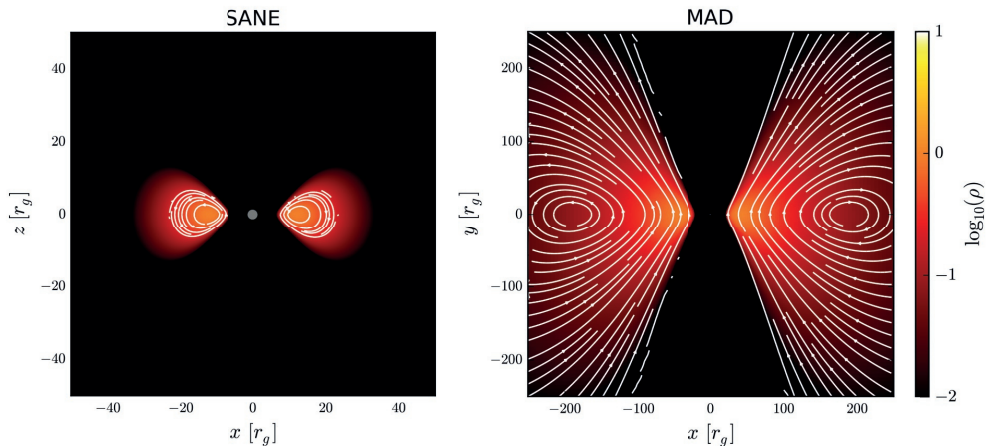


FIGURE 1.10: Initial conditions of GRMHD simulations. Left: Standard And Normal Evolution (SANE), right: Magnetically Arrested Disks (MAD). Both panels show the logarithm of the density, overplotted with magnetic field lines in white, gray area is location of event horizon.

The electromagnetic fields can then be computed via the electromagnetic tensor  $F^{\mu\nu} = \partial^\mu A^\nu - \partial^\nu A^\mu$ , where  $\partial^\mu = \partial/\partial x^\mu$  is the four gradient. One important constraint on the magnetic fields is that  $\vec{\nabla} \cdot \vec{B} = 0$  is conserved to machine precision. To this end we use in BHAC a staggered-mesh-based constrained transport algorithm that ensures machine precision conservation of  $\vec{\nabla} \cdot \vec{B} = 0$  (Olivares et al., 2019), in HARM a constraint transport scheme from T6th (2000) is used (Gammie et al., 2003).

In both cases the initial strength of the magnetic field is set such that  $\beta = p_{\text{fluid,max}}/p_{\text{B,max}} = 100$ . To speed up the development of MRI 4% of white noise is added to the fluid pressure. Besides a different initial magnetic vector potential also the disk size in the MAD case is substantially larger, where the SANE disk typically extends up to  $40 GM/c^2$  the MAD disk can extend beyond  $1000 GM/c^2$ . The result is that the initial conditions of the MAD consist of a poloidal dominated magnetic field. In the non-linear stage of the simulation this results to either low magnetic flux in the SANE case ( $\phi = \Phi/\sqrt{M} \approx 1$ , where  $\Phi$  is the magnetic flux on the event horizon), or maximum in the MAD case ( $\phi = \Phi/\sqrt{M} \approx 15$ ). When the MAD flow exceeds the MAD limit

of  $\phi = 15$ , the black hole rejects magnetic flux resulting in reconnection in the equatorial plane. The reconnection generates magnetic flux tubes that spiral outwards through the disk.

## 1.5 Radiation transport

In this thesis, I will study M87\* and Sgr A\*, both of these sources are low luminosity AGN, this means that they are radiatively inefficient since their luminosity is substantially lower than their Eddington luminosity. The advantage of this is that the radiation is decoupled from the global evolution of the plasma, which simplifies solving the GRMHD equation (no additional radiation terms need to be introduced). The validity of this assumption is studied by Dibi et al. (2012); Drappeau et al. (2013); Ryan et al. (2018), which includes radiation cooling into the GRMHD evolution. Dibi et al. (2012); Drappeau et al. (2013) conclude that radiative cooling is not important for Sgr A\*, while Ryan et al. (2018) shows that cooling is only moderately important for M87 within the inner  $10 GM/c^2$  of the accretion flow. To model the emission properties of these sources, post-processing of the GRMHD suffices. This is generally done by solving the radiation transport equations. In this section, I will explain general relativistic ray tracing and the electron physics needed to model my sources of interest.

### 1.5.1 General relativistic ray tracing

The GRMHD framework enables us to compute the geometry and dynamics of the accretion flow, but this does not include radiation or electron physics. To compute emission properties of the flow, these simulations, therefore, need to be post-processed with general relativistic radiative transfer (GRRT) codes (see e.g. (Broderick, 2006; Noble et al., 2007; Dexter & Agol, 2009; Shcherbakov & Huang, 2011; Vincent et al., 2011; Younsi et al., 2012; Chan et al., 2013; Younsi & Wu, 2015; Dexter, 2016; Schnittman et al., 2016; Chan et al., 2018; Mościbrodzka & Gammie, 2018; Bronzwaer et al., 2018)). The code I use and co-developed for the projects in this thesis is called the RAdboud Polarized integraTOR (RAPTOR) (Bronzwaer et al., 2018; Davelaar et al., 2018b; T. Bronzwaer, in prep). A ray tracing code computes null geodesics which start at a virtual camera outside of the GRMHD simulation domain. The camera consists of pixels which are assigned an initial photon wavevector  $k^\alpha$  and location  $x^\alpha$ . For every pixel on the camera, the code solves the geodesic equation, which is given by

$$\frac{d^2 x^\alpha}{d\lambda^2} = -\Gamma_{\mu\nu}^\alpha \frac{dx^\mu}{d\lambda} \frac{dx^\nu}{d\lambda}, \quad (1.22)$$

where  $\Gamma_{\mu\nu}^\alpha$  are the Christoffel symbols, and  $\lambda$  the affine parameter. The Christoffel symbols are computed by taking derivatives of the metric,

$$\Gamma_{\mu\nu}^\alpha = \frac{1}{2} g^{\alpha\rho} [\partial_\mu g_{\nu\rho} + \partial_\nu g_{\mu\rho} - \partial_\rho g_{\mu\nu}]. \quad (1.23)$$

The initial wavevectors  $k^\alpha$  are needed as initial conditions along with the position of the camera  $x^\alpha$ . The original RAPTOR code (Bronzwaer et al., 2018) initialises rays (i.e., photon geodesics) using impact parameters determined from coordinate locations on the observer's image plane (Bardeen et al., 1972), and uses Boyer-Lindquist coordinates. This method does not include potential

camera motion and is not generally applicable to arbitrary coordinate systems. For this thesis, it was extended to the procedure of Noble et al. (2007) to use an orthonormal tetrad basis for the construction of initial photon wave vectors, distributing them either uniformly as a function of  $\theta \in [0, \pi]$  and  $\phi \in [0, 2\pi]$  over a unit sphere or a segment on this sphere. This method is fully covariant and can be used in any coordinate system. The geodesic equation is then integrated with a fourth-order Runge-Kutta algorithm. This is done for  $x^\alpha$  and  $k^\alpha$ , by evaluation the RK4 coefficients given by (see Bronzwaer et al. (2018)),

$$C_{1,x^\alpha} = \Delta\lambda k^\alpha, \quad (1.24)$$

$$C_{2,x^\alpha} = \Delta\lambda \left( k^\alpha + \frac{1}{2}C_{1,x^\alpha} \right), \quad (1.25)$$

$$C_{3,x^\alpha} = \Delta\lambda \left( k^\alpha + \frac{1}{2}C_{2,x^\alpha} \right), \quad (1.26)$$

$$C_{4,x^\alpha} = \Delta\lambda \left( k^\alpha + C_{3,x^\alpha} \right), \quad (1.27)$$

$$C_{1,k^\alpha} = \Delta\lambda f^\alpha \left( \lambda, x^i, k^i \right), \quad (1.28)$$

$$C_{2,k^\alpha} = \Delta\lambda f^\alpha \left( \lambda + \frac{1}{2}\Delta\lambda, x^i + \frac{1}{2}C_{1,x^i}, k^i + \frac{1}{2}C_{1,k^i} \right), \quad (1.29)$$

$$C_{3,k^\alpha} = \Delta\lambda f^\alpha \left( \lambda + \frac{1}{2}\Delta\lambda, x^i + \frac{1}{2}C_{2,x^i}, k^i + \frac{1}{2}C_{2,k^i} \right), \quad (1.30)$$

$$C_{4,k^\alpha} = \Delta\lambda f^\alpha \left( \lambda + \Delta\lambda, x^i + C_{3,x^i}, k^i + C_{3,k^i} \right), \quad (1.31)$$

where  $\Delta\lambda$  is the stepsize for the affine parameter,  $f^\alpha$  is the right-hand side of the geodesic equation, which depends on all components of  $x^\alpha$  and  $k^\alpha$ . The updated values can then be found with,

$$x_{new}^\alpha = x^\alpha + \frac{1}{6} (C_{1,x^\alpha} + 2C_{2,x^\alpha} + 2C_{3,x^\alpha} + C_{4,x^\alpha}) + O(\Delta\lambda^5), \quad (1.32)$$

$$k_{new}^\alpha = k^\alpha + \frac{1}{6} (C_{1,k^\alpha} + 2C_{2,k^\alpha} + 2C_{3,k^\alpha} + C_{4,k^\alpha}) + O(\Delta\lambda^5). \quad (1.33)$$

When integrating the geodesic equation the code simultaneously solves the radiation transfer equation for the Lorentz invariant specific intensity  $I_\nu/\nu^3$ , where  $I_\nu$  is the specific intensity at frequency  $\nu$ . The transfer equation is then given by

$$\frac{d}{d\lambda} \left( \frac{I_\nu}{\nu^3} \right) = \frac{j_\nu}{\nu^2} - \nu\alpha_\nu \left( \frac{I_\nu}{\nu^3} \right), \quad (1.34)$$

where  $j_\nu$  is the emission coefficient,  $\alpha_\nu$  is the absorption coefficient, and  $\nu$  is the frequency in the comoving plasma frame computed via  $\nu = -k^\alpha u_\alpha$ , where  $u_\alpha$  is the plasma velocity. When integrating backward in time it is possible to solve this equation keeping track of the absorption along the ray, for every point the contribution  $j_\nu/\nu^2$  that is added to the intensity is then scaled with the total absorption until that point, such that,

$$\frac{d}{d\lambda} \left( \frac{I_{\nu,\text{obs}}}{\nu_{\text{obs}}^3} \right) = \frac{j_\nu}{\nu^2} \exp \left( -\tau_{\nu,\text{obs}}(\bar{\lambda}) \right), \quad (1.35)$$

with

$$\tau_{\nu,\text{obs}}(\lambda) = \int_{\lambda_{\text{obs}}}^{\lambda} \alpha_\nu(\lambda') \nu d\lambda'. \quad (1.36)$$

In RAPTOR emission and absorption coefficients for both thermal (Leung et al., 2011) and non-thermal distributions (Pandya et al., 2016) are present. An example image of RAPTOR is shown in 1.11.

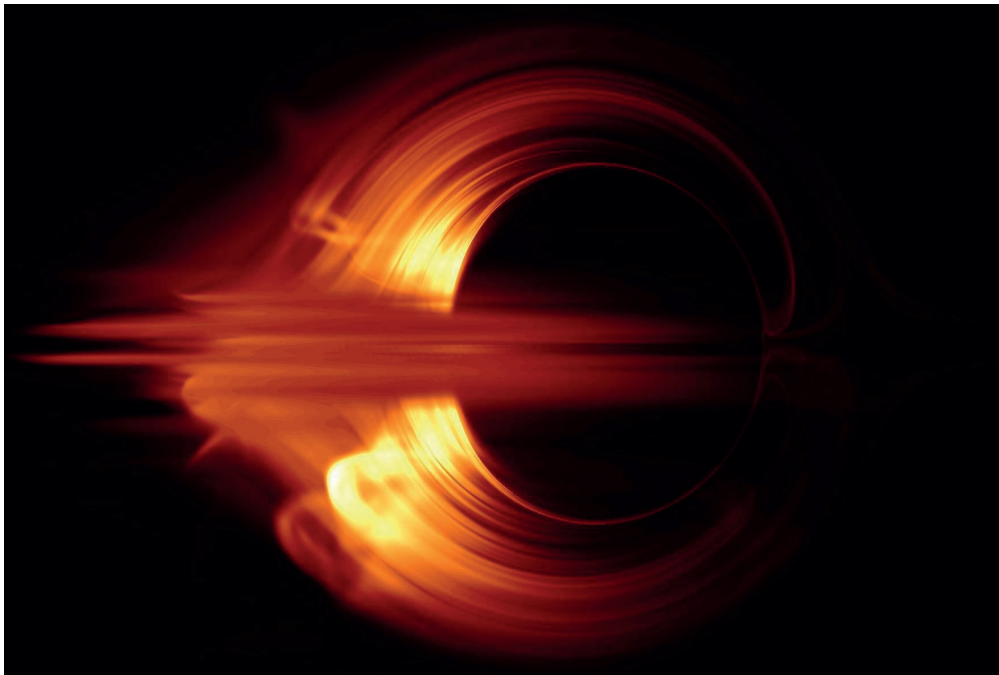


FIGURE 1.11: GRRT image of a black hole accretion flow. The model shows a  $230\text{GHz}$  disk model of Sgr A\* at a viewing angle, with respect to the black hole spin axis, of  $i = 90^\circ$ . The left/right asymmetry is caused by relativistic Doppler boosting. Clear lensed geometry visible, with a darkening in the center caused by the presence of a black hole. The rotating of the black hole causes the shadow to be asymmetric.

In figure 1.11, a 230 GHz synthetic image of Sgr A\* is shown. The viewing angle in this image is edge-on,  $i = 90^\circ$  with respect to the black hole spin axis. Multiple GR effects can be distinguished in this image. The ring-like structure is caused by gravitational lensing, geodesics follow the curvature of spacetime, and emission from behind the black hole is visible above and below the accretion disk. The left side of the image is brighter than the right side, and this is caused by relativistic Doppler boosting. The emission itself is optically thin, allowing us to see the shadow of the black hole in the center. The shadow in the image looks very similar to the ones presented in Falcke et al. (2000b), but the models in figure 1.11 3D GRMHD models which take the full evolution of the plasma into account, as explained in the previous section.

### 1.5.2 Electron temperature models

Traditionally GRMHD simulations compute the plasma as a single fluid. Therefore, only information about the dynamically important ions is present. Since electrons are the primary source of emission in LLAGN, a prescription to split the fluid into two components, namely the ions and electrons, is needed. The first models used a constant temperature ratio between the two species; this was done by Goldston et al. (2005a); Dexter & Agol (2009); Mościbrodzka et al.

(2009). These models were capable of fitting the 230 GHz emission and recovered the correct source sizes at that frequency. Mościbrodzka et al. (2009) also recovered the X-ray emission. Mościbrodzka & Falcke (2013); Mościbrodzka et al. (2014) extend these models by assuming that inside the accretion disk, the temperature ratio was large, so the electron temperature compared to the proton temperature is low in the disk and high in the jet. Within the outflow, the electron temperature has a constant value, the best fit value is  $\Theta_e = kT/m_e c^2 = 20$ . This isothermal jet model was inspired by the earlier analytical work by Blandford & Königl (1979) and Falcke et al. (1998). The model by Mościbrodzka & Falcke (2013) was capable of both recovering the full radio spectrum as well as obtaining correct source sizes for Sgr A\*.

For M87\* a new model was introduced by Mościbrodzka et al. (2016b) where the temperature ratio was set by the following parametrization,

$$\frac{T_p}{T_e} = R_{\text{high}} \frac{\beta^2}{1 + \beta^2} + R_{\text{low}} \frac{1}{1 + \beta^2}, \quad (1.37)$$

where  $\beta = \frac{P}{P_{\text{mag}}}$  is the ratio between the gas and magnetic pressure. In the regions where  $\beta$  is large the ratio is set by  $R_{\text{high}}$  and when  $\beta$  is small by  $R_{\text{low}}$ , where typically  $R_{\text{high}} \gg R_{\text{low}}$ , such that the jet is hot and the disk is cold. The best fit model for M87\* was for  $R_{\text{high}} = 100$ , in this case the model was consistent with radio, mm and X-ray observations.

More recently, an effort was made to include electron physics within the GRMHD equations. This was done by Ressler et al. (2015a) who extended the single fluid equations of section 1.4 to a multi-fluid by defining two separate stress-energy tensors for electrons and protons and adding heat sources  $q_{e/p}^\mu$  and a general stress-energy tensor  $\tau_{e/p}^{\mu\nu}$  that accounts for viscosity effects. These electron/proton stress-energy tensors are given by,

$$T_e^{\mu\nu} = (\rho_e + u_e + P_e)u_e^\mu u_e^\nu + P_e g^{\mu\nu} + \tau_e^{\mu\nu} + q_e^\mu u_e^\nu + q_e^\nu u_e^\mu \quad (1.38)$$

$$T_p^{\mu\nu} = (\rho_p + u_p + P_p)u_p^\mu u_p^\nu + P_p g^{\mu\nu} + \tau_p^{\mu\nu}. \quad (1.39)$$

The first two equations that are solved do not change. These again include the conservation of mass and the conservation of momentum and energy but now for both species. Given that the number of free parameters increased, an additional set of equations needs to be solved, namely the entropy equations for the electrons. For this extra set of equations, there is still one unknown left, a prescription for the heat sources. In the literature three different sources are used, by using isotropic heat fluxes (Ressler et al., 2015a; Chandra et al., 2015), turbulent heating (Howes, 2010; Chael et al., 2018a, 2019; Anantua et al., 2020), reconnection heating (Rowan et al., 2017; Chael et al., 2018a, 2019; Anantua et al., 2020). The first two show similar behavior as the  $\beta$  prescription with a large  $R_{\text{high}}$  value, with high temperatures in the jet and low temperatures in the disk. The reconnection prescription shows more uniform heating throughout the flow. The disadvantage of methods like this is that the underlying plasma physics still is unresolved, the heating prescription relies on the assumption that these physical processes happen on the subgrid-scale, which is not always per se the case. For example, in the case of MAD accretion flows, turbulence is absent. Also, the methods only recover the energy content of the distribution functions, and there is no information on the shape; for example, reconnection or heating could result in the formation of power-laws or multi-Maxwellian distributions.

In the past, studies including non-thermal electron emission were performed by Özel et al. (2000); Dexter et al. (2012b); Mao et al. (2017); Ball et al. (2016). Özel et al. (2000) used semi-analytical RIAF models to model SgrA\*. The electron distribution function was assumed to have a constant power-law index throughout the full domain. Overall they see that the NIR emission is enhanced (tail) as well as the low-frequency part of the radio spectrum (shoulder). Mao et al. (2017) found a similar effect when using GRMHD simulations, where they also set the power-law index constant in the full domain. Ball et al. (2016) deviated from this by only assuming a power-law in the region of low plasma  $\beta$ . Similar efforts for M87 were made by Dexter et al. (2012b), where the energy in the power-law was set by the local available electromagnetic energy.

## 1.6 Approaching the event horizon

Since the start of the 21st century, astronomers opened the window towards the event horizon. First by the first detection of gravitational waves from binary black hole mergers by LIGO/VIRGO, followed by many subsequent events. A second feat is the observations performed by the GRAVITY instrument, which detected and spatially resolved NIR flares at the ISCO of Sgr A\*. The latest triumph is the first black hole shadow image as released by the Event Horizon Telescope Collaboration on April 10th, 2019.

### 1.6.1 GRAVITY

The GRAVITY instrument is a combination of the Very Large Telescope Interferometer (VLTI) by using near-infrared (NIR) interferometry. The effective resolution for astrometry is  $20 - 70 \mu\text{as}$ . During the observational campaign in 2018 (Gravity Collaboration et al., 2018), three bright NIR flares were observed, and their centroid motion was tracked as they moved through the accretion flow of Sgr A\*. One of the three flares is shown in figure 1.12.

GRRT simulations of analytical hotspots around non-rotating black holes were compared to the data to obtain the parameters of the orbit of these flares. The resulting parameters suggest that both flares originated close to the ISCO ( $r = 7 \pm 0.5 GM/c^2$ ) and that the viewing angle with respect to hot spot angular momentum axis is almost face-on  $i = 160^\circ$  (Gravity Collaboration et al., 2018) or more recently around  $i = 140^\circ$  (GRAVITY Collaboration et al., 2020). Besides intensity also the polarization fractions were measured. The polarized signal shows smooth loops in a  $Q - U$  plane, which suggests that polarization is orthogonal to the orbit of the flare. This result hints at that the underlying magnetic field is in a poloidal configuration, which also supports a face-on viewing angle (Gravity Collaboration et al., 2018). The modeling used to interpret the flares does not take into account the dynamics of the accretion flow or include any non-thermal effects on the underlying particle distributions.

### 1.6.2 The Event Horizon Telescope

In April 2019 the Event Horizon Telescope Collaboration released the first image of the shadow of the supermassive black hole in Messier 87 (Event Horizon Telescope Collaboration et al., 2019a,b,c,d,e,f). This image was one of the main results of an observational campaign in April 2017, where for the first time, the Atacama Large Millimeter Array (ALMA) joined the observ-

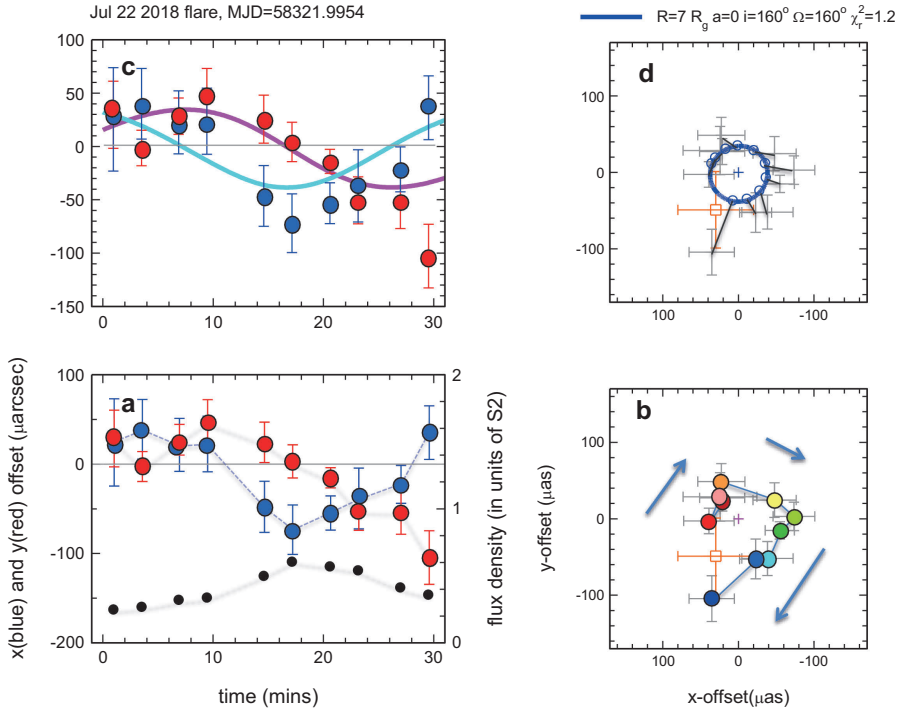


FIGURE 1.12: Flare observed by the GRAVITY collaboration. Top left panel, position offset as a function of time with respect to Sgr A\* along the x or y axis overplotted with a model of a hot spot orbiting the black hole (cyan and pink lines). Top right: projected motion of the model of the orbiting hot spot around Sgr A\* and the data, yellow cross shows Sgr A\* position. Bottom left:  $x$  and  $y$  offset as function of time based on the July 22 flare data as observed by GRAVITY. Bottom right: project centroid motion of the flare around Sgr A\* of the flare. Figure credit: Gravity Collaboration et al. (2018).

ing campaign of the EHT. Together with ALMA, the following stations participated: Atacama Pathfinder Experiment (APEX), James Clerk Maxwell Telescope (JCMT), Submillimeter Array (SMA), Submillimeter Telescope (SMT), Large Millimeter Telescope Alfonso Serrano (LMT), Pico Veleta 30 m telescope (PV), and the South Pole Telescope (SPT). The current array configuration and historic telescopes used in previous observing runs are shown in Figure 1.13.

The EHTC uses a technique in radio astronomy called Very Long Baseline Interferometry (VLBI). This method is based on using telescopes at different locations on the Earth that independently record radio waves from the same source. The signal is digitized and labeled with a timestamp from an atomic clock. At computing centers, the signals from the telescopes are then correlated, resulting in complex visibilities measured between two different telescopes. A complex visibility is a complex cross-correlation between the measured electromagnetic waves. The projected distance between the telescopes, called a baseline  $b$ , sets the resolution scale that

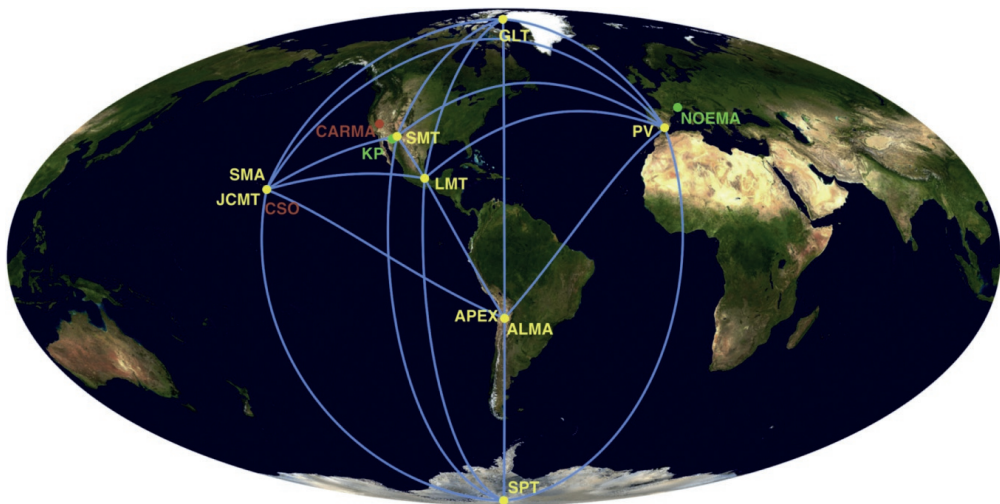


FIGURE 1.13: The 2017 EHT array and additional historical telescope sites used in the past by the EHTC. Image taken from (Event Horizon Telescope Collaboration et al., 2019c).

is probed. The larger the baseline, the smaller the resolution,  $\theta \propto \lambda/b$ . In the case of the EHTC 2017 array, the effective resolution was  $\theta \approx 20 \mu\text{as}$ .

The observing schedule of the EHTC was a ten-day window with the opportunity to observe on five days within this window, during four days M87\* was observed. Every observing day of M87\* consisted of subsequent five minute long scans, alternating between M87\* and one calibrator, 3C 279 (Kim et al., 2020).

Besides the 1.3 mm campaign of the EHTC, various observatories joined the observational campaign, covering the spectral energy distribution (SED, measured flux as a function of observing frequency) from radio to gamma-rays. An overview of the different groups and their observing time is shown in Figure 1.14. This multi-wavelength information is especially crucial for constraining models since multi-wavelength emission is sensitive to the underlying electron distribution.

Two classes of imaging methods are used within the EHTC to construct images based on the complex visibility information recorded at the telescopes. The first one is called inverse modeling. In this process, one typically starts with performing a direct Fourier transform, which is called a “dirty image”. This first trial is then used by methods like CLEAN (Högbom, 1974; Clark, 1980) to subtract point sources with their dirty beam and restore them with the clean beam. The point sources vary in location and their flux densities. After every iteration, the resulting image is compared to the data. The process is stopped after some user-defined end criterion is met. The EHTC uses the DIFMAP software package (Shepherd, 1997) for this imaging class. The second method class is forward imaging. In this case, the image is constructed based on an array of pixels. At every iteration, the algorithm adds or subtracts flux to this image plane, and via a Fourier transform, the model image is compared to the data, and via  $\chi^2$  optimization, the best fit is found. In the EHT forward imaging software called the eht-imaging (Chael et al., 2016, 2018b) and SMILI packages (Akiyama et al., 2017) are used. In the top panels of figure 1.15 the

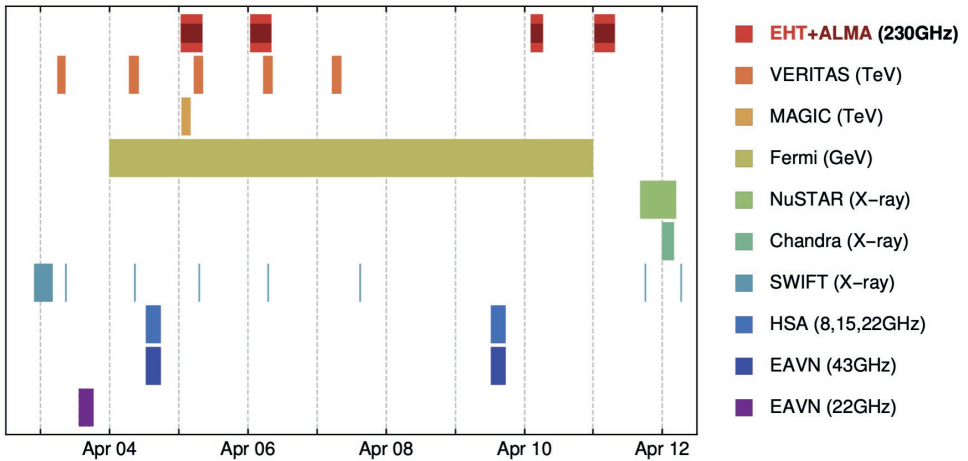


FIGURE 1.14: The multiwavelength coverage of M87\* during the 2017 observation campaign. Image credit: M. Johnson, CfA/SAO

final images for both three software packages are shown, all three show a consistent ring, with similar size and asymmetry. In the bottom panel of figure 1.15, the consensus image is shown for all four observing days.

For the theoretical interpretation of the results, GRMHD simulations are performed. The spin of the black hole is set to be  $a \in (-15/16, -1/2, 0, 1/2, 15/16)$ , and both MAD and SANE simulations are performed. The GRMHD codes BHAC (Porth et al., 2017), HAMR (Liska et al., 2018), KORAL (Sądowski et al., 2013, 2017), and *iharm* (Gammie et al., 2003) were used, which were all benchmarked in (Porth et al., 2019). The output cadence is every  $10 GM/c^3$ . To compare to the data these snapshots are post-processed with the GRRT codes, RAPTOR (Bronzwaer et al., 2018), BHOSS (Younsi & Wu, 2015) and *ipole* (Noble et al., 2007; Mościbrodzka & Gammie, 2018). The parameters varied in the GRRT simulations are the inclination and the  $R_{\text{high}}$  parameter. The mass accretion rate is set such that the models produce a core flux of  $F_{230\text{GHz}} = 0.6$  Jy. The electrons are assumed to be in a thermal distribution function. The resulting image library contains 60.000 images. The images are then processed in the scoring pipeline of the EHTC. The models are compared to the data by finding the best fit value for the mass and position angle (the orientation of the black hole spin axis). The mass is altered by rescaling the field of view of the original image. The position angle is changed by rotating the images. The model images are compared to the data in the Fourier domain. The resulting Average Imaging Score is then a measure of how well the model fits the data. Within the EHTC, there are two scoring pipelines present, THEMIS (a Monte Carlo Markoff Chain method, Broderick et al. (2020)) and GENA (evolutionary algorithms, Fromm et al. (2019)). Both pipelines are used to perform the fitting of the GRRT images. A best-fit model with and without a telescope beam filter, together with the observed image, is shown in Figure 1.16.

The parameter extraction that was done by the EHTC resulted in an angular size on the sky of  $GM/c^2 D = 3.8 \pm 0.4 \mu\text{as}$ , using a distance of  $D = 16.8_{-0.7}^{+0.8}$  Mpc. This results in a mass of

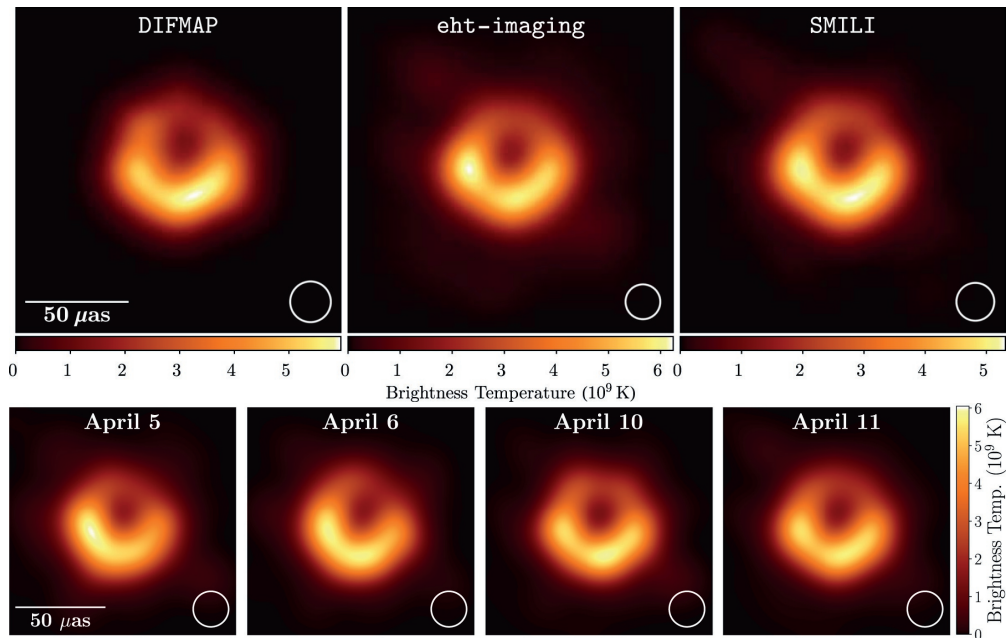


FIGURE 1.15: Top panel: resulting images from different imaging methods, from Event Horizon Telescope Collaboration et al. (2019d). Bottom panel: consensus images for all four observing days for M87, image from Event Horizon Telescope Collaboration et al. (2019d).

$6.5 \pm 0.7 \times 10^9 M_{\odot}$ . The angular size was extracted by comparing analytic crescent models and GRMHD models to data, and by directly extracting the size from the data. The majority of the flux originates ( $>50\%$ ) from the ring. Inside the ring, a flux depression of factor ten is seen. The mass estimate of the EHT is in agreement with the measurement based on the stellar dynamics. The observations are, within the observational constraints, consistent with GR.

## 1.7 Kinetic plasma physics

One of the open questions in the field of computational astrophysics is how to both recover the small scale and large scale physics, which is referred to as a scale separation problem. GRMHD simulations, such as the ones used by Event Horizon Telescope Collaboration et al. (2019e), tend to recover the overall global structures accurately when the MRI wavelength is properly resolved, but they do not hold any information on microphysics that governs radiation and electron physics. The connection between the micro and macro scales is to this date unresolved. The kinetic properties of the plasma are governed by the electron physics on the subscales of the system, in the case of supermassive black hole accretion flows of LLAGN this is below  $10^8$  cm which ten orders of magnitude smaller than the typical system size.

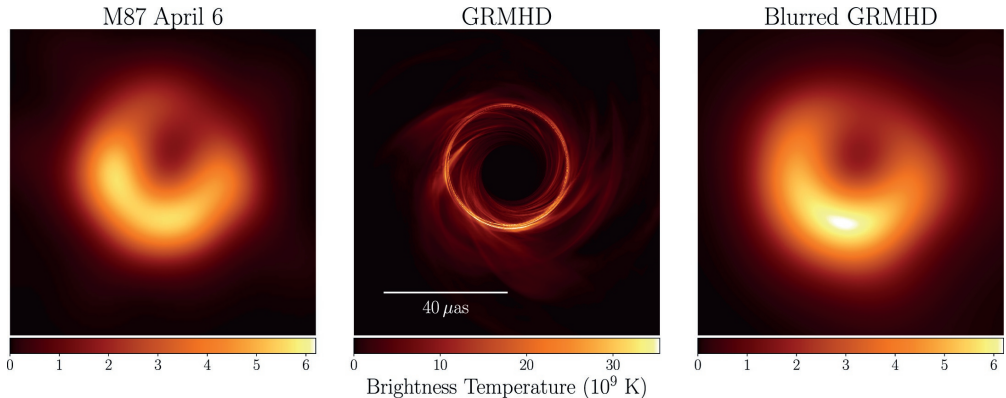


FIGURE 1.16: Comparison between the data and typical GRMHD model from Event Horizon Telescope Collaboration et al. (2019e). Left panel show the observations, middle panel the GRMHD model, right panel the GRMHD model convolved with a Gaussian beam of 20  $\mu\text{as}$ . Image taken from Event Horizon Telescope Collaboration et al. (2019e).

Kinetic effects are important when the plasma is collisionless, which means that the mean free path of an electron is much larger than the actual system size. The mean free path is given by

$$l_{\text{mfp}} = \left(\frac{v}{c}\right)^4 \frac{1}{4\pi n_e \sigma_T \ln \Lambda}, \quad (1.40)$$

where  $\sigma_T$  is the Thomson cross-section and  $\Lambda$  the Coulomb logarithm. If collisions are frequent, the scattering of particles will result in a distribution function that can be described by a single temperature. When a plasma is collisional, it is possible to treat it as a fluid, which is the underlying assumption in MHD. In the collisionless case, this is only true for large scales or large temporal variants. In the case of supermassive black holes that are studied by the Event Horizon Telescope collaboration the mean free path of an electron is typical  $l_{\text{mfp}} \geq 10^8 GM/c^2$ , the actual shape of the distribution function is, therefore, unknown since it cannot be assumed to be purely thermal in GRMHD. However, collisionless systems can be simulated using Particle-in-Cell based methods which solve for particle motions in time-varying electromagnetic fields in a self-consistent way. These simulations are, however, mainly performed in local contexts, first global simulations of black hole magnetospheres are currently only possible in a 2D setup, and this setup does not include realistic inflow conditions or accretion disks. This highlights the importance of building a connection between these two methods where information on the local small scales computed in PIC is connected to the large-scale simulations that can be performed with GRMHD.

### 1.7.1 Particle-in-Cell methods

Particle-in-Cell (PIC) methods are used to perform kinetic simulations of plasma, which self consistently solve both the motion of charged particles as well as electromagnetic fields. This method is widely used in astronomy to simulate: pulsars magnetospheres (Philippov et al., 2015; Cerutti et al., 2016), shocks (Spitkovsky, 2008), reconnection (Loureiro et al., 2007; Sironi &

Spitkovsky, 2014; Werner et al., 2016), and black hole magnetospheres (Parfrey et al., 2019; Crinquand et al., 2020).

The first set of equations that needs to be solved in PIC are the Maxwell equations given by,

$$\vec{\nabla} \cdot \vec{E} = 4\pi\rho, \quad (1.41)$$

$$\vec{\nabla} \cdot \vec{B} = 0, \quad (1.42)$$

$$\vec{\nabla} \times \vec{E} = -\frac{1}{c} \frac{\partial \vec{B}}{\partial t}, \quad (1.43)$$

$$\vec{\nabla} \times \vec{B} = \frac{1}{c} \frac{\partial \vec{E}}{\partial t} + \frac{4\pi}{c} \vec{J}. \quad (1.44)$$

The simulation grid typically used in PIC methods is a Yee staggered grid (Yee, 1966). The grid is a staggered grid which means that different electromagnetic components are assigned to different positions on the grids. This is done in such a way that the circulation of  $\vec{B}$  or  $\vec{E}$  corresponds to flux in either  $\vec{E}$  or  $\vec{B}$ , see Figure 1.17. The electric field components typically lie along vertices, while magnetic components are perpendicular to the face centers. The Maxwell equations are then solved via either implicit or explicit integrators. The two unknowns are however the local charge and current densities which are generated by the charged particles in the plasma.

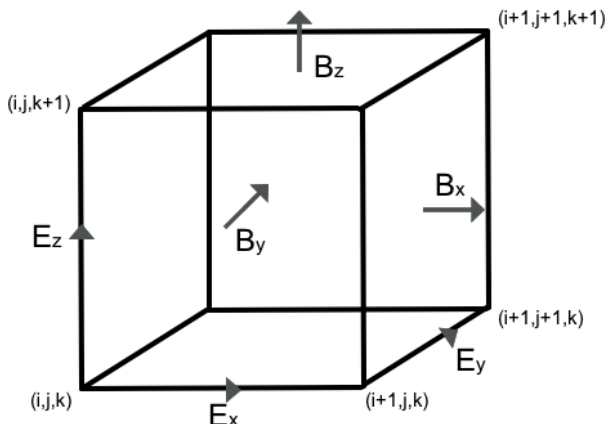


FIGURE 1.17: The staggered Yee grid with the electromagnetic components drawn on top of it. The magnetic field is face centered, while the electric fields are along the borders of the cell.

The charged particles are located within the grid cells where they, under the influence of electric and magnetic fields, gyrate and accelerate or decelerate due to the Lorentz force. Their equation of motion (EOM) is given by

$$\frac{d\vec{x}}{dt} = \vec{p} \frac{d\vec{p}}{dt} = F_{\text{Lorentz}} = \frac{q}{m} (\vec{E} + \frac{1}{c} \vec{v} \times \vec{B}). \quad (1.45)$$

Before solving the EOM for the particles, the fields are first interpolated to the current position of the particle. The particle position is then updated by using a particle pusher. One of the widely used pushers is the Boris pusher (Boris, 1970), for a comparison between different solvers see

Bacchini et al. (2019). The Boris pusher is an implicit method for solving the Lorentz equation using a leapfrog scheme. The EOM is split in a first half step update on the electric field, one full step on the magnetic fields, and then one more half step on the electric field. This method ensures energy conservation to machine precision such that gyro motions are well recovered.

The particles position and velocities are then used to compute the total charge and current densities onto the Yee mesh

$$\rho(\vec{x}) = \sum_i q_i \delta(\vec{x} - \vec{x}_i) \quad (1.46)$$

$$\vec{J}(\vec{x}) = \sum_i q_i \delta(\vec{x} - \vec{x}_i) \vec{p}_i / m_i. \quad (1.47)$$

This last step is called current deposition. In this formula, I described particles with a delta function, in practice, people use different shape function that smear out the charge distribution of a particle over a slightly larger volume, for example a triangular shape or a Gaussian profile. This is used to decrease noise within the the simulation.

Simulations are then initialized with an electromagnetic field configuration and the particle distributions to support these fields. At every time step, the above-explained steps are performed until an end criterion is met. The steps within a PIC code are schematically shown in Figure 1.18.

An important free parameter of PIC simulations is the skin depth  $\sigma_{\text{skin}}$  which is connected to the plasma frequency  $\omega_p$  via  $\sigma_{\text{skin}} = c/\omega_p$ . This parameter sets how well the kinetic scale is resolved compared to the typical length scale of the system (for example, the length of a current sheet, the size of a jet or the size of the simulation domain), if the ratio of these two length scales is too small, the system is affected by the kinetic scale, and the global evolution is not accurately captured.

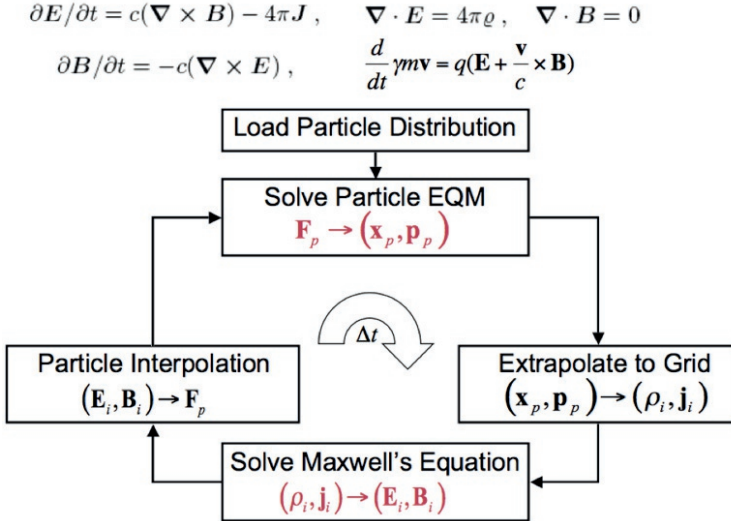


FIGURE 1.18: The equations that are solved in PIC and a flow diagram of steps needed in kinetic plasma simulations. Image courtesy: A. Philippov

### 1.7.2 Reconnection

One of the proposed mechanisms for non-thermal emission in AGN jets is reconnection (Romanova & Lovelace, 1992; Giannios, 2013) or shocks (Heavens & Drury, 1988). In Sironi et al. (2015) it is argued that in magnetized environments such as at the jet launching footpoint of M87 shocks are inefficient particle accelerators. Shocks can, however, become important again at larger radii when most of the electromagnetic energy is dissipated. In chapter 3, I will use prescriptions of reconnection from Ball et al. (2018) to model the NIR emission of M87\*. In this section, I will summarize the general properties of this mechanism by giving a historical overview of the research conducted on this topic.

Magnetic reconnection is an efficient mechanism that converts magnetic energy into kinetic energy by changing the topology of magnetic field lines. The electrons or ions that undergo acceleration to high Lorentz factors produce high energetic non-thermal emission. Astrophysical sources for which reconnection is thought to be the main emission mechanism are, the magnetosonic tail of the Earth (Dungey, 1961), the solar corona (Low & Wolfson, 1988), AGN jets (Romanova & Lovelace, 1992; Giannios, 2013; Sironi et al., 2015), pulsars and pulsar wind nebula (Lyubarsky & Kirk, 2001; Kirk & Skjaraasen, 2003; Pétri & Lyubarsky, 2007; Cerutti et al., 2013), and GRBs (Thompson, 1994; Spruit et al., 2001; Lyutikov & Blandford, 2003).

The Parker and Sweet model (Parker, 1957) is the first analytical prescription of reconnection. In their model, magnetic field lines of opposite sign are advected towards each other. In the region where these lines meet, a current sheet develops, which results in an outflow of material parallel to the original field lines. A schematic sketch is shown in Figure 1.19.

When reconnection is treated in steady-state the electric field generated in the sheet is given by

$$\vec{E} = -\frac{\vec{v}_{\text{in}} \times \vec{B}}{c}, \quad (1.48)$$

where  $v_{\text{in}}$  is the inflow velocity and  $B$  the magnetic field strength outside of the current sheet. The reconnection rate can be defined from mass conservation,

$$n\delta v_{\text{out}} = nLv_{\text{in}} \quad (1.49)$$

$$r_{\text{rate}} = \frac{\delta}{L} = \frac{v_{\text{in}}}{v_{\text{out}}} \quad (1.50)$$

In steady-state flows the outflowing velocity is close to the Alfvénic velocity,  $v_A = c\sqrt{\sigma/(\sigma+1)}$ . The Lundquist number is a measure of the importance of kinetic effects, and is defined as  $S = v_AL/\eta$ , where  $\eta$  is the resistivity of the plasma. The reconnection rate can then be rewritten such that

$$r_{\text{rate}} \approx \frac{1}{\sqrt{S}}. \quad (1.51)$$

This equation shows a large limitation of the steady-state Sweet-Parker model. The typical value for  $S$  in astrophysical systems is of the order of  $10^{20}$ , resulting in low reconnection rates. This value is in contradiction with, for example, observations of flares in the solar corona or from AGN which show fast reconnection rates of  $r_{\text{rate}} \approx 0.1$ .

The Sweet-Parker model's blind spot lies in what happens in the non-ideal current sheet. Non-ideal effects violate flux freezing and introduce effects from the kinetic scales. This sheet is shown

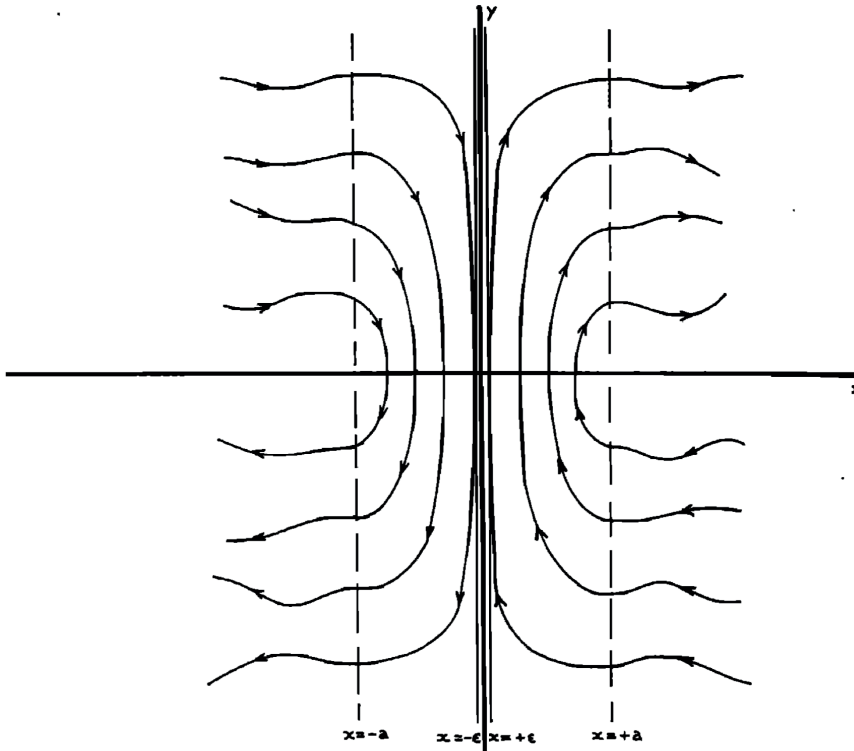


FIGURE 1.19: Schematic overview of magnetic reconnection as published by Parker (1957). The field lines left and right show opposite polarity and at  $x = \pm\epsilon$  a current sheet is shown.

to be unstable to tearing and plasmoid instabilities (Furth et al., 1963; Loureiro et al., 2007). An example of a plasmoid unstable current sheet can be seen in figure 4.4. These instabilities result in tearing of the current sheet and fragmenting it in smaller sheets. The results in the generation of X-points in the current sheet where reconnection happens that are alternated by magnetic islands. This shortens the effective length of the current sheet and therefore increases the reconnection rate. Plasmoid formation in reconnection is extensively studied with PIC simulations of Harris sheets. A Harris sheet is a 1D equilibrium that has a flip of the magnetic field x-component over a distance  $\delta$  along the y-axis and is given by

$$B_x = B \tanh \frac{y}{\delta}. \quad (1.52)$$

PIC simulations showed that reconnection can efficiently accelerate electrons to maximum Lorentz factors of  $\gamma \approx 4\sigma$  (Werner et al., 2016), and have reconnection rates of the order of  $r_{\text{rate}} \approx 0.01-0.1$ . The resulting particle distribution function is a combination of a thermal core connected to a power-law. PIC simulations for various  $\sigma$  and  $\beta$  values were studied by Werner & Uzdensky (2017); Ball et al. (2018), where they found that the power-law index  $p$ , as a function of  $\sigma$  and  $\beta$ ,

is given by

$$p = A_p + B_p \tanh(C_p \beta) \quad (1.53)$$

$$A_p = 1.8 + 0.7/\sqrt{\sigma} \quad (1.54)$$

$$B_p = 3.7 \sigma^{-0.19} \quad (1.55)$$

$$C_p = 23.4 \sigma^{0.26}. \quad (1.56)$$

In 3D simulations, the long term evolution of the distribution function is studied and Petropoulou et al. (2016); Petropoulou & Sironi (2018) found that the maximum gamma grows with  $\gamma_{\max} \propto t^{1/2}$ .

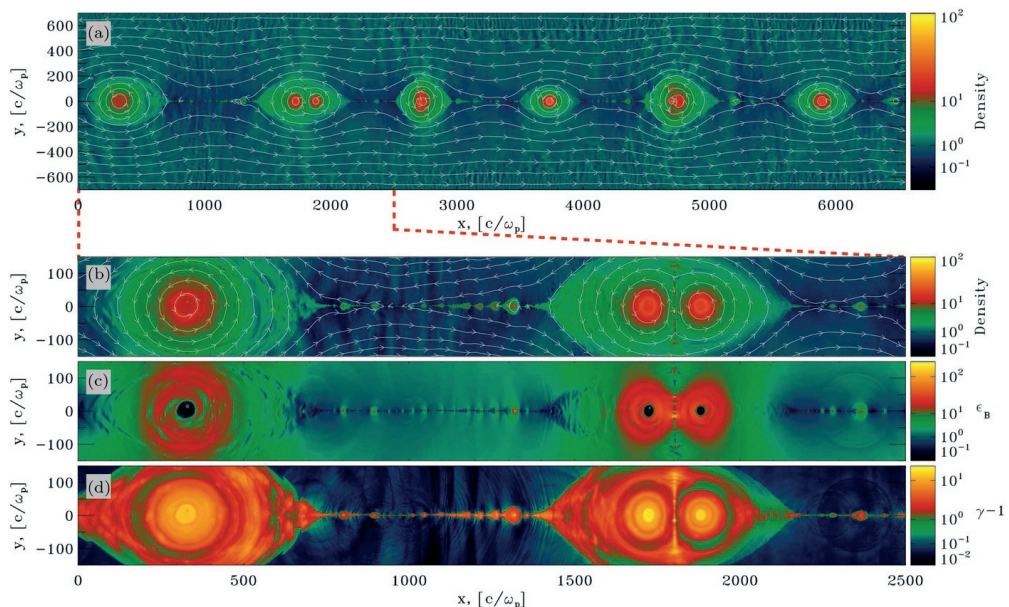


FIGURE 1.20: Reconnection simulation from Sironi & Spitkovsky (2014). Top panel shows density; bottom three panels show zoom-in of the left part of the top panel, shown are from top to bottom: density, electromagnetic energy, and inverse Lorentz factor. The current sheet is located at  $y = 0 c/\omega_p$ ; due to tearing and plasmoid instabilities, the formation of plasmoids can be seen. Plasmoid formation is a hierarchical process. After a plasmoid forms, it moves along the current sheet and merges with other plasmoids. At  $x \approx 1800 c/\omega_p$  a merger of two plasmoids is seen where a secondary sheet in between them is formed that also produces secondary plasmoids.

### 1.7.3 Kink instability

Reconnection is often studied in plasma physics by studying idealized setups described by Harris sheets. It is, however, unclear how and if such sheets can form in astrophysical systems such as AGNs and GRBs. When a jet, such as the one in M87, is launched from a compact object, it initially moves along radial lines when it is in pressure balance with a hot corona or supported by the wind of the accretion disk. When the jet encounters a sudden change in the ambient

environment, the pressure difference can alter the topology of the magnetic field. In the case of a GRB, this happens when the jet reaches the stellar envelope. While in the case of an AGN, the ambient medium changes rapidly when the jet reaches, for example, the ISM. Due to a sudden increase in pressure, the jet contracts as it tries to evolve towards a new equilibrium. This is found when, in the comoving frame of the jet, the poloidal and toroidal field components are of the same magnitude. This newly formed state is called a jet nozzle. During this contraction, the jet core becomes toroidally dominated, and it returns into causal contact, resulting in becoming prone to current-driven instabilities (CDI), such as the kink instability.

The kink instability manifests itself as helical deformation of the jet column. Linear analysis was performed by Lyubarskii (1999) and Appl et al. (2000) who showed that the CDI modes grow when the condition  $\vec{k} \cdot \vec{B} = 0$  is satisfied. In cylindrical coordinates this results in  $kB_z + m/rB_\phi = 0$  which can be rewritten as  $kP + m = 0$  by defining the pitch as  $P = rB_z/B_\phi$ . The pitch is a measure of the winding of the field, which means that when a full rotation along a field line is performed, the pitch sets the amount of displacement in  $z$ . The larger  $P$  is, the larger the displacement. The resonant condition for the kink mode ( $m = -1$ ) results in a wavenumber of  $k = 1/P$ . Linear analyses showed that this is not the only mode that grows; a full spectrum of wavenumbers is excited with varying growth rates. The maximum of this spectrum is located at  $k_{\max} = 0.756/P$  with a growth rate of  $r_{\text{growth}} = 0.133V_A/P$ .

In MHD, we studied (Bromberg et al., 2019) the non-linear phase of the instability. For the initial magnetic field configuration, we used force-free setups from Mizuno et al. (2009); Bodo et al. (2013) for varying pitch profiles. The pitch profile in the kink unstable core is either monotonically increasing (IP), decreasing (DP), or surrounded by a uniform axial magnetic field (EP). The evolution of the kink instability for these three setups can be seen in Figure 1.21. We found that our simulations in the linear phase are in perfect agreement with the analytical predictions from the linear analysis. In the non-linear phase the dissipation rate is given by  $dU_{\text{em}}/dt = -U_{\text{em}}/\tau$ , where  $U_{\text{em}}$  is the electromagnetic energy and  $\tau$  is the linear growth time of the instability. In the final stage, 40-60% of the electromagnetic energy is dissipated, and the instability relaxed to a Taylor state

$$\vec{J} = \alpha \vec{B}, \quad (1.57)$$

where  $\alpha$  is a constant given by

$$\alpha = \frac{\vec{B} \cdot (\vec{\nabla} \times \vec{B})}{B^2}. \quad (1.58)$$

In (Bromberg et al., 2019), we only studied the global MHD behavior of the plasma, essential questions on the kinetic behavior of this instability, such as electron heating and acceleration, remain. Alves et al. (2018) studied kink instability in pressure supported jets and showed that particle energization only happens via ideal electric fields. The assumption of pressure support is, however, for AGN not necessarily valid. In global simulations of jets, a force-free state is observed, see, for example, Bromberg & Tchekhovskoy (2016). PIC simulations of force-free configurations are therefore needed to see how particle energization mediated by the kink instability happens at recollimation sites in AGN and GRBs.

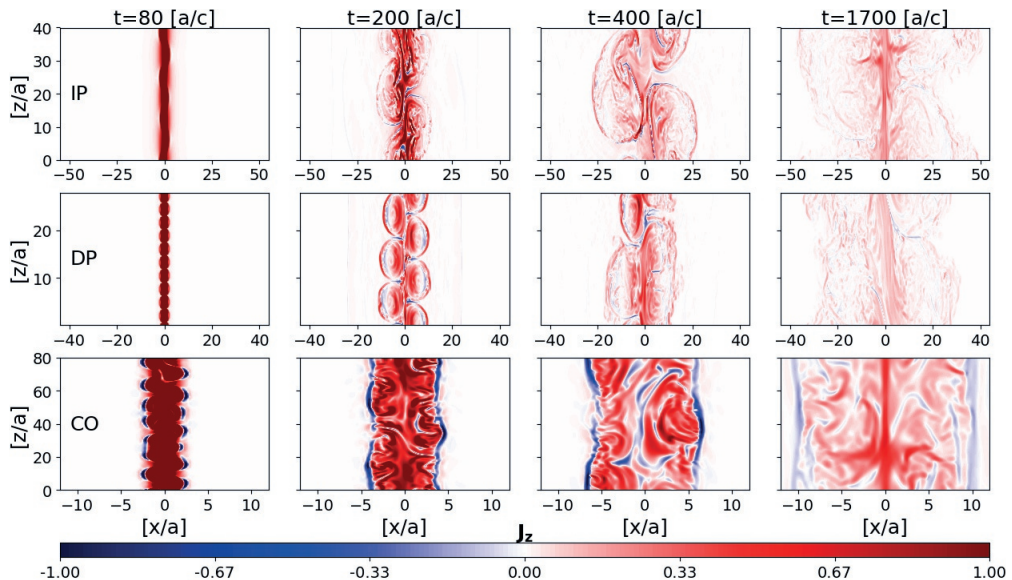


FIGURE 1.21: Evolution of the kink instability in the non-linear phase. Top row shows increasing pitch, middle row decreasing pitch, bottom row corona setup (kink unstable core within uniform field). Image taken from Bromberg et al. (2019).

## 1.8 In this thesis

Since the first theoretical prediction of black holes over a century ago, direct images of event horizon scales are possible. This opens new opportunities not only to test GR in the strong-field limit but allows tests of our understanding of black hole accretion and jet formation. To this end, we need radiative models that capture not only the geometry of the underlying accretion flow but also contain some information on the electron microphysics. One key ingredient in accreting black hole models is the shape of the electron distribution function. The actual shape in the current analysis performed by Gravity Collaboration et al. (2018) and Event Horizon Telescope Collaboration et al. (2019e) is mainly assumed to be a thermal Maxwellian. However, the assumption that the electrons are in thermal equilibrium in these collisionless plasmas is highly unlikely, and electron acceleration via, for example, reconnection, is likely to happen in the magnetized jet. In this thesis: I will study how electron acceleration alters the emission properties and appearance of Sgr A\* and M87\*, I will investigate how the kink instability accelerates electrons in jets, and finally build visualizations of our accreting black holes models in 360° VR.

In chapter 2, I modeled Sgr A\* with a high-resolution 2D GRMHD simulation, with enhanced resolution in the region where the accretion disk and jet reside. I used this simulation to compute spectral energy distributions (SED) for varying electron distribution functions by using the relativistic  $\kappa$ -distribution function and combinations of the  $\kappa$ -distribution function and a thermal Maxwell distribution. I conclude that the SED of Sgr A\* is well fitted in quiescence when less than 1% of the electrons are in a power-law tail, while in flaring state around 5-10% is needed.

In chapter 3, I study the effects of non-thermal electrons on spectra and images of M87\*. I performed 3D Cartesian Kerr-Schild GRMHD simulations. These new simulations allow to properly resolve the jet to large radii in 3D. The simulation shows at horizon scales consistent results with simulations performed on spherical grids but shows a much better-resolved jet. To be able to model M87\*, I post-processed these simulations by enabling **RAPTOR** to perform ray-tracing in non-uniform grids. I added non-thermal electrons by using a relativistic  $\kappa$  distribution function (Xiao, 2006), which is a combination of a thermal core and a power-law tail. I parametrized the  $\kappa$  parameter, which sets the slope of the distribution function, with a fit function from local PIC simulations of trans-relativistic reconnection. The resulting SED for the non-thermal model recovers the radio and NIR emission, the measured core shift, and source sizes of the M87 radio core.

In chapter 4, I study how electron acceleration in AGN jets or for gamma-ray bursts can be mediated by the kink instability. I do this by studying force-free non-rotating jets with first-principle PIC simulations. The kink-instability generates large scale current sheets, which later on break up into small-scale turbulence. The particles are first accelerated in the current sheets via a non-ideal electric field, while in the turbulent phase, acceleration by the ideal electric fields takes over. The non-ideal electric fields are generated by strong guide-field reconnection. The PIC simulations show the same overall behavior, as was found in earlier MHD simulations of the kink instability.

In chapter 5, I develop a virtual reality visualization of accretion black hole based on 3D GRMHD simulations. These visualizations are made with the aim to increase public engagement in black hole research. The 360° VR visualization models Sgr A\* by combining ray-traced images at multiple frequencies where the camera moves along a physically motivated trajectory. In this chapter, I explain the methods I developed to build this visualization.



---

# GENERAL-RELATIVISTIC MAGNETOHYDRODYNAMICAL $\kappa$ -JET MODELS FOR SAGITTARIUS A\*

Jordy Davelaar, Monika Mościbrodzka, Thomas Bronzwaer, and Heino Falcke

*A&A*, 2018, 612, 34

## Abstract

The observed spectral energy distribution of an accreting supermassive black hole typically forms a power-law spectrum in the Near Infrared (NIR) and optical wavelengths that may be interpreted as a signature of accelerated electrons along the jet. However, the details of acceleration remain uncertain. In this paper, we study the radiative properties of jets produced in axisymmetric GRMHD simulations of hot accretion flows onto underluminous supermassive black holes both numerically and semi-analytically, with the aim of investigating the differences between models with and without accelerated electrons inside the jet. We assume that electrons are accelerated in the jet regions of our GRMHD simulation. To model them, we modify the electrons' distribution function in the jet regions from a purely relativistic thermal distribution to a combination of a relativistic thermal distribution and the  $\kappa$ -distribution function (the  $\kappa$ -distribution function is itself a combination of a relativistic thermal and a non-thermal power-law distribution, and thus it describes accelerated electrons). Inside the disk, we assume a thermal distribution for the electrons. In order to resolve the particle acceleration regions in the GRMHD simulations, we use a coordinate grid that is optimized for modeling jets. We calculate jet spectra and synchrotron maps by using the ray-tracing code `RAPTOR`, and compare the synthetic observations to observations of Sgr A\*. Finally, we compare numerical models of jets to semi-analytical ones. We find that in the  $\kappa$ -jet models, the radio-emitting region size, radio flux, and spectral

index in NIR/optical bands increase for decreasing values of the  $\kappa$  parameter, which corresponds to a larger amount of accelerated electrons. This is in agreement with analytical predictions. In our models, the size of the emission region depends roughly linearly on the observed wavelength,  $\lambda$ , independently of the assumed distribution function. The model with  $\kappa = 3.5$ ,  $\eta_{\text{acc}} = 5 - 10\%$  (the percentage of electrons that are accelerated), and observing angle  $i = 30^\circ$  fits the observed Sgr A\* emission in the flaring state from the radio to the NIR/optical regimes, while  $\kappa = 3.5$ ,  $\eta_{\text{acc}} < 1\%$ , and observing angle  $i = 30^\circ$  fit the upper limits in quiescence. At this point, our models (including the purely thermal ones) cannot accurately reproduce the observed source sizes, probably due to the assumption of axisymmetry in our GRMHD simulations. The  $\kappa$ -jet models naturally recover the observed nearly-flat radio spectrum of Sgr A\* without invoking the somewhat artificial isothermal jet model that was suggested earlier. From our model fits, we conclude that between 5% to 10% of the electrons inside the jet of Sgr A\* are accelerated into a  $\kappa$  distribution function when Sgr A\* is flaring. In quiescence, we match the NIR upper limits when this percentage is less than 1%.

## 2.1 Introduction

In general relativistic magnetohydrodynamics (GRMHD) global simulations of a weakly radiating accretion flow onto a black hole, the electron energy distribution function is not explicitly modeled. In these simulations, the accreting plasma is collisionless (i.e., the Coulomb mean free path for electrons is much larger than  $GM/c^2$ ), which means that the electrons are decoupled from the dynamically important, more massive protons. The processes that control the electron distribution function, such as magnetic reconnection, dissipation of turbulent energy, shocks, or other plasma effects that particle-in-cell simulations show, cannot be resolved with the current computational grids used in global simulations of the accretion flows. To predict the radiative properties of GRMHD accretion flows, and to improve the predictive power of the theory of accretion with respect to observations, sub-grid models for electron heating and acceleration have to be invoked.

Sagittarius A\* (Sgr A\*) is a supermassive black hole system that allows one to observationally test the aforementioned GRMHD models of accretion flows (Goddi et al. 2017). Millimeter-Very Long Baseline Interferometry (mm-VLBI) is capable of resolving the shadow of the event horizon (Falcke et al. 2000b), making this an ideal laboratory not only to tests Einstein's General Theory of Relativity (GR) but also to investigate electron acceleration in the vicinity of a black hole. Most of the radiative models for Sgr A\*, which are based on post-processing GRMHD simulations, assume that electrons have a thermal, relativistic (Maxwell-Jüttner) distribution function, and that the proton-to-electron temperature ratio is constant across the simulation domain (Goldston et al. 2005b, Noble et al. 2007, Mościbrodzka et al. 2009, Dexter et al. 2010, Dexter et al. 2012a, Shcherbakov et al. 2012). When the proton-to-electron temperature is constant, the disk dominates the images and spectra since most of the matter resides there. We have recently extended these radiative models by making the temperature ratios a function of the plasma  $\beta$  parameter, where  $\beta = \frac{P_{\text{gas}}}{P_{\text{B}}}$  is the ratio of gas to magnetic pressures. In these extended models, the electrons are hotter in the more magnetized plasma, which is usually outflowing from the

system. The reason for this is that the previously mentioned models do not recover the flat radio spectra. The  $\beta$  parameterization enforces that the disk emission is suppressed by significantly decreasing the temperature of the electrons in those regions. As a consequence of this, the jet will be the dominant source of emission. These modifications to the electron temperature model allowed us to recover some basic observational characteristics of Sgr A\* (a roughly flat radio spectral slope and a size vs. wavelength relationship that is in agreement with observations) (Mościbrodzka et al. 2014, Chan et al. 2015b, Chan et al. 2015a, Gold et al. 2017). Our model for the electron temperatures as a function of the  $\beta$  plasma parameter is now roughly confirmed with extended-GRMHD simulations that self-consistently take into account the evolution of the electron temperatures (Ressler et al. 2015b, Ressler et al. 2017). Moreover, GRMHD simulations with the new electron temperatures can naturally explain the symbiosis of disks and jets observed in many accreting black hole systems (Falcke & Biermann 1995, Mościbrodzka et al. 2016a).

Observations of Sgr A\* show flares in the NIR/optical wavelengths with a spectral index of  $\alpha \approx -0.7 \pm 0.3$  (Bremer et al. 2011). These flares are indicators of accelerated non-thermal electrons in the accretion flow, which is not accounted for in our previous models of Sgr A\*.

Due to computational constraints, it is challenging to make a first-principles model for particle acceleration in GRMHD simulations (but see Chael et al. 2017). A simpler approach can be adopted in which the non-thermal particles are included in a phenomenological prescription. The accelerated electrons can be described by a hybrid distribution function that is constructed by ‘stitching’ a power-law tail onto a thermal distribution function. The hybrid distribution function is then described by a few free parameters: the power-law index ( $p$ ), the acceleration efficiency ( $\eta$ , which is the amount of energy in the accelerated electrons compared to the total energy budget), and the maximum Lorentz factor ( $\gamma_{max}$ ) or the Lorentz factor at which radiative cooling starts to dominate ( $\gamma_c$ ). The minimum Lorentz factor ( $\gamma_{min}$ ) is then calculated at the ‘stitching’ point. With an underlying model for the accreting plasma, these free parameters can then be constrained by comparing the model emission to the observational data.

One of the first attempts to model electrons around Sgr A\* with the hybrid distribution function is presented in Özel et al. (2000). Their underlying model for the accreting plasma is a semi-analytical radiatively inefficient accretion flow (RIAF) (Narayan & Yi 1994, Narayan & Yi 1995a, Narayan & Yi 1995c, and Chen et al. 1995). Özel et al. (2000) found that the observed low-frequency shoulder of the Sgr A\* spectrum is well described by emission from RIAF electrons described by a hybrid distribution function with  $\eta \approx 0.01$  and  $p = 3 - 3.5$ . Similar conclusions were later reached by, e.g., Yuan et al. 2003 and Broderick et al. 2016.

Recently, Mao et al. (2017) studied the effects of accelerated electrons in GRMHD simulations on the mock spectra and millimeter images of Sgr A\* using either a hybrid distribution function (with  $p = 3.5$  and various values of  $\eta$ ) or a multi-Maxwellian distribution function. They found that the accelerated, high energy electrons not only alter the observed spectral energy distribution shape but also lead to more extended and diffuse resolved millimeter images of the source in the case of the hybrid distribution function. This has a few interesting implications for interpreting the VLBI observations of Sgr A\* (Bower et al. 2004, Shen et al. 2005, Doeleman et al. 2008, Bower et al. 2014, Brinkerink et al. 2016). Similarly to early semi-analytical model by Özel et al. (2000), Mao et al. (2017) assumed constant acceleration parameters in the entire simulation

domain, which is reasonable but does not have to be the case. For example, Ball et al. (2016) insert accelerated electrons in low- $\beta$  regions where particle acceleration is expected to occur via magnetic reconnection) of GRMHD simulations of Sgr A\*, and study the impact of accelerated electrons on the emitted SED with the goal to explain near-infrared (NIR) and X-ray flares observed in Sgr A\*. Their best fit model assumes the electron acceleration efficiency  $\eta = 0.1$  and a power-law index  $p = 3.5$ . A similar approach (with  $p = 3 - 3.5$  and acceleration efficiency proportional to magnetic energy) was earlier adopted by Dexter et al. (2012b) to model the size of the near-horizon emission in M87 radio core (hereafter M87\*).

In this paper, we study the effects of particle acceleration on spectra and images of axisymmetric GRMHD models of accretion flows with jets. The goal is to extend our current models with electron acceleration to see if it is possible to obtain the nearly flat SED of Sgr A\* and set constraints on the amount of electron acceleration during NIR/optical flares. Our underlying accretion model assumes that the proton-to-electron temperature ratio is a function of the plasma  $\beta$  parameter and that electrons are hotter in low- $\beta$  regions of the simulations that are associated with the jet outflow. We model emission from radio to NIR/optical frequencies. The primary source of photons in the magnetized, relativistically hot plasma studied here is the synchrotron process. We ignore inverse-Compton scatterings, hence do not model the X-ray emission.

The accelerated electrons investigated in this paper are described by the  $\kappa$  distribution function (Vasyliunas, 1968) instead of the hybrid distribution function. The  $\kappa$  distribution function smoothly connects the thermal core to the power-law tail (which is not the case in the hybrid model), and better describes processes such as first-order Fermi acceleration (Livadiotis & McComas, 2013). The derivation of the function can be found in Livadiotis & McComas (2009). The  $\kappa$  distribution function is related to the thermal distribution function as a limit

$$\begin{aligned} f_{\text{thermal}}(\Theta_e, \gamma) &\propto e^{-(\gamma-1)/\Theta^2} \\ &= \lim_{\kappa \rightarrow \infty} \left(1 + \frac{\gamma-1}{\kappa\Theta_e}\right)^{-\kappa-1} \propto \lim_{\kappa \rightarrow \infty} f_{\kappa}(\Theta_e, \gamma), \end{aligned} \quad (2.1)$$

where  $\kappa$  is a free parameter of the distribution function, and  $\Theta_e$  is the dimensionless temperature of the electrons involved. In the power-law part of the distribution function, the parameter  $\kappa$  is related to the power-law index  $p$  by  $\kappa = p + 1$ , such that in the limit of  $\gamma \gg 1$  the  $\kappa$  distribution function asymptotically approaches  $f_{\kappa}(\Theta, \gamma) \propto \gamma^{-p}$ . The  $\kappa$  distribution function has been used to describe plasma in the solar wind (Decker & Krimigis, 2003) and plasmas in, e.g., coronal flares on the Sun (Livadiotis & McComas, 2013). Theoretically Kunz et al. (2016) found that the distribution function of accelerated particles in accreting systems follows a  $\kappa$  distribution.

The paper is organized as follows. In Sections 2.2.1 and 2.2.2, we explain how the GRMHD simulations are set up. In section 2.2.3, we describe radiative transfer parameters and the acceleration of electrons. We present and discuss the results in Sections 2.3 and 2.4, respectively.

## 2.2 Methods

### 2.2.1 GRMHD simulation

Our accreting plasma model is based on GRMHD simulations of magnetized gas around a supermassive, spinning black hole. The simulation begins with a torus in hydrostatic equilibrium

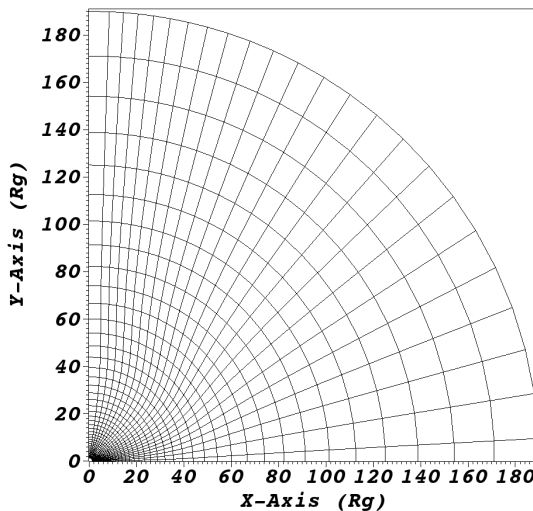


FIGURE 2.1: The upper half of an MMKS coordinate system that focuses the grid resolution in the polar regions. For clarity, a lower resolution grid is displayed.

in a Keplerian orbit around a Kerr black hole (Fishbone & Moncrief, 1976). The size of the initial torus is set by two parameters: the inner edge of the torus  $r_{\text{in}} = 6 GM/c^2$ , and the radius  $r_{\text{max}} = 12 GM/c^2$  of the pressure maximum of the torus, where  $GM/c^2$  is the simulation length unit. We evolve the flow with the GRMHD code `HARM2D`, where we used the standard setup for reconstruction schemes and constrained transport as described in Gammie et al. (2003).

The initial torus is seeded with a weak poloidal magnetic field where the topology follows the isodensity contours of the torus. The strength of the magnetic field is set via the dimensionless plasma  $\beta$  parameter defined as:

$$\beta = \frac{P_{\text{gas}}}{P_{\text{mag}}} = \frac{u(\gamma_{\text{ad}} - 1)}{B^2}, \quad (2.2)$$

where  $\gamma_{\text{ad}}$  is the adiabatic index,  $u$  is the internal energy density, and  $B$  is the magnetic field strength. The initial torus has a minimum  $\beta = 100$ ; in other words, initially, the magnetic fields are relatively weak.

We are interested in modeling  $\nu = 10^9 - 10^{15}$  Hz emission originating from the inner accretion flow (high-energy end of the spectrum) and the extended jet (low-energy end of the spectrum). Models of low-frequency emission from the jet require the simulation to be radially extended to an outer radius of  $r_{\text{out}} = 1000 GM/c^2$ . We evolve the simulation until the final time  $t_f = 4000 GM/c^3$ , where  $GM/c^3$  is the simulation time unit. This  $t_f$  allows the jet to reach the outer boundary of the computational domain. The simulation duration corresponds to 15 orbital periods of the torus.

## 2.2.2 Numerical grid for simulating disks and jets

The dynamical simulation is carried out in mixed modified Kerr-Schild (MMKS) coordinates (Noble et al. 2007)  $(X_0, X_1, X_2, X_3)$ , which are related to standard Kerr-Schild coordinates  $(t, r, \theta, \phi)$  by:

$$t = X_0, \quad (2.3)$$

$$r = e^{X_1}, \quad (2.4)$$

$$\theta = \pi X_2 + \frac{2h_{\text{slope}}}{\pi} \sin(2\pi X_2) \arctan(s(x_0 - X_1)), \quad (2.5)$$

$$\phi = X_3, \quad (2.6)$$

where  $h_{\text{slope}}$ ,  $s$ , and  $x_0$  are free parameters of the coordinates system that can be used to refine the coordinate grid near the equatorial plane, where the most dense region of the disk resides, and in the polar regions where a jet is expected to form. The parameter  $h_{\text{slope}}$  controls the grid spacing near the equatorial plane in the innermost region of the simulation. The parameter  $x_0$  is defined as  $x_0 \equiv \log(r_{\text{tr}})$ , where  $r_{\text{tr}}$  is a transition radius at which the grid transitions from a parabolic to a conical shape along the jet axis, and  $s$  defines how rapidly this transition occurs.

The simulation is performed in two dimensions, with a grid resolution of  $N_{X_1} \times N_{X_2} = 512 \times 528$  and grid parameters  $h_{\text{slope}} = 0.35$ ,  $s = 2$ , and  $r_{\text{tr}} = 50 GM/c^2$ . A visualization of the MMKS coordinate system is presented in Figure 2.1.

## 2.2.3 Radiative transfer model and electron distribution functions

The SEDs and images of the GRMHD accretion flow models are computed using the general-relativistic, ray-tracing radiative transport code **RAPTOR** (Bronzwaer et al., 2018).

The GRMHD simulations are scale-free; this means that the quantities obtained are unitless. Calculation of mock observations of these models requires scaling them to c.g.s. units. The scaling depends on observational constraints such as distance, the mass of the black hole, and the matter content of the accretion disk. The simulation length unit is  $\mathcal{L} = GM/c^2$ , the time unit is  $\mathcal{T} = GM/c^3$ , and the mass unit is  $\mathcal{M}$ . While a good estimate of the black hole mass,  $M$ , exists for Sgr A\* (hence the length unit [cm] and time unit [s] are reasonably well-known), the accretion mass unit,  $\mathcal{M}$  is a free parameter of the system, which has to be constrained by fitting our model spectrum to observations. The parameter  $\mathcal{M}$  determines the density of the accretion flow, and thus the mass accretion rate onto the black hole. The dimensionless accretion rate  $\dot{M}_{\text{sim}}$  can be converted to the accretion rate in c.g.s. units by  $\dot{M} = \dot{M}_{\text{sim}} \mathcal{M} \mathcal{T}^{-1}$ . To convert the plasma density, specific internal energy, and magnetic field strength from code units to c.g.s. units we use the following scaling factors:  $\rho_0 = \mathcal{M}/\mathcal{L}^3$ ,  $u_0 = \rho_0 c^2$ , and  $B_0 = c\sqrt{4\pi\rho_0}$ .

In the GRMHD simulation, we only evolve protons. We, therefore, need assumptions for the electron distribution functions and how the density and temperature of the electrons depend on the computed plasma variables.

We divide the simulation volume into three regions: the disk, the jet-sheath, and the jet-spine. In each region, we assume different electron distribution functions. In the disk region, we assume that electrons have a thermal (Maxwell-Jüttner) distribution function. We accelerate electrons

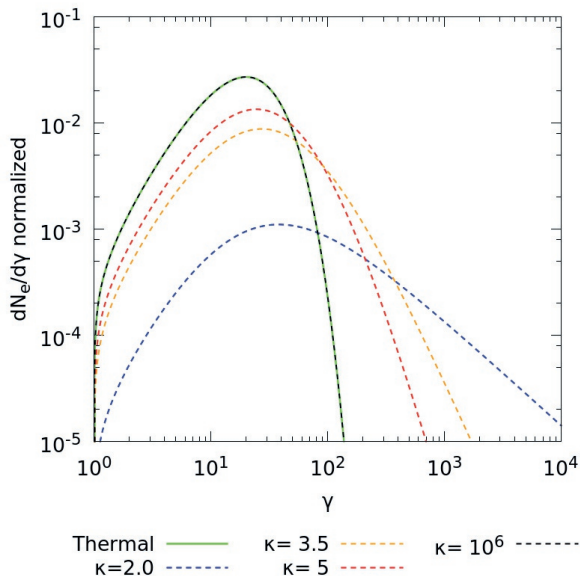


FIGURE 2.2: The  $\kappa$  distribution function for different values of the  $\kappa$  parameter (dashed lines). In the limit of large  $\kappa$  (black dashed line) the relativistic thermal distribution function is recovered (green solid line).

in the jet-sheath region, defined using the Bernoulli parameter  $Be = -hu_t > 1.02$  (Mościbrodzka & Falcke, 2013) with  $h$  the gas enthalpy and  $u_t$  the time component of the four-velocity. We neglect any emission from the jet-spine region, defined using the magnetization parameter  $\sigma = \frac{B^2}{\rho}$ . The matter content and energy content of jet-spine is set by numerical floor values. These numerical floor values can result in unphysical large fluctuations in temperature that must be excluded from the synthetic images. This is caused by the conservative nature of the scheme that HARM2D uses; the magnetic energy is large while the internal energy is low. Therefore, tiny fluctuations of the magnetic energy can result in large fluctuations in the internal energy because the codes will enforce energy conservation. This behavior in the jet spine can be found in regions close to  $\theta = 0$  and  $\pi$  where  $\sigma > 1.0$ , any radiation from these regions is ignored.

The electron temperature,  $T_e$ , is computed assuming that the proton-to-electron coupling depends on plasma magnetization (Mościbrodzka et al. 2016b; Mościbrodzka et al. 2017). We use the following law for the coupling of the electron and proton temperatures:

$$\frac{T_p}{T_e} = R_{\text{low}} \frac{1}{1 + \beta^2} + R_{\text{high}} \frac{\beta^2}{1 + \beta^2}, \quad (2.7)$$

where  $\beta = \frac{P_{\text{gas}}}{P_{\text{mag}}}$  is the ratio of the gas pressure to the magnetic field pressure  $P_{\text{mag}} = B^2/2$ .  $R_{\text{low}}$  and  $R_{\text{high}}$  are free parameters. In a strongly magnetized plasma,  $\beta \ll 1$  and  $T_p/T_e \rightarrow R_{\text{low}}$ . In a weakly magnetized plasma,  $\beta \gg 1$  and so  $T_p/T_e \rightarrow R_{\text{high}}$ . We set  $R_{\text{low}} = 1$  and  $R_{\text{high}} = 25$  so that the electrons are cooler in the disk and hotter toward the jet.

The energy distribution function of accelerated electrons in the jet-sheath is described by a combination of a thermal distribution and the relativistic  $\kappa$  distribution function (Livadiotis & McComas 2009):

$$\frac{dn_e}{d\gamma} = N\gamma\sqrt{\gamma^2 - 1} \left(1 + \frac{\gamma - 1}{\kappa\Theta}\right)^{-(\kappa+1)}, \quad (2.8)$$

where  $\kappa$  is a free parameter,  $\Theta$  is the dimensionless temperature defined as  $\Theta_e \equiv k_b T_e / m_e c^2$ , and  $N$  is a normalization (that depends on  $\Theta_e$  and  $\kappa$ ) such that  $\int_1^\infty \frac{dn_e}{d\gamma} d\gamma = n_e$ . The  $\kappa$  distribution function consists of a non-thermal power-law tail that smoothly connects to a thermal-like core. In the limit of  $\kappa \rightarrow \infty$ , the  $\kappa$  function asymptotically approaches the thermal distribution function with temperature  $\Theta_e$ . Figure 2.2 shows the  $\kappa$  distribution function for a few values of the  $\kappa$  parameter.

For large  $\gamma$ , the distribution function asymptotically approaches a power law with index  $p$  that is related to  $\kappa$  by  $\kappa \equiv p + 1$ . Hence, the spectral index  $\alpha$  of the optically thin part of the observed spectrum (where the observed flux density is  $F_\nu \propto \nu^\alpha$ ) is associated with the  $\kappa$  parameter via  $\alpha = \frac{1-p}{2} = \frac{2-\kappa}{2}$  (Rybicki & Lightman 1979).

Fit formulas for the synchrotron emissivities and absorptivities for thermal and  $\kappa$  distribution functions, which are used in the radiative transfer models, were taken from Pandya et al. (2016).

To capture all of the emission at low and high frequencies, we need a field of view for our camera of  $2000 GM/c^2$  (the extent of the GRMHD simulation domain). The code calculates the total flux density at every frequency by calculating null geodesics and simultaneously performing radiative transport calculations (Bronzwaer et al., 2018). Therefore it has the same field of view at every frequency. In the case of a uniform camera grid, one needs a very high resolution to resolve the source at both low and high frequencies simultaneously. This is because the high-frequency emission originates mainly from near the event horizon, a region that is much smaller than the extended jet structures seen at lower frequencies. In order to resolve the horizon with a uniform camera at this large field of view, one needs resolutions of around  $10.000^2$  pixels, increasing the runtime of the code significantly. To overcome this runtime issue, and to obtain converged SEDs, we implemented a polar logarithmic camera grid into **RAPTOR**. We describe the camera grid in Appendix 2.A and show that our SEDs are converging if we use 512 pixels in  $\log(r)$  and 256 pixels in  $\theta$ .

## 2.3 Results

### 2.3.1 GRMHD jet structure

In Figure 2.3, we show the density, magnetic field strength, and electron temperature of a time slice of the GRMHD simulation. In each panel, the color maps are overplotted with contours of  $\sigma = 1$  and  $\text{Be} = 1.02$ , which define the jet-sheath region where electrons experience acceleration. The rightmost panel in Figure 2.3 shows that a thin sheath of high-temperature gas coincides with the unbound, outflowing matter.

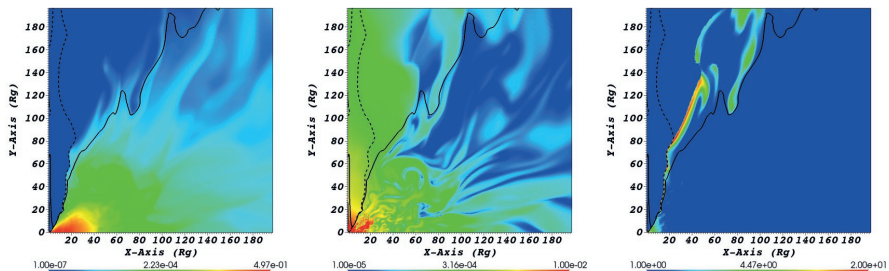


FIGURE 2.3: Color maps of the plasma density (left panel), the magnetic field strength (middle panel), and the dimensionless electron temperature at  $t = 4000 GM/c^3$  of the simulation. We show the inner regions of the upper half of the simulation domain. The gas density and magnetic field strength are given in the simulation code units. The electron temperature is computed using Eq. 2.7 with  $R_{\text{low}} = 1$  and  $R_{\text{high}} = 25$  (right panel). Each panel also shows contours of constant  $\sigma = 1$  (dashed contour) and  $Be = 1.02$  (solid contour). Regions where  $Be > 1.02$  are outflowing.

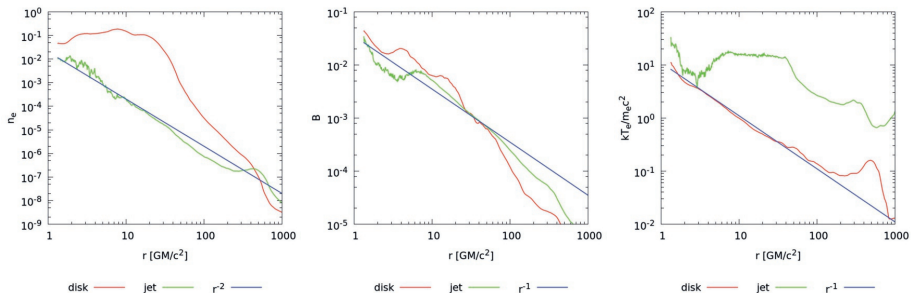


FIGURE 2.4: Radial profiles of the dimensionless number density (left panel), the magnetic field strength (middle panel), and the dimensionless electron temperature (right panel) shown in Figure 2.3. Here, the simulation data is additionally time- and shell- averaged. Green and red lines correspond to plasma in the jet-sheath and accretion disk, respectively. Left and middle panels: blue lines represent the analytical model from BK79. Right panel: blue line represents the virial temperature profile.

Figure 2.4 displays time- and shell-averaged radial profiles of  $n_e$ ,  $B$ , and  $T_e$  in the simulation. The radial profiles are calculated using the following definition:

$$\langle q(r) \rangle = \frac{1}{\Delta t} \int_{t_{\min}}^{t_{\max}} \frac{\int_0^{2\pi} q(t, r, \theta, \phi) \sqrt{-g(r, \theta)} d\theta d\phi}{\int_0^{2\pi} \sqrt{-g(r, \theta)} d\theta d\phi} dt, \quad (2.9)$$

where  $t_{\min} = 3000 GM/c^3$  and  $t_{\max} = 4000 GM/c^3$  and  $\Delta t = t_{\max} - t_{\min}$ . The averaging uses 100 time slices of the GRMHD model, which corresponds to 5.47 hours.

Figure 2.4 shows that the radial profiles of the quantities of interest follow power laws. We compare the radial dependencies of these quantities to the Blandford-Königl jet model (Blandford & Königl 1979, hereafter BK79, see also Falcke & Biermann 1995), which is often invoked to explain the flat-spectrum radio cores observed in the centers of active galactic nuclei. In the

BK79 model, the jet density decreases with radius as  $n_e \propto r^{-2}$ , the magnetic field strength as  $B \propto r^{-1}$ , and the electron temperature  $T_e$  is constant.

We find that in our GRMHD simulations, the electron temperatures are roughly constant up to  $100 GM/c^2$  in the jet-sheath. A possible explanation for the temperature deviation from isothermality at larger radii is that the initial torus is relatively small compared to the size of the computational domain, and thus cannot collimate the jet at large radii; without the pressure support of a large disk, the outflowing plasma in the jet decompresses adiabatically, which results in the observed temperature decrease. In the accretion disk, the electron temperature follows a virial temperature profile,  $T \propto r^{-1}$ , as expected. In our simulation, the radial profile of the magnetic field strength does not resemble  $B \propto r^{-1}$ , but it is slightly steeper. It is likely that the radial profile of the  $B$  field strength along the jet in our numerical model is an artifact associated with the axisymmetric character of the simulation and the corresponding numerical difficulties. This difficulty arises because the turbulence in the magnetic field weakens due to the azimuthal symmetry of the 2D simulation. The radial structures of the inflows and outflows in the axisymmetric GRMHD simulation carried out here are consistent with those presented in similar axisymmetric models presented in Noble et al. (2007) and in Mościbrodzka & Falcke (2013).

### 2.3.2 SEDs and synchrotron maps of $\kappa$ -jet models

In this section, we present spectral energy distributions (SEDs) and radio, millimeter, and near-IR images of models where all electrons in the jet-sheath are described by the  $\kappa$  distribution function. The adopted free parameters of the model are listed in Table 2.1. We investigate how the model SEDs and images of the source change with the  $\kappa$  parameter and with the observing angle. We measure the source sizes at various wavelengths using image moments (Hu, 1962). Aside from model-to-model comparison, we qualitatively compare the synthetic SEDs and source sizes to Sgr A\* observational data collected from the literature.

Figure 2.5 (upper panels) shows model SEDs at three observing angles. Since the observational data are collected non-simultaneously, the model SEDs are time-averaged over  $\Delta t = 500 GM/c^3 = 2.74$  hours. The best-fit model SED is for  $\kappa = 5$  and  $i = 30^\circ$ . With these parameters, the model shows similar flux levels to the observed fluxes at radio frequencies (Melia & Falcke 2001 and references therein), and is consistent with observational constraints at NIR frequencies (upper limits of NIR fluxes and flares). Unless the fact that we recover the correct flux values the spectral index of the best fit model is inconsistent with observational constraints ( $\alpha \approx -0.7 \pm 0.3$  (Bremer et al. 2011)). Therefore a model where the electrons are distributed into a single  $\kappa$  distribution function is, in the case of Sgr A\*, ruled out, but can still be of interest for other sources, e.g., M87\*.

To decrease the spectral index, lower  $\kappa$  values are needed. One could decrease the amount of NIR emission by decreasing the number of accelerated electrons at the jet launching point by having a mix of electrons in the  $\kappa$  distribution function and a thermal distribution function. This idea is explored in Sect. 2.3.3.

Figure 2.5 (lower panels) displays the spectral slopes as a function of observing frequency. Between  $\nu = 10$  and 230 GHz, the spectra for models with accelerated electrons have flatter spectral slopes compared to the spectral slopes of the thermal model. At the NIR/optical frequencies, we

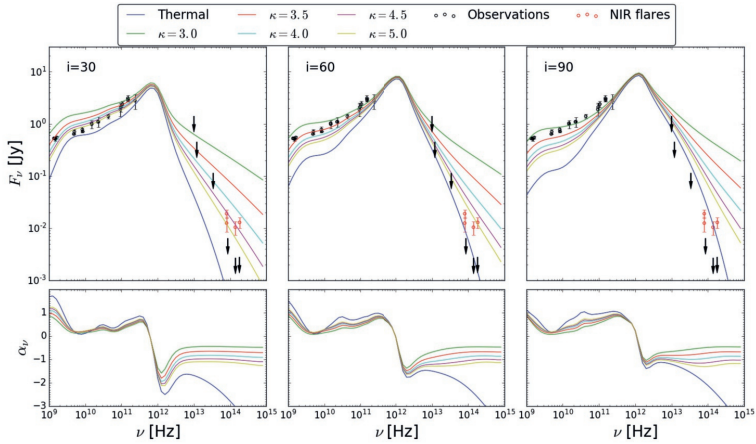


FIGURE 2.5: SED overplotted with observational data (top) and spectral index (down) for thermal and  $\kappa$  models for Sgr A\* at three different observing angles. Observational data from Melia & Falcke (2001), NIR flares from Genzel et al. (2003) and Dodds-Eden et al. (2009).

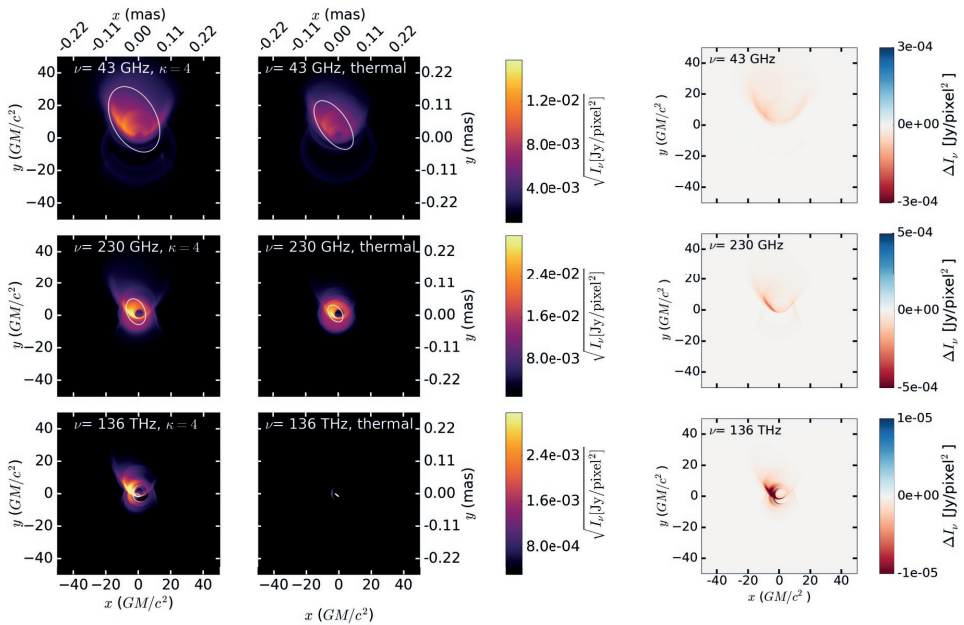


FIGURE 2.6: Synthetic images for  $\kappa$  models (left) and thermal models (middle) for Sgr A\* at three different frequencies for an observing angle  $i = 30^\circ$  (with respect to the black hole spin axis). The spatial resolution and field of view of our camera is  $0.2GM/c^2$  and  $100GM/c^2$  respectively. Overplotted in white are the source sizes estimates, major and minor axis, and orientation of the ellipse, which are calculated by using image moments. Right panels: the additional emission for Sgr A\* in the  $\kappa = 4$  model at three different frequencies. This emission is localized by subtracting the thermal synthetic images from the  $\kappa = 4$  images.

TABLE 2.1: List of parameters that are used in the radiative transfer simulations of Sgr A\*. The mass and distance of Sgr A\* are taken from Gillessen et al. (2009a).

Parameter	value for Sgr A*
$i$	$30^\circ, 60^\circ, 90^\circ$
$D$	8 kpc
$M_{\text{BH}}$	$4.0 \times 10^6 M_\odot$
$\mathcal{L}$	$5.9 \times 10^{11}$ cm
$\mathcal{T}$	19.7 s
$\mathcal{M}$	$10^{21}$ g
$\langle \dot{M} \rangle_t$	$1.95 \times 10^{-8} M_\odot \text{yr}^{-1}$
$\rho_0$	$4.85 \times 10^{-15}$ [g cm $^{-3}$ ]
$n_0$	$2.9 \times 10^9$ [cm $^{-3}$ ]
$B_0$	7409 [Gauss]
$R_{\text{high}}$	25
$R_{\text{low}}$	1
$e^-$ accel.	jet sheath
$\kappa$	3,3.5,4,4.5,5

observe a relation between the spectral index  $\alpha$  and  $\kappa$  given by  $\alpha = \frac{2-\kappa}{2}$ . This is expected behavior of optically-thin synchrotron emission because  $\kappa = p + 1$  (Rybicki & Lightman, 1979).

Our models demonstrate a strong dependence between the radio flux and the observer's viewing angle as predicted, e.g., by Falcke & Biermann 1995. At lower inclinations, the jet points more towards the observer, the relativistic velocities inside the jet ( $\gamma\beta \approx 5$ ), boost the emission to higher flux values. In the thermal model, we see lower flux values at radio frequencies ( $\nu < 10^{10}$  Hz) compared to fluxes obtained by Mościbrodzka & Falcke (2013). This is because the authors of that paper assumed an isothermal jet up to  $1000 GM/c^2$ , by setting the  $T_{e,\text{jet}} = \text{constant}$  inside the outflowing region of the simulation. When adding accelerated electrons in the jet, we observe an increase in flux at the low and high-frequency sides of the synchrotron bump. This is in agreement with results obtained by Özel et al. (2000) and Yuan et al. (2003). As already mentioned in the introduction, these previous works used RIAF models, where the electrons are accelerated in the accretion disk. Our calculations show that it is also possible to recover the low-frequency "shoulder" and high-frequency "tail" by inserting the accelerated electrons in the jet outflow.

Figures 2.6, 2.7, and 2.8 show time-averaged radio, millimeter, and NIR synthetic images of Sgr A\* for  $\kappa = 4$  (left panel) and for a relativistic thermal electron distribution function (right panel) at three observing angles. The choice for  $\kappa = 4.0$  is arbitrary and serves as an illustration of the difference between the  $\kappa$  and thermal models. The synchrotron maps are overplotted with ellipses that represent the  $FWHM$  of the major and minor axes of the source, as well as its orientation on the sky. In models with accelerated electrons, the jet is more elongated compared to the models without electron accelerations. The difference in size is most noticeable in the NIR band. The extra emission produced by electrons in the high-energy tail is evident when subtracting the thermal model from the  $\kappa = 4$  model, as in the rightmost panels in Figs. 2.6, 2.7, and 2.8.

Finally, Figure 2.9 compares the synthetic and observed (intrinsic, i.e., after subtraction of the scattering screen that is detected towards the Sgr A\*) sizes of the emitting region for different  $\kappa$  models at three observing angles in the optically thick part of the spectrum. We plot both the major and minor axes of the source. Observationally, the source size follows a power-law relationship as a function of  $\lambda$ :  $\text{size} \sim \lambda^q$ , where  $q = 1$  (Bower et al. 2006). We find that the major and minor size of the source model increase with increasing observing wavelength  $\lambda$ , which is consistent with observations. At each wavelength, the model size increases with decreasing  $\kappa$  and decreases with increasing observing angle. Which  $\kappa$  parameter recovers the observed size- $\lambda$  relationship best? The size of the minor axes is marginally consistent with the 1.3 mm observations in the case of the thermal and  $\kappa$ -jet models at  $i = 60^\circ$  and  $i = 90^\circ$  (see, two right top panels in Fig. 2.9). All models produce jets with sizes consistent with the error margins of the observations, but only down to  $\lambda=7$  mm. At  $\lambda < 7$ mm, all models overestimate the size of Sgr A\*. There are two possible explanations for this:

i) The axisymmetry of our simulations causes the appearance of ring-like structures in the flow, which are also visible in the synthetic images. These ring-like structures are not present in 3D simulations, which may decrease the source size of the models.

ii) Time-averaging the synthetic images results in concentrated emission that is smeared out over a larger volume as it propagates outwards, thereby increasing the measured model source sizes.

High-resolution, fully three-dimensional, radially extended GRMHD model of an accreting black hole with phenomenological prescriptions for the shape of non-thermal electron distribution function along the jet will be explored in a subsequent publication.

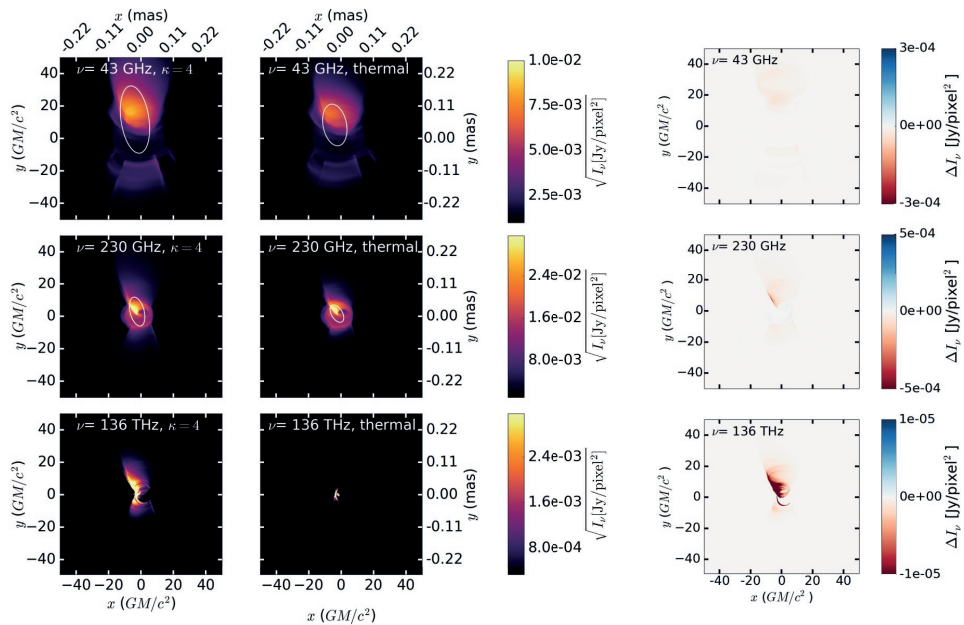
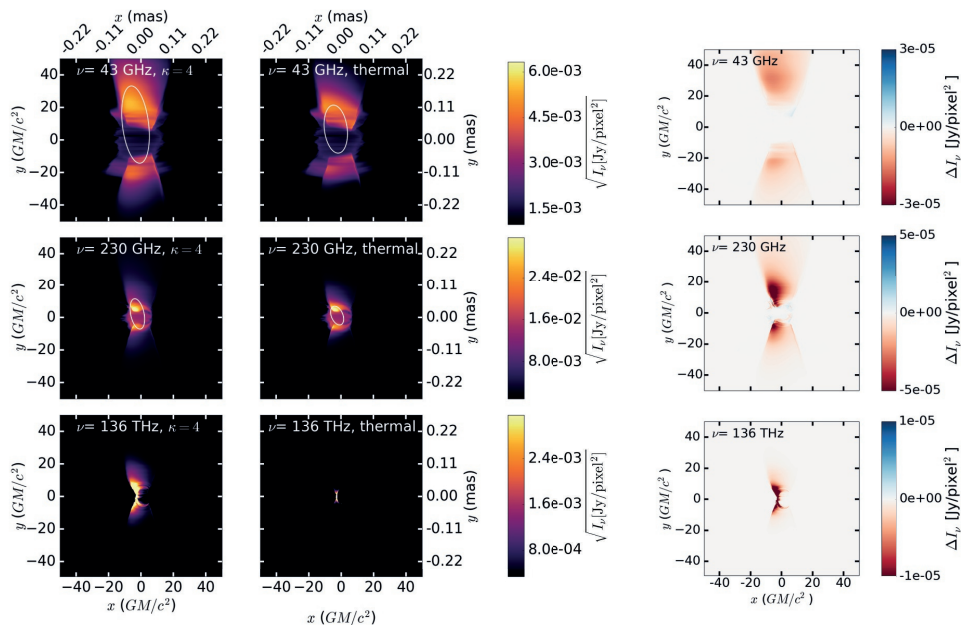
### 2.3.3 Fitting the particle distribution function of Sgr A\*

From observations of NIR flares, the spectral index of Sgr A\* is  $\alpha \approx -0.7 \pm 0.3$  (Bremer et al. 2011). This would result in a  $\kappa$  value of 3.5. The  $\kappa = 3.5$  models, however, overproduce the amount of flux in the NIR band. This is caused by injecting too many accelerated electrons in the jet sheath. In order to control the number of accelerated electrons, we use a superposition of a relativistic thermal and a  $\kappa$  distribution in the jet sheath. The percentage of  $\kappa$  distributed electrons is given by the free parameter  $\eta_{\text{acc}}$ . The result of these fits for various values of  $\eta_{\text{acc}}$  can be seen in Figure 2.10. The model where  $\eta_{\text{acc}} = 1\%$  fits the quiescence NIR observations, while a value of  $\eta_{\text{acc}} = 5 - 10\%$  fits the NIR flares. In both, the quiescence and flaring states, we recover the observed spectral index of  $\alpha \approx -0.7 \pm 0.3$  (Bremer et al. 2011).

## 2.4 Discussion

### 2.4.1 SEDs of the jet launching zone as a function of electron distribution functions

Various electron temperature models were used in the past to explain the flat-to-inverted SEDs of radio jets. In Mościbrodzka & Falcke (2013) and Mościbrodzka et al. (2014), an isothermal jet model was introduced, the electron temperature was set to a constant value inside outflowing regions of the accretion flow, and in the disk, the temperature ratio was set to a constant value.


 FIGURE 2.7: As Fig. 2.6, but for an observing angle of  $i = 60^\circ$ .

 FIGURE 2.8: As Fig. 2.6, but for an observing angle of  $i = 90^\circ$ .

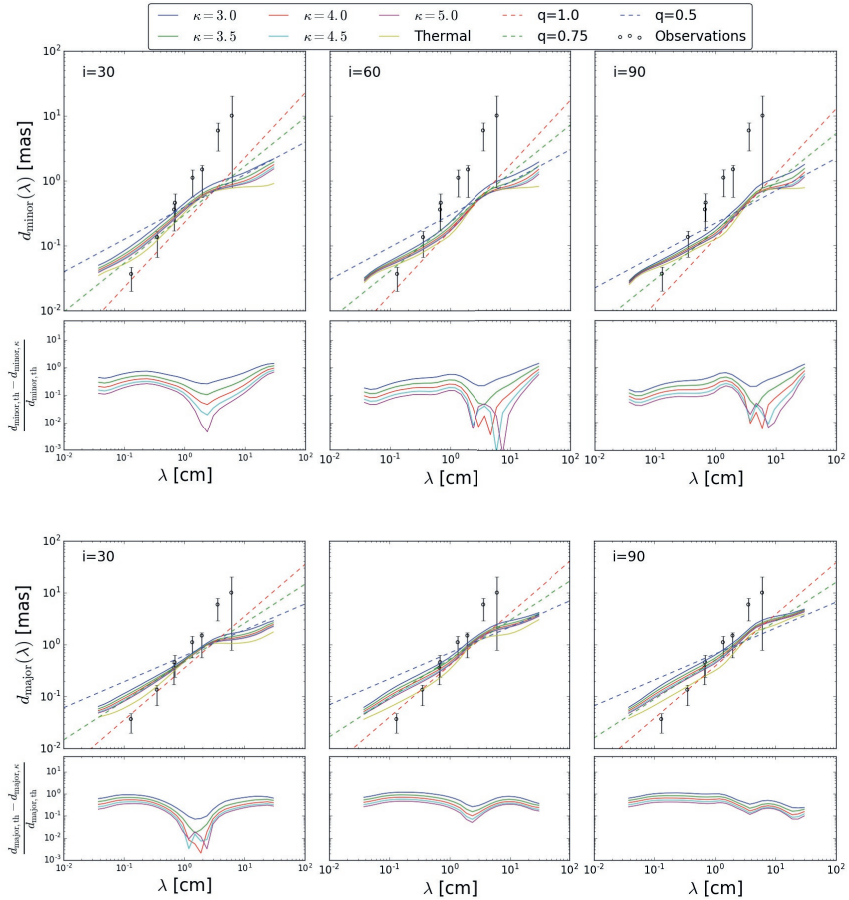


FIGURE 2.9: First and third row: the major (first row) and minor (third row) axis sizes of the jet model as a function of observing wavelength for both thermal and  $\kappa$  electrons together with measured intrinsic sizes of Sgr A\* reported by Bower et al. (2006) and Doeleman et al. (2008). Dotted lines are  $d(\lambda) = d_{th}(3cm) \left(\frac{\lambda}{3cm}\right)^q$  for three values of  $q$ . Second and fourth rows: relative difference between  $\kappa$ -jet and thermal-jet size for the major (second row) and minor axes (fourth row).

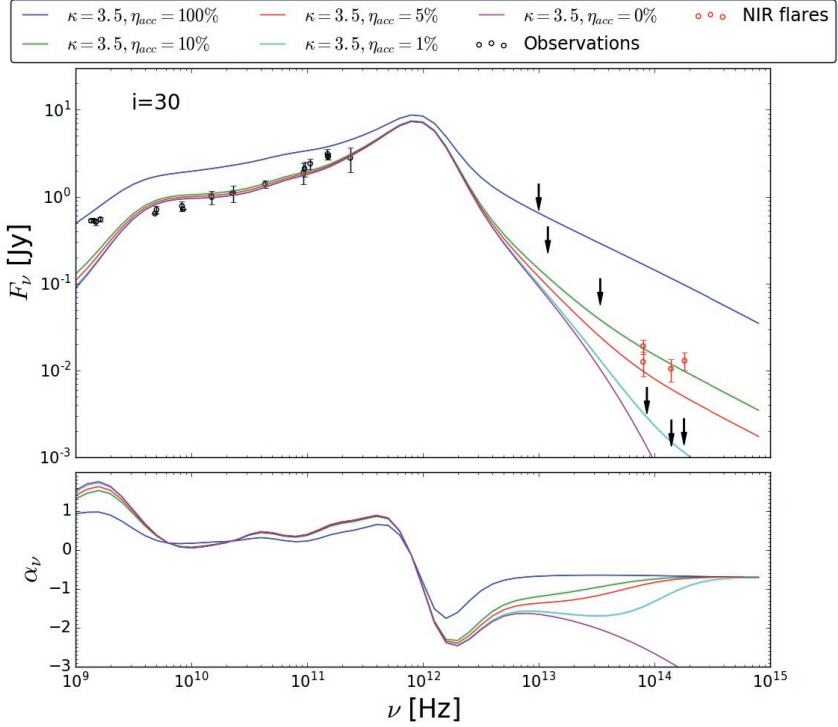


FIGURE 2.10: SED overlotted with observational data (top) and spectral index (down) for various ratios of thermal and  $\kappa$  models for Sgr A\* at an observing angle of  $i = 30^\circ$ . Observational data from Melia & Falcke (2001), NIR flares from Genzel et al. (2003) and Dodds-Eden et al. (2009).

In Mościbrodzka et al. (2016b), the temperature ratio between the protons and electrons was described as a function of the plasma  $\beta$  parameter. More recent work by Ressler et al. (2015b) showed that there is indeed a relation between temperature and plasma  $\beta$ .

In this work, we present a new set of models. We use the plasma  $\beta$  prescription for the proton-to-electron temperature ratio in the disk, and we add accelerated electrons along the jet. The accelerated electrons are described by the  $\kappa$  distribution function for electrons. With these  $\kappa$ -jet models, we recover the flat-to-inverted SEDs reported by observers, while we relax the assumption of an isothermal jet. The best fit pure  $\kappa$  model fits the radio and NIR flux when  $\kappa = 5.0$  and  $i = 30$ , but does not recover the spectral index of  $\alpha = -0.7$  in the NIR. Therefore a mixed model of  $\kappa$  distributed electrons and thermal electrons is favored.

If we use a mixed distribution (a superposition of a thermal and a  $\kappa$  distribution) to describe the electrons inside the jet, instead of  $\kappa$  only, we obtain a better fit to the observed SEDs. For NIR upper limits in quiescence, we obtain a fit with  $\kappa = 3.5$ ,  $\eta_{\text{acc}} < 1\%$ , and an observing angle  $i = 30^\circ$ , while for flaring states we obtain  $\kappa = 3.5$ ,  $\eta_{\text{acc}} = 5 - 10\%$ , and an observing angle  $i = 30^\circ$ . With these values we also recover the observed spectral index of  $\alpha = -0.7 \pm 0.3$ . By considering

$\eta_{\text{acc}}$  as a free parameter, we add an extra degree of freedom to our models. We think that it is justified to assume that only a subsection of the electrons will encounter the shock structures. All of our 100%  $\kappa$  jet models do not fit the spectral index of Sgr A\*; these models could, on the other hand, be valuable for different sources where the percentage of electrons that are accelerated could be large, e.g., M87\*. Current GRMHD simulation cannot resolve shocks and are unable to capture the micro-physics of electron heating. Future particle-in-cell simulations are necessary to fully understand the micro-physics involved.

In the case of our best fit model where the percentage of electrons in the  $\kappa$  distribution is  $\eta_{\text{acc}} = 5\% - 10\%$ , we can calculate the electrons acceleration efficiency as explained in 2.C. Our electrons acceleration efficiency  $\eta$  for the mixed model results in  $\eta = 0.06 - 0.12$ , which is also similar to Mao et al. (2017) and Ball et al. (2016), unless the fact that Mao et al. (2017) and Ball et al. (2016) insert the accelerated electrons in different regions.

The best fit viewing angle is inconsistent with earlier papers like Markoff et al. (2007), where an inclination of  $i > 75^\circ$  is favored, and Broderick et al. 2009 and Dexter et al. (2010), who report an inclination of  $i = 50^\circ$ . The inconsistency arises because lower viewing angles are necessary to fit the radio frequencies. This is a consequence of the relaxation of an isothermal jet since Mościbrodzka & Falcke 2013 obtained fits with higher viewing angles. In our  $\kappa$ -jet models, inclinations higher than  $\approx 60^\circ$  are excluded.

BK79 introduced an analytical model of a jet to describe nearly-flat spectra radio cores of galaxies. Similar work was done by Falcke & Biermann (1995), who showed a strong connection between the disk and the jet to explain the radiative properties of accreting black holes, such as radio luminosity and source size. It was assumed that the emitting electrons were in a power-law distribution; we repeated these calculations in Appendix 2.B, but using the  $\kappa$  distribution function instead. We find a strong correlation between the source radio-flux as a function of the  $\kappa$  parameter, which decreases with increasing  $\kappa$  values, as can be seen in Figure 2.12. We recover a radio flux that is independent of  $\nu$ , which is in agreement with both the BK79 model and Falcke & Biermann (1995).

The difference between the  $\kappa$  and thermal models are relatively large at low- (radio) and high-frequency (optical/NIR) emission compared to the mm-wavelengths. The mm-emission is produced close to the disk, and the relatively small difference in flux density between the  $\kappa$  and thermal models shows that the mm-emission is produced by the thermal electrons.

### 2.4.2 Intrinsic size of the $\kappa$ -jet model as a function of $\lambda$

The synthetic radio images clearly show a more extended jet structure for Sgr A\* when emission from accelerated electrons is included in the outflows. By adding accelerated electrons, the energy in the population increases. In this circumstance, the more energetic electrons emit photons at higher frequencies compared to their thermal counterparts. In general, for a given radiation frequency, the electrons radiate in different regions of the jet; the further away from the black hole one looks, the lower the amount of emission is (since the magnetic field strength and the number density decay with increasing radius). When we accelerate the electrons in the jet, the energy available for emitting radiation increases. This results in a larger contribution to the total emission at larger radii compared to the thermal case, and hence in a more extended source.

The observed and modeled core size follow a size-wavelength dependency  $FWHM \propto \lambda^q$ . In all  $\kappa$ -jet models,  $q > 1$  for  $\lambda > 3$  cm. Our results can be understood in terms of a simple model presented in Appendix 2.B, where we derive an analytical expression that explains the source size as a function of  $\kappa$ .

## 2.5 Conclusion

We analyzed the radial structure of jets produced in two-dimensional GRMHD simulations of an accreting black hole. Our simulations show a clear, thin jet-sheath region that follows the BK79 jet model in the inner  $100GM/c^2$ , consistent with previous findings. The effects of various initial and boundary conditions on the thermal structure of the radially extended jets should be investigated in fully 3D models, because in 2D, the turbulence weakens due to azimuthal symmetry, and the accretion rate, and hence the outflow rate decrease over time.

We analyzed the impact of the particle acceleration in the jet-sheath on the observed radio flux and the jet emission region size. Our numerical results are confirmed by a simple semi-analytic jet model. We show that both the radio flux and the size of the emitting region in the jet, increase with decreasing  $\kappa$  parameter. At this time, all our models are too large compared to observational constraints from Sgr A\* system, which is again likely an artifact of axisymmetry. However, our model easily recovers a nearly-flat radio SED of Sgr A\* while relaxing the assumption of a fully isothermal jet. Our  $\kappa$ -jet model with  $\kappa = 3.5$ ,  $\eta_{\text{acc}} = 1\%$  and observing angle  $i = 30^\circ$  fits the Sgr A\* emission in quiescence. Additionally, our  $\kappa$ -jet model with  $\kappa = 3.5$ ,  $\eta_{\text{acc}} = 5\% - 10\%$ , and observing angle  $i = 30^\circ$ , fits the observed fluxes of Sgr A\* when the source is in flaring state.

### Acknowledgements

This work was funded by the ERC Synergy Grant “BlackHoleCam-Imaging the Event Horizon of Black Holes” (Grant 610058). We thank Jason Dexter for useful comments on the manuscript. This research has made use of NASA’s Astrophysics Data System.

## 2.A Polar logarithmic camera

In order to resolve the emission profile at all frequencies, we adapted the camera of RAPTOR to a logarithmic polar camera. In the case of a uniform camera grid, one needs a very high resolution to resolve both the low and high frequency in one SED. We therefore distribute our impact parameters (see Bronzwaer et al. (2018)) as follows:

$$\alpha = r \cos(\theta), \quad (2.10)$$

$$\beta = r \sin(\theta), \quad (2.11)$$

where  $r$  and  $\theta$  are given by

$$r = \exp\left(\log(r_{\text{cam}}) \frac{i}{N_r}\right) - 1, \quad (2.12)$$

$$\theta = \frac{2\pi j}{N_\theta}, \quad (2.13)$$

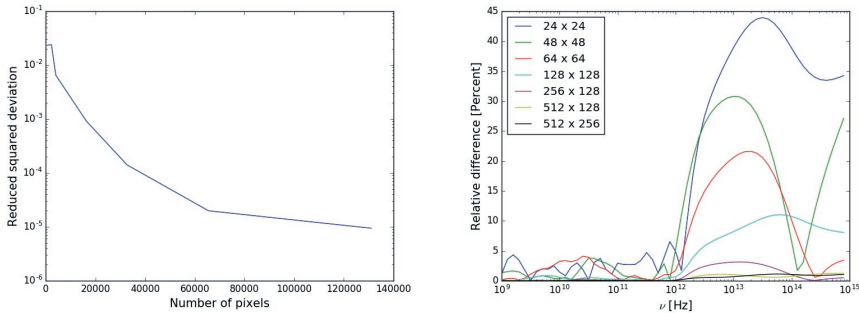


FIGURE 2.11: Left: The total frequency integrated relative difference between SEDs at different resolutions with respect to an SED at a resolution of  $1024 \times 1024$ . Right: The relative difference as a function of frequency between SEDs at different resolutions with respect to an SED at a resolution of  $1024 \times 1024$ .

where  $i, j$  are the pixel indices and  $N_r, N_\theta$  are the number of pixels in  $r$  and  $\theta$  respectively.

After the radiative transfer calculations, each intensity must be scaled by the size of the corresponding pixel; in polar coordinates, this surface element is given by  $dA = r dr d\theta$ , where

$$dr = \frac{dr}{di} di = \frac{\log(r_{cam})}{N_r} \exp\left(\log(r_{cam}) \frac{i}{N_r}\right), \quad (2.14)$$

$$d\theta = \frac{d\theta}{dj} dj = \frac{2\pi}{N_\theta}. \quad (2.15)$$

We calculated the convergence rate of this image grid by first calculating the square of the relative difference between the resolution under consideration and a high resolution polar grid of  $1024 \times 1024$ . We then sum this result over all frequencies, and divide this by the number of frequencies to calculate the reduced squared deviation. The deviation with respect to the high resolution run rapidly decreases several orders of magnitude with increasing resolution, as can be seen in Figure 2.11. We show in right panel of Figure 2.11 that the difference between our polar grid resolution of  $512 \times 256$  is converged up to  $\mathcal{O}(1)$  percent at all frequencies. It is evident from this image that, especially in order to resolve the high frequency emission, one needs a high resolution image grid.

## 2.B The size of a synchrotron photosphere as a function of $\kappa$ and wavelength

Here we calculate the source size and source radio luminosity of a relativistic magnetized jet as a function of the  $\kappa$  parameter. We follow the same approach as Falcke & Biermann (1995) (FB95), the only difference being that our distribution function is not a power-law distribution function but the  $\kappa$  distribution function. The jet in FB95 is assumed to be conically shaped, the opening angle of the jet being given by

$$\phi \geq \arcsin \mathcal{M}^{-1}, \quad (2.16)$$

where  $\mathcal{M}$  is the relativistic Mach number.

Our particle distribution function is given by:

$$\frac{dn_{e|p}}{d\gamma} = K_{e|p} \gamma \sqrt{\gamma^2 - 1} \left(1 + \frac{\gamma - 1}{\kappa w}\right)^{-(\kappa+1)}, \quad (2.17)$$

where  $\gamma$  is the Lorentz factor,  $w$  is a parameter that is equal to the dimensionless temperature of the particles in the GRMHD simulation,  $\kappa$  is a free parameter that in the optically thin regime is related to the power-law index  $p$  by  $\kappa = p + 1$ , and  $K_{e|p}$  is a normalization constant that determines the total amount of particles.

For simplicity, we assume that  $w$  and  $\kappa$  are the same for both the electrons and protons. Similarly to FB95, we assume that there is an equipartition between the magnetic energy  $U_B$  and the energy of the particles  $U_{e+p}$  within a factor  $k_{e+p}$ , such that

$$k_{e+p} \frac{B^2}{8\pi} = K_e \int \gamma m_e c^2 \frac{dn_e}{d\gamma} d\gamma + K_p \int \gamma m_p c^2 \frac{dn_p}{d\gamma} d\gamma, \quad (2.18)$$

where  $B$  is the magnetic field strength,  $m_e$  is the electron mass,  $c$  is the speed of light, and  $m_p$  is the mass of the proton.

Integrating Equation 2.18 results in

$$\begin{aligned} k_{e+p} \frac{B^2}{8\pi} &= \frac{m_e c^2 K_e + m_p c^2 K_p}{\Gamma(\kappa + 1)} 2^{\kappa-3} \kappa w \left(1 - \frac{1}{\kappa w}\right)^{-\kappa} \\ &\quad \left(\frac{1}{\kappa w - 1}\right)^{-\kappa} \left(\kappa \Gamma\left(\frac{\kappa - 3}{2}\right) \Gamma\left(\frac{\kappa + 1}{2}\right)\right) \\ &\quad {}_3F_2\left(\frac{\kappa}{2} - \frac{3}{2}, \frac{\kappa}{2} + \frac{1}{2}, \frac{\kappa}{2} + 1; \frac{1}{2}, \frac{\kappa}{2}; (\kappa w - 1)^2\right) \\ &\quad - \kappa(\kappa + 1)(\kappa w - 1) \Gamma\left(\frac{\kappa}{2} - 1\right) \Gamma\left(\frac{\kappa}{2}\right) \\ &\quad {}_3F_2\left(\frac{\kappa}{2} - 1, \frac{\kappa}{2} + 1, \frac{\kappa}{2} + \frac{3}{2}; \frac{3}{2}, \frac{\kappa}{2} + \frac{1}{2}; (\kappa w - 1)^2\right) \\ &= (m_e c^2 K_e + m_p c^2 K_p) \Lambda(\kappa, w), \end{aligned} \quad (2.19)$$

where  $\Gamma(x)$  is the Gamma function,  ${}_3F_2$  is the third hypergeometrical function of the second kind, and the function  $\Lambda(\kappa, w)$  contains all dependencies on  $\kappa$  and  $w$ .

We can then use this result to obtain an expression for the normalization factor  $K_e$  to find

$$\begin{aligned} K_e &= \frac{k_{e+p} B^2}{8\pi \Lambda m_e c^2} \left(1 + \frac{m_p K_p}{m_e K_e}\right) \\ &= \frac{k_{e+p} B^2}{8\pi \Lambda m_e c^2} \mu_{p/e} \\ &= \frac{B^2}{8\pi f m_e c^2}, \end{aligned} \quad (2.20)$$

where

$$f = \frac{\Lambda \mu_{p/e}}{k_{e+p}}, \quad (2.21)$$

and  $\mu_{p/e}$  is the proton to electron ratio:

$$\mu_{p/e} = \left(1 + \frac{m_p K_p}{m_e K_e}\right). \quad (2.22)$$

With the normalization factors known, we can now calculate the number density of the electrons by integrating equation 2.17:

$$\begin{aligned}
 n_{\text{e|p}} &= \frac{K_{\text{e|p}}}{(k^2 - 4)\Gamma(\kappa + 1)} 2^{\kappa-2} \left(1 - \frac{1}{\kappa w}\right)^{-\kappa-1} \\
 &\left( (\kappa w - 1)^2 \right)^{\kappa/2} \left( 4\sqrt{\kappa w - 1}^2 \Gamma\left(\frac{\kappa}{2} + 2\right) \Gamma\left(\frac{\kappa}{2}\right) \right. \\
 &{}_2F_1\left(\frac{\kappa - 2}{2}, \frac{\kappa + 2}{2}; \frac{1}{2}; (\kappa w - 1)^2\right) + 2\Gamma\left(\frac{\kappa - 1}{2}\right) \\
 &\Gamma\left(\frac{\kappa + 3}{2}\right) \left( \kappa w(2 - \kappa w) {}_2F_1\left(\frac{\kappa - 1}{2}, \frac{\kappa + 3}{2}; -\frac{1}{2}; (\kappa w - 1)^2\right) \right. \\
 &\quad \left. + (2\kappa((\kappa + 1)w(\kappa w - 2) + 1) + 1) \right. \\
 &\quad \left. {}_2F_1\left(\frac{\kappa - 1}{2}, \frac{\kappa + 3}{2}; \frac{1}{2}; (\kappa w - 1)^2\right) \right) \Big) \\
 &= K_{\text{e|p}} \Phi = \frac{B^2}{8\pi f m_e c^2} \Phi(\kappa, w),
 \end{aligned} \tag{2.23}$$

where  ${}_2F_1$  is the second hypergeometrical function of the first kind, and  $\Phi(\kappa, w)$  again contains all dependencies on  $\kappa$  and  $w$ .

Similarly to FB95, we can define a ratio between the total number density and the electron number density as

$$x_e = \frac{n_e}{n_{\text{tot}}}, \tag{2.24}$$

and a modified ratio as

$$x'_e = \frac{x_e}{\Phi(\kappa, w)}, \tag{2.25}$$

such that

$$n_{\text{tot}} = \frac{B^2}{8\pi f x'_e m_e c^2}. \tag{2.26}$$

The mass supply of the jet is in FB95 given as a fraction of the mass supply of the disk, which results in

$$\dot{M}_{\text{jet}} = q_m \dot{M}_{\text{disk}} = \gamma_j \beta_j c n_{\text{tot}} m_p \pi (r_{\text{nozz}} R_g)^2, \tag{2.27}$$

where  $q_m$  is the matter fraction of the outflowing matter,  $\gamma_j$  is the Lorentz factor of the bulk of the jet,  $\beta_j$  is the bulk velocity of the jet, and  $r_{\text{nozz}}$  is the width of the jet nozzle.

We can use this expression to calculate  $n_{\text{tot}}$ , which is given by

$$n_{\text{tot}} = \frac{q_m \dot{M}_{\text{disk}}}{\gamma_j \beta_j c m_p \pi (r_{\text{nozz}} R_g)^2}. \tag{2.28}$$

We now use the result of equation 2.26 to find, for  $B_{\text{nozz}}$ ,

$$B_{\text{nozz}} = \sqrt{\frac{8q_m \dot{M}_{\text{disk}} m_e c x'_e f}{\gamma_j \beta_j m_p}}. \tag{2.29}$$

We have now obtained all initial conditions for the jet at the nozzle.

We use the same function for  $r_{jet}(z_{jet})$  as FB95, which is given by

$$r_{jet}(z_{jet}) = r_{nozz} + (z_{jet} - z_{nozz})/\mathcal{M}, \quad (2.30)$$

where  $r_{nozz}$  is the size of the nozzle of the jet, and  $\mathcal{M}$  is the Mach number. This relation asymptotically approaches

$$r_{jet}(z_{jet}) = z_{jet}/\mathcal{M}, \quad (2.31)$$

if  $z_{jet} \gg z_{nozz}$ .

Conservation of mass and magnetic energy results in expressions for  $B$  and  $n_e$  as a function of radius given by

$$B = B_{nozz}\mathcal{M}/z_{jet}, \quad (2.32)$$

$$n_e = n_{e,nozz}/z_{jet}^2. \quad (2.33)$$

The internal energy also follows  $z_{jet}^{-2}$ , resulting in an isothermal jet.

According to FB95, the Mach number is given by

$$\mathcal{M} = \frac{\gamma_j \beta_j}{\beta_s}, \quad (2.34)$$

which is the ratio between the proper flow speed and the sound speed of the jet. The sound speed is given by

$$\beta_s = \sqrt{u_{j0}(\Gamma^2 - \Gamma)fx'_e m_e/m_p}. \quad (2.35)$$

The optical depth of a conical jet is given by

$$\tau = 2r_{jet}R_g\alpha_\kappa/\sin(i). \quad (2.36)$$

The location at which  $\tau = 1$  is the point where the jet becomes Synchrotron self-absorbed; this is a measure of the size of the jet. To find this distance  $Z_{ssa}$ , we use the absorptivity based on the  $\kappa$  distribution function, where we assume that we are in the low frequency limit;

$$\begin{aligned} \alpha_\kappa &= \frac{n_e}{B\sin(\theta)} X_\kappa^{-5/3} 3^{1/6} \frac{10}{41} \frac{(2\pi)^2}{(w\kappa)^{16/3-\kappa}} \\ &\quad \frac{(\kappa-2)(\kappa-1)\kappa}{3\kappa-1} \Gamma\left(\frac{5}{3}\right) {}_2F_1\left(\kappa - \frac{1}{3}, \kappa + 1, \kappa + \frac{2}{3}, -\kappa w\right) \\ &= \frac{n_e}{B\sin(\theta)} X_\kappa^{-5/3} \chi(\kappa, w), \end{aligned} \quad (2.37)$$

where

$$X_\kappa = \frac{\nu}{(w\kappa)^2 \sin(\theta) \nu_c}, \quad (2.38)$$

$$\nu_c = \frac{eB}{2\pi m c}, \quad (2.39)$$

and  $\chi(\kappa, w)$  again contains only dependencies on  $\kappa$  and  $w$ .

## 2.B THE SIZE OF A SYNCHROTRON PHOTOSPHERE AS A FUNCTION OF $\kappa$ AND WAVELENGTH

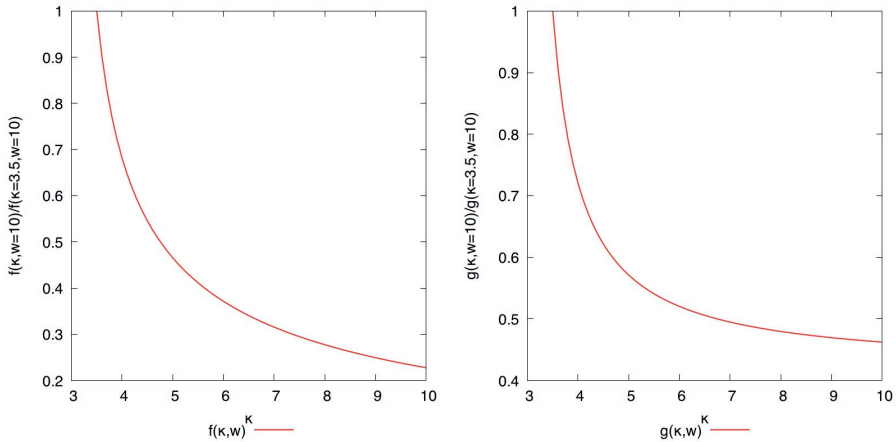


FIGURE 2.12: Left: The source size at a given frequency as a function of  $\kappa$ , where the size is defined as the radius at which the source transitions from optically thick to thin. Right: The radio flux in the optically thick part of the SED as a function of  $\kappa$ .

Inserting  $B(z_{jet})$ ,  $n_e(z_{jet})$  and solving for  $Z_{ssa}$  results in

$$Z_{ssa} = \left( \frac{\mathcal{M} \sin(i)}{2} \right)^{-3/5} n_{noz z}^{3/5} B_{noz z}^{2/5} \nu^{-1} \sin(\theta)^{2/5} \left( \frac{m_e c^2}{e(w\kappa)^2} \right)^{-1} \chi^{3/5}. \quad (2.40)$$

We find a relation for the size as a function of frequency given by  $Z_{ssa} \propto \frac{1}{\nu}$ . As a function of wavelength this results in  $Z_{ssa} \propto \lambda$  which is in agreement with recent observations of Sgr A\* (Doeleman et al. 2008 and Bower et al. (2006)). Inserting  $\mathcal{M}$ ,  $B_{noz z}$  and  $n_{noz z}$  results in a relation between the source size and the  $\kappa$  parameter given by

$$Z_{ssa} \propto (w\kappa)^2 \chi^{3/5} \left( \frac{\Lambda}{\Phi} \right)^{4/5} = f(\kappa, w), \quad (2.41)$$

where the function  $f(\kappa, w)$  is plotted in left panel of Figure 2.12.

We can now also calculate the total radio luminosity by integrating

$$L_\nu = \int_{Z_{noz z}}^{Z_{ssa}} \epsilon(z_j) \kappa \pi (z_j / \mathcal{M})^2 dz_j, \quad (2.42)$$

where we use that the emissivity is given by

$$\begin{aligned} \epsilon(z_j) &= \frac{n_e e^2 \nu_c \sin(\theta)}{c} X_\kappa^{1/3} \frac{4\pi \Gamma\left(\kappa - \frac{4}{3}\right)}{3^{7/3} \Gamma(\kappa - 2)} \\ &= \frac{n_e e^2 \nu_c \sin \theta}{c} X_\kappa^{1/3} \Theta(\kappa, w), \end{aligned} \quad (2.43)$$

and  $\Theta(\kappa, w)$  again only depends on  $\kappa$  and  $w$ .

If we assume that we can neglect the lower boundary of the integral (where  $\tau \gg 1$ ), we obtain

$$L_\nu = \frac{12\pi e^3}{mc^3} \sin^{-1/5}(\theta) \left( \frac{\mathcal{M} \sin(i)}{2} \right)^{-1/5} n_{nozz}^{6/5} B_{nozz}^{4/5} \chi^{3/5}. \quad (2.44)$$

The total radio flux is independent of frequency, as one would expect. Inserting  $\mathcal{M}$ ,  $B_{nozz}$  and  $n_{nozz}$  results in a relation between  $L_\nu$  and  $\kappa$  given by

$$L_\nu \propto \left( \frac{\Lambda(\kappa, w)}{\Phi(\kappa, w)} \right)^{3/5} \chi(\kappa, w)^{1/5} = g(\kappa, w). \quad (2.45)$$

The resulting function  $g(\kappa, w)$  is plotted in the right panel of Figure 2.12.

## 2.C Particle acceleration efficiency

What is the electron acceleration efficiency in our pure  $\kappa$ -jet models as a function of  $\kappa$  parameter? The  $\kappa$  distribution function smoothly connects a power law to a thermal core; it is, therefore, difficult to define the electron acceleration efficiency, as was done in previous works. To compute the efficiency, we introduce our modified acceleration efficiency  $\eta_{mod}$ , which is defined as the ratio of the electrons that got shifted to higher  $\gamma$  values (the power-law part), compared to a purely thermal distribution, and the electrons that experience only a small shift (the thermal core). The thermal core and power-law part of the  $\kappa$  distribution function are defined in Figure 2.13 (left panel). If we compare a purely thermal distribution with a  $\kappa$  distribution we can distinguish three different regions;  $S_1$ ,  $S_2$ , and  $S_3$ .  $S_1$  is the region where the thermal distribution is larger than the  $\kappa$  distribution,  $S_2$  is the region where they overlap, and  $S_3$  is the region where the  $\kappa$  distribution is larger. Since both distribution functions are normalized to the same value, we know that  $S_1$  and  $S_3$  have to have an equal surface, and therefore, contribute an equal amount of electrons to the total amount of electrons. The consequence of this is that, when comparing a  $\kappa$  model to the thermal case, the number of electrons in  $S_1$  in the thermal models is shifted towards higher energies in the region  $S_3$  in the case of the  $\kappa$ -jet models. The region  $S_2$  is the number of electrons in the thermal core of the  $\kappa$  distribution function. This enables us to quantify the number of electrons that shift to higher energies by integrating the difference between the thermal and  $\kappa$  distribution up to the point  $\gamma_{max}$  where the two distribution functions are equal ( $n_{thermal}(\gamma_{max}, \Theta_e) = n_\kappa(\gamma_{max}, \Theta_e)$ )

Figure 2.13 (middle panel) shows the ratio between the electrons that get shifted to the power-law tail and the total number density of electrons along the jet as a function of the distance from the core for adopted values of the  $\kappa$  parameter. Note that the particle number densities in the  $S_1$  and  $S_3$  regions in Figure 2.13 (left panel) are equal, hence the fractional number density of electrons in the power-law tail can be defined as:

$$\mu(r) = \frac{\int_1^{\gamma_{max}} (n_{thermal}(\gamma, \Theta_e) - n_\kappa(\gamma, \Theta_e)) d\gamma}{\int_1^\infty n_{thermal}(\gamma, \Theta_e) d\gamma}, \quad (2.46)$$

where integration in the numerator is carried out between 1 and  $\gamma_{max}$  and where the electron temperature  $\Theta_e(r)$  is a function of radius as displayed in the rightmost panel in Figure 2.4. The fractional number density in the jet region increases with decreasing  $\kappa$  values, and is nearly constant as a function of radius.

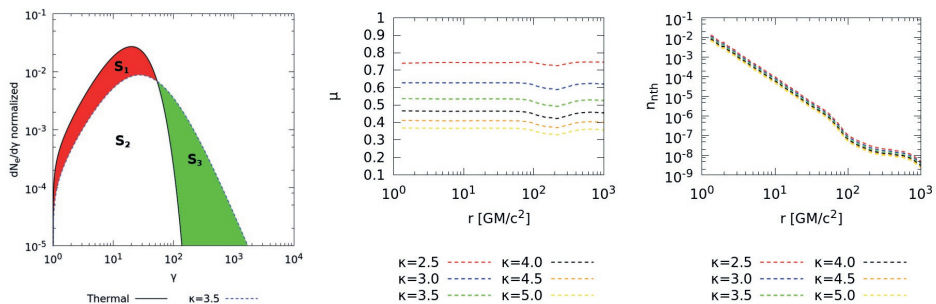


FIGURE 2.13: Left panel: an illustration of the calculation of  $\mu$  (Eq. 2.46) for one value of  $\kappa$ . Middle: ratio of particle number densities between the power law tail and the thermal core of the  $\kappa$  distribution function along the jet. Right panel: Number density, in code units, of electrons in the power-law part of the  $\kappa$  distribution function.

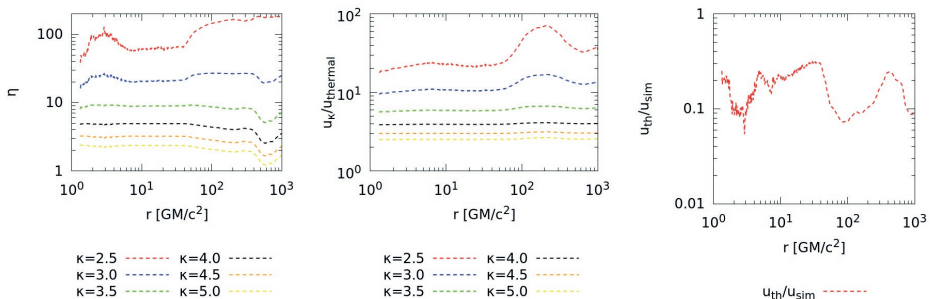


FIGURE 2.14: Left panel: our modified energy efficiency  $\eta_{mod}$ . Middle: ratio of kinetic energy in  $\kappa$  to a purely relativistic Maxwell-Jüttner distribution function along the jet. The electron temperatures along the jet are shown in Figure 2.4 (right panel). Right panel: ratio between the energy in the thermal distribution to the simulation energy.

Figure 2.13 (right panel) displays the number density of electrons in the  $\kappa$  distribution function that occupies the power-law part of the distribution function. Note that the particle number density is given here in code units. To convert these values to [particles/cm<sup>3</sup>], one has to multiply with  $n_0$ , which is given for Sgr A\* in Table 2.1.

Finally, we define the modified acceleration efficiency  $\eta_{mod}$  as the ratio of the total energy of the electrons in the S3 region to those in the S2 region, i.e. the ratio of energy in the power-law tail to the energy in the quasi-thermal core:

$$\eta_{mod} = \frac{\langle u \rangle_\kappa(S3)}{\langle u \rangle_\kappa(S2)}, \quad (2.47)$$

where  $\langle u \rangle_\kappa = \int (\gamma - 1) n_\kappa(\gamma, \Theta_e) d\gamma$  is the kinetic energy of electrons integrated over the energy distribution function. Figure 2.14 (left panel) shows the modified particle acceleration efficiency for various values of  $\kappa$ .

In Figure 2.14 (middle panel), we compare the total energy in the  $\kappa$  distribution to the total energy in a purely relativistic thermal distribution function. The ratio of  $\kappa$  and thermal kinetic energies is given by

$$\frac{\langle u \rangle_{\kappa}(S2 + S3)}{\langle u \rangle_{\text{thermal}}} = \frac{\int(\gamma - 1)n_{\kappa}(\gamma, \Theta_e)d\gamma}{\int(\gamma - 1)n_{\text{thermal}}(\gamma, \Theta_e)d\gamma}. \quad (2.48)$$

We find that for the smallest  $\kappa$  parameter, the energy within a radius of  $100 GM/c^2$  is about 20 times higher compared to a purely relativistic thermal distribution, and this increases to 70 times higher at larger radii, where the temperature in the jet decreases, and can, therefore, explain the increase in energy ratio. The Maxwell-Jüttner distribution function narrows for small values of  $\Theta_e$ , hence adding a power law has a larger relative effect on the energy content while the absolute difference is smaller.

How much energy is in thermal electrons (and the  $\kappa$  distribution function) compared to the energy available in the simulation? The total energy in thermal electrons is analytically given by (Gammie & Popham 1998)

$$u_{\text{thermal}} = a(\Theta_e)N_{\text{thermal}}m_e c^2 \Theta_e, \quad (2.49)$$

where

$$a(\Theta_e) \approx \frac{6 + 15\Theta_e}{4 + 5\Theta_e}. \quad (2.50)$$

Figure 2.14 (right panel) shows the ratio  $u_{\text{thermal}}/u_{\text{sim}}$ , the energy in a thermal distribution to the energy available in the simulations:

$$u_{\text{sim}} = u_{\text{int}} + B^2/2, \quad (2.51)$$

where  $u_{\text{int}}$  is the internal energy density, and  $B$  the magnetic field strength. The value of this ratio is around 0.1 – 0.3. We can therefore only use radiative transfer models that are self consistent, i.e.  $\frac{u_{\kappa}}{u_{\text{thermal}}} \frac{u_{\text{thermal}}}{u_{\text{sim}}} < 1.0$ , which is the case for  $\kappa > 3$ .

In the case of mixed  $\kappa$  models, we can calculate the particle acceleration efficiency as follows

$$\eta = \eta_{\text{acc}} \frac{\eta_{\text{mod}}}{1 + \eta_{\text{mod}}} \frac{u_{\kappa}}{u_{\text{th}}} \frac{u_{\text{th}}}{u_{\text{sim}}} \quad (2.52)$$

---

# MODELING NON-THERMAL EMISSION FROM THE JET-LAUNCHING REGION OF M 87 WITH ADAPTIVE MESH REFINEMENT

Jordy Davelaar, Hector Olivares, Oliver Porth, Thomas Bronzwaer, Michael Janssen, Freek Roelofs, Yosuke Mizuno, Christian M. Fromm, Heino Falcke, and Luciano Rezzolla

*A&A, 2019, 653, A2*

## Abstract

The galaxy M 87 harbors a kiloparsec-scale relativistic jet, whose origin coincides with a compact source thought to be a supermassive black hole. Observational millimeter very long baseline interferometry campaigns are capable of resolving the jet-launching region at the scale of the event horizon. To provide a context for interpreting these observations, realistic general-relativistic magnetohydrodynamical (GRMHD) models of the accretion flow are constructed. Electrons in the jet are responsible for the observed synchrotron radiation emitted in frequencies ranging from radio to near-infrared (NIR) and optical. The characteristics of the emitted radiation depend on the shape of the electrons' energy-distribution function (eDF). The dependency on the eDF is omitted in the modeling of the first Event Horizon Telescope results. In this work, we aim to model the M 87 spectral-energy distribution from radio up to optical frequencies using a thermal-relativistic Maxwell-Jüttner distribution, as well as a relativistic  $\kappa$ -distribution function. The power-law index of the eDF is modeled based on sub-grid, particle-in-cell parametrizations for sub-relativistic reconnection. A GRMHD simulation in Cartesian-Kerr-Schild coordinates, using eight levels of adaptive mesh refinement (AMR), forms the basis of our model. To obtain spectra and images, the GRMHD data was post-processed with the ray-tracing code `RAPTOR`, which is capable of ray tracing through GRMHD simulation data that is stored in multi-level

AMR grids. The resulting spectra and synthetic synchrotron maps are compared with observations. We obtain radio spectra in both the thermal-jet and  $\kappa$ -jet models consistent with radio observations. Additionally, the  $\kappa$ -jet models also recover the NIR and optical emission. The images show a more extended structure at 43 GHz and 86 GHz and more compact emission at 228 GHz. The models recover the observed source sizes and core shifts and obtain a jet power of  $\approx 10^{43}$  ergs/s. In the  $\kappa$ -jet models, both the accretion rates and jet powers are approximately two times lower than the thermal-jet model. The frequency cut-off observed at  $\nu \approx 10^{15}$  Hz is recovered when the accelerator size is  $10^6 - 10^8$  cm. This could potentially point to an upper limit for plasmoid sizes in the jet of M 87.

### 3.1 Introduction

More than a century ago, a bright jet in the Virgo cluster was discovered by Curtis (1918). The jet originates from a nucleus that resides in the center of M 87, which is an elliptical galaxy. Since its discovery, the jet of M 87 has been subject to extensive radio observations (Bolton et al., 1949; Mills, 1952; Baade & Minkowski, 1954; Turland, 1975; Owen et al., 2000; de Gasperin et al., 2012), and various millimeter observations; 7 mm (43 GHz) (Junor et al., 1999; Ly et al., 2004; Walker et al., 2008; Hada et al., 2011, 2013, 2016; Walker et al., 2018), 3 mm (86 GHz) (Krichbaum et al., 2006; Hada et al., 2013; Kim et al., 2018), and 1.3 mm (228 GHz) (Doeleman et al., 2012). At millimeter-wavelengths, the radio emission shows a source morphology that is consistent with a jet launched from the putative supermassive black hole in the center of the radio core with a mass of  $M_{\text{BH}} = 6.2 \times 10^9 M_{\odot}$  (Gebhardt et al., 2011) and at a distance of  $d = 16.7$  Mpc (Mei et al., 2007). This black hole is one of the primary targets of global millimeter very long baseline interferometry (mm-VLBI) observations by the Event Horizon Telescope Collaboration, which has the aim to spatially resolve black-hole shadows (Falcke et al., 2000b; Goddi et al., 2017), and succeeded in the case of M 87 (Event Horizon Telescope Collaboration et al., 2019a,b,c,d,e,f). The shadow of a black hole is a depression of flux in the radiation field surrounding the black-holes event horizon, for a non-rotating black hole its size on the sky is given by  $2\sqrt{27}GM/(c^2D)$ , with  $G$  the Gravitational constant,  $M$  the black-hole mass,  $c$  the speed of light, and  $D$  the distance to the black hole. Due to the large set of observations available across the electromagnetic spectrum (see, e.g., Prieto et al., 2016) and the event horizon scale mm-VLBI observations, it is possible to use the M 87 jet as a laboratory to study jet launching and particle acceleration.

Since the discovery of M 87, relativistic jets have been studied in great detail in theory. The analytical model by Blandford & Königl (1979) describes an isothermal jet model that can explain the observed flat radio spectra of jets. They recover the observed relation between source size ( $r$ ) and frequency ( $\nu$ ) to be  $r \propto \nu^{-1}$ . An addition to this model was made by Falcke & Biermann (1995), who connected the accretion rate to the jet.

Broderick et al. (2009) modeled M 87 with an analytic, force-free jet model. Their best-fit model is consistent with 43 GHz observations. The model parameters include a black-hole spin of  $a_* = Jc/GM^2 = 0.998$ , a viewing angle of  $i = 25^\circ$ , and a jet foot-point at  $r = 10 GM/c^2$ , where the gravitational radius  $GM/c^2$  is defined as  $GM/c^2 = GM/c^2$ . The disk consists of both

thermal and accelerated electrons, but the fraction of accelerated electrons is low (around one percent). Inside the jet, only an accelerated electron population is present. Their model uses a black-hole mass of  $M = 3.4 \times 10^9 M_\odot$  (Walsh et al., 2013).

General-relativistic magnetohydrodynamical (GRMHD) simulations are often used to study the dynamics of accretion flows. Next, we review some of the earlier GRMHD based models of the M87 jet. The first model of M87 based on GRMHD simulations was presented by Dexter et al. (2012a), who computed synthetic synchrotron maps based on a high-spin GRMHD simulation. Their models included a thermal electron population in the disk and a power law based electron population in the jet. Their best-fit model, at an inclination of  $25^\circ$ , showed counter-jet dominated emission, meaning that most of the radiation detected by the observer originates in the jet that points away from the observer. Dexter et al. (2012a) obtained a mass-accretion rate of  $\dot{M} \approx 10^{-3} M_\odot/\text{yr}$ , and a power-law index of the non-thermal electron distribution function of  $p = 3.25 - 3.5$ , where they used a constant electron-to-proton temperature ratio of  $T_p/T_e = 10$ .

Mościbrodzka et al. (2016b) used GRMHD simulations and a Monte Carlo-based radiative-transfer code to model the full spectral energy distribution (SED) of an accreting supermassive black hole from radio to X-ray, as well as ray-traced images of the accretion flow at 43, 86 GHz, and 230 GHz. A thermal distribution function of the electrons was assumed across the simulation domain, and the electron physics was modeled by coupling the ion-to-electron temperature as a function of plasma  $\beta = P/P_{\text{mag}}$ , where  $P$  is the gas pressure and  $P_{\text{mag}}$  the magnetic pressure. The electrons were thermally distributed both in the disk and the jet. The authors obtained a mass accretion rate of  $\dot{M} \approx 9 \times 10^{-3} M_\odot$ , a favored inclination angle of  $20^\circ$  or  $160^\circ$  and an ion-to-electron temperature ratio in the disk of  $T_i/T_e = 100$ . Smaller values of the ion-to-electron temperature ratio resulted in an excess of X-ray emission. The 230 GHz images showed counter-jet dominated emission. Subsequently, Mościbrodzka et al. (2017) performed polarized radiative transfer calculations of the jet launching footpoint of M87 to obtain Faraday rotation measurements. It is shown that the best-fit jet-dominated model from Mościbrodzka et al. (2016b) recovers the observed 1% polarization fraction and rotation measure of the jet base in M87.

Recently, Ryan et al. (2018) performed 2D-axisymmetric two-temperature GRMHD simulations that include radiative cooling. The authors conclude that radiative cooling is important in the inner region ( $r < 10 GM/c^2$ ) of the accretion flow, and that the black-hole mass of  $M = 6.2 \times 10^9 M_\odot$  and spin  $a_* = 0.9375$  simulation recovers the observed radio and X-ray emission and image size at 230 GHz. The jet-opening angle in their model at lower frequencies is too narrow compared to the millimeter-observations of the jet base in M87, and the model assumes a thermal electron population in the entire simulation domain. Chael et al. (2019) also performed a two-temperature radiative GRMHD model of a magnetically arrested disc (MAD) (Narayan et al., 2003; Tchekhovskoy et al., 2011). The model recovers observables such as jet-opening angle, image size, core shift, and radio SED. This model also considers a thermal electron population and, therefore, does not fit the NIR and optical emission.

In 2019, the Event Horizon Telescope published its first set of results, showing an asymmetric ring-like structure in the radio core of M87 at 228 GHz. This ring-like structure is evidence for the existence of a black hole shadow and consistent with predictions from GRMHD models (Event Horizon Telescope Collaboration et al., 2019a,b,c,d,e,f). A detailed comparison of GRMHD models

with the data can be found in Event Horizon Telescope Collaboration et al. (2019e). The main assumption in these models that we want to address in this work is that the electron distribution function is taken to be *thermal* in the entire simulation domain.

All of the models have in common that they are based on GRMHD simulations that use spherical polar coordinates with a radial grid that is logarithmically spaced. Such a grid has the advantage of high resolution close to the event horizon but introduces a polar axis that needs careful treatment, potentially resulting in numerical issues that affect the jet outflow. GRMHD codes often track only the dynamically important ion fluid, with no direct knowledge of the electrons available. One of the open questions in modeling the electromagnetic radiation emerging from accreting black holes is, therefore, the shape of the distribution function of the radiatively important electrons. The often-made assumption that the electrons in the full simulation domain are in a thermal-relativistic Maxwell-Jüttner distribution potentially breaks down in regions where non-ideal effects are important.

These non-ideal effects are expected to be strongest in the highly magnetized regions of the jet, where they can be associated with magnetic reconnection accelerating electrons to very large energies. In the case of M87, features of electron acceleration are observed in the NIR and optical wavebands (see, e.g., Prieto et al., 2016, and references therein). We, therefore, need a distribution function that describes the electrons that are not in thermal equilibrium. Particle ensembles that are not in thermal equilibrium can be described in the framework of Tsallis statistical mechanics (Tsallis, 1988). In this framework, the  $\kappa$ -distribution function plays a key role. In Fig. 3.1 we show that the  $\kappa$ -distribution function is a combination of a thermal core at low values of the Lorentz factor  $\gamma$ , which asymptotically turns into to a power law with power-law index  $p = \kappa - 1$  for large  $\gamma$  values. In the limit of  $\kappa \rightarrow \infty$ , the  $\kappa$ -distribution becomes the Maxwell-Jüttner distribution function (Rezzolla & Zanotti, 2013). The  $\kappa$ -distribution function is observed at a variety of astrophysical systems such as the solar wind, solar magnetosphere, Jovian magnetospheres, planetary nebula, and many others (see for a review Pierrard & Lazar (2010) and references therein).

In Davelaar et al. (2018c), we introduced a  $\kappa$ -jet model for the accreting black hole in the center of the Milky Way, Sagittarius A\* (Sgr A\*). This model is a combination of a thermal and a  $\kappa$ -distributed electron population. In the accretion disk, we set the eDF to a thermal distribution function, while in the jet we use a mix of thermal and  $\kappa$ -distributed electrons. The ratio between the two species is a free parameter of the model. In the case of Sgr A\*, we found that  $\sim 5 - 10\%$  of the electrons is  $\kappa$ -distributed in the event of flares, and they are negligible in the quiescent state. The non-thermal prescription used in this model was an electron distribution with a constant power law in the outflow of the simulation domain with a fixed power-law index.

To improve the model, we here connect the electron-acceleration parameters to information from local kinetic plasma simulations. Kinetic plasma, or particle-in-cell (PIC) simulations, can resolve the micro-physics scales that GRMHD simulations cannot reach. Although local, these simulations can provide first-principle parametrizations of particle-acceleration processes. For our model, we consider a parametrization of the power-law index for trans-relativistic reconnection as found by Ball et al. (2018). Reconnection is known to be an efficient particle accelerator in magnetized environments (see, e.g., Sironi & Spitkovsky, 2014; Guo et al., 2014; Sironi et al., 2015; Werner et al., 2016; Petropoulou et al., 2016; Werner & Uzdensky, 2017; Werner et al.,

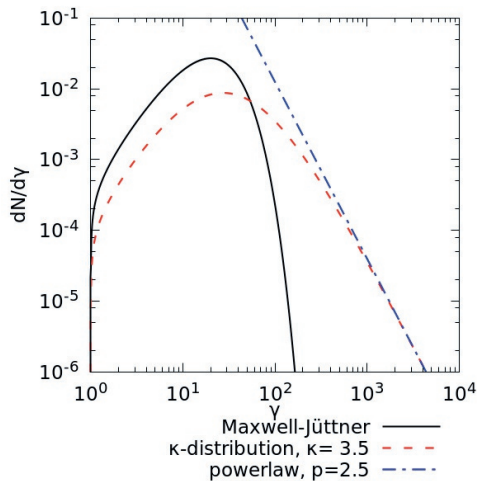


FIGURE 3.1: The  $\kappa$ -distribution function is a combination of a powerlaw with a thermal core. In this figure we show an example of the  $\kappa$ -distribution (orange) for a  $\kappa$  value of 3.5, and for comparison a Maxwell-Jüttner distribution (black), and a power-law distribution (yellow) with  $p = 2.5$ .

2018). Besides this parametrization, we also extended our model with an injection radius, which corresponds to the jet’s footpoint where electron acceleration can become important.

In this work, we apply thermal and  $\kappa$ -jet models to the accreting black hole in M87. The dynamics of the accretion flow are drawn from GRMHD simulations performed in Cartesian-Kerr-Schild (CKS) coordinates. This prevents numerical artifacts and directional biases of the jet caused by the presence of a polar axis, this will be studied in detail a future work. In addition, the use of adaptive mesh refinement (AMR) It allows us to capture the instabilities in the jet sheath and, at the same time, resolve the magneto-rotational instability (MRI) in the disk. We use the results of this simulation to generate SEDs, synthetic synchrotron maps (images), and optical-depth maps of the jet-launching region in M87. We extend the general-relativistic-ray-tracing (GRRT) code `RAPTOR`, rendering it compatible with AMR data structures. We fit synthetic SEDs obtained from our GRRT simulations to observational data.

The paper’s structure is as follows: in Section 3.2, we describe our GRMHD simulation setup and the electron model that we use in our radiative-transfer calculations. In Section 3.3, we compute SEDs, synchrotron and opacity maps, source sizes, and core shifts. In Section 3.4, we compare our results to previous works and observations. We summarize our results in Section 3.5.

## 3.2 Methods

In this Section, we describe the GRMHD simulation setup, the coordinates used to simulate the accretion flow and radiation transport, and introduce our electron-physics model.

### 3.2.1 GRMHD simulations

The dynamics of the accretion flow onto the black hole are simulated using the Black Hole Accretion Code (BHAC, Porth et al., 2017), which solves the GRMHD equations

$$\nabla_{\mu}(\rho u^{\mu}) = 0, \quad (3.1a)$$

$$\nabla_{\mu} T^{\mu\nu} = 0, \quad (3.1b)$$

$$\nabla_{\mu} {}^*F^{\mu\nu} = 0, \quad (3.1c)$$

where  $\nabla_{\mu}$  denotes the covariant derivative,  $\rho$  the rest-mass density,  $u^{\mu}$  the fluid 4-velocity,  $T^{\mu\nu}$  the energy-momentum tensor of the combined perfect fluid and electromagnetic fields, and  ${}^*F^{\mu\nu}$  the dual of the Faraday tensor ( $F^{\alpha\beta}$ ).

The system is closed by the ideal-MHD approximation corresponding to a plasma with infinite conductivity  $F^{\mu\nu}u_{\nu} = 0$ , and by the equation of state of an ideal fluid (see, e.g., Rezzolla & Zanotti, 2013)  $h(\rho, P) = 1 + \frac{\hat{\gamma}}{\hat{\gamma}-1} \frac{P}{\rho}$ , where  $h$  and  $P$  are the specific enthalpy and gas pressure in the fluid frame, and the adiabatic index  $\hat{\gamma} = 4/3$ . The simulation is initialized with a Fishbone-Moncrief torus (Fishbone & Moncrief, 1976) with its inner radius at  $6 GM/c^2$  and its pressure maximum at  $12 GM/c^2$ . The initial configuration of the magnetic field is a single poloidal loop described by the vector potential  $A_{\phi} \propto \max(\rho/\rho_{\max} - 0.2, 0)$ . The initial density and pressure are normalized so that  $\rho_{\max} = 1$ . The initial magnetic field is also normalized such that the ratio between maximum gas pressure  $P_{\max}$  and maximum magnetic pressure  $P_{\text{mag,max}}$  is  $P_{\max}/P_{\text{mag,max}} = 100$ . The disk is, therefore, weakly magnetized. In order to break the initial equilibrium state and accelerate the development of the MRI, we add 5% ‘white noise’ random perturbations to the pressure. This triggers the MRI, which transports angular momentum and allows accretion onto the black hole (Balbus & Hawley, 1991).

The black-hole’s dimensionless spin parameter was set to be  $a_* = 0.9375$ , where  $J$  is the angular momentum. For this value of  $a_*$  the inner horizon is at  $r \approx 1.34799 GM/c^2$ .

### 3.2.2 AMR grid in Cartesian-Kerr-Schild coordinates

Level	jet	disk
8	2	2
7	50	22
6	100	25
5	150	40
4	200	100
3	400	200
2	800	400
1	1000	1000

TABLE 3.1: Maximum AMR refinement radii in  $GM/c^2$  for the different AMR levels. The jet region is defined as the region where  $\theta < 15^\circ$  or  $\theta > 165^\circ$ , while the disk region is defined as  $15^\circ < \theta < 165^\circ$ .

The simulation is performed on a Cartesian (rectangular) grid. The covariant metric  $g_{\mu\nu}$  of a rotating black hole in Cartesian-Kerr-Schild (CKS) coordinates is given by (Kerr, 1963; Rezzolla & Zanotti, 2013)

$$g_{\mu\nu} = \eta_{\mu\nu} + fl_{\mu}l_{\nu}, \quad (3.2)$$

where  $\eta_{\mu\nu} = (-1, 1, 1, 1)$  is the Minkowski metric, and

$$f = \frac{2r^3}{r^4 + a_*^2 z^2}, \quad (3.3a)$$

$$l_{\nu} = \left( 1, \frac{rx + a_*y}{r^2 + a_*^2}, \frac{ry - a_*x}{r^2 + a_*^2}, \frac{z}{r} \right), \quad (3.3b)$$

where  $r$  is given by

$$r^2 = \frac{R^2 - a_*^2 + \sqrt{(R^2 - a_*^2)^2 + 4a_*^2 z^2}}{2}, \quad (3.4)$$

and

$$R^2 = x^2 + y^2 + z^2. \quad (3.5)$$

All units of length are scaled by the gravitational radius  $GM/c^2$  which is given by  $GM/c^2 = GM/c^2$ . In the limit of  $R \gg a_*$ , the radius  $r \rightarrow R$ . The contravariant metric is given by

$$g^{\mu\nu} = \eta^{\mu\nu} - fl^{\mu}l^{\nu}, \quad (3.6)$$

where  $l^{\nu}$  is given by

$$l^{\nu} = \left( -1, \frac{rx + ay}{r^2 + a_*^2}, \frac{ry - a_*x}{r^2 + a_*^2}, \frac{z}{r} \right). \quad (3.7)$$

The use of AMR allows us to increase the resolution in regions of interest during runtime. The decision to refine is made based on the Löhner scheme (Löhner, 1987), which quantifies variations of the density and the plasma magnetization  $\sigma$ , defined as  $\sigma = b^2/\rho$ , where  $b = \sqrt{b^{\mu}b_{\mu}}$  is the magnetic-field strength in the fluid frame. The code is allowed to refine up to a maximum level of refinement. The allowed maximum level depends on the location in the computational domain; larger refinement levels are allowed in the regions where the jet is expected to form, and the disk is expected to reside. This distinction is made based on a radius  $r$  and polar angle  $\theta$ , and for the jet this region is between  $\theta < 15^\circ$  or  $\theta > 165^\circ$ . The maximum allowed refinement level as a function of radius and polar angle is shown in Table 3.1. The base resolution of the grid is  $96 \times 96 \times 192$  cells in  $x$ ,  $y$ , and  $z$ -directions, respectively. The simulation domain is  $x \in (-500 GM/c^2, 500 GM/c^2)$ ,  $y \in (-500 GM/c^2, 500 GM/c^2)$  and  $z \in (-1000 GM/c^2, 1000 GM/c^2)$ . We simulate up to  $t_f = 10^4 GM/c^3$ , which corresponds to 37.5 orbital periods of the accretion disk at the pressure maximum. At the end of the simulation, the domain contains around 70 million cells.

### 3.2.3 Ray tracing in AMR CKS grid

In order to perform general-relativistic ray-tracing calculations in Cartesian coordinates within the block-based AMR data structure of BHAC, it has been necessary to extend our general-relativistic ray-tracing code **RAPTOR** (Bronzwaer et al., 2018). In particular, the initial conditions

for the rays, also called the “virtual camera”, employ a tetrad basis in which the initial wave-vectors are described (Noble et al., 2007), a description of the implementation of this in **RAPTOR** can be found in Davelaar et al. (2018b). The tetrad camera uses a set of trial vectors to generate a tetrad basis by using a Gram-Schmidt orthogonalization procedure. In spherical coordinate systems, the trial vectors are unit vectors pointing along the  $t, r, \theta, \phi$ -directions. In our case, we have to transform this into Cartesian coordinates. The virtual camera is constructed at a position  $(x_c, y_c, z_c)$  in space which is computed based on the following parameters: (i) the radial distance between the camera and the black hole  $r_c$ ; (ii) the inclination with respect to the black hole spin axis  $\theta_c$ ; (iii) the azimuthal angle around the black hole spin axis  $\phi_c$ . The tetrad trial vectors can then be defined as

$$t_0^\mu = (1, 0, 0, 0), \quad (3.8a)$$

$$t_1^\mu = (0, -\sin(\theta_c) \cos(\phi_c), -\sin(\theta_c) \sin(\phi_c), -\cos(\theta_c)), \quad (3.8b)$$

$$t_2^\mu = (0, -\sin(\phi_c), \cos(\phi_c)), \quad (3.8c)$$

$$t_3^\mu = (0, -\cos(\theta_c) \cos(\phi_c), -\cos(\theta_c) \sin(\phi_c), -\sin(\theta_c)). \quad (3.8d)$$

The choice of trial vectors results in a right-handed basis where the observer is facing the black hole.

The integration of the geodesic equations is done by solving the second-order differential equation

$$\frac{d^2 x^\alpha}{d\lambda^2} = -\Gamma_{\mu\nu}^\alpha \frac{dx^\mu}{d\lambda} \frac{dx^\nu}{d\lambda}. \quad (3.9)$$

where  $\Gamma_{\mu\nu}^\alpha$  are the connection coefficients,  $x^\alpha$  is the geodesic position, and  $\lambda$  is the affine parameter. We use a fourth-order Runge-Kutta algorithm, where the connection coefficients are evaluated using a finite-difference method to compute the derivatives of the metric.

The step-sizing for the geodesic integration in **RAPTOR** was adopted since it relies on spherical logarithmic coordinates. First, we compute a required step-size based on the geodesic wave-vector

$$d\lambda_x = \Delta / (|k^x| + \delta), \quad (3.10a)$$

$$d\lambda_y = \Delta / (|k^y| + \delta), \quad (3.10b)$$

$$d\lambda_z = \Delta / (|k^z| + \delta), \quad (3.10c)$$

$$d\lambda_{\text{geod}} = \frac{R}{|d\lambda_x|^{-1} + |d\lambda_y|^{-1} + |d\lambda_z|^{-1}}, \quad (3.10d)$$

where  $k^{x,y,z}$  are the wave-vector components in the  $x, y, z$  directions,  $\delta$  is a small real number to prevent divisions by zero, and  $\Delta$  is a scale factor for the step-size (typically  $\Delta \approx 0.01$ ). Then we compute a required step-size based on the AMR cell size  $dx$

$$k_{\text{max}} = \max(k^x, \max(k^y, k^z)), \quad (3.11a)$$

$$d\lambda_{\text{grid}} = \frac{dx}{nk_{\text{max}}}, \quad (3.11b)$$

where  $n$  sets the number of steps per cell. We typically use at least two steps per cell. We then compare both the geodesic and AMR based step-sizes and use the smallest of the two to ensure convergence;  $d\lambda = \min(d\lambda_{\text{geod}}, d\lambda_{\text{grid}})$ .

For the radiative-transfer part of the ray-tracing calculation, we need the plasma variables at the geodesics location. We interfaced RAPTOR with the AMR data structure of BHAC, and reconstruct the full AMR grid. The BHAC AMR block-based data structure is parsed by the code. When we integrate the geodesics, we use a nearest-neighbor approach to interpolate the grid-based plasma variables to the geodesics.

### 3.2.4 Electron model and radiative-transfer model parameters

Since GRMHD simulations are scale-free, we have to re-scale the plasma variables from code units to c.g.s. units. Units of length are scaled with  $\mathcal{L} = GM/c^2$ , while units of time are scaled with  $\mathcal{T} = GM/c^3$ , the mass unit is set by  $\mathcal{M}$ . Estimates of the mass of M87 are used to constrain the length and time units. We use a mass of  $M = 6.2 \times 10^9 M_\odot$  (Gebhardt et al., 2011), the mass used in this work is slightly smaller than the mass of  $M = (6.5 \pm 0.7) \times 10^9 M_\odot$  reported in Event Horizon Telescope Collaboration et al. (2019a), but the used value for the black hole mass is within the error margins. The mass unit  $\mathcal{M}$ , which sets the accretion rate, however, is unknown. It is, therefore, a fit parameter. The mass unit is directly proportional to the accretion rate via  $\dot{M}_{\text{cgs}} = \dot{M}_{\text{sim}} \mathcal{M} \mathcal{T}^{-1}$ , where  $\dot{M}_{\text{sim}}$  is the accretion rate in simulation units. In order to scale the relevant plasma quantities to c.g.s units, the following scaling operations are performed:  $\rho_0 = \mathcal{M}/\mathcal{L}^3$ ,  $u_0 = \rho_0 c^2$ , and  $B_0 = c\sqrt{4\pi\rho_0}$ .

As mentioned before, our GRMHD simulation only simulates the dynamically important protons. Therefore, we need to parametrize the electron properties, such as their distribution functions, densities, and temperatures, in post-processing. The plasma is assumed to be charge-neutral, so that  $n_e = n_p$  throughout the domain. For the electron temperature we employ the parametrization of Mościbrodzka et al. (2016b):

$$T_{\text{ratio}} = T_p/T_e = R_{\text{low}} \frac{1}{1 + \beta^2} + R_{\text{high}} \frac{\beta^2}{1 + \beta^2}, \quad (3.12a)$$

$$\Theta_e = \frac{U(\hat{\gamma} - 1)m_p/m_e}{\rho T_{\text{ratio}}}, \quad (3.12b)$$

where  $m_p$  is the proton mass,  $m_e$  is the electron mass,  $U$  is the internal energy, which is related to  $h$  and  $\rho$  via  $h(\rho, U) = 1 + \hat{\gamma} \frac{U}{\rho}$ , therefore,  $P = U(\gamma - 1)$ , where  $P$  is the gas pressure. The dimensionless electron temperature  $\Theta_e$  can be re-scaled to c.g.s units via  $T = \Theta_e m_e c^2 / k_b$ , where  $k_b$  is the Boltzmann constant. The parameters  $R_{\text{low}}$  and  $R_{\text{high}}$  are free parameters of the model;  $R_{\text{low}}$  sets the temperature ratio in the jet, where  $\beta \ll 1$ , and  $R_{\text{high}}$  sets the temperature ratio in the disk where  $\beta \gg 1$ .

For the electrons' energy-distribution function, we follow a similar recipe as described in Davelaar et al. (2018c). we use the relativistic isotropic  $\kappa$ -distribution function for the electrons, which is given by (Xiao, 2006)

$$\frac{dn_e}{d\gamma} = N \gamma \sqrt{\gamma^2 - 1} \left( 1 + \frac{\gamma - 1}{\kappa w} \right)^{-(\kappa+1)}, \quad (3.13)$$

where  $\gamma$  is the Lorentz factor of the electrons,  $\kappa$  is the parameter that sets the power-law index  $p$  via  $p = \kappa - 1$ ,  $w$  sets the width of the distribution function and  $N$  is a normalization factor such that the electron distribution function contains  $n_e$  electrons.

The width  $w$  of the  $\kappa$  distribution sets the amount of energy in the distribution. In the case that  $\kappa w \gg 1$  the total energy in the  $\kappa$  distribution is given by

$$E_\kappa = \frac{3\kappa}{\kappa - 3} n_e w. \quad (3.14)$$

We couple this energy to the energy present in a thermal distribution ( $E_{\text{thermal}} = 3n_e \Theta_e$ ) and add a source term based on the magnetic energy

$$E_\kappa = \frac{3\kappa}{\kappa - 3} n_e w = 3n_e \Theta_e + \tilde{\epsilon} \frac{B^2}{8\pi}, \quad (3.15)$$

here  $\tilde{\epsilon}$  is used to join smoothly between the  $\kappa$ -distribution and magnetic energy. After a bit of algebra, we can rewrite the width as

$$w = \frac{\kappa - 3}{\kappa} \Theta_e + \tilde{\epsilon} \frac{\kappa - 3}{6\kappa} \frac{m_p}{m_e} \sigma. \quad (3.16)$$

In the limit of  $\sigma \ll 1$ , the  $\kappa$ -distribution energy is set by the thermal energy, while in the magnetized regime, the energy is set by the magnetic energy. The  $\tilde{\epsilon}$  parameter is set by

$$\tilde{\epsilon} = \epsilon \frac{1}{2} (1 + \tanh(r - r_{\text{inj}})), \quad (3.17)$$

where  $r_{\text{inj}}$  is the injection radius from which the magnetic energy contributes to the  $w$  parameter, and  $\epsilon$  is the base value for radii larger than  $r_{\text{inj}}$ ; hereafter, we will consider two cases: where  $\epsilon$  is zero or non-zero. Here,  $\epsilon$  is a parameter expressing the equipartition between the energy in the distribution function and that available in magnetic energy (see, e.g., Falcke & Biermann 1995; Markoff et al. 2008; Prieto et al. 2016).

The power-law index of the electrons distribution functions (eDFs) is based on sub-grid particle-in-cell (PIC) simulations of trans-relativistic reconnection by Ball et al. (2018), who simulated two-dimensional reconnection layer (Harris sheath) for an electron-ion plasma for multiple values of the plasma  $\beta$  and of the magnetization  $\sigma$ . One of the benefits of this type of plasma simulation is that one obtains eDFs from first principles. In Ball et al. (2018) these eDFs are then used to fit the power-law index  $p$  as a function of  $\beta$  and  $\sigma$  as

$$p = A_p + B_p \tanh(C_p \beta) \quad (3.18a)$$

$$A_p = 1.8 + 0.7/\sqrt{\sigma} \quad (3.18b)$$

$$B_p = 3.7 \sigma^{-0.19} \quad (3.18c)$$

$$C_p = 23.4 \sigma^{0.26}. \quad (3.18d)$$

These fits are obtained for  $10^{-4} < \beta < 1.5$  and  $0.1 < \sigma < 7.2$ , which corresponds to the typical values that we find in the jet sheath, which is the main source of synchrotron emission in our jet-models.

Finally, we exclude all emission from regions where  $\sigma > 5.0$ , this is what we call the jet spine. These regions are unreliable for modeling since the thermal energy in highly magnetized regions is unreliable in GRMHD simulations. We also exclude all emission from regions where floor values are applied, these regions typically resides inside the magnetized jet. This results in three regions

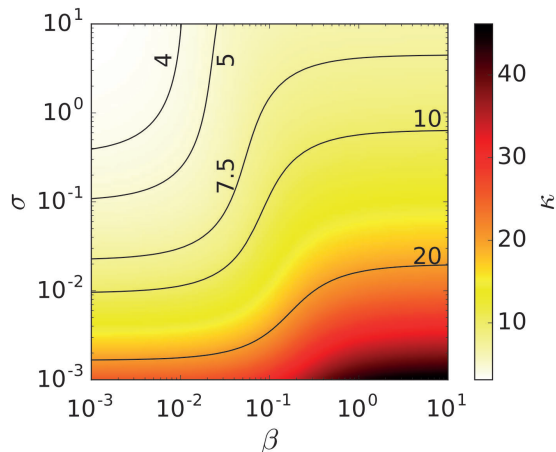


FIGURE 3.2: Parameterization of the  $\kappa$  parameter.  $\kappa$  as function of  $\beta$  and  $\sigma$  as found by Ball et al. (2018). A high value of  $\kappa$  corresponds to steep particle spectra with power-law index  $p = \kappa - 1$ . We overlotted contours of constant  $\kappa$  in black.

inside our simulation domain; the disk, the jet sheath, and the jet spine. The disk resides where  $\sigma$  is much smaller than one, and plasma  $\beta$  is large than one, the jet sheath resides where  $\sigma$  is of the order unity, and  $\beta$  is smaller than one. In the case of our  $\kappa$ -jet model, we set the electron distribution function to a relativistic  $\kappa$ -distribution function into the disk and jet sheath, and no electrons are present in the jet spine.

The emission and absorption coefficients for the thermal electron distributions are taken from Leung et al. (2011), and in the case of the  $\kappa$ -distribution, the fit formula taken are from Pandya et al. (2016).

### 3.2.5 SED cut-off

The SED of M 87 shows a clear cut-off in flux around  $\nu = 10^{15}$  Hz (Prieto et al., 2016). We will consider three potential sources for this cut-off.

First, we assume that the cut-off is caused by synchrotron cooling in the jet, which becomes important when the synchrotron-cooling time of the electron is comparable with the typical dynamical time. Under these conditions, the cooling (cut-off) frequency is given by

$$\nu_{\text{cool}} = \frac{18\pi m_e c^2 e}{\sigma_T^2 B^3 z_{\text{jet}}}, \quad (3.19)$$

where  $\sigma_T$  is the Thomson cross-section, and  $z_{\text{jet}}$  the position along the jet.

Second, we assume that the break occurs at the synchrotron burn-off limit, that is, at the maximum energy that a particle can gain while emitting synchrotron radiation. The maximum Lorentz factor in this case is

$$\gamma_{\text{max}} = \sqrt{\frac{3m_e^2 c^4 E}{4\pi e^3 B^2}}, \quad (3.20)$$

where  $E$  is the electric field, and the cut-off frequency is then given by

$$\nu_{\text{cut-off}} = \frac{3}{2} \gamma_{\text{max}}^2 \nu_c, \quad (3.21)$$

with  $\nu_c = eB/(2\pi m_e c)$ .

Finally, we assume that break is given by the Hillas criterion (Hillas, 1984), stating that the maximum Lorentz factor achievable can be estimated by equating the gyration radius of the electron and the size of the acceleration region  $L$ . This results in a maximum Lorentz factor of

$$\gamma_{\text{max}} = \frac{eBL}{m_e c^2}, \quad (3.22)$$

which results in a cut-off frequency of  $\nu \approx 10^{15}$  Hz after using Eq. (3.22) in (3.21). In this way, we can also estimate the typical size  $L$  of the acceleration-region

$$L = \sqrt{\frac{4\pi\nu_{\text{cut-off}} m_e^3 c^5}{e^3 B^3}} \approx 4.5 \times 10^7 \text{ cm} \sqrt{\frac{(\nu_{\text{cut-off}}/10^{15} \text{ Hz})}{(B/1 \text{ G})^3}}. \quad (3.23)$$

Interestingly, the maximum size  $L$  can be interpreted as the size of plasmoids as was done by Petropoulou et al. (2016) and Christie et al. (2019) for blazars.

### 3.3 Results

In this Section, we present the results of our GRMHD simulations. We post-process the simulations to compute SEDs which are fitted to observational data. We produce synthetic synchrotron maps at three observational relevant frequencies at two inclinations. We also compute the source size and core shifts, and compare them with the observations.

#### 3.3.1 Structure of the accretion disk and jet in the AMR simulation

A representative snapshot of the simulation is shown in Fig. 3.3. The simulation produces a well-resolved relativistic jet up to the edge of the simulation domain at  $1000 GM/c^2$  in the  $z$ -direction. At  $z = 40 GM/c^2$  the jet diameter is resolved with 160 cells, and with 32 cells at  $z = 1000 GM/c^2$ . The accretion rate through the event horizon is shown in the left panel of Fig. 3.4 as a function of time; the accretion rate initially increases sharply and then settles around 0.2 (in code units) at later times. The jet and wind power are instead shown in the right panel of Fig. 3.4; both of the quantities are calculated by performing the integral over the constant  $r = 100 GM/c^2$  surface

$$\dot{E} = \int_0^{2\pi} \int_0^\pi (-T_t^r - \rho u^r) \chi_{(\cdot)} \sqrt{-g} d\theta d\phi \quad (3.24)$$

where the function  $\chi_{(\cdot)}$  selects only material in the jet, wind, or disk following the setting

$$\chi_{\text{jet}} = (b^2/\rho > 1 \text{ or } \mu > 2) \quad (3.25a)$$

$$\chi_{\text{wind}} = (\text{not } \chi_{\text{jet}} \text{ and } -hu_t > 1) \quad (3.25b)$$

$$\chi_{\text{disk}} = (\text{not } \chi_{\text{jet}} \text{ and not } \chi_{\text{wind}}), \quad (3.25c)$$

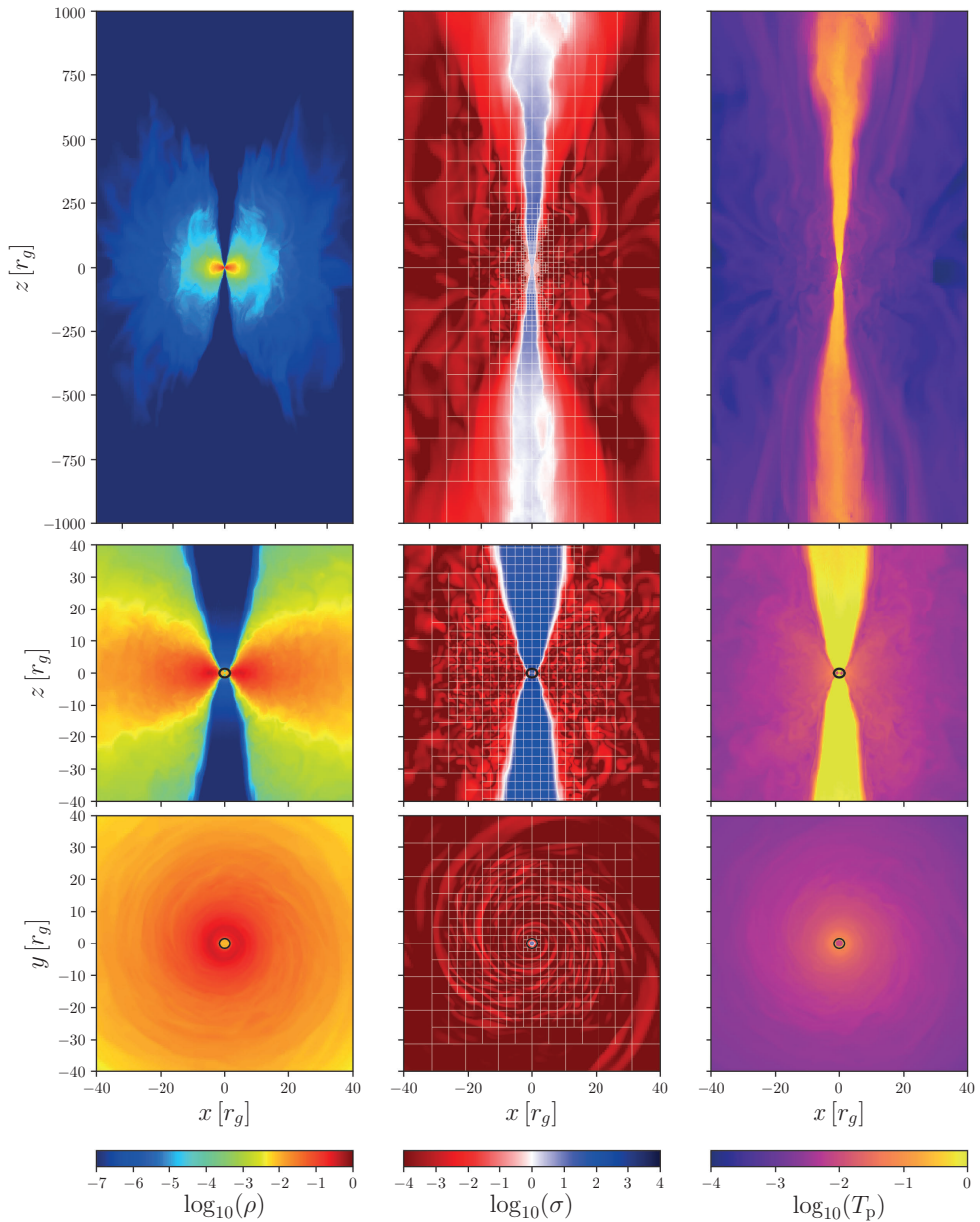


FIGURE 3.3: GRMHD simulation snapshot. Left panels: slice in the  $(x, z)$  and  $(x, y)$  planes of the density in code units. Middle panels: slice along the  $(x, z)$  and  $(x, y)$  planes of the magnetization parameter  $b^2/\rho$ , over-plotted with the grid block sizes. Right panels: slice along the  $(x, z)$  and  $(x, y)$  planes of the dimensionless ion temperature. Shown with a black circle is the location of the event horizon.

and  $\mu$  denotes the energy flux normalized to the rest-mass energy in the radial direction  $\mu = (-T_t^r - \rho u^r)/(\rho u^r)$ . Hence, the jet is defined as the region which reaches asymptotic Lorentz factors of at least 2. The optional condition  $b^2/\rho > 1$  also selects the flow in the inner axial region, where the Poynting flux necessarily vanishes. The disk wind is then the remaining unbound material, and the disk itself is composed of the bound material.

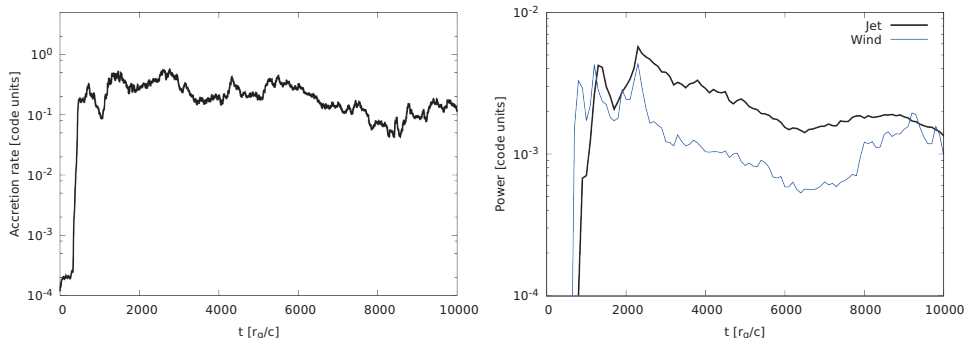


FIGURE 3.4: Mass accretion rate and jet and wind power. We computed global quantities of the Cartesian GRMHD simulation, accretion rate in code units as a function of time (left panel), and jet and wind power in code units as a function of time (right panel).

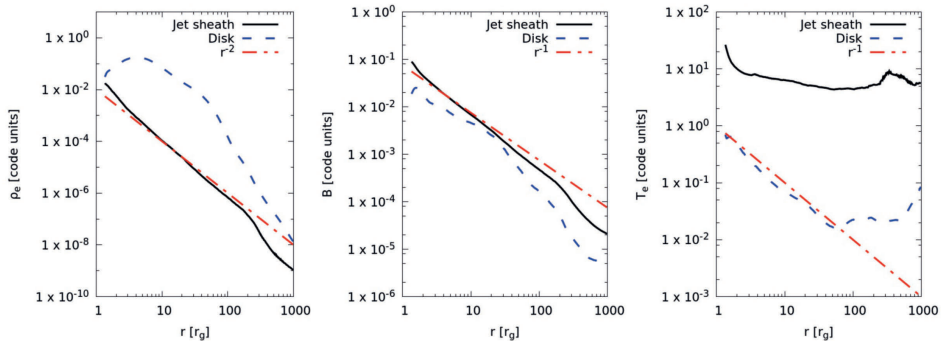


FIGURE 3.5: Lineprofiles. To compare our simulation with analytical prediction for plasma quantities by Blandford & Königl (1979) and Falcke & Biermann (1995) in the jet we computed radial profiles. We show radial profiles of the dimensionless electron density (left), magnetic-field strength (middle) and electron temperature (right). Black lines correspond to jet averaged quantities, dashed yellow lines to disk-averaged quantities and the red dashed lines correspond to power-law profiles predicted in analytical works. Also, the jet sheath is close to isothermality.

Analytic work on radial profiles of relativistic jets was performed by Blandford & Königl (1979) and subsequently by Falcke & Biermann (1995). In these Blandford-Königl jet-models, the electron density decreases as a function of radius as  $\rho_e \propto r^{-2}$ , the magnetic field strength as  $B \propto r^{-1}$ , and the equipartition electron temperature in the jet is constant. The temperature in the disk is set by the virial theorem and follows  $T_e \propto r^{-1}$ . To compare our simulations with these

analytical formulae, we compute averages on spherical shells at different fixed radii of the electron density  $\rho_e$ , magnetic-field strength  $B$ , and electron temperature  $T_e$ . This is done by performing the following integral

$$q(r) = \frac{1}{\Delta t} \int \left( \frac{\int \int_0^{2\pi} q(t, r, \theta, \phi) \sqrt{-\gamma(r, \theta)} d\theta d\phi}{\int \int_0^{2\pi} \sqrt{-g(r, \theta)} d\theta d\phi} \right) dt. \quad (3.26)$$

where  $\gamma(r, \theta)$  is the determinant of the three metric. The integral in the  $\theta$ -direction depends on the local plasma criteria. We consider two regions of interest; a jet sheath, for which  $0.1 < \sigma < 5.0$ , and the accretion disk,  $\sigma < 0.1$ . The time average is performed by using simulation snapshots between  $t = 5000 GM/c^3$  and  $t = 10^4 GM/c^3$ , with a total of hundred snapshots. The computed radial profiles are shown in Fig. 3.5 and are over-plotted with the analytic predictions (Blandford & Königl, 1979; Falcke & Biermann, 1995). The equipartition electron temperature in the jet (right panel) shows a flat profile up to  $200 GM/c^2$ , followed by is an increase of temperature that correlates with the break in the profile of the electron density. The break is caused by decollimation of the jet, which could be caused by the limited initial size of the torus. The wind emitted by the disk effectively acts as a collimation agent; however, because of its limited size, the collimation stalls at radii  $r > 200 GM/c^2$ .

We computed maps of  $\kappa$  [based on Eqs. (3.18)] and  $w$  (based on Eq. (3.16)), for both  $\epsilon = 0$  and  $\epsilon = 0.015$ , these are shown in Figure 3.6. The maps show that  $\kappa$  is low in the sheath, and  $w$  peaks in the sheath, therefore, most of the non-thermal emission will be produced in this region.

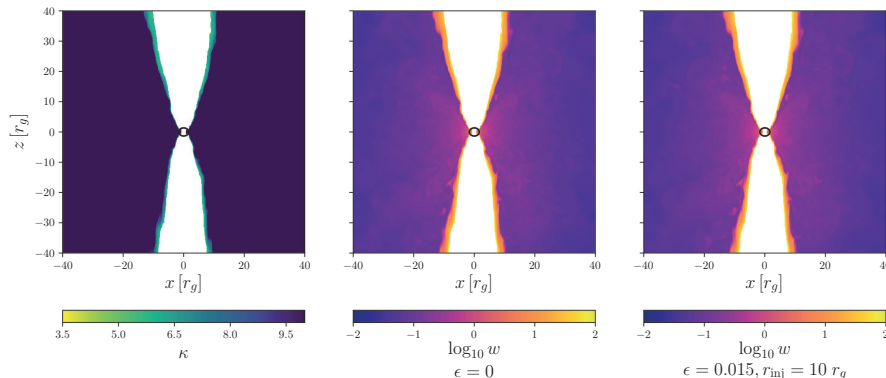


FIGURE 3.6:  $\kappa$  and  $w$  parameter. Left panel: map of the  $\kappa$  parameter based on Eqs. (3.18), where the jet spine is excluded ( $\sigma < 5$ ). The map shows that the  $\kappa$  parameter is small in the jet sheath and large in the disk. Middle panel: map of the  $w$  parameter when  $\epsilon = 0$ , showing large values in the sheath compared to the disk. Right panel: same as middle panel but now for  $\epsilon = 0.015$ , the sheath has slightly larger values compared to the  $\epsilon = 0$  case.

### 3.3.2 Spectra and synchrotron images: dependency on electron distribution function

In this Section, we discuss the spectral energy distributions (SEDs) of our thermal-jet and  $\kappa$ -jet models. The SEDs are calculated at an inclination of  $i = 160^\circ$ . This choice ensures that the emitting region is in the south, as suggested by the EHT results (Event Horizon Telescope Collaboration et al., 2019a,e). Furthermore, the field-of-view of the camera is set to be  $1000 GM/c^2$  in both the  $x$  and  $y$ -directions, while the resolution is set to be  $2000 \times 2000$  pixels.

#### 3.3.2.1 Fitting the SED

After averaging in time the SEDs from our models between  $t = 5000 GM/c^3$  and  $t = 10^4 GM/c^3$ , these have been fit to non-simultaneous observations by Doeleman et al. (2012); Akiyama et al. (2015); Prieto et al. (2016); Walker et al. (2018); Kim et al. (2018). The fit parameters are shown in Table 3.2, which highlights that the thermal-jet and  $\kappa$ -jet models differ in the accretion rate by a factor  $\approx 2$ . The corresponding SEDs are shown in Fig. 3.7, which shows that  $\kappa$ -jet models recover the NIR flux. Comparing the  $\epsilon = 0.0$  and the  $\epsilon = 0.015$  models (the latter uses an injection radius of  $r_{\text{inj}} = 10 GM/c^2$  and has a slightly lower accretion rate), the  $\epsilon = 0.015$  model has a more luminous and flatter radio spectrum at frequencies below  $\nu = 228$  GHz.

Parameter	Thermal	$\kappa, \epsilon = 0$	$\kappa, \epsilon = 0.015$
$i$	$160^\circ$	$160^\circ$	$160^\circ$
$\mathcal{M}$ [g]	$1.8 \times 10^{29}$	$10^{29}$	$8 \times 10^{28}$
$P_{\text{jet}}$ [erg s $^{-1}$ ]	$1.1 \times 10^{43}$	$5.9 \times 10^{42}$	$4.7 \times 10^{42}$
$\langle \dot{M} \rangle_t$ [ $M_\odot \text{yr}^{-1}$ ]	$8.4 \times 10^{-3}$	$4.7 \times 10^{-3}$	$3.8 \times 10^{-3}$
$B_0$ [G]	$1.6 \times 10^3$	$1.2 \times 10^3$	$1.1 \times 10^3$
$n_0$ [cm $^{-3}$ ]	$1.34 \times 10^8$	$7.5 \times 10^7$	$6 \times 10^7$
$R_{\text{high}}$	100	100	100
$R_{\text{low}}$	1	1	1
$r_{\text{inj}}$	-	-	$10 GM/c^2$

TABLE 3.2: Model parameters. List of parameters are used in the radiative-transfer simulations.

After 228 GHz both  $\kappa$ -jet models recover a power law with an index of  $\alpha \approx -0.7$ , where  $\alpha = -(p - 1)/2$  for a power law distribution of non-thermal electrons  $F_\nu \propto \nu^\alpha$ . Furthermore, when compared to the thermal model, the flux in the  $\kappa$ -jet models is higher at lower frequencies ( $\nu < 10^{11}$  Hz) and at the higher frequencies ( $5 \times 10^{12} \text{Hz} < \nu$ ).

When considering the various cut-off models, the cooling cut-off turned out to be unimportant, in agreement with the findings of (Mościbrodzka et al., 2016b; Broderick et al., 2015). When using the synchrotron burn-off, the correct cut-off is obtained if  $E/B \approx 10^{-6}$ , but no physical model is possible that recovers such a ratio. The only criterion that recovers the cut-off frequency is the Hillas criterion, which is obtained when the plasmoid size is set to  $L \approx 10^5 - 10^7$  cm, depending on the local magnetic field strength.

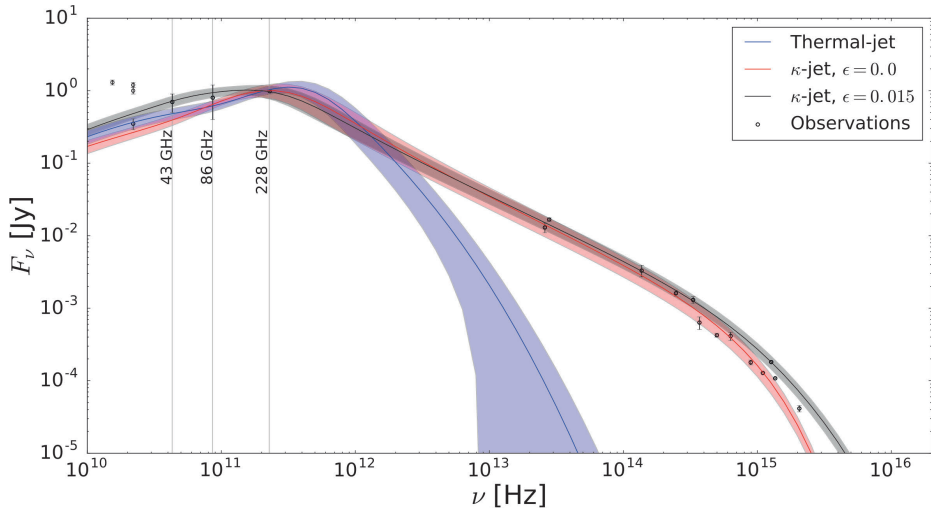


FIGURE 3.7: Spectral energy distributions. Shown are the thermal-jet (orange) and  $\kappa$ -jet with  $\epsilon = 0$  (orange) and  $\epsilon = 0.015$  (black) with their corresponding rms, overplotted with observational data points by Doeleman et al. (2012); Akiyama et al. (2015); Prieto et al. (2016); Kim et al. (2018).

### 3.3.2.2 Synchrotron maps

The synthetic synchrotron maps are computed at three frequencies: 43, 86, and 228 GHz. The same inclination used for the SEDs is employed here and the images for the thermal case are shown in the top rows of Fig. 3.8, with the  $\kappa$ -jet models shown in the second and third rows. The maps shown are computed with a single GRMHD snapshot at  $t = 10^4 GM/c^3$ . The forward jet at 43 GHz is aligned with the observed jet position angle at 43 GHz VLBI observations (Janssen et al., 2019), namely,  $250^\circ$ . The assumed mass and distance are  $M_{\text{BH}} = 6.2 \times 10^9 M_\odot$  (Gebhardt et al., 2011) and  $d = 16.7$  Mpc (Mei et al., 2007), which results in a field of view of 0.744, 0.372 and 0.186 mas for the 43, 86, and 228 GHz maps, respectively.

The thermal-jet and  $\epsilon = 0.0$   $\kappa$ -jet model show a similar source morphology at 43 GHz and 86 GHz, and  $\epsilon = 0.015$   $\kappa$ -jet model is more extended in jet length. At 228 GHz both  $\kappa$ -jet models deviate from the thermal-jet model, the width of the ring around the shadow decreases when particle acceleration is present. In all 228 GHz images two rings are visible, the outer ring is the photon ring and marks the shadow of the black hole, the fainter smaller ring is emission originating from the jet facing the observer, see Appendix 3.A for more details.

The logarithmic optical-depth maps at 228 GHz are shown in Fig. 3.9, where the size of the optically thick region (in blue) decreases when particle acceleration is present. This is in agreement with the less extended structure visible in the intensity-maps of Fig. 3.8. The reason behind this behavior is that lower mass-accretion rates decrease both the density and the magnetic field strength, hence decreasing the optical thickness of the jet base. As a result, for any given frequency, accelerated particles at lower mass-accretion rates produce more emission than their thermal counterpart.

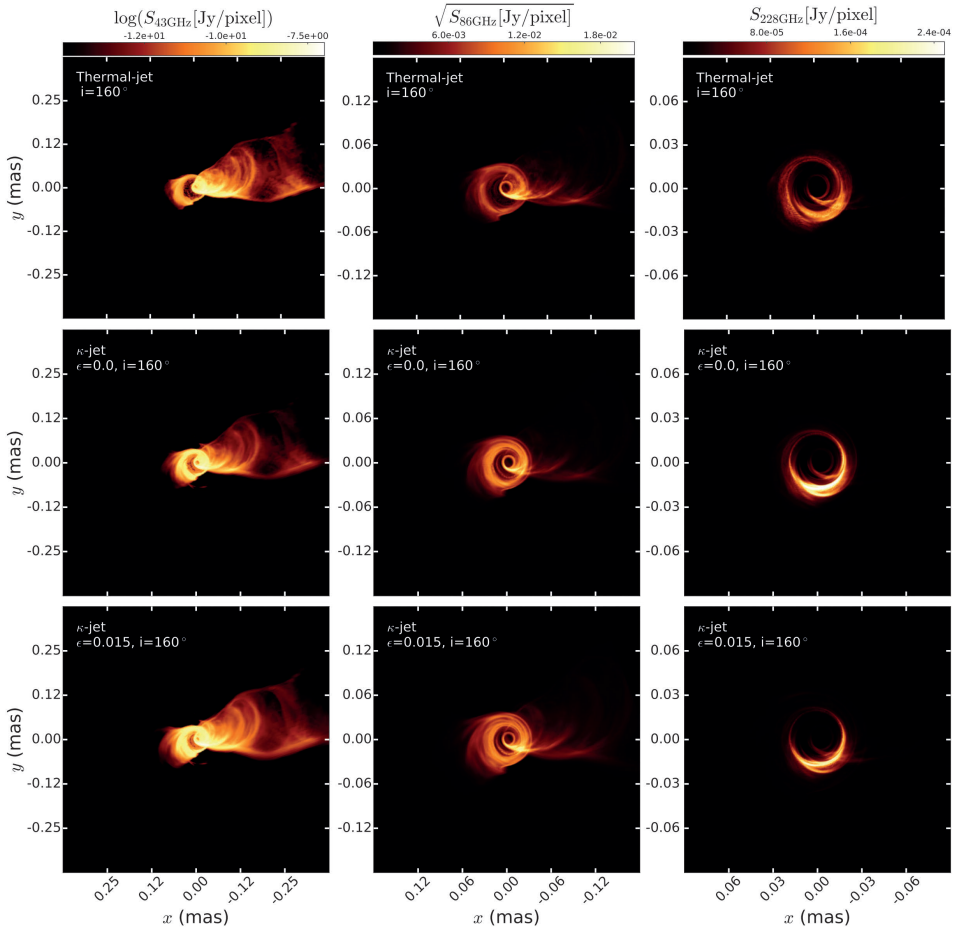


FIGURE 3.8: Synthetic synchrotron maps. Shown are all our models at three astronomically relevant frequencies. From left to right: 43, 86, and 228 GHz. Top row: synthetic images at a single snapshot of the thermal-jet at an inclination of  $i = 160^\circ$ . Second row: same as top row but for the  $\epsilon = 0.0$   $\kappa$ -jet. Bottom row: same as the first and second row but for the  $\epsilon = 0.015$   $\kappa$ -jet.

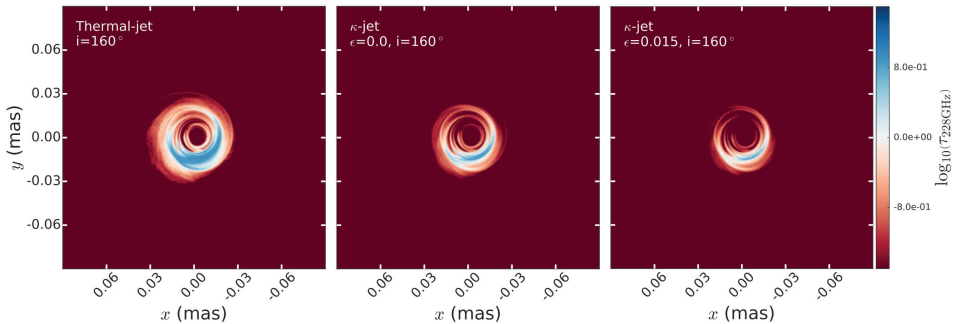


FIGURE 3.9: Logarithmic optical-depth maps. Single snapshot at 228 GHz of the models at an inclination of  $i = 160^\circ$ .

### 3.3.2.3 Origin of the jet emission

To obtain a quantitative understanding of how much flux originates either from the forward or the counter-jet, the jet facing towards or away from the observer, we computed synthetic images where the emission coefficient was set to zero either in the southern or northern hemisphere, while keeping the absorption coefficients in place. We computed the time-averaged ratios and the spread of the flux originating from the southern to flux from the northern hemisphere of both our models for all slices between 5000 and  $10^4 GM/c^3$  at 43, 86, and 228 GHz and have reported them in Table 3.3. When electron acceleration is present, the overall trend is that at 43 and 86 GHz, the ratio shifts to the counter-jet, while at 228 GHz, no large shifts are seen. Therefore, we conclude that the counter jet at 43 and 86 GHz is more dominant in the  $\kappa$ -jet models compared to the thermal models. Overall, the forward jet is dominant at 43 GHz and 86 GHz, while at 230 GHz, the counter jet dominates, this in agreement with earlier findings by Mościbrodzka et al. (2016b). Appendix 3.A provides a simple phenomenological model that is capable of reproducing this effect, where it is caused by a combination of gravitational lensing and the blocking of light by the black-hole’s event horizon.

	43 GHz	86 GHz	228 GHz
Thermal-jet	$8.3 \pm 2.2$	$2.3 \pm 0.6$	$0.4 \pm 0.1$
$\kappa$ -jet, $\epsilon = 0.0$	$2.6 \pm 0.7$	$0.9 \pm 0.2$	$0.3 \pm 0.09$
$\kappa$ -jet, $\epsilon = 0.015$	$2.6 \pm 0.7$	$1.1 \pm 0.3$	$0.5 \pm 0.2$

TABLE 3.3: Forward jet to counter jet ratio. Table showing the ratio in flux between the forward and counter jet at 43, 86, and 228 GHz for the thermal-jet and  $\kappa$ -jet models.

### 3.3.2.4 Core size and shift

We computed the source size of our models at 43, 86, and 228 GHz by using image moments (Hu, 1962). The source sizes are computed over a range of 5000 to  $10^4 GM/c^3$ . In Table 3.4 we report the time-averaged major and minor full-width half maxima (FWHM) and their corresponding spread.

We computed the core shift with respect to the black-hole’s center at the following observational frequencies; 2.3, 5, 8.4, 15.4, 23.8, 43, 86, and 228 GHz. The core shift was calculated by computing the first-order image moments of time-averaged images and the comparison of the values obtained with the observational fit of Hada et al. (2011), meaning  $r_{\text{RA}}(\nu) = (1.4 \pm 0.16)\nu^{-0.94 \pm 0.09}$ , is shown in Fig. 3.10. The observed core shift is in agreement with the analytical predictions for which the core position should shift for a conical jet as a function of frequency as  $r_{\text{core}} \propto \nu^{-1}$  (Blandford & Königl, 1979; Falcke & Biermann, 1995; Davelaar et al., 2018c), and in agreement with simulations of collimated jets (Porth et al., 2011). The  $\kappa$ -jet models show smaller core shifts with respect to the thermal-jet model, probably because the counter-jet is more dominant than the forward jet.

$\theta_{\text{major}}$ ( $\mu\text{as}$ )	43 GHz	86 GHz	228 GHz
Thermal-jet	$141 \pm 25$	$87 \pm 12$	$45 \pm 4$
$\kappa$ -jet, $\epsilon = 0.0$	$128 \pm 20$	$73 \pm 9$	$41 \pm 3$
$\kappa$ -jet, $\epsilon = 0.015$	$142 \pm 18$	$87 \pm 10$	$53 \pm 6$
$\theta_{\text{minor}}$ ( $\mu\text{as}$ )			
Thermal-jet	$56 \pm 4$	$43 \pm 2$	$33 \pm 1$
$\kappa$ -jet, $\epsilon = 0.0$	$54 \pm 3$	$43 \pm 1$	$32 \pm 1$
$\kappa$ -jet, $\epsilon = 0.015$	$60 \pm 3$	$48 \pm 2$	$36 \pm 2$

TABLE 3.4: Source size. To compare our models to observation we computed the source size of our model by using imaging moments. The table list the FWHM of all our models. Top: FWHM along the major axis for the thermal-jet and  $\kappa$ -jet at 43,86, and 228 GHz. Bottom: same as top but along the minor axis.

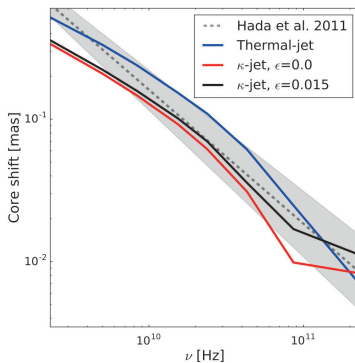


FIGURE 3.10: Core shift. RA offset from the 43 GHz core as a function of frequency. Orange triangles correspond to a thermal-jet, black dots to a  $\kappa$ -jet, grey line represent the observational fit  $r_{\text{RA}}(\nu) = (1.4 \pm 0.16)\nu^{-0.94 \pm 0.09}$  to the M87 core by Hada et al. (2011).

### 3.3.2.5 Comparison with 43 GHz data

Finally, we compared our thermal-jet and  $\kappa$ -jet models with the 43 GHz VLBI observations, where M87 was tracked for 8 hours with all VLBA stations<sup>1</sup>. The data was recorded with a bandwidth of 256 MHz, with the data’s calibration and imaging described by Janssen et al. (2019).

To compare with this observational data, we re-computed synthetic images with a large field of view of 3.7 mas and convolved them with a  $0.3 \times 0.1 \text{ mas}^2$  beamsize by using the eht-imaging library (Chael et al., 2016, 2018b). The comparison can be seen in Fig. 3.11 and highlights that the  $\kappa$ -jet models show more extended structure with respect to the thermal-jet model. At 43 GHz all models deviate from the VLBI observations at larger scales. Furthermore, in the observed image, the flux levels upstream of the jet are higher, and the jet-opening angle is wider.

<sup>1</sup>PI: R. Craig Walker, project code: BW0106

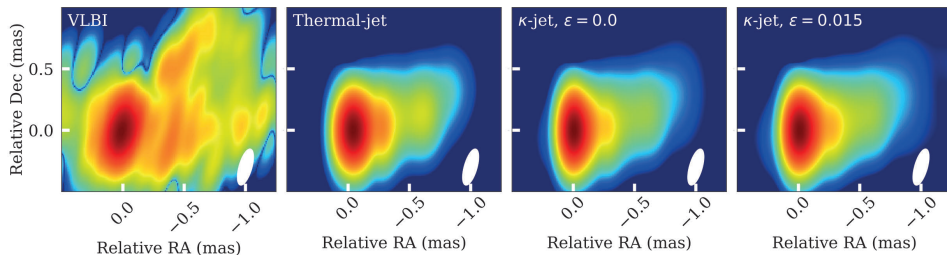


FIGURE 3.11: 43 GHz radio map. Comparison of our thermal and  $\kappa$ -jet model with a VLBI map of M87 at 43 GHz. The first panel from the left: 43 GHz radio map of M87 (Janssen et al., 2019). Second panel: synchrotron map of the thermal-jet model, convolved with a 2D Gaussian beam. Third panel: same as the second panel but now for a  $\kappa$ -jet model with  $\epsilon = 0.0$ . Fourth panel: Same as the third panel but now with  $\epsilon = 0.015$ . The white ellipse indicates the beam used to convolve the images. All models produce a jet that is too narrow compared to the VLBI map. The extent of the jet increases when electron acceleration is present, and is maximum for  $\epsilon = 0.015$ .

## 3.4 Discussion

### 3.4.1 CKS GRMHD simulations

Current models of the radio emission near the supermassive black hole in M87 are based on GRMHD simulations using spherical polar coordinates. In this work, we used instead Cartesian coordinates, which do not require specialized treatment of the polar axis, which represents a coordinate singularity (of the inverse metric) in spherical coordinates. The addition of AMR resulted in a highly resolved jet region, the jet diameter at  $z = 40 GM/c^2$  is resolved by 160 cells, and at  $z = 1000 GM/c^2$  is resolved by 32 cells. The obtained jet resolution is well above the values of 20-26 cells per jet radius reported in convergence studies of jets by Anjiri et al. (2014); Massaglia et al. (2016). We computed the mass-accretion rate, and radial profiles of density, magnetic-field strength and temperature, which are consistent with their spherical counterparts, the comparison of this can be found in Porth et al. (2019). The downside of the Cartesian grid is that in spherical grids, it is possible to use a logarithmic grid in the radial direction, which results in higher resolutions close to the horizon. To ensure that the MRI is well resolved, we have computed the relativistic MRI quality factors (Noble et al., 2010) and find that they are above ten in the bulk of the accretion disk, thus satisfying the requirements for a sufficiently resolved MRI found by Sano et al. (2004). Furthermore, in parallel works (Olivares et al., 2019; Porth et al., 2019) it was shown that the CKS simulations show similar behavior in the non-linear phase compared to the spherical simulations, a short summary of these works can be found in Appendix 3.B.

### 3.4.2 The effect of electron acceleration on the SED

We computed spectra for our thermal-jet model and  $\kappa$ -jet models, wherein the latter case we parametrize the power-law index of the eDF based on sub-grid PIC simulations by Ball et al. (2018). The addition of accelerated electrons in the jet sheath leads to a fit to the observational

data from radio up to the NIR. Our  $\kappa$ -jet model is an extension of the model presented by Mościbrodzka et al. (2016b), which only studied the thermal-jet case. Our models use their best-fit inclination angle of  $i = 160^\circ$ , such that the emitting region is in the south, and the orientation of the asymmetry is in agreement with the image in Event Horizon Telescope Collaboration et al. (2019a). The radio SED shows a flat spectrum in both the thermal and  $\kappa$ -jet models. This is consistent with more recent work by Ryan et al. (2018); Chael et al. (2019), who have evolved the thermal electron population as a separate fluid in the GRMHD simulation.

In contrast to previous works, our  $\kappa$ -jet models also recover the observed NIR flux by extending the optically thin emission with a power-law. The results are similar to the ones presented by Dexter et al. (2012a), who also modeled accelerated electrons based on the amount of available magnetic energy. The  $\kappa$ -jet models yield a jet power of the order of  $10^{43}$  ergs  $s^{-1}$ , which is in agreement with observations of the jet core power by Reynolds et al. (1996), and is approximately two times lower than the thermal-jet models. This is probably because in the  $\kappa$ -jet models, there is a larger contribution of electrons in the tail of the distribution functions with respect to the thermal-models. Since these electrons emit at higher  $\gamma$  values, this results in a higher flux contribution per unit mass.

After defining the radiative efficiency as  $\epsilon_{\text{rad}} = L/\dot{M}c^2$ , we found that the thermal-jet has  $\epsilon_{\text{rad}} = 0.003$ . Compared to  $\epsilon_{\text{rad}} = 0.013$  and  $\epsilon_{\text{rad}} = 0.020$  for the  $\kappa$ -jet models with  $\epsilon = 0.0$  and  $\epsilon = 0.015$ , respectively. An important note is that we do not include X-ray emission in this work. Although, the obtained values are well below the thin disk efficiency, thus justifying our assumption that the radiation can be decoupled from the evolution of the dynamics of the plasma.

### 3.4.3 The effect of electron acceleration on synchrotron maps

At 43 and 86 GHz, both  $\kappa$ -jet models show a more dominant counter-jet when compared to the thermal-jet model, hinting to behavior that could be observable by future GMVA-ALMA observations. There is also a clear difference in the extent of the emission of the forward jet in the  $\epsilon = 0.015$   $\kappa$ -jet model when compared to the  $\epsilon = 0.0$   $\kappa$ -jet and to the thermal-jet model, with the emitting region being more compact in the  $\kappa$ -jet models at 228 GHz. The reason for this is that more energy is available at higher  $\gamma$  in the eDF, resulting in a higher flux contribution per unit mass. To obtain a fit to the data, a lower mass-accretion rate is needed. Since our mass-accretion rate sets the scaling of the densities and magnetic fields, it also changes the optical thickness of the source. As a result, a more optically thin model shows a more compact emission region.

A comparison with the result from Mościbrodzka et al. (2016b) shows that similar source morphologies at all frequencies for the thermal model. However, at 228 GHz our images show a more optically thick inner ring feature that partially blocks the view to the shadow. The reason for this is that our initial conditions differ from those of Mościbrodzka et al. (2016b), as they used a disk with a pressure maximum at  $24 GM/c^2$ , resulting in an outer radius of  $r = 240 GM/c^2$ , while we used a pressure maximum at  $12 GM/c^2$  and outer radius of  $r = 40 GM/c^2$ . A larger disk is initially seeded with larger toroidal magnetic-field loops, and a larger loop increases the magnetic flux at the horizon at later times. These stronger magnetic fields will affect the overall source morphology, resulting in wider opening angles, which lead to less obscuration of the shadow by the forward jet.

### 3.4.4 Core size, shift, and jet-opening angle

The obtained core sizes for our models are close to the observed values:  $\theta^{43 \text{ GHz}} = 0.13 \pm 0.01$ ,  $\theta^{86 \text{ GHz}} = 0.079 \pm 0.021$  (Hada et al., 2013), and  $\theta^{228 \text{ GHz}} = 0.040 \pm 0.002$  (Doeleman et al., 2012). If we compare these to values reported in Tables 3.4, we find that our models at 43 and 86 GHz are within the error margins of the observations. At 228 GHz, the  $\epsilon = 0.0$   $\kappa$ -jet recovers the observational value. The thermal-jet model is slightly larger, this is probably caused by the larger emission region around the shadow. In the  $\epsilon = 0.015$  case, the deviation is caused by a more pronounced jet feature.

We obtain core-shift relations for both our models by calculating the core position that follows the trend found by Hada et al. (2011). They computed the core shift with respect to the 43 GHz core. Their obtained fit is then extrapolated to higher frequencies, where they find an offset of 40  $\mu\text{as}$  at 228 GHz. At frequencies below 10 GHz, deviations with the fit from Hada et al. (2011) are present. A possible explanation for this is the limited simulation domain of 1000  $GM/c^2$  and the de-collimation of the jet after  $r \approx 300 GM/c^2$ .

An important remark to make is that we have here considered a Standard And Normal Evolution (SANE) simulation. This results in a lower magnetic flux at the event horizon compared to MAD simulations which have the maximum amount of flux that can penetrate the event horizon (Narayan et al., 2003; Tchekhovskoy et al., 2011). If we compare our results with the MAD simulation from Chael et al. (2019), our jet-opening angle is smaller, and our models are inconsistent with the observational constraints on the jet-opening angle at 43 GHz ( $55^\circ$  Walker et al. 2018; Janssen et al. 2019); by contrast, Chael et al. (2019) showed that their thermal MAD simulations do match the observed opening angle.

### 3.4.5 Reconnection as the source of particle acceleration

The electrons' energy-distribution function is one of the key open questions in modeling the appearance of jets launched by supermassive black holes. Simulations of these acceleration mechanisms rely on non-ideal effects, which are not captured in GRMHD-based simulations. Fully resistive treatments of the plasma using non-ideal GRMHD simulations (Palenzuela et al., 2009; Ohsuga et al., 2009; Dionysopoulou et al., 2013; Bucciantini & Del Zanna, 2013; Del Zanna et al., 2016; Qian et al., 2017, 2018; Del Zanna & Bucciantini, 2018; Mignone et al., 2019; Ripperda et al., 2019) or general-relativistic PIC simulations (Watson & Nishikawa 2010; Levinson & Cerutti 2018; Parfrey et al. 2018) are being developed and will help to provide detailed answers to these questions in the future. In principle, alternative acceleration mechanisms could be at work, such as shocks. In our model, the main region of emission is where the magnetization  $\sigma$  is around unity, where shocks are known to be less efficient (see e.g., Sironi et al., 2015).

### 3.4.6 The Event Horizon Telescope results

In Event Horizon Telescope Collaboration et al. (2019e), GRMHD models were used to interpret the first image of a black hole. In the post-processing of the GRMHD models, only models with a thermal distribution function were considered. In this work, we show the effect of electron acceleration by performing a comparison with a purely thermal model. The overall trend is that

the emission region is optically thinner and smaller in size. Also, the accretion rates and jet-power drop, which could have implications for some of the models reported in Event Horizon Telescope Collaboration et al. (2019e). In this work, we performed a model-to-model comparison where we use best-fit parameters (such as  $R_{\text{high}} = 100$ ) from previous works by e.g. Mościbrodzka et al. (2016b). From these works, we know that when  $R_{\text{high}}$  is decreased, the spectral slope of the radio spectrum will increase. If we vary our newly introduced parameters we see that decreasing the  $r_{\text{inj}}$  parameter will result in overproducing the NIR emission while increasing  $\eta$  would result in overproducing the radio in the jet, but it must be noted that in this work we did not perform a detailed parameter scan over the full parameter domain as is done in for example Event Horizon Telescope Collaboration et al. (2019e). A full parameter scan combined with a detailed comparison with respect to the EHT data is beyond the scope of this work and will be addressed in future works. A first step to generate realistic synthetic data based on the models presented here will be discussed by Roelofs et al. (2019).

### 3.5 Conclusion

We have presented a  $\kappa$ -jet model for the accreting black hole in M87 based on an AMR GRMHD simulation in Cartesian-Kerr-Schild coordinates, coupled to radiative-transfer calculations that include sub-grid models for electron acceleration based on reconnection in the magnetized jet. The use of a Cartesian grid with AMR resulted in a high-resolution jet simulation that we used to model the jet launching point in M87. We have demonstrated that we can obtain a fit for the M87 SED from radio up to NIR if there is an accelerated electron population present in the jet. The model does not evolve the electron distribution function in time and does not include cooling; both of these aspects will be considered in future works. The jet-opening angle at 43GHz is too narrow, Chael et al. (2019) showed that a MAD type accretion flow could recover this opening angle, and we plan to explore this setup in future works with the addition of particle acceleration. The model reproduces the broadband SED from radio up to NIR, observed source sizes, core shifts and recovers a jet power that is consistent with

#### Acknowledgements

The authors thank M. Moscibrodzka, C. Gammie, A. Philippov, Z. Younsi, and B. Ripperda for valuable discussions and feedback during the project. We thank the referee Luca Del Zanna for thoughtful review and constructive comments to improve our article. This work was funded by the ERC Synergy Grant "BlackHoleCam-Imaging the Event Horizon of Black Holes" (Grant 610058, Goddi et al. (2017)). The GRMHD simulations were performed on the Dutch National Supercomputing cluster Cartesius and are funded by the NWO computing grant 16431. The VLBA data shown in Fig. 3.11 is from project code: BW0106 PI: R. Craig Walker. This research has made use of NASA's Astrophysics Data System.

*Software:* BHAC (Porth et al., 2017), RAPTOR (Bronzwaer et al., 2018), eht-imaging (Chael et al., 2016, 2018a), python (Oliphant, 2007; Millman & Aivazis, 2011), scipy (Jones et al., 2001), numpy (van der Walt et al., 2011), matplotlib (Hunter, 2007), and rPICARD (Janssen et al., 2019).

### 3.A Phenomenological model explaining the dominance of the counter-jet

In certain GRMHD-based models of M87, when imaged at 228 GHz at low ( $\sim 20$  deg) inclination angles, it is observed that most of the emission that reaches the observer originates from the ‘counter-jet’, the jet facing away from the observer. Here we describe a simple phenomenological model that is capable of reproducing this effect.

Figure 3.12 shows a schematic overview of our model, which consists of two rings of luminous material. The model is symmetric with respect to the equatorial plane, and the black-hole’s rotation axis passes through the center of the rings. The rings are meant to be an approximation of the ‘jet base’ which appears on both sides of the equatorial plane in many GRMHD simulations. We assume that the luminous rings are perfectly optically thin (equivalently, we ignore absorption in this model).

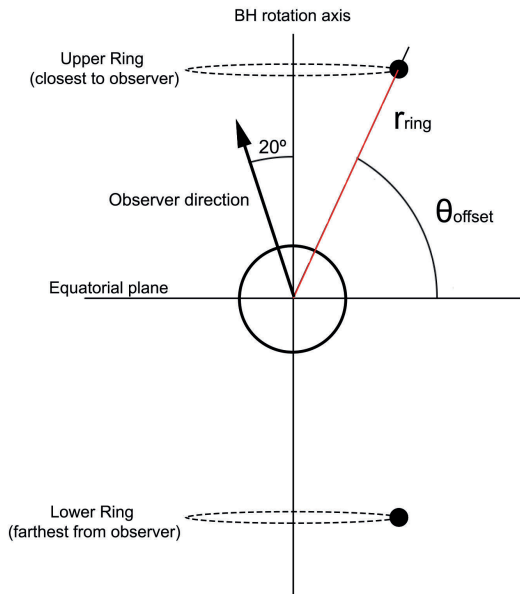


FIGURE 3.12: Schematic diagram of the model. A diagram of our phenomenological model of the dominant counter-jet. The central circle represents the black-hole’s event horizon. Two parameters control the placement of the rings (the model is symmetric with respect to the equatorial plane). The ring’s thickness is set to  $1 \text{ GM}/c^2$ .

Two main parameters define the geometry of the rings:  $\theta_{\text{offset}}$  and  $r_{\text{ring}}$  determine their principal diameter and distance from the equatorial plane. A step-function-based emissivity profile is then used, which relates the emissivity at a location in space to the distance between that location

and the nearest point on the ring; it is equal to unity if that distance is smaller than  $0.25 GM/c^2$ , and zero otherwise. In other words, the cross-sectional thickness of the ring is  $0.5 GM/c^2$ .

We also assign a velocity vector to the material in the ring; this is done using a simple Keplerian model for the orbital velocity of a particle with orbital radius  $r_{\text{ring}}$ . The effect of this velocity vector is to cause the characteristic relativistic-boosting effect seen in most of our simulations; the ring is slightly brighter on the approaching side. This effect is minor in the present case, due to our low inclination angle.

Figure 3.13 shows a typical image of our model, with its key features annotated for clarity. Figure 3.14 illustrates the effect of varying  $r_{\text{ring}}$ . Figure 3.15 compares two images that show only the upper (lower) ring. The flux observed from the lower ring is 30% higher than that of the upper ring. The lensed image(s) of the lower ring always appear ‘outside’ (but near) the black-hole’s photon ring, potentially causing the observer to overestimate the black-hole shadow size. Although the black-hole mass can be derived from the size of the black-hole shadow, such an estimate should be seen as an upper limit in the present context.

In this model, gravitational lensing causes most of the radiation emitted in the ‘polar regions’ of a black hole to be redirected toward the opposite side of the black hole with respect to its origin. This effect could explain why the counter-jet in optically thin simulations of M87 dominates over the observer-facing jet.

Figure 3.16 shows an illustration of the lensing effect that causes an observer to record *two* images of the lower ring, and only one of the upper ring. We can understand this feature by considering the rays shown in Fig. 3.16 from left to right (i.e., decreasing the rays’ impact parameter): the deflection angle increases as the rays curve more and more. The first object with which the rays intersect is the lower ring - hence we see that as the widest object on the observer’s image. The next rays, curving even more, intersect the lower ring again, but now they are moving back toward the observer (having traveled around the black hole). Moving on to rays with still smaller impact parameters, the rays now come very close to the photon ring. At this point, the deflection angle begins to diverge, causing rays to orbit the black hole an arbitrary number of times. These rays image the entire sky infinitely many times, producing a multitude of images of the environment. However, all of these images are very small (and thus they don’t contribute much flux), and they are confined to a thin ring, which is infinitesimally close to the photon ring.

The doubling effect is only visible at low inclination angles, when the system is viewed in a face-on manner; the effect vanishes entirely at inclination angles near 90 degrees (symmetry demands that both rings then contribute equally to the integrated flux density of the image). Complications also arise when absorption is taken into account; an optically thick accretion disk may absorb much of the lensed radiation originating from the lower ring.

As a final comment, we note that the doubling of the lower ring due to gravitational lensing occurs everywhere along the lower ring. Therefore, a partial ring or even a very compact structure (e.g., a plasmoid or ‘Gaussian hot-spot’) will show the same behavior; most of the radiation will come from the hot-spot on the opposite side of the black hole, away from the observer.

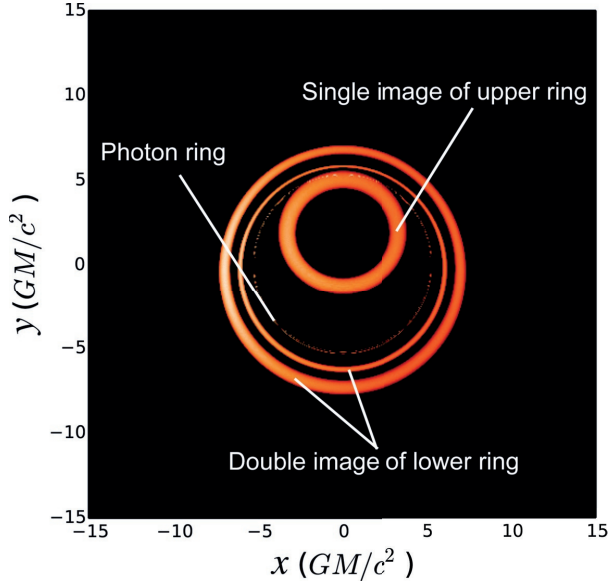


FIGURE 3.13: Example image. Shown is the case of a Schwarzschild black hole ( $a_* = 0$ ). The observer inclination  $i$  is 20 deg.  $\theta_{\text{offset}} = 1$  rad,  $r_{\text{ring}} = 6 GM/c^2$ . Note the double image of the lower ring, which appears larger in size than the upper ring due to lensing. The doubled image of the lower ring appears close to the photon ring, but is slightly larger.

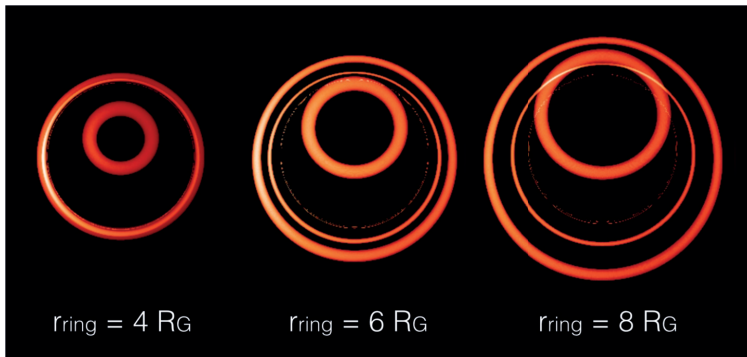


FIGURE 3.14: Varying  $r_{\text{ring}}$ . Illustration of the effect of changing  $r_{\text{ring}}$ , for a Schwarzschild black hole ( $a_* = 0$ ) imaged with  $i = 20$  deg and  $\theta_{\text{offset}} = 1$  rad. Note how the two images of the lower ring coincide for the case  $r_{\text{ring}} = 4 GM/c^2$ .

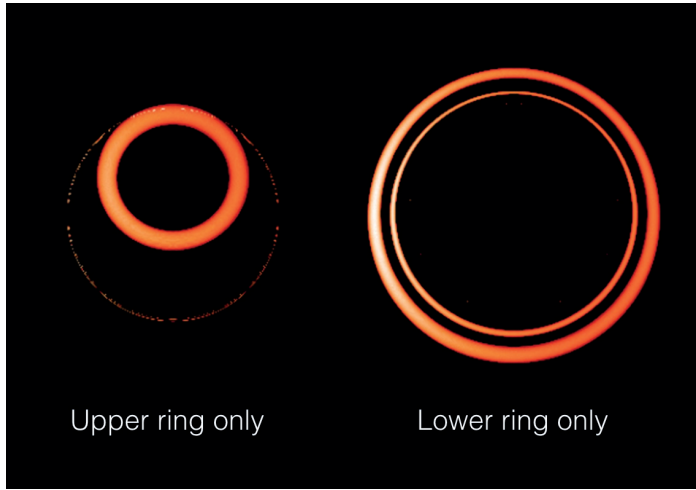


FIGURE 3.15: Upper and lower ring. Comparison of images which show only the upper (left) or lower (right) ring, omitting the other (as before,  $a_* = 0$ ,  $i = 20$  deg,  $\theta_{\text{offset}} = 1$  rad,  $r_{\text{ring}} = 6 GM/c^2$ ). The integrated flux density received from the lower ring is about 30% higher than that from the upper ring, due to gravitational lensing.

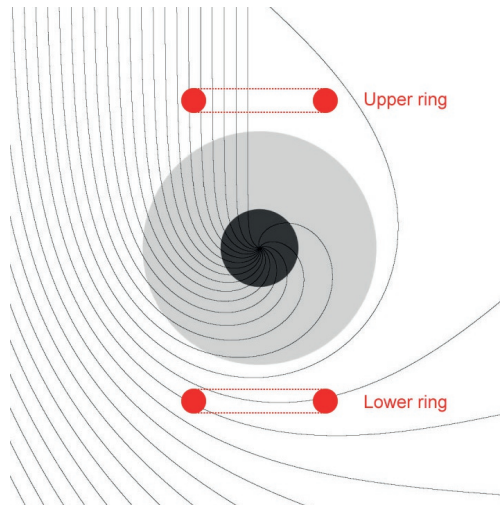


FIGURE 3.16: Visualization of the ‘doubling effect’. The observer in this image is directly above the black hole (i.e., the inclination angle is zero). The black-hole’s event horizon is marked by the dark-grey circle, while the light-grey circle marks the unstable-photon region. Gravitational lensing enhances the overall size of the lower ring, although the divergence of the rays near the lower ring causes its images to have a reduced thickness. Two images of the lower ring appear; one due to rays that intersect the ring while moving away from the observer, the other due to rays that curve around the black hole and intersect the ring while moving toward the observer. This causes most of the flux that reaches the observer to originate in the lower ring, on the far side of the black hole. Adapted from an image by Alessandro Roussel.

### 3.B Comparison with spherical grids

We benchmarked our CKS simulation to a spherical simulation in modified Kerr-Schild (MKS) coordinates evolved from the same initial condition. The MKS simulation used an effective resolution of  $512 \times 192 \times 192$  in  $\log(r)$ ,  $\theta$  and  $\phi$ , where the radial domain extended up to  $r_{\text{out}} = 3333 GM/c^2$ . We compared the accretion rate  $\dot{M}$  and magnetic flux through the horizon  $\Phi_{\text{BH}}$  from both simulations, which are shown in Fig. 3.17. In the non-linear phase, both the accretion rate and magnetic flux are of the same order of magnitude. At the end of the simulation, the normalized magnetic flux is, in both cases,  $\Phi_{\text{BH}}/\sqrt{\dot{M}} \approx 1.0$ . Therefore, the CKS model belongs to the category of Standard and Normal Evolution (SANE) (Tchekhovskoy et al., 2012).

The MRI quality factor  $Q_{\text{MRI}}^{(\theta)}$  is shown in Fig. 3.18. In the majority of the disk, the values of the quality factor are sufficiently above six as recommended in Sano et al. (2004), although close to the horizon, a drop is visible. However, this does not reflect into significant differences in the reported accretion rates and magnetic fluxes from Fig. 3.17. Throughout the jet, the resolution of the Cartesian grid exceeds that of the spherical grid significantly.

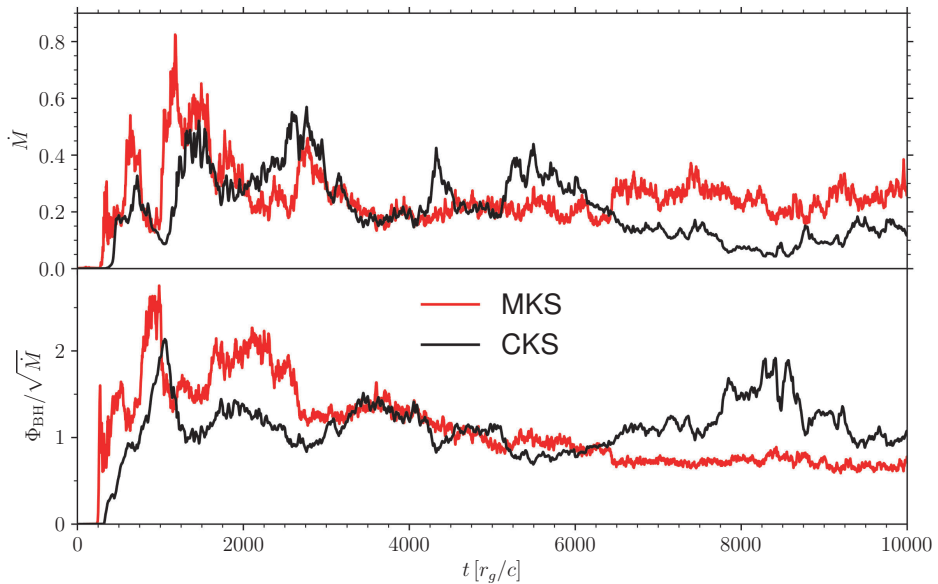


FIGURE 3.17: Comparing Cartesian with a spherical simulation. Top panel: accretion rate through the event horizon as a function of time for the CKS simulations used in this work and a reference simulation in spherical MKS coordinates. Bottom panel: normalized magnetic flux through the horizon for the same pair of simulations. Both quantities show a consistent behavior.

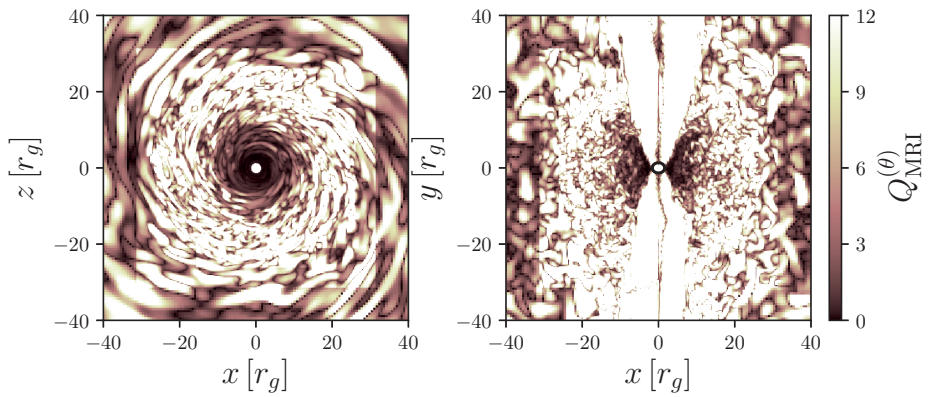


FIGURE 3.18: MRI quality factor  $Q_{\text{MRI}}^{(\theta)}$ . Shown is the  $xy$  plane (left) and on the  $xz$  plane (right).  $Q_{\text{MRI}}^{(\theta)}$  is sufficient in most of the disk, with a drop visible only very close to the event horizon.

---

# PARTICLE ACCELERATION IN KINK-UNSTABLE JETS

Jordy Davelaar, Alexander A. Philippov, Omer Bromberg, and Chandra B. Singh

*ApJL*, 2020, 896, 2

## Abstract

Magnetized jets in gamma-ray burts and active galactic nuclei are thought to be efficient accelerators of particles. However, the process responsible for the acceleration is still a matter of active debate. In this work, we study the kink-instability in non-rotating force-free jets using first-principle particle-in-cell simulations. We obtain similar overall evolution of the instability as found in magnetohydrodynamics simulations. The instability first generates large-scale current sheets, which at later times break up into small-scale turbulence. Reconnection in these sheets proceeds in the strong guide field regime, which results in a formation of steep power laws in the particle spectra. Later evolution shows heating of the plasma, which is driven by small-amplitude turbulence induced by the kink instability. These two processes energize particles due to a combination of ideal and non-ideal electric fields.

## 4.1 Introduction

Magnetized relativistic jets are efficient particle accelerators. They are observed in a wide variety of astronomical sources, e.g., X-ray binaries, Active Galactic Nuclei (AGN), and gamma-ray bursts (GRBs), see for example Pudritz et al. (2012) for a review on jets. These sources are typically observed over the entire electromagnetic spectrum from radio to  $\gamma$ -rays, and are considered as main candidates for accelerating ultra-high-energy cosmic rays. Their observed spectral energy distributions suggest that a large fraction of the radiatively important electrons are non-thermal.

However, the way these jets accelerate electrons is still uncertain. An effective mechanism for particle acceleration in highly magnetized flows is the dissipation of magnetic energy via reconnection in thin current sheets (Zenitani & Hoshino, 2001; Cerutti et al., 2014; Sironi & Spitkovsky, 2014; Guo et al., 2014). The reconnection is driven by the plasmoid instability (Loureiro et al., 2007), which continuously breaks current sheets into plasmoids separated by X-points. In the case of relativistic reconnection, strong electric fields in the vicinity of X-points accelerate electrons up to  $\gamma_{\max} \approx 4\sigma$  (Werner et al., 2016), where  $\sigma = B^2/(4\pi m_e n c^2)$ ,  $B$  is the magnetic field strength,  $m_e$  is the electron mass, and  $n$  is the plasma number density. A secondary acceleration phase that happens inside the plasmoids pushes particles to higher energies (Petropoulou & Sironi, 2018). The study of reconnection is usually done with kinetic plasma simulations, which model reconnection from first principles by using Harris sheets as initial conditions. However, it is still unknown if and where such sheets can form in realistic jets, and what the geometry of the reconnecting magnetic field is.

Global magnetohydrodynamics (MHD) simulations show that near the launching site jets expand and quickly lose transverse causal contact, making them stable for current-driven instabilities (Tchekhovskoy & Bromberg, 2016; Bromberg & Tchekhovskoy, 2016). As the pressure of the confining medium becomes important, the flow is recollimated and regains causal contact. As a result, the toroidal hoop stress becomes effective, and compresses the flow into forming a nozzle, which may become prone to internal kink-instability. In the context of astrophysical jets, the kink instability is generally divided into two types: *internal kink*, which grows at the jet's core and is not affecting the jet boundaries and, *external kink*, which grows on the jet boundaries and perturbs the entire jet body. Bromberg & Tchekhovskoy (2016) and Tchekhovskoy & Bromberg (2016) showed that internal kink mode that grows at recollimation nozzles of collimated jets could lead to efficient magnetic energy dissipation, reducing the jet's magnetization parameter,  $\sigma$ , which is high before the flow enters the nozzle, down to  $\sigma \approx 1$  Bromberg & Tchekhovskoy (2016). At this point, the poloidal and toroidal magnetic field components in the frame comoving with the jet are comparable.

Kink-instability has been studied both analytically (Rosenbluth et al., 1973; Begelman, 1998; Lyubarskii, 1999; Appl et al., 2000; Das & Begelman, 2019) and using MHD simulations (Mizuno et al., 2009, 2012; O'Neill et al., 2012; Bromberg et al., 2019). It triggers reconnection in current sheets, which dissipates magnetic energy into plasma energy. The importance of this process has been discussed in the context of GRBs (Drenkhahn & Spruit, 2002; Giannios & Spruit, 2006; McKinney & Uzdensky, 2012) and AGNs (McKinney & Blandford, 2009). Kink instability has also been studied in laboratory experiments. For example, Duck et al. (1997) observed a resonant kink mode, where  $B_\phi/B_z \approx 1.0$  (hereafter,  $z$  defines the direction along the jet's axis, and  $\phi$  corresponds to a toroidal direction with respect to the same axis). Coincidentally, similar conditions are expected in collimation nozzles of relativistic jets.

Particle acceleration in the process of kink instability was studied using particle-in-cell (PIC) simulations by Alves et al. (2018). They considered a pressure-supported jet where the toroidal magnetic field component dominates and found significant particle acceleration solely due to the generation of an ideal coherent electric field along the jet axis. Since their setup is pressure supported, force balance implies,  $\nabla p = \vec{J}/c \times \vec{B}$ , which effectively translates to  $p \approx B^2/8\pi$

(hereafter,  $p$  is the plasma pressure, and  $\vec{J} = c\nabla \times \vec{B}/4\pi$  is the plasma current density). Therefore, their setup considers an effective, "hot", magnetization  $\sigma_h = B^2/4\pi w \approx 1$ , where  $w = \varepsilon + p$  is the gas relativistic enthalpy, and  $\varepsilon$  is the plasma internal energy. AGN jets are, however, thought to be launched with  $\sigma_h \gg 1$  and exhibit force-free behavior close to their origin (Tchekhovskoy & Bromberg, 2016; Bromberg & Tchekhovskoy, 2016). Without an additional dissipation process, jet cores will remain highly magnetized and cold until they become kink unstable at the nozzle.

In Bromberg et al. (2019) we studied the long-term evolution of the kink instability in force-free non-rotating jets using MHD simulations. We showed that the system relaxes to a Taylor state while conserving the net magnetic helicity and axial magnetic flux. Depending on the initial field configuration and the box size, 10–50% of the magnetic energy is dissipated during the relaxation process. In this Letter, we investigate the mechanisms responsible for the particle acceleration during the process of kink instability by performing particle-in-cell (PIC) simulations. We consider the same magnetic field configurations as in Bromberg et al. (2019) and study the regime of  $\sigma_h \gg 1$  and  $B_\phi/B_z \approx 1.0$ . We find no coherent axial electric field in our setups, and find that particle acceleration occurs due to a combination of reconnection and turbulence.

## 4.2 Numerical setup

The first setup we consider is a force-free non-rotating jet originally investigated with MHD simulations by Mizuno et al. (2009) and by Bromberg et al. (2019). The magnetic field profile consists of a strong vertical field,  $B_z$ , dominated core surrounded by a region dominated by a toroidal field component,  $B_\phi$ . The magnetic field profile is given by,

$$B_z = \frac{B_0}{[1 + (r/r_{\text{core}})^2]^\zeta}, \quad (4.1)$$

$$B_\phi = B_z \frac{r_{\text{core}}}{r} \sqrt{\frac{[1 + (r/r_{\text{core}})^2]^{2\zeta} - 1 - 2\zeta(r/r_{\text{core}})^2}{2\zeta - 1}}, \quad (4.2)$$

where  $B_0$  is a scale factor that determines the value of magnetization parameter at the axis,  $r_{\text{core}}$  sets the size of the kink-unstable core, and  $r$  is the cylindrical radius. For  $r \gg r_{\text{core}}$  both field components asymptotically approach zero. The free parameter  $\zeta$  sets the behavior of the magnetic pitch,  $P = rB_z/B_\phi$ . For  $\zeta < 1$  the pitch is increasing with  $r$ , for  $\zeta = 1$  the pitch is constant, and for  $\zeta > 1$  the pitch is decreasing with  $r$ . In this work we consider two representative values of  $\zeta$ ,  $\zeta = 0.64$  (Increasing Pitch, IP) and  $\zeta = 1.44$  (Decreasing Pitch, DP). The radial profile of the pitch is important for the global evolution of the instability. In the case where the pitch is increasing with the cylindrical radius, resonant surfaces confine the instability to the kink-unstable core (Rosenbluth et al., 1973), while in the case of a decreasing pitch profile the instability becomes disruptive.

We also consider a force-free setup by Bodo et al. (2013), which has a non-monotonic pitch profile and a strong confining vertical magnetic field outside of the kink-unstable core. We term this profile as embedded pitch (EP, same as CO in Bromberg et al. 2019). The magnetic field in this case is given by

$$B_\phi = \frac{B_0 R}{r} \sqrt{\left(1 - e^{-(r/r_{\text{core}})^4}\right)}, \quad (4.3)$$

$$B_z = \frac{B_0 R P_0}{r_{\text{core}}^2} \sqrt{\left(1 - \sqrt{\pi} (r_{\text{core}}/P_0)^2 \operatorname{erf} \left[ (r/r_{\text{core}})^2 \right]\right)}, \quad (4.4)$$

where  $R$  is the cylindrical radius of the domain's outer boundary, and the parameter  $P_0$  is the value of the magnetic pitch at the axis. We consider a value of  $P_0 = 1.5 r_{\text{core}}$ . The magnetic field configuration qualitatively differs from the IP and DP setups, since for  $r > r_{\text{core}}$  the axial component of the magnetic field,  $B_z$ , asymptotes to a constant value. This vertical magnetic field leads to a strong confinement of the jet.

We perform our simulations in the frame comoving with the jet, thus the plasma is initially at rest. We use the relativistic PIC code *Tristan-MP* (Spitkovsky, 2005). The simulations are performed in a Cartesian three-dimensional computational box. The box length in  $z$ ,  $L_z$ , is set to fit two wavelengths of the fastest-growing kink mode  $\lambda_{\text{max}} = 8\pi P_0/3$  where  $P_0$  is the value of the pitch at the axis (Appl et al., 2000). We initialize our calculations with a cold uniform electron-positron plasma with temperature  $T = 10^{-2} m_e c^2/k_B$ , and a density of ten particles per cell giving a total of  $\sim 10^{11}$  particles in the simulation box. We set both electrons and positrons to drift in opposite directions with velocities  $\vec{v}_{\text{dr}} = \pm \vec{J}/2ne$  to generate the currents that support the initial magnetic field profile. The simulations are run up to  $t = 300 r_{\text{core}}/V_A$ , where  $V_A$  is the Alfvén speed defined as  $V_A = c\sqrt{\sigma_0/(1+\sigma_0)}$ , and  $\sigma_0$  is the magnetization at the jet axis,  $\sigma_0 = B_0^2/(4\pi m_e n c^2)$ . We set  $r_{\text{core}} = 60$  cells, and use grid sizes of: a) DP,  $3000^2 \times 900$ , b) IP,  $3000^2 \times 1300$  and c) EP,  $1200^2 \times 1600$  in the  $(x, y, z)$  directions respectively. We studied the dependence of our results on the scale separation by varying the ratio between the size of the kink-unstable core and the plasma skin depth,  $d_e = c/\omega_p$ , where  $\omega_p = \sqrt{4\pi e^2 n/m_e}$  is the plasma frequency. We varied  $d_e$  from three to six cells. The simulations presented in this Letter use a scale separation of  $r_{\text{core}}/d_e = 20$ , where  $d_e = 3$  cells, which is sufficient to recover the overall MHD evolution (see Bromberg et al. (2019) and Appendix A). In the  $z$  direction, we apply periodic boundary conditions, while at the boundary in the  $x$ - $y$  plane we have an absorbing layer for both fields and particles (Cerutti et al., 2015). For all three setups, we present simulations for three values of the magnetization parameter at the axis,  $\sigma_0 = 10, 20, 40$ , which correspond to  $\beta = 8\pi n T/B_0^2 = 2(k_B T/m_e c^2)(1/\sigma_0) = [20, 10, 5] \times 10^{-4}$ . Larmor gyration period  $2\pi/\sqrt{\sigma_0}\omega_p$  is resolved with at least a few time steps for all simulation setups.

### 4.3 Results

Our PIC simulations show the same global behavior found in our MHD simulations (Bromberg et al., 2019). The sufficiently large separation between fluid and kinetic scales allows us to obtain similar growth-rates in the linear stage, and a comparable amount of electromagnetic energy dissipation as in the MHD simulations (between 15-20% of the initial electromagnetic energy

in all three setups, see appendix A). Initially, the most unstable mode is a kink mode with a longitudinal wavenumber  $l = 2$ , and an azimuthal wavenumber  $m = -1$ <sup>1</sup>. It gives rise to a global helical current sheet at the edge of the kink-unstable core. Later on the  $l = 2$  mode transforms into an  $l = 1$  mode. Eventually, the global current sheet breaks up generating small-scale current sheets and turbulence that mediate further dissipation of the magnetic energy. Similar behavior was observed in our MHD simulations.

In all three setups, we observe particle energization due to an electric field that is parallel (non-ideal) or perpendicular (ideal) to the local magnetic field direction. As the instability becomes nonlinear, we observe a strong burst of particle energization due to a non-ideal electric field, which takes place in current sheets at the jet's periphery. A 3D visualization of the location of a subset of the energized particles, colour coded by their Lorentz factor is shown in Fig. 4.1. Fig. 4.2 demonstrates the location of the current sheets where particle energization takes place. It shows slices of the current density in the x-z and x-y planes, overplotted by energetic particles colour-coded according to their  $\vec{E} \cdot \vec{B}$  at their location. These sheets have strong guide fields. In the periphery the guide field is comparable in strength to the reconnecting field, while in the core it is approximately five times stronger. The presence of a strong guide field suppresses particle acceleration and leads to the formation of steep power laws in the particle distribution function (hereafter, DF). Werner & Uzdensky (2017) studied relativistic reconnection in pair plasmas with strong guide fields using local PIC simulations, and found a relation between the strength of the guide field and the power law index,  $\alpha$ , of the DF,  $f(\gamma) \propto \gamma^{-\alpha}$ . In our work, we find  $\alpha \approx 3 - 5$ , which is in agreement with their results for comparable strengths of the reconnecting and guide magnetic field components. At this stage, we find the maximum energy of accelerated particles to scale as  $\gamma_{\max} \approx \chi r_{\text{core}}/r_{\text{L}0}$ , where  $r_{\text{L}0} = m_e c^2/eB_0$  is a nominal cold relativistic gyroradius, and  $\chi \approx 1/6$ <sup>2</sup>.

In all our setups, we find that the self-excited turbulence has a small amplitude, e.g. the mean field is stronger compared to the fluctuating component. We evaluate the amplitude of turbulence as  $\xi = |(B(\vec{x}) - \langle B(\vec{x}) \rangle)|/\langle B(\vec{x}) \rangle$ , where  $\langle B(\vec{x}) \rangle = \int B(\vec{x}') e^{-|\vec{x} - \vec{x}'|^2/2\sigma_{\text{std}}^2} d\vec{x}'$  is the magnetic field strength averaged with a Gaussian kernel, and  $\sigma_{\text{std}} = r_{\text{core}}/3$ . We varied the size of the kernel in the range  $\sigma_{\text{std}} \in [r_{\text{core}}/6, r_{\text{core}}/2]$  and found no qualitative differences in our conclusion based on this analysis. The value of  $\xi$  itself varies spatially. We quantify the amplitude of turbulent motions by measuring the range of  $\xi$  inside the kink-unstable core. In all three setups we find  $\xi \leq 0.1$ . The small-amplitude turbulence leads to heating of the plasma, which forms a secondary Maxwellian in the DF (see panels b and e in Fig. 4.1). The temperature of this Maxwellian scales with the initial magnetization parameter, namely,  $k_B T/m_e c^2 \propto \sigma_0$ . Particle energization at this stage is dominated by the perpendicular component of the electric field. To quantify the importance of both parallel and perpendicular electric fields during the evolution of the instability, we trace

<sup>1</sup>The longitudinal wavenumber is defined as  $l = k_z L_z/2\pi$ , where  $k_z$  is the component of the wave vector in the z direction. The azimuthal wavenumber,  $m$ , defines the type of mode, where modes with  $|m| = 1$  are known as kink modes. For a more detailed discussion on the properties and behavior of the unstable mode, see Bromberg et al. 2019

<sup>2</sup>This conclusion is based on our simulations with different strengths of the jet's magnetic field. Increasing the jet's size is numerically expensive in our current setups, as the jet significantly expands laterally during the simulation time. We will conduct a systematic study of the dependence of  $\gamma_{\max}$  on the jet's size in the future work.

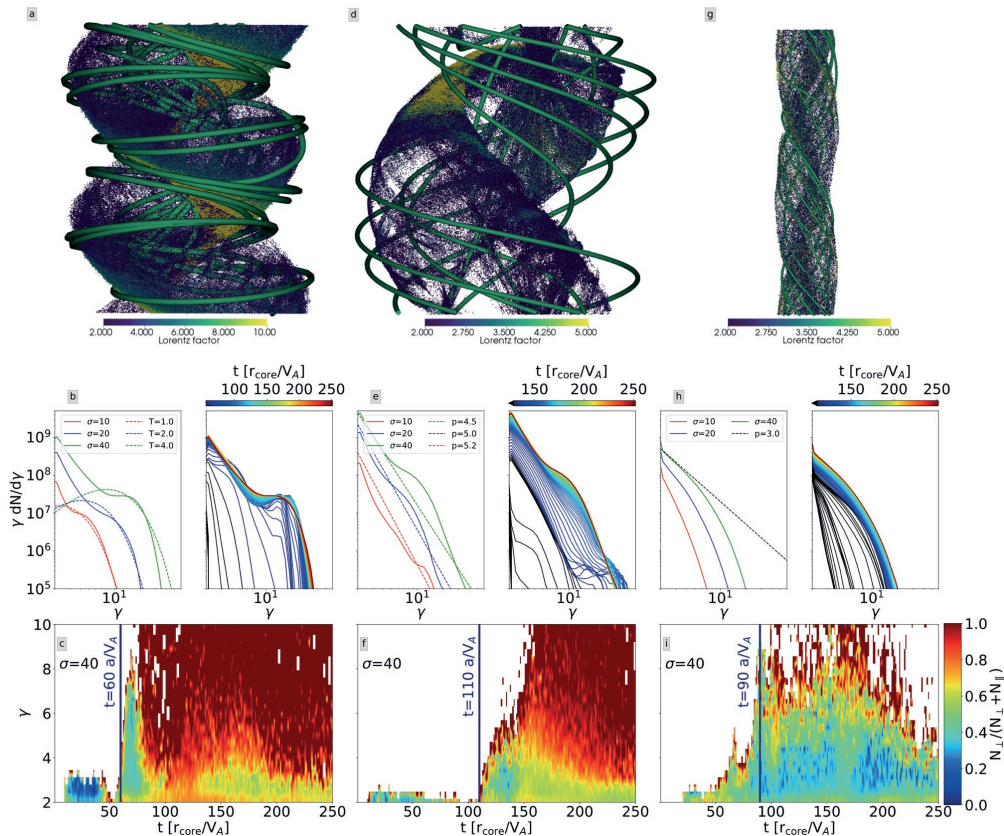


FIGURE 4.1: From left to right: decreasing pitch (DP), increasing pitch (IP), and embedded pitch (EP) cases. In the top row, thick green lines show magnetic field lines. Subsampled distribution of energetic particles is visualized as dots color-coded by their Lorentz factors. Plots are computed at  $t = 60, 110, 90 r_{\text{core}}/V_A$  correspondingly, the onset times of the acceleration episode in each configuration (see bottom panel). The middle row shows distribution functions (DFs) for all three setups, each set of two plots shows DFs at the end of the simulation on the left for all three  $\sigma_0 = 10, 20, 40$  values, and the time evolution of the spectrum of the  $\sigma_0 = 40$  run on the right. Panel b also includes Maxwellians fitted to the DFs, panel e, and h show power laws fitted to the DFs. The bottom row shows statistics of the acceleration events as a function of simulation time and particle energy. For a given particle at a particular energy, we classify the acceleration episode based on if parallel or perpendicular electric field dominates particle energization.  $N_{\parallel}$  and  $N_{\perp}$  are the numbers of parallel and perpendicular acceleration events, respectively. Initial particle distribution is a Maxwellian with a low temperature,  $10^{-2} m_e c^2/k_B$ , and all the spectra correspond to energized particles with  $\gamma > 2$ .

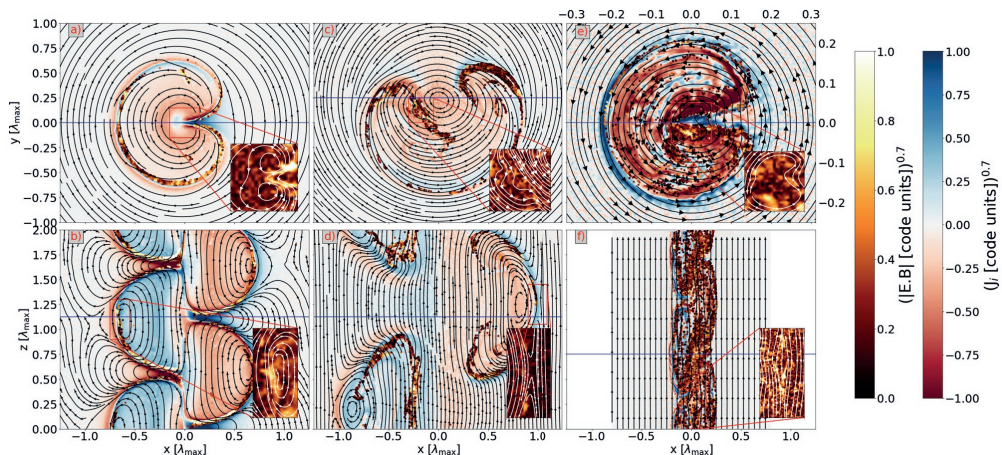


FIGURE 4.2: Formation of strong current layers in the onset of the nonlinear stage of the kink instability. From left to right columns: DP, IP, and EP cases. First row: slices of the axial component of the current,  $j_z$ , in the  $x$ - $y$  plane. Second row: slices of the toroidal component of the current,  $j_\phi$ , in the  $x$ - $z$  plane. Black/white lines show the in-plane components of the magnetic field. Insets show the distribution of  $E \cdot B$  as color and highlight the  $E \cdot B \neq 0$  regions where in-plane magnetic field components show antiparallel orientation. A subsample of particles with  $\gamma > 2$  is shown as dots, color-coded with the local  $E \cdot B$  values they experience. Their locations clearly correlate with strong current layers. The  $E \cdot B$  color bar is assigned to both the insets and the particle color-coding.

every tenth particle in our simulations with  $\gamma > 2$ . We classify individual acceleration events based on if the parallel or the perpendicular electric field component dominates the acceleration by looking at the absolute values of energy gained by each process. The statistics of acceleration episodes are shown in Fig. 4.1, bottom row. In all three setups, a large fraction of the particles undergoes parallel acceleration immediately after the instability becomes nonlinear, while in the IP and DP case the perpendicular acceleration dominates at larger energies. We find that the number of acceleration events due to the parallel electric field increases at higher values of the magnetization parameter.

In Fig. 4.3 we show an example of two particle trajectories in the IP case that exhibit acceleration due to either a parallel or a perpendicular electric field. In the case of parallel acceleration (particle 1), the energization happens in the current sheet at the edge of the kink-unstable core, where  $E \cdot B \neq 0$ . In the perpendicular case (particle 2), the particle is initially accelerated by a parallel electric field and then ends up in the turbulent core, where it undergoes further acceleration to higher energies mediated by the perpendicular electric field. These particle trajectories are representative for all three setups, although the relative contribution of parallel and perpendicular episodes differs, as can be seen in Fig. 4.1.

The DP simulation shows a strong acceleration event around  $t = 60 r_{\text{core}}/V_A$ , as is shown in Fig. 4.1c. At this time, the  $l = 2$  mode forms a helical current sheet at the edge of the kink-

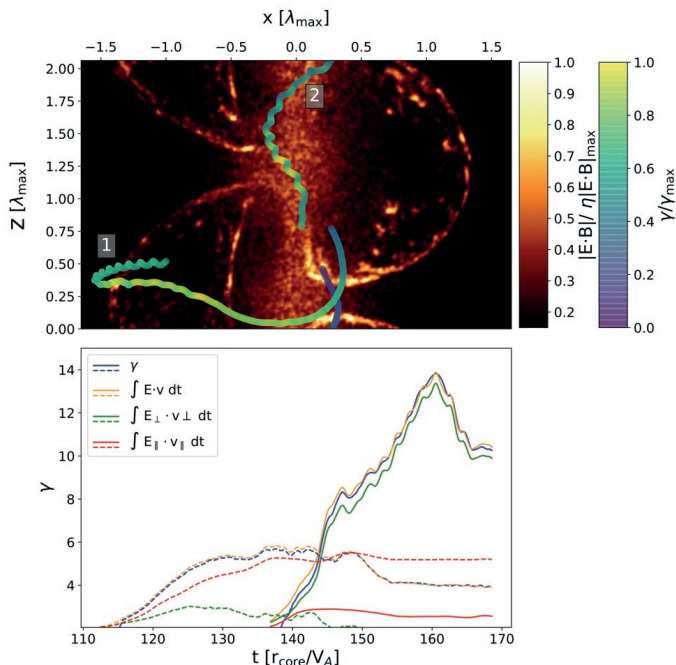


FIGURE 4.3: Trajectories of two accelerated particles in the IP case. Top panel shows  $E \cdot B$  in the  $x$ - $z$  plane, overplotted with trajectories of a particle (1) that undergoes mainly parallel acceleration, and a particle (2) that undergoes perpendicular acceleration. Lower panel shows the time-integrated work of the electric field,  $E \cdot v$ , along the trajectory of these particles, the contribution of parallel and perpendicular components to the integrated  $E \cdot v$ , and particle Lorentz factors as a function of time. The dashed lines correspond to particle 1, and solid lines correspond to particle 2. Particle 1 is predominantly accelerated by a parallel electric field in the current layer at the edge of the kink-unstable core, while particle 2 experiences strong acceleration by perpendicular electric fields in the jet's core.

unstable core, see Fig. 4.1a. The sheet is produced by the relative shear between the magnetic field inside the jet's core and at the periphery and is supported by strong currents (see Fig. 4.2a). These current layers contain most of the energized particles and correlate with locations where  $E \cdot B \neq 0$ . In these layers, some of the magnetic field components exhibit antiparallel orientations, see inset in Fig. 4.2d where  $B_z$  is the reconnecting field component. This shows that non-ideal electric fields in current sheets are the driving mechanism of the energization. The statistics of acceleration events in the DP case is shown in Fig. 4.1c, where the burst of acceleration events at  $t = 60 r_{\text{core}}/V_A$  coincides with the increasing number of non-thermal particles in the DF (see Fig. 1b, right panel). Clearly, a majority of the particles are initially accelerated via parallel electric fields. At later times a second acceleration stage due to a perpendicular electric field in turbulence pushes the particles to higher  $\gamma$  values. For all three values of  $\sigma_0$ , the DF shows the growth of a secondary Maxwellian with a temperature that scales linearly with  $\sigma_0$ , as is expected

from the energy conservation argument<sup>3</sup>. The measured amplitude of the turbulence for  $\sigma_0 = 40$  is of the order of  $\xi \leq 0.1$  in the kink-unstable core.

In the IP case, the first acceleration event is seen at  $t = 110 r_{\text{core}}/V_A$ . At this time, the  $l = 1$  mode develops a current sheet at the jet's periphery. Again, the location of particle acceleration correlates with current sheets where  $E \cdot B \neq 0$ , as can be seen in Fig. 4.2. The statistics of acceleration events in Fig. 4.1f clearly shows that at this time, the majority of particles are accelerated due to parallel electric fields. The resulting spectra in Fig. 4.1 shows a power law with  $\alpha \approx 4.5$  for  $\sigma_0 = 40$ , and a secondary Maxwellian that slowly grows over time. We measure the amplitude of turbulence in the core to be of the order of  $\xi \leq 0.05$ , which is smaller compared to the DP simulation. This can explain the slower growth of the secondary Maxwellian in the spectra.

For the EP case, at  $t = 50 r_{\text{core}}/V_A$  the particle acceleration starts when the  $l = 2$  mode grows. Again, current sheets coincide with locations of  $E \cdot B \neq 0$ , where particles are accelerated due to parallel electric fields. The resulting DF shows a clear power law with index  $\alpha \approx 3$  for  $\sigma_0 = 40$ , and a modest steepening of the spectrum for lower values of  $\sigma_0$ . The turbulence in the EP setup has a small amplitude, of the order of  $\xi \leq 0.01$ , which could explain the lack of a secondary Maxwellian in the spectra. This correlates with a strong dominance of parallel acceleration events in the particle energization history, which takes place over the entire simulation duration in the EP case, as shown in Fig. 4.1i.

Thin current sheets are known to be unstable to a tearing instability, and subsequent plasmoid instability of secondary sheets (Loureiro et al., 2007). While limited scale separation of our global simulations prevents us from observing the plasmoid instability, we do observe the initial tearing of current sheets generated by the relative shear of the magnetic field at the jet's boundary. An example of the IP case is presented in Fig. 4.4, where different quantities show plasmoid-like structures in different parts of the current sheet at the jet's boundary. We plan to study kink-unstable configurations presented in this work with relativistic resistive MHD simulations with adaptive mesh refinement (Ripperda et al., 2017), in order to better resolve plasmoid chains in these current sheets.

## 4.4 Discussion and conclusion

Reconnection and turbulence in collisionless plasma were studied so far in idealized periodic boxes. Our study shows how they can be self-consistently excited and energize particles in the process of kink instability in highly magnetized jets. We find that acceleration in current sheets dominates at low particle energies; and happens due to non-ideal electric fields that lead to the formation of steep power laws in the DF, due to strong guide fields at the reconnection sites. The presence of acceleration due to non-ideal electric fields is in contrast with the study of Alves et al. (2018). This difference is likely caused by the fact that their pressure-supported jet configuration corresponds

---

<sup>3</sup>The Larmor radius of particles with  $\gamma = \sigma_0$  in the jet's core is  $r_L = \sigma_0 r_{L0} = \sqrt{\sigma_0} d_e$ , which corresponds to  $0.3 r_{\text{core}}$  for  $\sigma_0 = 40$ . The size of the kink-unstable core, however, grows to  $\sim 0.75 \lambda_{\text{max}} \sim 10 r_{\text{core}}$  in the nonlinear stage, so further particle acceleration is in principle possible. The plasma skin depth,  $d_e = \sqrt{m_e c^2 \langle \gamma \rangle / 4 \pi e^2 n}$ , also increases as a result of the heating (see also Appendix A for the discussion of the scale separation in the DP case).

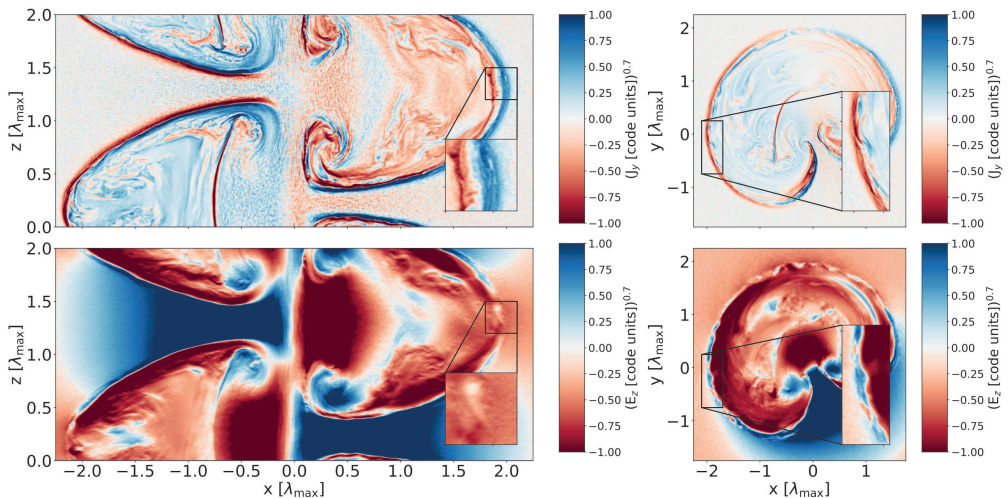


FIGURE 4.4: Formation of plasmoids in the IP setup. The first row presents the  $y$  component of the current in  $x$ - $z$  and  $x$ - $y$  planes. The second row shows the  $z$  component of the electric field. In all panels, insets zoom into plasmoid-like structures. In all panels, distances are measured in units of the fastest-growing kink mode  $\lambda_{\max} = 8\pi P_0/3$ , where  $P_0$  is the value of the pitch on the axis.

to the case  $\sigma_h \approx 1$ . As we discuss above, we also find no coherent axial electric field in our highly magnetized, force-free setups.

While we observe plasmoid formation, our limited scale separation does not allow the formation of a full plasmoid chain, and a study of the Fermi-like process of particle acceleration in plasmoids (Petropoulou & Sironi, 2018). Future large-scale local simulations of reconnection with a strong guide field are needed to investigate this potentially important mechanism of particle acceleration (Drake et al., 2006). We further find that energization due to scatterings on small-amplitude turbulent fluctuations leads mostly to plasma heating. This is in contrast to local simulations of particle energization in high-amplitude turbulence (Zhdankin et al., 2013, 2017; Comisso & Sironi, 2018), which showed the formation of prominent power laws. Motivated by our results in the DP case, where particle energization in turbulence erases the initial reconnection spectra, for the cases of large-amplitude turbulence, we anticipate the power laws to extend up to energies corresponding to the confinement condition,  $\gamma_{\max} \sim r_{\text{core}}/r_{L0}$  (Zhdankin et al., 2017).

Future work should incorporate realistic jet structures, including rotation and velocity shear, and develop an understanding of how to extrapolate the results of simulations with limited scale separation, such as ours, to parameters of astrophysical systems. Similarly to this work, these studies will identify the geometry of current sheets and quantify the amplitude of the excited turbulence and, thus, allow to quantify particle acceleration and emission of energetic photons from kink-unstable jets in GRBs and AGNs from first principles.

### Acknowledgements

The authors thank A. Bhattacharjee, L. Comisso, H. Hakobyan, B. Ripperda, L. Sironi, A. Spitkovsky and A. Tchekhovskoy for insightful comments over the course of this project. J.D. is funded by the ERC Synergy Grant 610058, Goddi et al. (2017). The authors thank the anonymous referee for insightful comments. O.B. and C.S. were funded by an ISF grant 1657/18 and by an ISF (I-CORE) grant 1829/12. O.B. and S.P. were also supported by a BSF grant 2018312. S.P. acknowledges support by the National Science Foundation under Grant No. AST-1910248. The Flatiron Institute is supported by the Simons Foundation.

*Software:* `Tristan-MP` (Spitkovsky, 2005), `python` (Oliphant, 2007; Millman & Aivazis, 2011), `scipy` (Jones et al., 2001), `numpy` (van der Walt et al., 2011), `matplotlib` (Hunter, 2007), `VisIt` (Childs et al., 2005).

## 4.A Comparison with MHD

In order to ensure that our simulations probe the large-scale behavior correctly, we compare the growth rates of the kink instability and electromagnetic dissipation rates of our PIC simulation with MHD simulations of the same configurations from Bromberg et al. (2019). The simulation box sizes are identical, and we choose  $\sigma_0 = 10$ , the separation between the size of the kink-unstable core and the plasma skin depth in the case of PIC  $r_{\text{core}}/d_e=20$ , for this comparison. To compute dissipation rates in both PIC and MHD simulations, we correct for the electromagnetic energy that leaves through the box boundary  $\mathcal{A}$  (edge of the absorbing boundary for PIC, and the edge of the box with standard outflow boundary condition in the case of MHD).

The growth rates of the electric energy are shown in the top panels of Fig. 4.5. In the PIC simulations, the onset of the instability is slightly delayed with respect to MHD. We, therefore, shifted the PIC curves so that they overlap with the MHD curves to ease the comparison of the rates by eye. The linear growth shows very similar rates in PIC and MHD. In the PIC simulations, the instability initially kicks in on kinetic scales at the jet’s boundary, which is not observed in the MHD simulations. This behavior is significantly more prominent in simulations with  $r_{\text{core}}/d_e = 10$ , which highlights the importance of using large-scale separation in PIC simulations. The small-scale plasma instabilities cause some discrepancies between the linear growth rates at the very early times. Also, the initial amplitude of the electric field is higher in the PIC runs because of the particle noise. However, when the kink instability grows and the jet expands at  $t \geq 50r_{\text{core}}/V_A$ , the growth rate in PIC becomes indistinguishable from the one observed in MHD (see Bromberg et al. (2019) for MHD simulations). At this stage, the growth rates are observed to be nearly identical in PIC and MHD for all three setups. The magnetic field dissipation is shown in the bottom row of Fig. 4.5. In the DP, IP, and EP cases, the evolution and dissipation rates up to  $t = 200 r_{\text{core}}/V_A$  are very similar. This comparison shows excellent agreement between the large-scale behavior of the kink instability in the PIC simulations presented here and the MHD simulations from Bromberg et al. (2019). In the DP case the MHD simulation continues to dissipate, while PIC saturates at around  $E_{\text{EM}}/E_{\text{EM},t=0} \approx 0.8$ . The discrepancy is likely due to the fact that the separation between the jet scale and the skin depth scale shrinks because of the plasma heating during the turbulent stage of the instability, which is most prominent in the

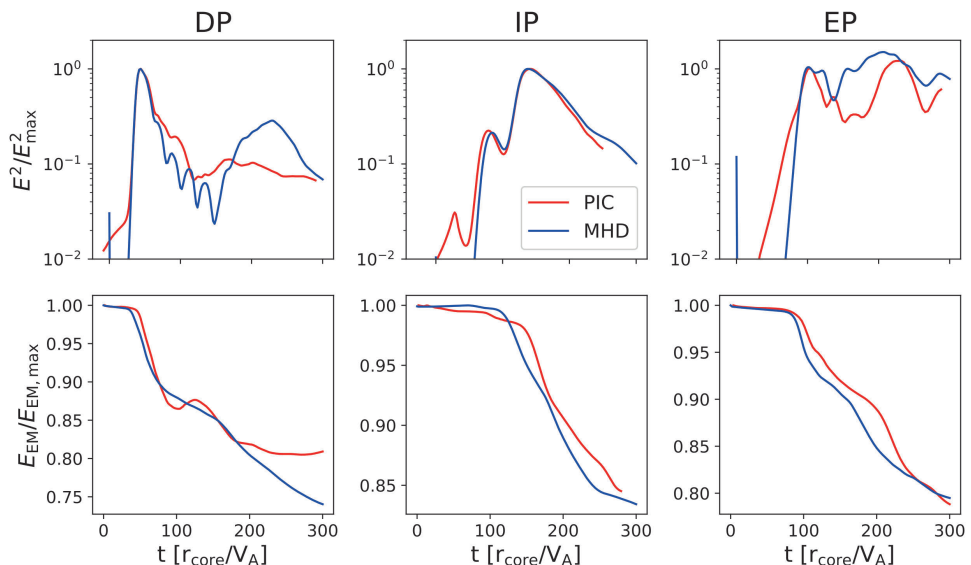


FIGURE 4.5: Comparison of the linear growth rates of the instability and electromagnetic energy dissipation in PIC and MHD simulations. From left to right: DP, IP, and EP case. Panels in the top row show the evolution of electric energy as a function of time, which highlights a stage of exponential growth. Panels in the bottom row show the dissipation of electromagnetic energy. In all panels, red lines represent PIC simulations, and blue lines correspond to MHD simulations.

DP case. For our box size,  $L_z = 2\lambda_{\max}$ , running MHD simulations further does not lead to a larger amount of the dissipation for the cases of IP and EP. However, the final state is not fully relaxed, and at least twice larger simulation box (in all directions, since the jet also expands more prominently if a larger amount of most unstable modes is present) is required to observe a Taylor state (Bromberg et al., 2019). About twice the amount of dissipation is observed in simulations, which lead to full relaxation,  $\sim 30\%$  and  $\sim 40\%$  for the IP and EP cases, correspondingly (see Fig. 6 in Bromberg et al. 2019). A significantly higher, up to 40%, amount of dissipation is observed in MHD simulations of the DP case with the same box size as chosen in this Letter. As we mentioned above, the decreased scale separation is a likely reason for this discrepancy.

---

# OBSERVING SUPERMASSIVE BLACK HOLES IN VIRTUAL REALITY

Jordy Davelaar, Thomas Bronzwaer, Daniel Kok, Ziri Younsi,  
Monika Mościbrodzka, and Heino Falcke

*CompAC, 2018, 5.1*

## Abstract

We present a full  $360^\circ$  (i.e.,  $4\pi$  steradian) general-relativistic ray-tracing and radiative transfer calculations of accreting supermassive black holes. We perform state-of-the-art three-dimensional general-relativistic magnetohydrodynamical simulations using the BHAC code, subsequently post-processing this data with the radiative transfer code RAPTOR. All relativistic and general-relativistic effects, such as Doppler boosting and gravitational redshift, as well as geometrical effects due to the local gravitational field and the observer's changing position and state of motion, are therefore calculated self-consistently. Synthetic images at four astronomically-relevant observing frequencies are generated from the perspective of an observer with a full  $360^\circ$  view inside the accretion flow, which is advected with the flow as it evolves. As an example, we calculated images based on recent best-fit models of observations of Sagittarius A\*. These images are combined to generate a complete  $360^\circ$  Virtual Reality movie of the surrounding environment of the black hole and its event horizon. Our approach also enables the calculation of the local luminosity received at a given fluid element in the accretion flow, providing important applications in, e.g., radiation feedback calculations onto black hole accretion flows. In addition to scientific applications, the  $360^\circ$  Virtual Reality movies we present also represent a new medium through which to interactively communicate black hole physics to a wider audience, serving as a powerful educational tool.

## 5.1 Introduction

Active Galactic Nuclei (AGN) are strong sources of electromagnetic radiation from the radio up to  $\gamma$ -rays. Their source properties can be explained in terms of a galaxy hosting an accreting supermassive black hole (SMBH) at its core. The Milky Way also harbors a candidate SMBH, Sagittarius A\* (Sgr A\*), which is subject to intensive Very-Long-Baseline Interferometric (VLBI) studies Krichbaum et al. (1998); Bower et al. (2004); Shen et al. (2005); Doeleman et al. (2008); Bower et al. (2014); Brinkerink et al. (2016). Sgr A\* is one of the primary targets of the Event Horizon Telescope Collaboration (EHTC), which aims to image for the very first time the “shadow” of a black hole Goddi et al. (2017). Theoretical calculations predict this shadow to manifest as a darkening of the inner accretion flow image anticipated to be observed due to the presence of a black hole event horizon, representing the region within which no radiation can escape Grenzebach (2016); Goddi et al. (2017); Younsi et al. (2016). The apparent size on the sky of this shadow is constrained by Einstein’s General Theory of Relativity (GR) Bardeen (1973); Cunningham & Bardeen (1973); Luminet (1979); Viergutz (1993); Falcke et al. (2000b); Johannsen & Psaltis (2010); Johannsen (2013); Younsi et al. (2016), and observational measurements of the black hole shadow size and shape can in principle provide a strong test of the validity of GR in the strong-field regime Johannsen & Psaltis (2010); Abdujabbarov et al. (2015); Younsi et al. (2016); Goddi et al. (2017).

The theoretical aspects of the observational study of Sgr A\* require the generation of general-relativistic magnetohydrodynamical (GRMHD) simulation data of the accretion flow onto a black hole, which is subsequently used to calculate synthetic observational data for physically-motivated plasma models, which can be compared to actual observational data. In the past, synthetic observational data was generated by ray-tracing radiative transfer codes which calculate the emission originating from the accreting black hole and measured by a faraway observer by solving the equations of radiative transfer along geodesics, i.e., the paths of photons (or particles) as they propagate around the black hole in either static spacetimes (e.g. Broderick, 2006; Noble et al., 2007; Dexter & Agol, 2009; Shcherbakov & Huang, 2011; Vincent et al., 2011; Younsi et al., 2012; Chan et al., 2013; Younsi & Wu, 2015; Dexter, 2016; Schnittman et al., 2016; Chan et al., 2018; Mościbrodzka & Gammie, 2018; Bronzwaer et al., 2018) or dynamical spacetimes Kelly et al. (2017); Schnittman et al. (2018).

These models vary only in the dynamics of the black hole accretion flow, with the observer remaining stationary through the calculations. In this work, we consider the most general case of an observer who can vary arbitrarily in both their position (with respect to the black hole) and their state of motion. In particular, the observer is chosen to follow the flow of the accreting plasma in a physically-meaningful manner through advection, and therefore all dynamical effects introduced by the motion of the observer around the black hole are also correctly included in the imaging calculation.

With recent developments in Graphical Processor Units (GPUs) and Virtual Reality (VR) rendering, it has become possible to visualize these astrophysical objects at high resolutions in a  $360^\circ$  (i.e.,  $4\pi$  steradian) format that covers the entire celestial sphere of an observer, enabling the study of the surroundings of an accreting black hole from within the accretion flow itself. Virtual Reality is a broad concept that encompasses different techniques, such as immersive visualization,

stereographic rendering, and interactive visualizations. In this work, we explore the first of these three, by rendering the full celestial sphere of the observer along a trajectory. The viewer can then look in any direction during the animation; this is also known as 360° VR. Another important feature of VR, stereographic rendering, presents different images to each eye so that the viewer experiences stereoscopic depth. For our application, however, this technique is not relevant, since the physical distance between the eyes of the observer is much smaller than the typical length scale of a supermassive black hole (which is  $6.645 \times 10^{11}$  cm for Sagittarius A\*), and therefore we would not see any depth in the image (just as we do not see stereoscopic depth when looking at the Moon). Interactive visualizations, where the viewer also has the freedom to change his or her position, would require real-time rendering of the environment, which is beyond the reach of current computational resources.

Our new way of visualizing black holes enables the study of accretion from the point of view of an observer close to the black hole event horizon, with the freedom to image in all directions, as opposed to the perspective of an observer far away from the source with a fixed position and narrow field of view. In the case of a distant observer, the source appears projected onto the celestial sphere (thus appearing two-dimensional). Since one cannot easily distinguish three-dimensional structures within the accretion flow, placing the observer inside the flow itself opens a new window in understanding the geometrical structure and dynamical properties of such systems. Several researchers have previously considered an observer moving around, or falling into a black hole, e.g.,

1. falling through the event horizon as illustrated through the gravitational lensing distortions of different regions (e.g., the ergo-region and event horizon), represented as checkerboard patterns projected onto an observer’s image plane Madore (2011),
2. a flight through a simulation of a non-rotating black hole Hamilton (1998),
3. a flight through an accretion disk of a black hole using an observer with a narrow field of view camera Luminet (2011),
4. a 360° VR movie of an observer falling into a black hole surrounded by vacuum with illumination provided exclusively by background starlight, i.e., without an accretion flow Younsi (2016),
5. a 360° VR movie of a hotspot orbiting a SMBH Moscibrodzka (2018), and
6. a 360° VR movie of an N-body/hydrodynamical simulation of the central parsec of the Galactic center Russell (2017).

In this study, we consider a self-consistent three-dimensional GRMHD simulation of the accretion flow onto a spinning (Kerr) black hole, determining its time evolution and what an observer would see in full 360° VR as they move through the dynamically evolving flow. To image accreting black holes in VR, we use the general-relativistic radiative-transfer (GRRT) code RAPTOR (Bronzwaer et al., 2018). The code incorporates all important general-relativistic effects, such as Doppler boosting and gravitational lensing in curved spacetimes, and can be compiled and run on both Central Processing units (CPU’s) and GPU’s by using NVIDIA’s OpenACC framework.

In this work, we investigate the environment of accreting black holes from within the accretion flow itself with a virtual camera. As an example astrophysical case we model the supermassive black hole Sgr A\*, although the methods presented in this work are generally applicable to any black hole as long as the radiation field’s feedback onto the accreting plasma has a negligible effect on the plasma’s magnetohydrodynamical properties, which is the case for Low Luminosity AGNs or low/hard state X-ray binaries.

The trajectory of this camera consists of two phases: a hovering trajectory, where the observer moves with a predefined velocity, and a particle trajectory, where the observer’s instantaneous velocity is given by a trajectory of a tracer particle computed with a separate axisymmetric GRMHD simulation. The tracer particle follows the local plasma velocity (specifically, it is obtained by interpolating the plasma velocity of the GRMHD simulation cells to the camera’s location).

We present a 360° VR simulation of Sgr A\*, demonstrating the applications of VR for studying not just accreting black holes but also for education, public outreach and data visualization and interpretation amongst the wider scientific community. In section 5.2 we describe the camera setup, present several black hole shadow lensing tests, describe the camera trajectories, and outline the radiative transfer calculation. In section 5.3 we present our 360° VR movie of an accreting black hole. In section 5.4 we discuss our results and outlook.

## 5.2 Methods

In this section, we introduce the virtual camera setup, present black hole shadow vacuum lensing tests using both stationary and free-falling observers at different radial positions, discuss the different camera trajectories used in the VR movie shown later in this article, and introduce the GRMHD plasma model that is used as an input for the geometry of the accretion flow onto the black hole.

The original **RAPTOR** code Bronzwaer et al. (2018) initialises rays (i.e., photon geodesics) using impact parameters determined from coordinate locations on the observer’s image plane Bardeen et al. (1972). This method is not suitable for VR since it only applies to distant observers where geometrical distortions in the image which arise from the strong gravitational field (i.e., spacetime curvature) of the black hole are negligible. To generate full 360° images as seen by an observer close to the black hole, we have extended the procedure of Noble et al. (2007) to use an orthonormal tetrad basis for the construction of initial photon wave vectors, distributing them uniformly as a function of  $\theta \in [0, \pi]$  and  $\phi \in [0, 2\pi]$  over a unit sphere.

The advantage of this approach is that all geometrical, relativistic, and general-relativistic effects on the observed emission is naturally and self-consistently folded into the imaging calculation, providing a complete and physically-accurate depiction of what would really be seen from an observer’s perspective.

The first step in building the tetrad basis is using a set of *trial vectors* (specifically, 4-vectors),  $t_{(a)}^\mu$ , to find the *tetrad basis vectors*,  $e_{(a)}^\mu$ . Herein, parenthesized lowercase Roman letters correspond to tetrad frame indices while Greek letters correspond to coordinate frame indices. Unless stated otherwise, all indices are taken to vary over 0–3, with 0 denoting the temporal component

and 1–3 denoting the spatial components of a given 4-vector. Given a set of  $\{\theta, \phi\}$  pairs (typically on a uniform grid), the corresponding wave vector components in the tetrad frame,  $k^{(a)}$ , are given by:

$$k^{(0)} = +1, \quad (5.1)$$

$$k^{(1)} = -\cos(\phi)\cos(\theta), \quad (5.2)$$

$$k^{(2)} = -\sin(\theta), \quad (5.3)$$

$$k^{(3)} = -\sin(\phi)\cos(\theta), \quad (5.4)$$

where it is trivial to verify that this wave vector satisfies  $k_{(a)}k^{(a)} = 0$ , as expected for null geodesics.

In order to determine the wave vector defined in eqs. (5.1)–(5.4) in the coordinate frame,  $k^\alpha$ , it is necessary to first construct the tetrad vectors explicitly. The first trial vector we use is the four-velocity of the observer,  $t_{(0)}^\mu = u_{\text{obs}}^\mu$ . This vector is, by virtue of sensible initial conditions and preservation of the norm during integration, normalized. Using the four-velocity as an initial trial vector also ensures that Doppler effects due to the motion of the camera are included correctly. It is then possible to build a set of orthonormal basis vectors  $e_{(a)}^\mu$  by using the Gram-Schmidt orthonormalization procedure. The required trial vectors for this procedure are given by:

$$t_{(1)}^\mu = (0, -1, 0, 0), \quad (5.5)$$

$$t_{(2)}^\mu = (0, 0, 1, 0), \quad (5.6)$$

$$t_{(3)}^\mu = (0, 0, 0, 1). \quad (5.7)$$

This set of trial vectors is chosen such that the observer always looks towards the black hole in a right-handed basis. Any other initialization, e.g., along with the velocity vector, could cause discomfort when used in VR due to high azimuthal velocities. The wave vector may now be found by taking the inner product of the tetrad basis vectors and the wave vector in the observer's frame as:

$$k^\mu = e_{(a)}^\mu k^{(a)}. \quad (5.8)$$

The observer's camera is then initialized at a position  $X_{\text{cam}}^\mu$  and uniformly-spaced rays are launched in all directions from this point. This method is fully covariant and is, therefore, valid in any coordinate system.

### 5.2.1 Black holes and gravitational lensing

In this work, we adopt geometrical units,  $G = M = c = 1$ , such that length and time scales are dimensionless. Hereafter  $M$  denotes the black hole mass, and setting  $M = 1$  is equivalent to rescaling the length scale to units of the gravitational radius,  $r_g := GM/c^2$ , and the time scale to units of  $r_g/c = GM/c^3$ . To rescale lengths and times to physical units, one simply scales  $r_g$  and  $r_g/c$  using the appropriate black hole mass. For Sgr A\* these scalings are given by  $r_g = 5.906 \times 10^{11}$  cm and  $r_g/c = 19.7$  seconds, respectively.

The line element in GR determines the separation between events in space-time, and is defined as:

$$ds^2 = g_{\mu\nu} dx^\mu dx^\nu, \quad (5.9)$$

where  $g_{\mu\nu}$  is the metric tensor and  $dx^\mu$  an infinitesimal displacement vector. The metric is a geometrical object that contains all the information concerning the space-time under consideration (in this study a rotating Kerr black hole) and is used to raise and lower tensor indices, e.g.,  $g_{\alpha\mu}A^{\mu\nu_1\nu_2\dots\nu_n} = A_\alpha^{\nu_1\nu_2\dots\nu_n}$ , where the Einstein summation convention is implicitly assumed. The line element for a rotating black hole is given by the Kerr metric Kerr (1963), which is written in Boyer-Lindquist coordinates  $x^\mu = (t, r, \theta, \phi)$  as:

$$ds^2 = - \left(1 - \frac{2r}{\Sigma}\right) dt^2 - \frac{4ar \sin^2 \theta}{\Sigma} dt d\phi + \frac{\Sigma}{\Delta} dr^2 + \Sigma d\theta^2 + \left(r^2 + a^2 + \frac{2ra^2 \sin^2 \theta}{\Sigma}\right) \sin^2 \theta d\phi^2, \quad (5.10)$$

where

$$\Delta := r^2 - 2r + a^2, \quad (5.11)$$

$$\Sigma := r^2 + a^2 \cos^2 \theta, \quad (5.12)$$

and  $a$  is the dimensionless spin parameter of the black hole.

In the above form, the Kerr metric has a coordinate singularity at the outer (and inner) event horizon, which presents difficulties for both the numerical GRMHD evolution and the GRRT calculations. This also prohibits the observer's camera from passing smoothly through this region. To avoid this we transform (5.10) from  $x^\mu$  into horizon-penetrating Kerr-Schild coordinates  $\tilde{x}^\mu = (\tilde{t}, \tilde{r}, \tilde{\theta}, \tilde{\phi})$  as:

$$\tilde{t} = t + \ln \Delta + 2\mathcal{R}, \quad \tilde{r} = r, \quad \tilde{\theta} = \theta, \quad \tilde{\phi} = \phi + a\mathcal{R}, \quad (5.13)$$

where

$$\mathcal{R} \equiv \frac{1}{r_{\text{out}} - r_{\text{in}}} \ln \left( \frac{r - r_{\text{out}}}{r - r_{\text{in}}} \right). \quad (5.14)$$

In eq. (5.14) the outer horizon is given by  $r_{\text{out}} \equiv 1 + \sqrt{1 - a^2}$ , and the inner horizon by  $r_{\text{in}} \equiv 1 - \sqrt{1 - a^2}$ . Hereafter the coordinate system employed in this study is the modified Kerr-Schild (MKS) system, denoted by  $X^\mu$ , which is related to the aforementioned Kerr-Schild coordinates,  $\tilde{x}^\mu$ , as:

$$X^0 = \tilde{t}, \quad X^1 = \ln \tilde{r}, \quad X^2 = \tilde{\theta}/\pi, \quad X^3 = \tilde{\phi}. \quad (5.15)$$

To visualize the effect of a moving camera compared to a stationary camera, we calculate light rays originating from both a stationary observer and a free-falling observer. This calculation is performed at two different positions, which in MKS coordinates are given by:

$$X_1^\mu = (0, \ln 10, 0, 0) \quad \text{and} \quad X_2^\mu = (0, \ln 3, 0, 0). \quad (5.16)$$

Consequently, the observer positions 1 and 2 correspond to radial distances of  $10 GM/c^2$  and  $3 GM/c^2$ , respectively. An observer at rest has a four-velocity of

$$u_0^\mu = (\alpha, 0, 0, 0), \quad (5.17)$$

where  $\alpha := (-g^{tt})^{-1/2}$  is the lapse function. At the positions  $X_1^\mu$  and  $X_2^\mu$  the free-falling observer has the following corresponding four-velocity components:

$$u_1^\mu = (1.10, -0.029, 0, -0.0011) \quad \text{and} \quad u_2^\mu = (1.34, -0.26, 0, -0.034). \quad (5.18)$$

The free-falling velocities were obtained by numerically integrating the geodesic equation for a free-falling massive particle.

To visualize the effect of the observer's motion on the observed field of view, we place a sphere around both the observer and the black hole, which is centered on the black hole. This is what we subsequently refer to as the "celestial sphere". The black hole spin is taken to be  $a = 0.9375$ , the exact value of the spin parameter for Sgr A\* is unknown; the chosen value was the best fit of a parameter survey Mościbrodzka et al. (2009). The observer is positioned in the equatorial plane of the black hole (i.e.,  $\theta = 90^\circ$ ), where the effects of gravitational lensing are most significant, and asymmetry in the shadow shape due to the rotational frame-dragging arising from the spin of the black hole is most pronounced.

Each quadrant of the celestial sphere is then painted with a distinct colour and lines of constant longitude and latitude are included to aid in the interpretation of the angular size and distortion of the resulting images. The celestial sphere in Minkowski spacetime, where we used cartesian coordinates to integrate the geodesics, as seen by an observer positioned at  $10 GM/c^2$  can be seen in Figure 5.1. The number of colored patches in the  $\theta$  and  $\phi$  directions is  $(n_\theta, n_\phi) = (8, 16)$ . Therefore, excluding the black lines of constant latitude and longitude (both  $1.08^\circ$  in width), each colored patch subtends an angle of  $22.5^\circ$  in both directions. We also calculated 25 light rays for each of these observers, distributing them equally over  $(\theta, \phi)$  in the frame of the observer (see bottom rows of Figs. 5.2 & 5.3) in order to interpret the geometrical lensing structure of the images in terms of their constituent light rays.

Figure 5.2 presents black hole shadow images and background lensing patterns for the Kerr black hole as seen by both a stationary observer (top panel) and a radially infalling observer (middle panel) located at a distance of  $10 GM/c^2$ . The angular size of the shadow is larger for the stationary observer. This observer, being in an inertial frame, is essentially accelerating such that the local gravitational acceleration of the black hole is precisely counteracted by the acceleration of their reference frame. This gives rise to a force on the observer directed away from the black hole itself, reducing the angular momentum of photons oriented towards the black hole (seen as the innermost four rays being bent around the horizon), effectively increasing the black hole's capture cross-section and producing a larger shadow. Strong gravitational lensing of the image due to the presence of the compact mass of the black hole is evident in the warping of the grid lines.

In Figure 5.3 the observers are now placed at  $3 GM/c^2$ , i.e., very close to the black hole. For the stationary observer, all photons within a field of view centered on the black hole of  $> 180^\circ$  in the horizontal direction and over the entire vertical direction, are captured by the black hole. Such an observer looking at the black hole would see nothing but the darkness of the black hole shadow in all directions. This is clear in the corresponding bottom-left plot of photon trajectories. As the observer approaches the event horizon, the entire celestial sphere begins to focus into an ever-shrinking point adjacent to the observer. For the infalling observer, the lensed image is far less extreme. Whilst the shadow presents a larger size in the observer's field of view, this is

mostly geometrical, i.e., due to the observer’s proximity to the black hole. There is also visible magnification of regions of the celestial sphere behind the observer. These results clearly follow from the photon trajectories in the bottom-right panel.

In all images of the shadow, repeated patches of decreasingly small area and identical colors are visible. In particular, multiple blue and yellow patches whose photons begin from behind the observer are visible near the shadow. These are a consequence of rays which perform one or more orbits of the black hole before reaching the observer, thereby appearing to originate from in front of the observer.

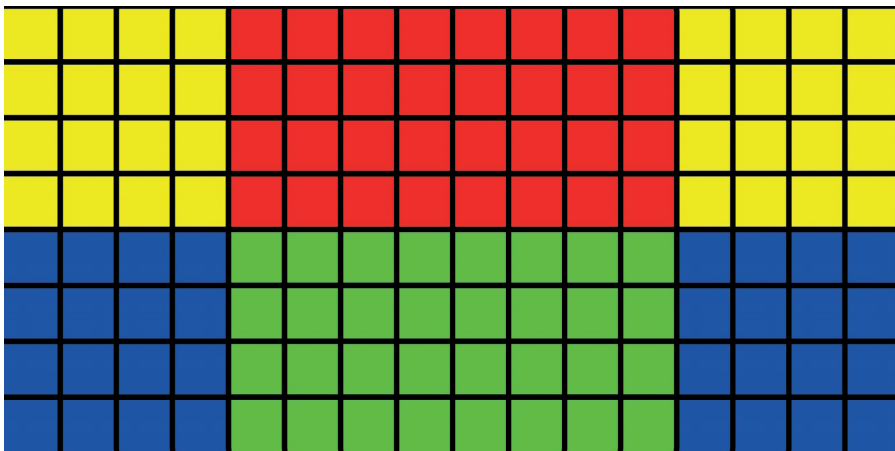


FIGURE 5.1: Celestial sphere in Minkowski spacetime for an observer at  $r = 10 GM/c^2$ . The different colors represent different quadrants of the sky, with yellow and blue being behind the observer, while red and green are in front of the observer. The black lines represent lines of constant longitude and latitude.

### 5.2.2 Camera trajectories

As described in Section 1, we consider two distinct phases for the camera trajectory. The first phase assumes a hovering observer positioned either at a fixed point or on a hovering trajectory around the black hole (i.e., the camera’s motion is unaffected by the plasma motion and is effectively in an inertial frame). For the second phase of the trajectory, the observer’s four-velocity is determined from an axisymmetric GRMHD simulation which includes tracer particles that follow the local plasma velocity. The choice to perform a separate tracer-particle simulation that is axisymmetric, in contrast to the 3D plasma simulation, was made to omit turbulent features in the  $\phi$  direction, which can be nauseating to watch in VR environments. This makes the movie scientifically less accurate, but is necessary to prevent viewers from experiencing motion sickness. Since the methods presented in this paper are not dependent on the dimensionality of the tracer particle simulation, they can be used for full 3D tracer particle simulations as well. In the following subsections, these two camera trajectories are described in detail.

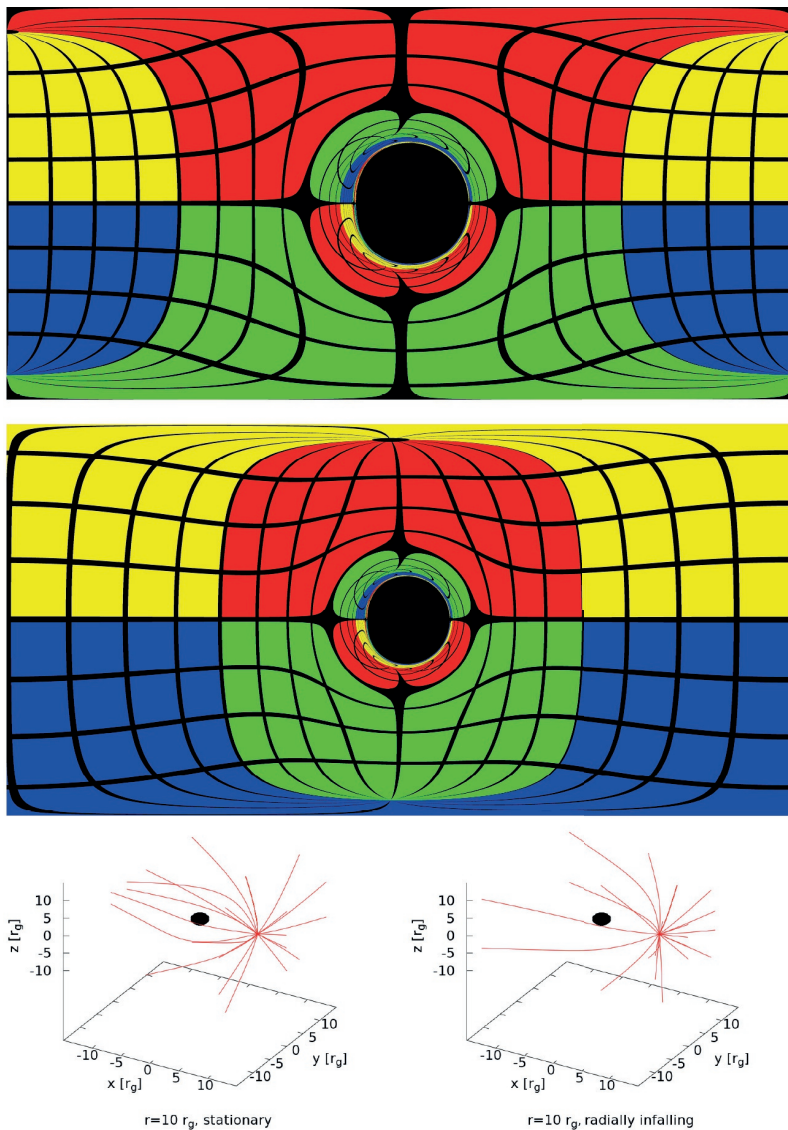


FIGURE 5.2: Celestial sphere and black hole shadow images for an observer located at  $r = 10 GM/c^2$ . Top panel: celestial sphere and shadow image as seen by a *stationary* observer. The different colors represent different quadrants of the sky, yellow and blue being behind the observer, while red and green are in front of the observer. The black lines represent lines of constant longitude and latitude while the black, circular region in the center is the black-hole shadow. Middle panel: as top panel, but seen by a *radially in-falling* observer. Bottom-left panel: photons originating from a stationary observer's camera, as used to generate the top panel. Bottom-right panel: photons originating from a radially in-falling observer's camera, as used to generate the middle panel. The black hole event horizon is shown as the black region in both bottom panels. The shadow sizes are similar in both panels, but differences are clearly visible. See the corresponding text for further discussion.

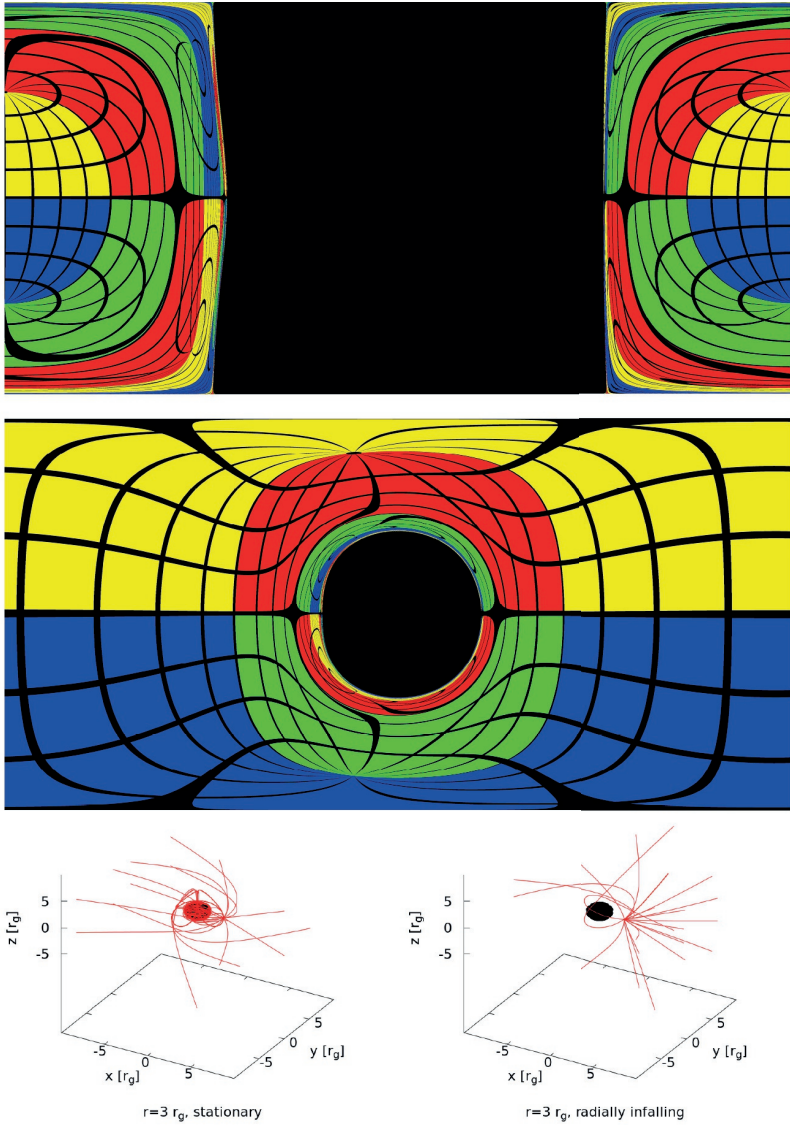


FIGURE 5.3: As in Fig. 5.2, now with the observer located at  $r = 3 GM/c^2$ . Differences between the shadow size and shape as seen by the two observers are now significant. See corresponding text for further discussion.

### 5.2.2.1 Hovering trajectory

In the first phase of the trajectory, the observer starts in a vacuum, with only the light from the distant background stars being considered in the calculation. The observer is initially at a radius of  $400 GM/c^2$  and moves inward to  $40 GM/c^2$ . After this, the observer rotates around the black hole, which we term the “initialization scene”, and comprises 1600 frames. Each frame is separated by a time interval of  $1 GM/c^3$ . The first phase of the movie, which includes the time-evolving accretion flow, consists of 2000 frames from the perspective of an observer at a radius of  $40 GM/c^2$  and an inclination of  $60^\circ$  with respect to the spin axis of the black hole. We refer to this first phase as “Scene 1”. We then subsequently rotate around the black hole whilst simultaneously moving inward to a radius of  $20 GM/c^2$  over a span of 1000 frames, which we refer to as “Scene 2”. Within Scene 2, after the first 500 frames, the observer then starts to decelerate until stationary once more.

### 5.2.2.2 Particle trajectory

For the second phase of the trajectory, the observer moves along a path that is calculated from an axisymmetric GRMHD simulation which includes tracer particles. The tracer particles act like test masses: their velocity is found by interpolating the local plasma four-velocity (which is stored in a grid-based data structure) to the position of the particle. A first-order Euler integration scheme is then employed to update the position of each particle. For the camera, we are concerned with particles that are initially located within the accretion disk, begin to accrete towards the black hole, and then subsequently leave the simulation domain via the jet. To identify particles that satisfy all of these conditions, we create a large sample of particle trajectories. The number of injected particles,  $\mathcal{N}_{\text{inj}}$ , within a grid cell with index  $\{i, j\}$  is set by two parameters: the plasma density,  $\rho$ , of the bounding cell, and the total mass,  $M_{\text{tot}}$ , within the simulation domain. The number of injected particles is then calculated as

$$\mathcal{N}_{\text{inj}}(i, j) = N_{\text{tot}} \left( \frac{\rho(i, j) V_{\text{cell}}}{M_{\text{tot}}} \right), \quad (5.19)$$

where the weight factor ensures that only a predefined number of particles,  $N_{\text{tot}}$ , after appropriate weighting, are then injected into a given simulation cell of volume  $V_{\text{cell}} = \sqrt{-g} dx^1 dx^2 dx^3$ , where  $g$  is the determinant of the metric tensor. The code then randomly distributes these particles inside the simulation cell. The particles are initially in Keplerian orbits and co-rotate with the accretion disk. The disk then quickly becomes turbulent due to the growth of the magneto-rotational instability (MRI). As the particles are advected with the flow, they can be classified into three different types:

1. *accreted particles* which leave the simulation at the inner radius (i.e., plunge into the event horizon) and remain gravitationally bound,
2. *wind particles* which become gravitationally unbound, travel through weakly magnetized regions and then exit the simulation at the outer boundary,
3. *accelerated jet particles*, which are similar to wind particles but additionally undergo rapid acceleration within the highly-magnetized jet sheath.

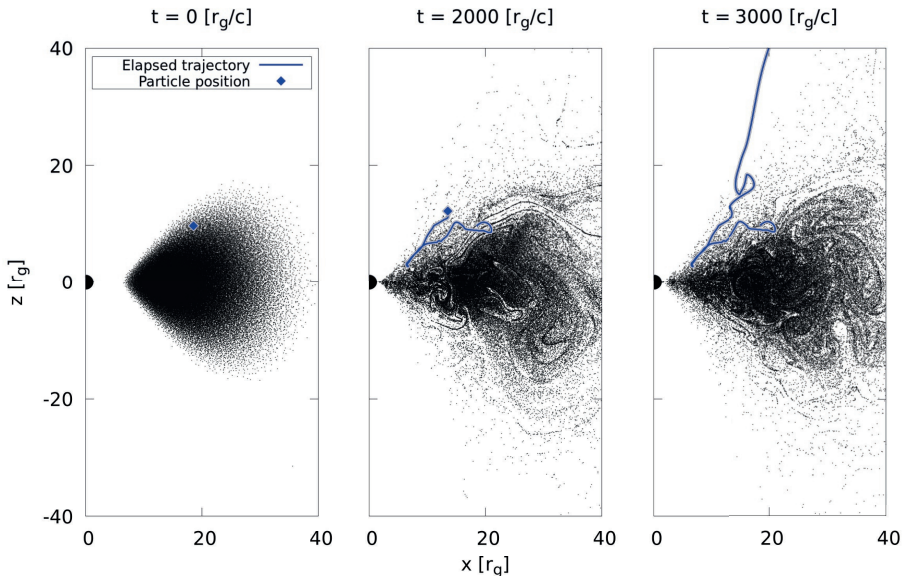


FIGURE 5.4: Left panel: initial distribution of particles inside the initial torus. Middle panel: snapshot of the advection HARM2D simulation at  $t = 2000 GM/c^3$ . Right panel: later snapshot at  $t = 4000 GM/c^3$ . The two times correspond to the advection simulation time, i.e., frames 4600–7600 in the resulting movie. The blue square represents the initial position of the tracer particle used for the camera. The blue curve shows the trajectory corresponding to this tracer particle.

To discriminate between these three types of particle, several key hydrodynamical and magneto-hydrodynamical criteria are examined. The first criterion is that the hydrodynamical Bernoulli parameter of the particle satisfies  $\text{Bern} = -hu_t > 1.02$ , where  $h$  is the (specific) enthalpy of the accretion flow and  $u_t$  is the covariant time component of the four-velocity. When this condition is satisfied, the particle is, by definition, unbound. The boundary transition between bound and unbound happens at  $\text{Bern} = -hu_t > 1.00$ , but we take a slightly larger value to select the part of the outflow that has a substantial relativistic velocity. A similar value for the Bernoulli parameter was used in e.g. Mościbrodzka et al. (2014); Davelaar et al. (2018c). The second criterion is that the particle resides in high magnetization regions where  $\sigma = B^2/\rho > 0.1$ , where  $B := \sqrt{b_\mu b^\mu}$  is the magnetic field strength and  $b^\mu$  is the magnetic field 4-vector. Satisfying this second criterion ensures that the particle ends up inside the jet sheath. The third criterion is that the particle's radial position is at a substantial distance from the black hole, typically  $r \gtrsim 300 GM/c^2$ , at the end of the simulation.

We simulate the particles with the axisymmetric GRMHD code HARM2D Gammie et al. (2003). The simulation begins with  $N_{\text{tot}} = 10^5$  particles, a simulation domain size of  $r_{\text{out}} = 1000 GM/c^2$ , and is evolved until  $t_{\text{final}} = 4000 GM/c^3$ . The spacetime is that of a Kerr black hole, and the dimensionless spin parameter is set to be  $a = 0.9375$ . For this value of the spin, the black hole (outer) event horizon radius is  $r_h = 1.344 GM/c^2$ , and the simulation inner boundary lies within

$r_h$  (i.e., we can track particles inside the event horizon). The specific particle used to initialize the camera trajectory is shown in Fig. 5.4 (blue square and curve). The full particle trajectory and velocity profile for all components of  $u^\mu$  are shown in Fig. 5.5. Rapid variations in the azimuthal 4-velocity,  $u^3$ , as well as the angular velocity,  $\Omega := u^3/u^0$ , in the right panel of Fig. 5.5 are consistent with the tightly wound trajectory in the left panel. This trajectory, which we term ‘‘Scene 3’’, begins immediately after Scene 2 (i.e. after frame 4600), and comprises 4000 frames, ending at frame 8599.

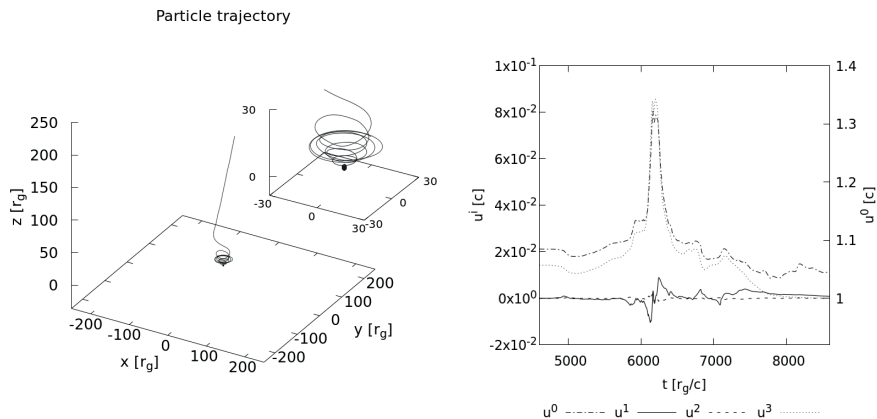


FIGURE 5.5: Left panel: the trajectory of the tracer particle that is used to initialize the camera trajectory. Right panel: the velocity profile of the tracer particle. The velocity peaks when the particle is closest to the black hole, where the angular velocity is high. The time shown on the x-axis is the time range of the frames used for Scene 3.

### 5.2.3 Radiative-transfer calculations and background images

To create images of an accreting black hole, it is necessary to compute the trajectories of light rays from the radiating plasma to the observer. For imaging applications, such as the present case, it is most computationally efficient to start the light rays at the observer instead - one for each pixel in the image the observer sees - and then trace them backward in time. Given a ray’s trajectory, the radiative-transfer equation is solved along that trajectory, in order to compute the intensity seen by the observer. The radiative-transfer code **RAPTOR** uses a fourth-order Runge-Kutta method to integrate the equations of motion for the light rays (i.e., the geodesic equation). It simultaneously solves the radiative-transfer equation using a semi-analytic scheme (for a more detailed description of **RAPTOR**, see Bronzwaer et al. (2018)). The same methodology is applied here in order to create images of the black hole accretion disk, with one small addition. When accretion disks, which tend to be roughly toroidal in shape, are filmed against a perfectly black background, the resulting animations fail to convey a natural sense of motion and scale for the observer as they orbit the black hole. In order to increase the immersiveness of the observer and provide a physically-realistic sense of scale and motion, the present work expands on the aforementioned radiative-transfer calculations by including an additional source of radiation in

the form of a background star-field that is projected onto the celestial sphere surrounding the black hole and observer.

This is achieved by expressing the intensity received by the observer in Lorentz-invariant form and integrating this intensity from the camera to its point of origin within the plasma, i.e., eq. (37) in (Bronzwaer et al., 2018). This can then be expressed in integral form (upon including a term for the background radiation) as

$$\frac{I_{\nu,\text{obs}}}{\nu_{\text{obs}}^3} = \left( \frac{I_{\nu,\infty}}{\nu_{\infty}^3} \right) e^{-\tau_{\nu,\text{obs}}(\lambda_{\infty})} + \int_{\lambda_{\text{obs}}}^{\lambda_{\infty}} \left( \frac{j_{\nu}}{\nu^2} \right) e^{-\tau_{\nu,\text{obs}}} d\lambda', \quad (5.20)$$

where the optical depth along the ray is calculated as

$$\tau_{\nu,\text{obs}}(\lambda) = \int_{\lambda_{\text{obs}}}^{\lambda} \nu \alpha_{\nu} d\lambda'. \quad (5.21)$$

Here,  $I_{\nu}$  describes a ray's specific intensity,  $\nu$  its frequency, and  $j_{\nu}$  and  $\alpha_{\nu}$  refer respectively to the plasma emission and absorption coefficients evaluated along the ray, which is itself parameterized by the affine parameter,  $\lambda$ . The subscript “ $\infty$ ” denotes quantities evaluated at the outer integration boundary (i.e., far from the black hole), while the subscript “obs” refers to the observer's current location. The background radiation is encoded in the term  $I_{\nu,\infty}/\nu_{\infty}^3$ . The first term on the right-hand-side of eq. (5.20) is constant and represents the intensity of the background radiation, weighted by the local optical depth. The second term on the right-hand-side of eq. (5.20) is evaluated at a given observer position,  $\lambda_{\text{obs}}$ , and specifies the accumulated intensity of emitted radiation after taking into account the local emissivity and absorptivity of the accreting plasma. See Fuerst & Wu (2004), Younsi et al. (2012), Bronzwaer et al. (2018) for further details.

A physical description of the radiation is needed for  $I_{\nu,\infty}/\nu_{\infty}^3$ . Since this quantity is projected onto the celestial sphere, it is a function of two coordinates ( $\hat{\theta}, \hat{\phi}$ ). Note that for the ray coordinates, in the limit  $r \rightarrow \infty$ , both  $\theta \rightarrow \hat{\theta}$  and  $\phi \rightarrow \hat{\phi}$ , i.e., space-time is asymptotically flat. We also note that only rays which exit the simulation volume (as opposed to rays which plunge towards the horizon) are assigned a non-zero background intensity after integration. In order to evaluate  $I_{\nu}$  for a given ray, we, therefore, take the ray's  $(\theta, \phi)$  coordinates *after* the ray leaves the simulation volume, and use them as the coordinates ( $\hat{\theta}, \hat{\phi}$ ) on the celestial sphere. Finally, we transform these coordinates into pixel coordinates  $(x, y)$  of a PNG image in order to evaluate the intensity. The transformation from celestial coordinates to pixel coordinates is given by

$$x = \left\lfloor \frac{\hat{\phi}}{2\pi} W \right\rfloor \quad \text{and} \quad y = \left\lfloor \frac{\hat{\theta}}{\pi} H \right\rfloor, \quad (5.22)$$

where  $\lfloor z \rfloor \equiv \text{floor}(z)$  is the floor function (which outputs the greatest integer  $\leq z$ ), and  $W$  and  $H$  are the width and height (in pixels) of the background image, respectively.

Using the scheme described above, it is possible to fold the background radiation field directly into the radiative transfer calculations of the accretion disk plasma. A second approach is to render separate movies for both the background and for the plasma, create a composite image for all corresponding time frames between the two movies in post-processing, and then create the new composite movie from the composite images. We adopt the second approach in all results shown in this paper.

We have chosen a background that is obtained from real astronomical star data from the Tycho 2 catalog, which are not in the Galactic Plane. The original equirectangular RGB 3K image was generated by Scott (2008) and converted to a greyscale 2K image.

### 5.2.4 Plasma and radiation models

In this work, we seek to model the SMBH Sgr A\*. To this end we use a black hole mass of  $M_{\text{BH}} = 4.0 \times 10^6 M_{\odot}$  Gillessen et al. (2009a), and a dimensionless spin parameter of  $a = 0.9375$ , consistent with the particle simulation. The plasma flow was simulated with the GRMHD code BHAC Porth et al. (2017). The simulation domain had an outer radius of  $r_{\text{outer}} = 1000 GM/c^2$ . The simulation is initialised with a Fishbone-Moncrief torus Fishbone & Moncrief (1976) with an inner radius of  $r_{\text{inner}} = 6 GM/c^2$ , and with a pressure maximum at  $r_{\text{max}} = 12 GM/c^2$ . Magnetic fields were inserted as poloidal loops that follow iso-contours of density, and the initial magnetization was low, i.e.,  $\beta = P_{\text{gas}}/B^2 = 100$ , where  $P_{\text{gas}}$  is the gas pressure of the plasma. The simulation was performed in three dimensions, with a resolution of 256, 128, 128 cells in the  $r$ ,  $\theta$ , and  $\phi$  directions, respectively. We simulated the flow up to  $t = 7000 GM/c^3$ .

The GRMHD simulation only simulates the dynamically-important ions (protons). We, therefore, require a prescription for the radiatively-important electrons in order to compute the observed emission. Most radiative models for Sgr A\* or M87 either assume that the coupling between the temperatures of the electrons and protons is constant or parameterised based on plasma variables, see e.g. Goldston et al. (2005b); Noble et al. (2007); Mościbrodzka et al. (2009); Dexter et al. (2010); Shcherbakov et al. (2012); Mościbrodzka & Falcke (2013); Mościbrodzka et al. (2014); Chan et al. (2015b,a); Gold et al. (2017). In this work we use, an electron model by Mościbrodzka et al. (2014) where the electrons are cold inside the accretion disk and hot inside the highly magnetized outflows. For the electron distribution function, we adopt a thermal distribution, where Davelaar et al. (2018c) showed that this model accurately describes the quiescent state of Sgr A\*. The used model Mościbrodzka et al. (2014) is capable of recovering the observational parameters of Sgr A\*, such as radio fluxes and intrinsic source sizes Falcke et al. (2000b); Bower et al. (2004); Doeleman et al. (2008); Bower et al. (2014).

We calculated the synthetic images at four different radio frequencies: 22 GHz (1.2 cm), 43 GHz (7 mm), 86 GHz (3 mm), and 230 GHz (1.3 mm). These frequencies were chosen since they correspond to the frequencies at which, e.g., the Very Long Baseline Array (VLBA) (1.2 mm, 7 mm, 3 mm), Global mm-VLBI Array (GMVA) (3 mm) and the Event Horizon Telescope (EHT) (1.3 mm) operate. After ray-tracing, these frequencies were converted into separate PNG image files, where distinct colormaps were chosen for each of the four frequencies. In post-processing, these images were then combined into a single image by averaging over the RGB channels of the four different input images. A star-field background was also included to serve as a reference point for the observer during their motion. This star-field background was rendered separately from the radio images, although the opacity at 22 GHz was used to obscure stars located behind the accretion disk. This background was then also averaged together with the radio images using the same RGB channel averaging. The four separate frequencies, the star-field background, and the resulting combined image are presented in Fig. 5.6.

### 5.3 VR movie

The resulting VR movie contains 8600 frames at a resolution of  $2000 \times 1000$  pixels. As a proof of concept, this resolution was chosen to balance image quality and computational resources. Current VR headsets also upscale the provided resolution with interpolation routines. We tested the resolution with the Oculus VR headset, which turned out to be sufficient. Since the provided methods are not limited by the resolution, a larger resolution can, in principle, be achieved. The movie is available on Youtube VR Davelaar et al. (2018a). In this section, we discuss several snapshots from this movie.

The first set of snapshots is shown in 5.7. In Fig. 5.7 we show a set of snapshots from Scene 1, (1600, 2300, 3000), matter starts to accrete onto the black hole, and the jet is launched. The jet then propagates through the ambient medium of the simulation, forming a collimated funnel that is mainly visible at lower frequencies. Since the accretion rate peaks at this point in the simulation (see Fig. 5.8), the black-hole shadow is barely visible.

In Fig. 5.9 we show snapshots from Scene 2 (3700, 4050, 4400), the jet propagates outward to the boundary of our simulation domain, the accretion rate settles and the black hole shadow becomes visible.

In Fig. 5.10 we show snapshot from Scene 3. When the observer moves along with the flow in Scene 3 (5100, 5800, 6150), small hot blobs of plasma orbiting the black hole are distinguishable. At the closest approach (around  $6 GM/c^2$ , frame 6150), the scene changes rapidly. This is not only due to the rapid rotation of the black hole but also to the rapid decrease of observed flux. It is hard to distinguish individual stars, and the only observable emission is at 230 GHz. At the end of Scene 3 (7200, 7900, 8599), the observer exits the accretion disk via the jet, whereafter, a rapid increase in radial velocity is clearly seen.

To obtain a better quantitative understanding of the movie we also calculate the total bolometric luminosity as received by the observer's camera. This is shown in the top panel of Fig. 5.11. At 6150 a decrease in luminosity is evident at the three lowest frequencies, which corresponds to where the observer is closest to the black hole event horizon and has entered the optically-thick accretion disk. A magnified version of this Figure in the optically-thick part is shown in the bottom panel of Fig. 5.11. A frame corresponding to this particular moment is shown in Fig. 5.10, panel 6150. At closest approach, the total luminosity detected at 230 GHz peaks, and the observer is exposed to  $\approx 25L_{\odot}$ .

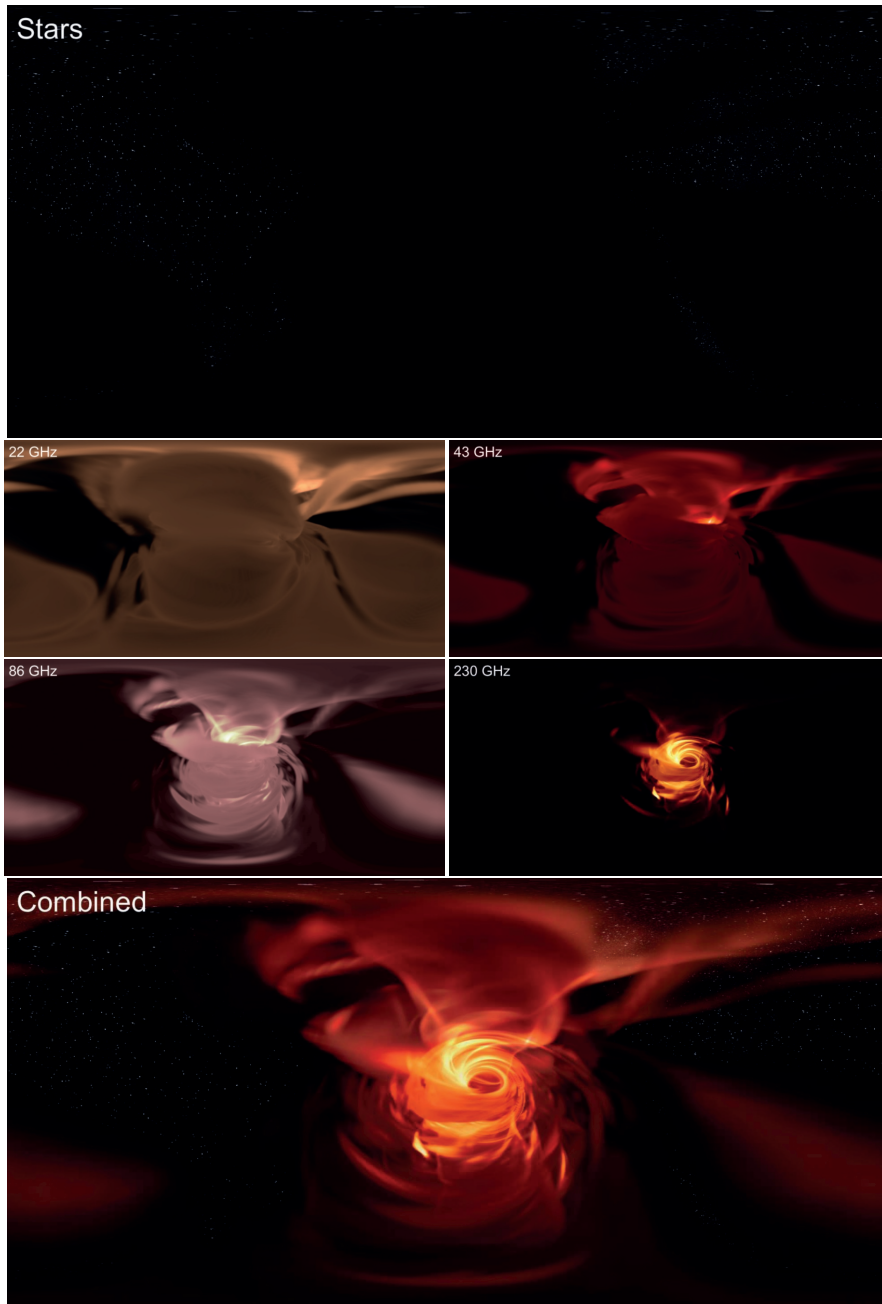


FIGURE 5.6: From left to right, top to bottom: snapshot panels at  $t = 3000 GM/c^3$  for: (i) background star field only image, (ii) 22 GHz image, (iii) 43 GHz image, (iv) 86 GHz image, (v) 230 GHz image, and (vi) combined (composite) image of (i)–(v).

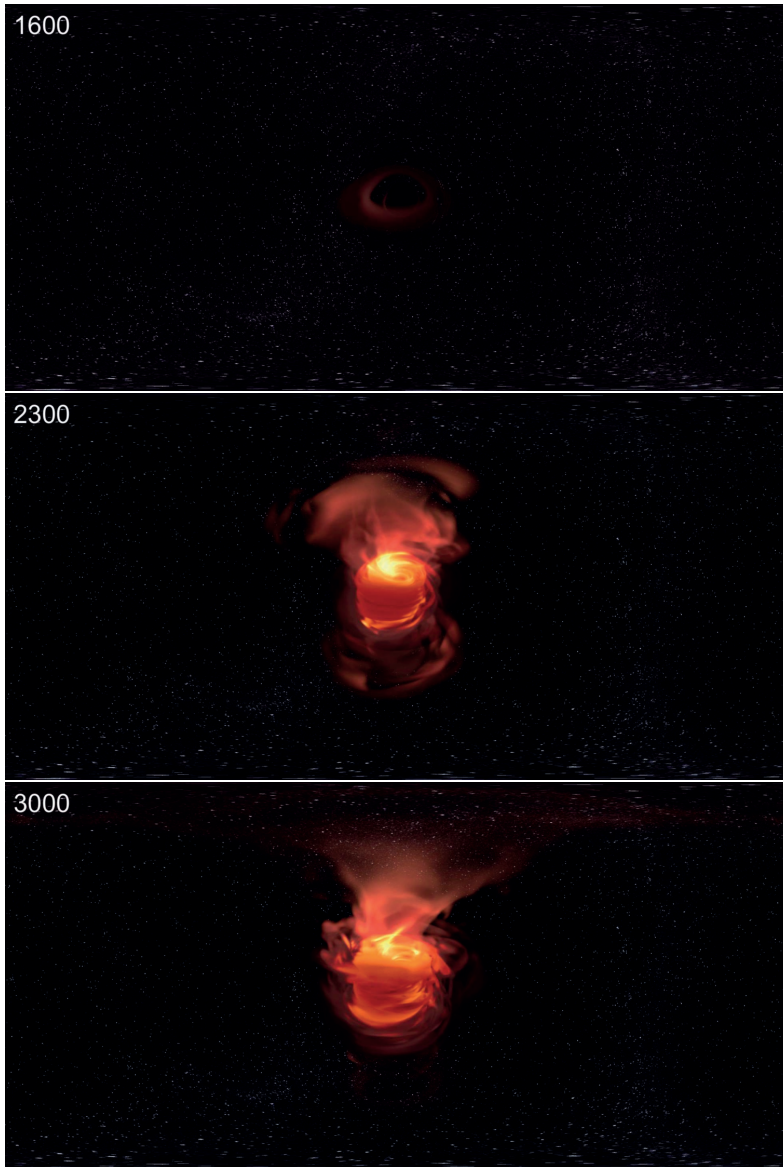


FIGURE 5.7: Movie snapshots from Scene 1. The simulation time (in units of  $GM/c^3$ ) is shown in the upper-left corner of all panels. From top to bottom: Scene 1 begins at frame 1600, where accretion onto the black hole has not yet begun, which can be seen as the faint, stationary equilibrium accretion torus configuration in the center of the image. By frame 2300 accretion has begun (see also Fig. 5.8) and the dim jet (upper half of image) and dimmer counter jet (lower half of image) propagate outwards through the ambient medium. At frame 3000, the jet has propagated further outwards, and angular momentum transport has shifted torus material outward, as can be seen by the increased angular size of the inner accretion flow. The black hole shadow is not visible since the accretion rate has yet to reach a quasi-stationary state.

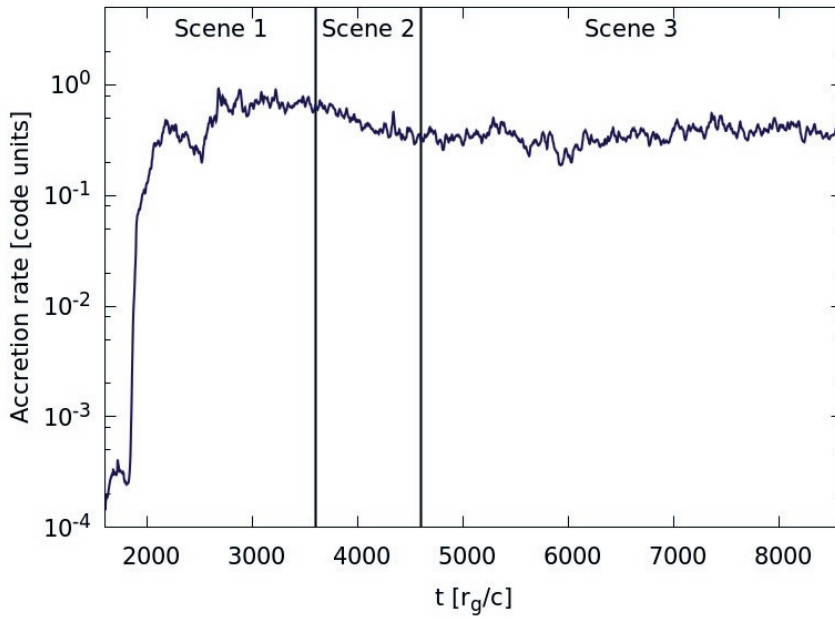


FIGURE 5.8: Simulation accretion rate as a function of time (in code units). At  $t=2500$  the MRI start to saturate. The time shown on the x-axis is the time of the frames used for “Scene 2” and “Scene 3”.

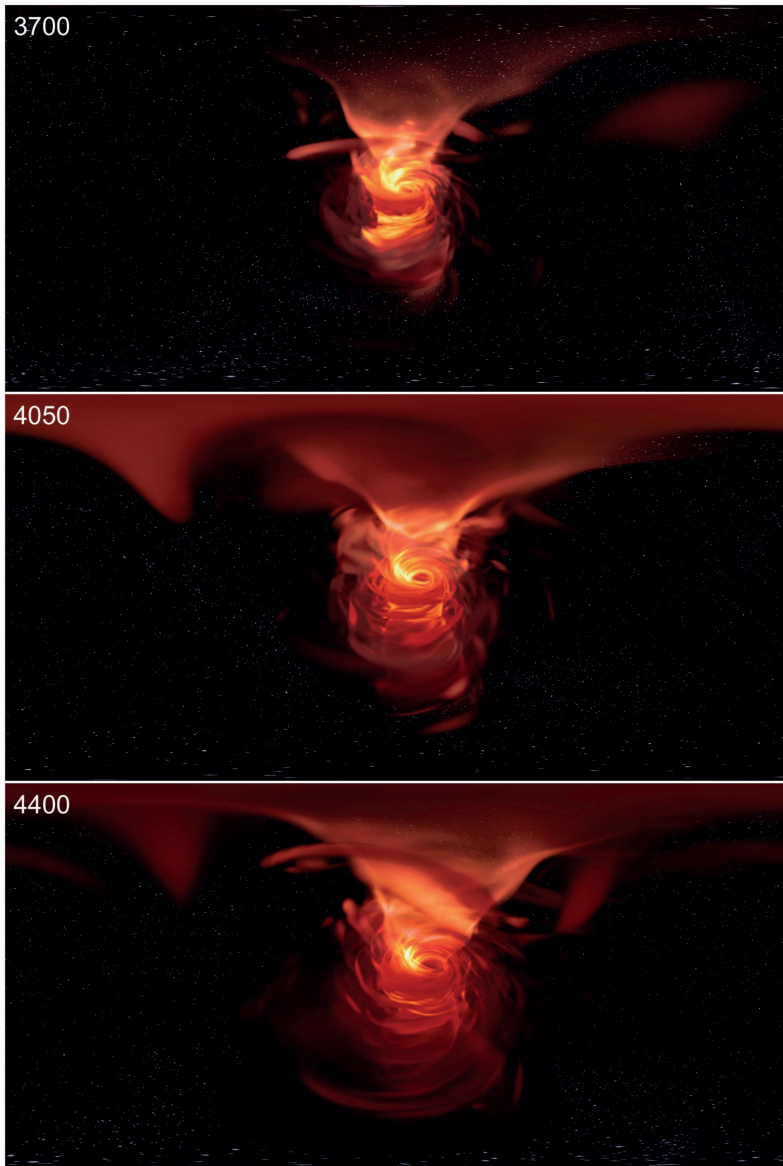


FIGURE 5.9: Movie snapshots from Scene 2. By frame 3700, the MRI has begun to saturate, and the accretion rate reaches a quasi-stationary state. At frame 4050 the jet and counter-jet have propagated further away from the black hole and reached the boundary of our simulation domain. Due to the steadier accretion rate, by frame 4400, the central region surrounding the event horizon becomes cooler and more optically thin. The upper half of the black-hole shadow is now visible.

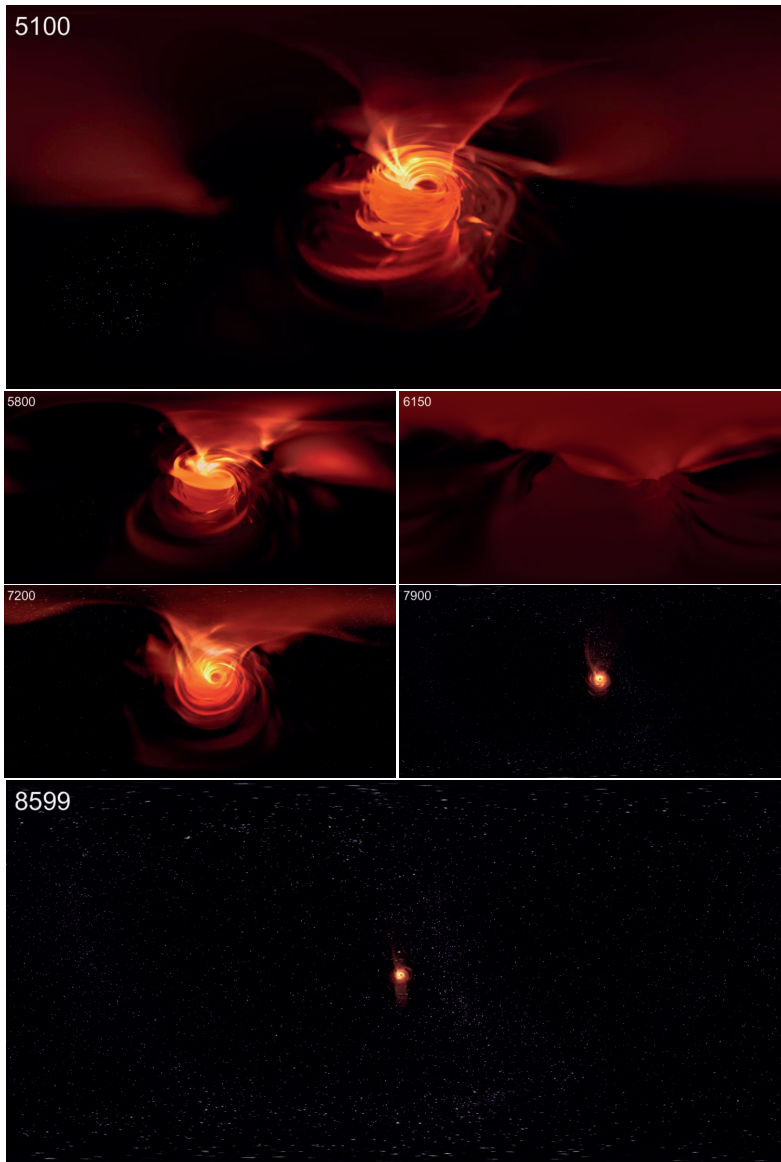


FIGURE 5.10: Movie snapshots from Scene 3. The observer now begins their journey through the accretion flow (panels with frames 5100–6150), before being advected away from the black hole via the large-scale jet (panels with frames 7200–8599). At frame 6150, the observer is at their point of closest approach to the black hole, where the incident flux is as high as  $\approx 25L_{\odot}$ . This region is highly optically thick, completely obscuring the observer’s view of the black hole shadow. As the observer is advected further away, by frame 8599 the angular size of the black hole and the surrounding accretion flow is greatly reduced and appears almost point-like.

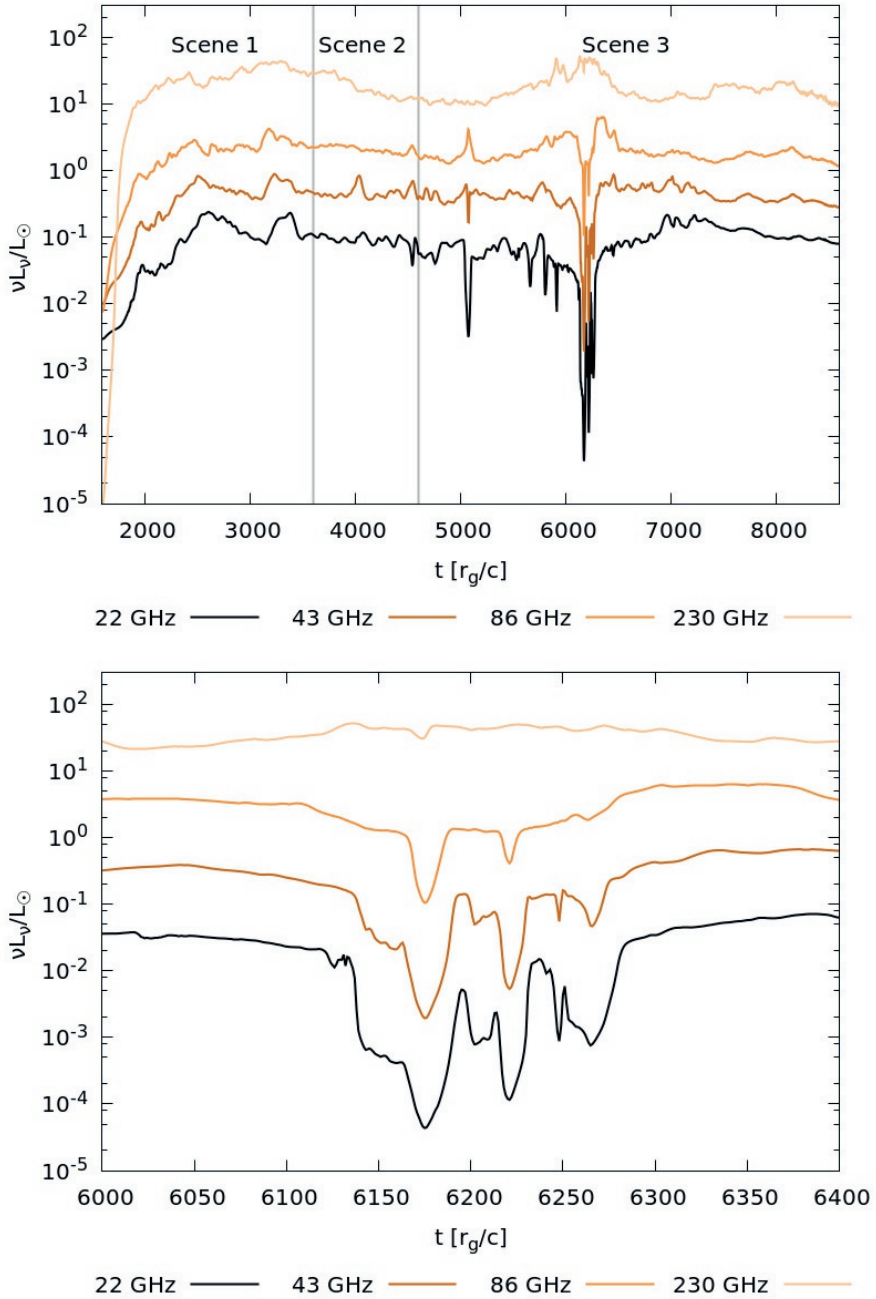


FIGURE 5.11: Top panel: total luminosity collected at the camera at each time step. Bottom panel: magnified view of the time range 6000–6400  $GM/c^3$ , where the camera passes through the optically thick part of the accreting plasma.

## 5.4 Discussion and conclusion

In this work, we have detailed our methods for visualizing the surroundings of accreting black holes in virtual reality. We presented a visualization of a three-dimensional fully-general-relativistic accreting black hole simulation in a full 360° VR movie with radiative models based on physically-realistic GRMHD plasma simulations. In order to produce representative images, the radiative-transfer capabilities of our code RAPTOR were extended to include background starlight and an observer in an arbitrary state of motion. To model the emission emerging from the vicinity of a black hole we coupled the GRMHD simulation with our radiative-transfer code to produce a VR movie based on our recent models for Sgr A\* Mościbrodzka et al. (2014); Davelaar et al. (2018c). These methods can be applied to accreting black holes of any size, so long as radiation feedback onto the accretion flow has a negligible impact on the flow’s magnetohydrodynamical properties.

The trajectory of the camera consisted of two phases: a hovering observer and an advected observer. For this second phase, we used an axisymmetric GRMHD simulation, in contrast to the plasma simulation used to calculate the radiation, which was fully-three-dimensional. This choice, whilst scientifically less accurate, was intentional and somewhat necessary. Turbulent features in the  $\phi$  direction were omitted since they can be nauseating to watch in VR environments and commonly lead to motion sickness. A composition of star-field and accretion flow images at four frequencies was then used to create a movie, consisting of 8600 frames, which is freely available on YouTube.

This movie couples GRMHD simulations with GRRT post-processing in VR. Since we do not make any strong a priori assumptions regarding the field-of-view of the observer, we can calculate the full radiation field measured at a specific point in the accretion disk, where we include all GR effects. This enabled us to calculate light curves of the total measured luminosity at multiple frequency bands at the position of a particle being advected in the flow. This way of calculating the full self-irradiation of the disk is of potential interest in, e.g., studies of X-ray reflection models in AGN, or coupling to GRMHD simulation to calculate the proper radiative feedback onto an emitting, absorbing (and even scattering) plasma in GR in a self-consistent way.

Finally, beyond the aforementioned scientific applications, VR represents a new medium for scientific visualization, which can be used, as demonstrated in this work, to investigate the emission that an observer would measure from *inside* the accretion flow. It is natural, and of contemporary interest even in the film industry (see e.g. James et al., 2015a,b) to ask the question as to what an observer would see if they were in the immediate vicinity of a black hole. In this work, we have sought to address this question directly by using state-of-the-art numerical techniques and astrophysical models in a physically-self-consistent manner. Given the EHTC is anticipated to obtain images of the black hole shadows in Sgr A\* and M87 in the near future, the calculations we have presented are timely. The VR movies presented in this work also provide an intuitive and interactive way to communicate black hole physics to wider audiences, serving as a useful educational tool.

**Acknowledgements**

The authors acknowledge support from the ERC Synergy Grant “BlackHoleCam: Imaging the Event Horizon of Black Holes” (Grant 610058). ZY acknowledges support from a Leverhulme Trust Early Career Fellowship. The authors thank Oliver Porth, Sera Markoff, Dimitrios Psaltis, Chi-Kwan Chan, Christiaan Brinkerink, Yosuke Mizuno, Luciano Rezzolla, and Robin Sip, for useful comments and discussions during this project. The GRMHD simulation was performed on the LOEWE computing facility at the CSC-Frankfurt, the advection simulation and radiative-transfer calculations were performed on the COMA computing facility at Radboud University Nijmegen. This research has made use of NASA’s Astrophysics Data System.

# BIBLIOGRAPHY

- Abbott, B. P., Abbott, R., Abbott, T. D., et al. 2016, *Phys. Rev. Lett.*, 116, 061102
- Abbott, B. P., Abbott, R., Abbott, T. D., et al. 2019, *Phys. Rev. X*, 9, 031040
- Abbott, B. P., Abbott, R., Abbott, T. D., et al. 2017, *Phys. Rev. Lett.*, 119, 161101
- Abdo, A., Ackermann, M., Ajello, M., et al. 2009, *The Astrophysical Journal*, 707, 55
- Abdujabbarov, A. A., Rezzolla, L., & Ahmedov, B. J. 2015, *Mon. Not. R. Astron. Soc.*, 454, 2423
- Abramowicz, M. A., Chen, X., Kato, S., Lasota, J.-P., & Regev, O. 1995, *ApJ*, 438, L37
- Abramowicz, M. A., Czerny, B., Lasota, J. P., & Szuszkiewicz, E. 1988, *ApJ*, 332, 646
- Abramowski, A., Acero, F., Aharonian, F., et al. 2012, *The Astrophysical Journal*, 746, 151
- Aharonian, F., Akhperjanian, A. G., Aye, K. M., et al. 2004, *A&A*, 425, L13
- Akiyama, K., Ikeda, S., Pleau, M., et al. 2017, *AJ*, 153, 159
- Akiyama, K., Lu, R.-S., Fish, V. L., et al. 2015, *ApJ*, 807, 150
- Albert, J., Aliu, E., Anderhub, H., et al. 2008, *The Astrophysical Journal Letters*, 685, L23
- Albert, J., Aliu, E., Anderhub, H., et al. 2006, *ApJ*, 638, L101
- Alves, E. P., Zrake, J., & Fiuza, F. 2018, *Phys. Rev. Lett.*, 121, 245101
- Anantua, R., Ressler, S., & Quataert, E. 2020, *MNRAS*, 493, 1404
- Anjiri, M., Mignone, A., Bodo, G., & Rossi, P. 2014, *MNRAS*, 442, 2228
- Appl, S., Lery, T., & Baty, H. 2000, *AAP*, 355, 818
- Archibald, A. M., Gusinskaia, N. V., Hessels, J. W. T., et al. 2018, *Nature*, 559, 73
- Baade, W. & Minkowski, R. 1954, *ApJ*, 119, 215
- Bacchini, F., Ripperda, B., Porth, O., & Sironi, L. 2019, *ApJS*, 240, 40
- Baganoff, F. K., Maeda, Y., Morris, M., et al. 2003, *The Astrophysical Journal*, 591, 891
- Balbus, S. A. & Hawley, J. F. 1991, *Astrophys. J.*, 376, 214
- Balbus, S. A. & Hawley, J. F. 1991, *ApJ*, 376, 214
- Balbus, S. A. & Hawley, J. F. 1998, *Reviews of Modern Physics*, 70, 1
- Balick, B. & Brown, R. L. 1974, *ApJ*, 194, 265
- Ball, D., Özel, F., Psaltis, D., & Chan, C.-k. 2016, *ApJ*, 826, 77
- Ball, D., Sironi, L., & Özel, F. 2018, *ApJ*, 862, 80
- Bambi, C., Freese, K., Harada, T., Takahashi, R., & Yoshida, N. 2009, *Phys. Rev. D*, 80, 104023
- Bardeen, J. M. 1973, in *Black Holes (Les Astres Occlus)*, eds. C. Dewitt & B. S. Dewitt, 241–289

## BIBLIOGRAPHY

- Bardeen, J. M. & Petterson, J. A. 1975, *The Astrophysical Journal*, 195, L65
- Bardeen, J. M., Press, W. H., & Teukolsky, S. A. 1972, *ApJ*, 178, 347
- Begelman, M. C. 1979, *MNRAS*, 187, 237
- Begelman, M. C. 1998, *ApJ*, 493, 291
- Biretta, J. A., Sparks, W. B., & Macchetto, F. 1999, *The Astrophysical Journal*, 520, 621
- Blandford, R. D. & Königl, A. 1979, *ApJ*, 232, 34
- Blandford, R. D. & Payne, D. G. 1982, *MNRAS*, 199, 883
- Blandford, R. D. & Znajek, R. L. 1977, *MNRAS*, 179, 433
- Bodo, G., Mamatsashvili, G., Rossi, P., & Mignone, A. 2013, *MNRAS*, 434, 3030
- Bolton, C. T. 1972, *Nature*, 235, 271
- Bolton, J. G., Stanley, G. J., & Slee, O. B. 1949, *Nature*, 164, 101
- Bondi, H. 1952, *Monthly Notices of the Royal Astronomical Society*, 112, 195
- Boris, J. P. 1970, in *Proc. Fourth Conf. Num. Sim. Plasmas*, 3–67
- Bower, G. C., Falcke, H., Herrnstein, R. M., et al. 2004, *Science*, 304, 704
- Bower, G. C., Goss, W. M., Falcke, H., Backer, D. C., & Lithwick, Y. 2006, *ApJ*, 648, L127
- Bower, G. C., Markoff, S., Brunthaler, A., et al. 2014, *ApJ*, 790, 1
- Bower, G. C., Markoff, S., Dexter, J., et al. 2015, *ApJ*, 802, 69
- Bowyer, S., Byram, E. T., Chubb, T. A., & Friedman, H. 1965, *Science*, 147, 394
- Braes, L. L. E. & Miley, G. K. 1971, *Nature*, 232, 246
- Bremer, M., Witzel, G., Eckart, A., et al. 2011, *A&A*, 532, A26
- Brinkerink, C. D., Müller, C., Falcke, H., et al. 2016, *MNRAS*, 462, 1382
- Broderick, A. E. 2006, *MNRAS*, 366, L10
- Broderick, A. E., Fish, V. L., Doeleman, S. S., & Loeb, A. 2009, *ApJ*, 697, 45
- Broderick, A. E., Fish, V. L., Johnson, M. D., et al. 2016, *ApJ*, 820, 137
- Broderick, A. E., Gold, R., Karami, M., et al. 2020, *ApJ*, submitted
- Broderick, A. E., Narayan, R., Kormendy, J., et al. 2015, *ApJ*, 805, 179
- Bromberg, O., Singh, C. B., Davelaar, J., & Philippov, A. A. 2019, *ApJ*, 884, 39
- Bromberg, O. & Tchekhovskoy, A. 2016, *MNRAS*, 456, 1739
- Bronzwaer, T., Davelaar, J., Younsi, Z., et al. 2018, *A&A*, 613, A2
- Brown, R. L. 1982, *ApJ*, 262, 110
- Bucciantini, N. & Del Zanna, L. 2013, *MNRAS*, 428, 71
- Capellupo, D. M., Haggard, D., Choux, N., et al. 2017, *ApJ*, 845, 35
- Cerutti, B., Philippov, A., Parfrey, K., & Spitkovsky, A. 2015, *MNRAS*, 448, 606
- Cerutti, B., Philippov, A. A., & Spitkovsky, A. 2016, *MNRAS*, 457, 2401
- Cerutti, B., Werner, G. R., Uzdensky, D. A., & Begelman, M. C. 2013, *The Astrophysical Journal*, 770, 147
- Cerutti, B., Werner, G. R., Uzdensky, D. A., & Begelman, M. C. 2014, *ApJ*, 782, 104
- Chael, A., Narayan, R., & Johnson, M. D. 2019, *MNRAS*, 486, 2873
- Chael, A., Rowan, M., Narayan, R., Johnson, M., & Sironi, L. 2018a, *MNRAS*, 478, 5209
- Chael, A. A., Johnson, M. D., Bouman, K. L., et al. 2018b, *ApJ*, 857, 23
- Chael, A. A., Johnson, M. D., Narayan, R., et al. 2016, *ApJ*, 829, 11
- Chael, A. A., Narayan, R., & Sađowski, A. 2017, *MNRAS*, 470, 2367

- Chan, C.-k., Medeiros, L., Özel, F., & Psaltis, D. 2018, *ApJ*, 867, 59
- Chan, C.-k., Psaltis, D., & Özel, F. 2013, *ApJ*, 777, 13
- Chan, C.-K., Psaltis, D., Özel, F., et al. 2015a, *ApJ*, 812, 103
- Chan, C.-K., Psaltis, D., Özel, F., Narayan, R., & Sądowski, A. 2015b, *ApJ*, 799, 1
- Chandra, M., Gammie, C. F., Foucart, F., & Quataert, E. 2015, *ApJ*, 810, 162
- Chatterjee, K., Liska, M., Tchekhovskoy, A., & Markoff, S. B. 2019, *MNRAS*, 490, 2200
- Chen, X., Abramowicz, M. A., Lasota, J.-P., Narayan, R., & Yi, I. 1995, *ApJ*, 443, L61
- Childs, H., Brugger, E. S., Bonnell, K. S., et al. 2005, *IEEE Visualization 2005*, 190
- Chirenti, C. B. M. H. & Rezzolla, L. 2007, *Classical and Quantum Gravity*, 24, 4191
- Christie, I. M., Petropoulou, M., Sironi, L., & Giannios, D. 2019, *MNRAS*, 482, 65
- Clark, B. G. 1980, *A&A*, 89, 377
- Clark, B. G. 2003, *Astronomical Society of the Pacific Conference Series*, Vol. 300, *A Review of the History of VLBI*, eds. J. A. Zensus, M. H. Cohen, & E. Ros, 1
- Clemence, G. M. 1947, *Rev. Mod. Phys.*, 19, 361
- Clerk Maxwell, J. 1865, *Philosophical Transactions of the Royal Society of London Series I*, 155, 459
- Comisso, L. & Sironi, L. 2018, *Physical Review Letters*, 121, 255101
- Crinquad, B., Cerutti, B., Philippov, A. e., Parfrey, K., & Dubus, G. 2020, *Phys. Rev. Lett.*, 124, 145101
- Cunningham, C. T. & Bardeen, J. M. 1973, *ApJ*, 183, 237
- Curtis, H. D. 1918, *Publications of Lick Observatory*, 13, 9
- Das, U. & Begelman, M. C. 2019, *MNRAS*, 482, 2107
- Davelaar, J., Bonzwaer, T., Kok, D., et al. 2018a, *Observing Supermassive Black Holes in Virtual Reality*, <https://www.youtube.com/watch?v=SXN4hvp977s>
- Davelaar, J., Bronzwaer, T., Kok, D., et al. 2018b, *Computational Astrophysics and Cosmology*, 5, 1
- Davelaar, J., Mościbrodzka, M., Bronzwaer, T., & Falcke, H. 2018c, *A&A*, 612, A34
- de Gasperin, F., Orrú, E., Murgia, M., et al. 2012, *A&A*, 547, A56
- De Villiers, J.-P. & Hawley, J. F. 2003, *ApJ*, 589, 458
- Decker, R. B. & Krimigis, S. M. 2003, *Advances in Space Research*, 32, 597
- Del Zanna, L. & Bucciantini, N. 2018, *MNRAS*, 479, 657
- Del Zanna, L., Papini, E., Landi, S., Bugli, M., & Bucciantini, N. 2016, *MNRAS*, 460, 4
- Del Zanna, L., Zanotti, O., Bucciantini, N., & Londrillo, P. 2007, *A&A*, 473, 11
- Dexter, J. 2016, *MNRAS*, 462, 115
- Dexter, J. & Agol, E. 2009, *ApJ*, 696, 1616
- Dexter, J., Agol, E., Fragile, P. C., & McKinney, J. C. 2010, *ApJ*, 717, 1092
- Dexter, J., Agol, E., Fragile, P. C., & McKinney, J. C. 2012a, in *Journal of Physics Conference Series*, Vol. 372, *Journal of Physics Conference Series*, 012023
- Dexter, J., McKinney, J. C., & Agol, E. 2012b, *MNRAS*, 421, 1517
- Dibi, S., Drapeau, S., Fragile, P. C., Markoff, S., & Dexter, J. 2012, *MNRAS*, 426, 1928
- Dionysopoulou, K., Alic, D., Palenzuela, C., Rezzolla, L., & Giacomazzo, B. 2013, *Phys. Rev. D*, 88, 044020

## BIBLIOGRAPHY

- Do, T., Ghez, A. M., Morris, M. R., et al. 2009, *ApJ*, 691, 1021
- Do, T., Hees, A., Ghez, A., et al. 2019, *Science*, 365, 664
- Do, T., Witzel, G., Gautam, A. K., et al. 2019, arXiv preprint arXiv:1908.01777
- Dodds-Eden, K., Porquet, D., Trap, G., et al. 2009, *ApJ*, 698, 676
- Doeleman, S. S., Fish, V. L., Schenck, D. E., et al. 2012, *Science*, 338, 355
- Doeleman, S. S., Weintroub, J., Rogers, A. E. E., et al. 2008, *Nature*, 455, 78
- Drake, J. F., Swisdak, M., Che, H., & Shay, M. A. 2006, *Nature*, 443, 553
- Drappeau, S., Dibi, S., Dexter, J., Markoff, S., & Fragile, P. C. 2013, *MNRAS*, 431, 2872
- Drenkhahn, G. & Spruit, H. C. 2002, *A&A*, 391, 1141
- Duck, R. C., Browning, P. K., Cunningham, G., et al. 1997, *Plasma Physics and Controlled Fusion*, 39, 715
- Dungey, J. W. 1961, *Phys. Rev. Lett.*, 6, 47
- Dyson, F. W., Eddington, A. S., & Davidson, C. 1920, *Philosophical Transactions of the Royal Society of London. Series A, Containing Papers of a Mathematical or Physical Character*, 220, 291
- Eckart, A., Baganoff, F., Morris, M., et al. 2004, *A&A*, 427, 1
- Eckart, A. & Genzel, R. 1997, *MNRAS*, 284, 576
- Einstein, A. 1915, *Sitzung der physikalische-mathematischen Klasse*, 25, 844
- Einstein, A. 1916, *Annalen der Physik*, 354, 769
- Einstein, A. et al. 1905, *Annalen der physik*, 17, 891
- Event Horizon Telescope Collaboration, Akiyama, K., Alberdi, A., et al. 2019a, *ApJ*, 875, L1
- Event Horizon Telescope Collaboration, Akiyama, K., Alberdi, A., et al. 2019b, *ApJ*, 875, L2
- Event Horizon Telescope Collaboration, Akiyama, K., Alberdi, A., et al. 2019c, *ApJ*, 875, L3
- Event Horizon Telescope Collaboration, Akiyama, K., Alberdi, A., et al. 2019d, *ApJ*, 875, L4
- Event Horizon Telescope Collaboration, Akiyama, K., Alberdi, A., et al. 2019e, *ApJ*, 875, L5
- Event Horizon Telescope Collaboration, Akiyama, K., Alberdi, A., et al. 2019f, *ApJ*, 875, L6
- Falcke, H. & Biermann, P. L. 1995, *A&A*, 293, 665
- Falcke, H., Goss, W. M., Matsuo, H., et al. 1998, *ApJ*, 499, 731
- Falcke, H., Melia, F., & Agol, E. 2000a, 522, 317
- Falcke, H., Melia, F., & Agol, E. 2000b, *ApJ*, 528, L13
- Fishbone, L. G. & Moncrief, V. 1976, *ApJ*, 207, 962
- Fromm, C. M., Younsi, Z., Baczko, A., et al. 2019, *A&A*, 629, A4
- Fuerst, S. V. & Wu, K. 2004, *Astron. Astrophys.*, 424, 733
- Furth, H. P., Killeen, J., & Rosenbluth, M. N. 1963, *Physics of Fluids*, 6, 459
- Gammie, C. F., McKinney, J. C., & Tóth, G. 2003, *ApJ*, 589, 444
- Gammie, C. F. & Popham, R. 1998, *ApJ*, 498, 313
- Gebhardt, K., Adams, J., Richstone, D., et al. 2011, *ApJ*, 729, 119
- Genzel, R., Schödel, R., Ott, T., et al. 2003, *Nature*, 425, 934
- Ghez, A. M., Klein, B. L., Morris, M., & Becklin, E. E. 1998, *ApJ*, 509, 678
- Ghez, A. M., Salim, S., Weinberg, N. N., et al. 2008, *ApJ*, 689, 1044
- Giannios, D. 2013, *MNRAS*, 431, 355
- Giannios, D. & Spruit, H. C. 2006, *A&A*, 450, 887

- Gillessen, S., Eisenhauer, F., Fritz, T. K., et al. 2009a, *ApJ*, 707, L114
- Gillessen, S., Eisenhauer, F., Trippe, S., et al. 2009b, *ApJ*, 692, 1075
- Goddi, C., Falcke, H., Kramer, M., et al. 2017, *International Journal of Modern Physics D*, 26, 1730001
- Gold, R., McKinney, J. C., Johnson, M. D., & Doeleman, S. S. 2017, *ApJ*, 837, 180
- Goldston, J. E., Quataert, E., & Igumenshchev, I. V. 2005a, *ApJ*, 621, 785
- Goldston, J. E., Quataert, E., & Igumenshchev, I. V. 2005b, *ApJ*, 621, 785
- Gravity Collaboration, Abuter, R., Amorim, A., et al. 2018, *A&A*, 618, L10
- Gravity Collaboration, Abuter, R., Amorim, A., et al. 2019, *A&A*, 625, L10
- GRAVITY Collaboration, Abuter, R., Amorim, A., et al. 2020, arXiv e-prints, arXiv:2004.07187
- Greenstein, J. L. 1963, *Nature*, 197, 1041
- Grenzebach, A. 2016, *The Shadow of Black Holes* (Springer International Publishing)
- Guo, F., Li, H., Daughton, W., & Liu, Y.-H. 2014, *Physical Review Letters*, 113, 155005
- Hada, K., Doi, A., Kino, M., et al. 2011, *Nature*, 477, 185
- Hada, K., Kino, M., Doi, A., et al. 2016, *ApJ*, 817, 131
- Hada, K., Kino, M., Doi, A., et al. 2013, *ApJ*, 775, 70
- Hamilton, A. 1998, *Falling Into a Black Hole*, <http://jila.colorado.edu/~ajsh/insidebh/intro.html>, accessed: 2018-05-20
- Harris, D. E., Cheung, C. C., Stawarz, Ł., Biretta, J. A., & Perlman, E. S. 2009, *ApJ*, 699, 305
- Hawley, J. F., Gammie, C. F., & Balbus, S. A. 1995, *ApJ*, 440, 742
- Hawley, J. F., Smarr, L. L., & Wilson, J. R. 1984, *ApJ*, 277, 296
- Hazard, C., Mackey, M. B., & Shimmings, A. J. 1963, *Nature*, 197, 1037
- Heavens, A. F. & Drury, L. O. 1988, *MNRAS*, 235, 997
- Hey, J. S., Parsons, S. J., & Phillips, J. W. 1946, *Nature*, 158, 234
- Hillas, A. M. 1984, *ARA&A*, 22, 425
- Hjellming, R. M. & Wade, C. M. 1971, *ApJ*, 168, L21
- Högbom, J. A. 1974, *A&AS*, 15, 417
- Howes, G. G. 2010, *Monthly Notices of the Royal Astronomical Society: Letters*, 409, L104
- Hoyle, F. 1966, *Nature*, 209, 751
- Hoyle, F. & Fowler, W. A. 1963a, *Nature*, 197, 533
- Hoyle, F. & Fowler, W. A. 1963b, *MNRAS*, 125, 169
- Hoyle, F. & Lyttleton, R. A. 1941, *Monthly Notices of the Royal Astronomical Society*, 101, 227
- Hu, M. 1962, *IRE Transactions on Information Theory*, 8, 179
- Hunter, J. D. 2007, *Computing in Science and Engineering*, 9, 90
- Ichimaru, S. 1977, *ApJ*, 214, 840
- Issaoun, S., Johnson, M. D., Blackburn, L., et al. 2019, *ApJ*, 871, 30
- James, O., von Tunzelmann, E., Franklin, P., & Thorne, K. S. 2015a, *Classical and Quantum Gravity*, 32, 065001
- James, O., von Tunzelmann, E., Franklin, P., & Thorne, K. S. 2015b, *American Journal of Physics*, 83, 486
- Janssen, M., Goddi, C., van Bemmelen, I. M., et al. 2019, *A&A*, 626, A75
- Jennison, R. C. & Das Gupta, M. K. 1953, *Nature*, 172, 996

## BIBLIOGRAPHY

- Johannsen, T. 2013, *ApJ*, 777, 170
- Johannsen, T. & Psaltis, D. 2010, *ApJ*, 718, 446
- Jones, E., Oliphant, T., Peterson, P., et al. 2001, *SciPy: Open source scientific tools for Python*, [Online]
- Junor, W., Biretta, J. A., & Livio, M. 1999, *Nature*, 401, 891
- Kellermann, K. I. & Moran, J. M. 2001, *ARA&A*, 39, 457
- Kelly, B. J., Baker, J. G., Etienne, Z. B., Giacomazzo, B., & Schnittman, J. 2017, *Phys. Rev. D*, 96, 123003
- Kerr, R. P. 1963, *Physical Review Letters*, 11, 237
- Kim, J.-Y., Krichbaum, T. P., Broderick, A. E., et al. 2020, *A&A*, Forthcoming article
- Kim, J. Y., Krichbaum, T. P., Lu, R. S., et al. 2018, *A&A*, 616, A188
- Kirk, J. G. & Skjaraasen, O. 2003, *The Astrophysical Journal*, 591, 366
- Krichbaum, T. P., Graham, D. A., Bremer, M., et al. 2006, in *Journal of Physics Conference Series*, Vol. 54, *Journal of Physics Conference Series*, eds. R. Schödel, G. C. Bower, M. P. Muno, S. Nayakshin, & T. Ott, 328–334
- Krichbaum, T. P., Graham, D. A., Witzel, A., et al. 1998, *A&A*, 335, L106
- Kunz, M. W., Stone, J. M., & Quataert, E. 2016, *Physical Review Letters*, 117, 235101
- Laplace, P.-S. 1796
- Lense, J. & Thirring, H. 1918, *Physikalische Zeitschrift*, 19, 156
- Leung, P. K., Gammie, C. F., & Noble, S. C. 2011, *ApJ*, 737, 21
- Levinson, A. & Cerutti, B. 2018, *A&A*, 616, A184
- LIGO Scientific Collaboration & Virgo Collaboration. 2016, *Phys. Rev. Lett.*, 116, 061102
- Liska, M., Hesp, C., Tchekhovskoy, A., et al. 2018, *MNRAS*, 474, L81
- Livadiotis, G. & McComas, D. J. 2009, *Journal of Geophysical Research (Space Physics)*, 114, A11105
- Livadiotis, G. & McComas, D. J. 2013, *Space Science Reviews*, 175, 183
- Löhner, R. 1987, *Computer Methods in Applied Mechanics and Engineering*, 61, 323
- Londrillo, P. & Del Zanna, L. 2000, *ApJ*, 530, 508
- Loureiro, N. F., Schekochihin, A. A., & Cowley, S. C. 2007, *Physics of Plasmas*, 14, 100703
- Low, B. & Wolfson, R. 1988, *The Astrophysical Journal*, 324, 574
- Luminet, J.-P. 2011, *Color Animation of a Black Hole with Accretion Disk*, <https://www.youtube.com/watch?v=5Oqop50ltrM>, accessed: 2018-05-20
- Luminet, J.-P. 1979, *A&A*, 75, 228
- Lüst, R. 1952, *Zeitschrift Naturforschung Teil A*, 7, 87
- Ly, C., Walker, R. C., & Wrobel, J. M. 2004, *AJ*, 127, 119
- Lynden-Bell, D. 1969, *Nature*, 223, 690
- Lynden-Bell, D. & Rees, M. J. 1971, *MNRAS*, 152, 461
- Lyubarskii, Y. E. 1999, *MNRAS*, 308, 1006
- Lyubarsky, Y. & Kirk, J. G. 2001, *ApJ*, 547, 437
- Lyutikov, M. & Blandford, R. 2003, *arXiv e-prints*, astro
- Madore, D. 2011, *Kerr black holes images and videos*, <http://www.madore.org/~david/math/kerr.html>, accessed: 2018-05-20

- Mao, S. A., Dexter, J., & Quataert, E. 2017, *MNRAS*, 466, 4307
- Markoff, S., Bower, G. C., & Falcke, H. 2007, *MNRAS*, 379, 1519
- Markoff, S., Nowak, M., Young, A., et al. 2008, *ApJ*, 681, 905
- Marshall, H. L., Miller, B. P., Davis, D. S., et al. 2002, *The Astrophysical Journal*, 564, 683
- Massaglia, S., Bodo, G., Rossi, P., Capetti, S., & Mignone, A. 2016, *A&A*, 596, A12
- Mayer-Hasselwander, H. A., Bertsch, D. L., Dingus, B. L., et al. 1998, *A&A*, 335, 161
- McKinney, J. C. & Blandford, R. D. 2009, *MNRAS*, 394, L126
- McKinney, J. C., Tchekhovskoy, A., & Blandford, R. D. 2012, *Monthly Notices of the Royal Astronomical Society*, 423, 3083
- McKinney, J. C. & Uzdensky, D. A. 2012, *MNRAS*, 419, 573
- Mei, S., Blakeslee, J. P., Côté, P., et al. 2007, *ApJ*, 655, 144
- Melia, F. & Falcke, H. 2001, *ARA&A*, 39, 309
- Michell, J. 1784, *Philosophical Transactions of the Royal Society of London*, 74, 35
- Mignone, A., Bodo, G., Massaglia, S., et al. 2007, *ApJS*, 170, 228
- Mignone, A., Mattia, G., Bodo, G., & Del Zanna, L. 2019, *MNRAS*, 486, 4252
- Millman, K. J. & Aivazis, M. 2011, *Computing in Science & Engineering*, 13, 9
- Mills, B. Y. 1952, *Nature*, 170, 1063
- Mizuno, Y., Lyubarsky, Y., Nishikawa, K.-I., & Hardee, P. E. 2009, *ApJ*, 700, 684
- Mizuno, Y., Lyubarsky, Y., Nishikawa, K.-I., & Hardee, P. E. 2012, *ApJ*, 757, 16
- Mizuno, Y., Nishikawa, K.-I., Koide, S., Hardee, P., & Fishman, G. J. 2006, *arXiv e-prints*, astro
- Moscibrodzka, M. 2018, Black hole event horizon and blob of matter on orbit around it in VR 360 degrees, <https://www.youtube.com/watch?v=oGTdZ4nDnaA>, accessed: 2018-05-29
- Mościbrodzka, M., Dexter, J., Davelaar, J., & Falcke, H. 2017, *MNRAS*, 468, 2214
- Mościbrodzka, M. & Falcke, H. 2013, *A&A*, 559, L3
- Mościbrodzka, M., Falcke, H., & Noble, S. 2016a, *A&A*, 596, A13
- Mościbrodzka, M., Falcke, H., & Shiokawa, H. 2016b, *A&A*, 586, A38
- Mościbrodzka, M., Falcke, H., Shiokawa, H., & Gammie, C. F. 2014, *A&A*, 570, A7
- Mościbrodzka, M. & Gammie, C. F. 2018, *MNRAS*, 475, 43
- Mościbrodzka, M., Gammie, C. F., Dolence, J. C., Shiokawa, H., & Leung, P. K. 2009, *The Astrophysical Journal*, 706, 497
- Nagar, N. M., Wilson, A. S., & Falcke, H. 2001, *ApJ*, 559, L87
- Narayan, R., Igumenshchev, I. V., & Abramowicz, M. A. 2003, *PASJ*, 55, L69
- Narayan, R. & Yi, I. 1994, *ApJ*, 428, L13
- Narayan, R. & Yi, I. 1995a, *ApJ*, 444, 231
- Narayan, R. & Yi, I. 1995b, *ApJ*, 452, 710
- Narayan, R. & Yi, I. 1995c, *ApJ*, 452, 710
- Noble, S. C., Krolik, J. H., & Hawley, J. F. 2010, *ApJ*, 711, 959
- Noble, S. C., Leung, P. K., Gammie, C. F., & Book, L. G. 2007, *Classical and Quantum Gravity*, 24, S259
- Novikov, I. D. & Thorne, K. S. 1973, in *Black Holes (Les Astres Occlus)*, 343–450
- Ohsuga, K., Mineshige, S., Mori, M., & Kato, Y. 2009, *Publications of the Astronomical Society of Japan*, 61, L7

## BIBLIOGRAPHY

- Oke, J. B. 1963, *Nature*, 197, 1040
- Oliphant, T. E. 2007, *Computing in Science & Engineering*, 9, 10
- Olivares, H., Porth, O., Davelaar, J., et al. 2019, *A&A*, 629, A61
- Olivares, H., Younsi, Z., Fromm, C. M., et al. 2018, arXiv e-prints, arXiv:1809.08682
- O’Neill, S. M., Beckwith, K., & Begelman, M. C. 2012, *MNRAS*, 422, 1436
- Orosz, J. A., McClintock, J. E., Aufdenberg, J. P., et al. 2011, *ApJ*, 742, 84
- Owen, F. N., Eilek, J. A., & Kassim, N. E. 2000, *ApJ*, 543, 611
- Özel, F., Psaltis, D., & Narayan, R. 2000, *ApJ*, 541, 234
- Palenzuela, C., Lehner, L., Reula, O., & Rezzolla, L. 2009, *Mon. Not. Roy. Astron. Soc.*, 394, 1727
- Pandya, A., Zhang, Z., Chandra, M., & Gammie, C. F. 2016, *ApJ*, 822, 34
- Parfrey, K., Philippov, A., & Cerutti, B. 2018, ArXiv e-prints, arXiv:1810.03613
- Parfrey, K., Philippov, A., & Cerutti, B. 2019, *Phys. Rev. Lett.*, 122, 035101
- Parker, E. N. 1957, *J. Geophys. Res.*, 62, 509
- Perlman, E. S., Adams, S. C., Cara, M., et al. 2011, *ApJ*, 743, 119
- Perlman, E. S., Sparks, W. B., Radomski, J., et al. 2001, *ApJ*, 561, L51
- Perlman, E. S. & Wilson, A. S. 2005, *The Astrophysical Journal*, 627, 140
- Pétri, J. & Lyubarsky, Y. 2007, *A&A*, 473, 683
- Petrich, L. I., Shapiro, S. L., Stark, R. F., & Teukolsky, S. A. 1989, *ApJ*, 336, 313
- Petropoulou, M., Giannios, D., & Sironi, L. 2016, *MNRAS*, 462, 3325
- Petropoulou, M. & Sironi, L. 2018, *MNRAS*, 481, 5687
- Philippov, A. A., Spitkovsky, A., & Cerutti, B. 2015, *ApJ*, 801, L19
- Pierrard, V. & Lazar, M. 2010, *Sol. Phys.*, 267, 153
- Poisson, E. & Israel, W. 1989, *Phys. Rev. Lett.*, 63, 1663
- Poisson, E. & Israel, W. 1990, *Phys. Rev. D*, 41, 1796
- Ponti, G., George, E., Scaringi, S., et al. 2017, *MNRAS*, 468, 2447
- Porth, O., Chatterjee, K., Narayan, R., et al. 2019, *ApJS*, 243, 26
- Porth, O., Fendt, C., Meliani, Z., & Vaidya, B. 2011, *ApJ*, 737, 42
- Porth, O., Olivares, H., Mizuno, Y., et al. 2017, *Computational Astrophysics and Cosmology*, 4, 1
- Porth, O., Xia, C., Hendrix, T., Moschou, S. P., & Keppens, R. 2014, *The Astrophysical Journal Supplement Series*, 214, 4
- Prieto, M. A., Fernández-Ontiveros, J. A., Markoff, S., Espada, D., & González-Martín, O. 2016, *MNRAS*, 457, 3801
- Pudritz, R. E., Hardcastle, M. J., & Gabuzda, D. C. 2012, *Space Sci. Rev.*, 169, 27
- Qian, Q., Fendt, C., Noble, S., & Bugli, M. 2017, *ApJ*, 834, 29
- Qian, Q., Fendt, C., & Vourellis, C. 2018, *ApJ*, 859, 28
- Rauch, C., Ros, E., Krichbaum, T. P., et al. 2016, *A&A*, 587, A37
- Reber, G. 1944, *ApJ*, 100, 279
- Rees, M. J., Begelman, M. C., Blandford, R. D., & Phinney, E. S. 1982, *Nature*, 295, 17
- Ressler, S. M., Tchekhovskoy, A., Quataert, E., Chand ra, M., & Gammie, C. F. 2015a, *MNRAS*, 454, 1848

- Ressler, S. M., Tchekhovskoy, A., Quataert, E., Chandra, M., & Gammie, C. F. 2015b, *MNRAS*, 454, 1848
- Ressler, S. M., Tchekhovskoy, A., Quataert, E., & Gammie, C. F. 2017, *MNRAS*, 467, 3604
- Reynolds, C. S., Fabian, A. C., Celotti, A., & Rees, M. J. 1996, *MNRAS*, 283, 873
- Rezzolla, L. & Zanotti, O. 2013, *Relativistic Hydrodynamics*
- Ripperda, B., Porth, O., Sironi, L., & Keppens, R. 2019, *MNRAS*, 485, 299
- Ripperda, B., Porth, O., Xia, C., & Keppens, R. 2017, *MNRAS*, 467, 3279
- Roelofs, F., Janssen, M., Natarajan, I., et al. 2019, *A&A*, in press.
- Rogers, A. E. E., Doeleman, S. S., & Moran, J. M. 1995, *AJ*, 109, 1391
- Romanova, M. M. & Lovelace, R. V. E. 1992, *A&A*, 262, 26
- Rosenbluth, M. N., Dagazian, R. Y., & Rutherford, P. H. 1973, *Physics of Fluids*, 16, 1894
- Rowan, M. E., Sironi, L., & Narayan, R. 2017, *The Astrophysical Journal*, 850, 29
- Russell, C. M. P. 2017, in *IAU Symposium*, Vol. 329, *The Lives and Death-Throes of Massive Stars*, eds. J. J. Eldridge, J. C. Bray, L. A. S. McClelland, & L. Xiao, 366–368
- Ryan, B. R., Ressler, S. M., Dolence, J. C., Gammie, C., & Quataert, E. 2018, *ApJ*, 864, 126
- Rybicki, G. B. & Lightman, A. P. 1979, *Radiative Processes in Astrophysics* (Wiley)
- Salpeter, E. E. 1964, *ApJ*, 140, 796
- Sano, T., Inutsuka, S.-i., Turner, N. J., & Stone, J. M. 2004, *ApJ*, 605, 321
- Schmidt, M. 1963, *Nature*, 197, 1040
- Schmitt, J. L. 1968, *Nature*, 218, 663
- Schnittman, J. D., Dal Canton, T., Camp, J., Tsang, D., & Kelly, B. J. 2018, *ApJ*, 853, 123
- Schnittman, J. D., Krolik, J. H., & Noble, S. C. 2016, *ApJ*, 819, 48
- Schwarzschild, K. 1999, arXiv e-prints, physics/9905030
- Scott, D. A. 2008, *Real 3D Stars*, <http://forums.newtek.com/archive/index.php/t-90366.html>
- Shakura, N. I. & Sunyaev, R. A. 1973, *A&A*, 500, 33
- Shapiro, I. I., Pettengill, G. H., Ash, M. E., et al. 1968, *Phys. Rev. Lett.*, 20, 1265
- Shcherbakov, R. V. & Huang, L. 2011, *MNRAS*, 410, 1052
- Shcherbakov, R. V., Penna, R. F., & McKinney, J. C. 2012, *ApJ*, 755, 133
- Shen, Z.-Q., Lo, K. Y., Liang, M.-C., Ho, P. T. P., & Zhao, J.-H. 2005, *Nature*, 438, 62
- Shepherd, M. C. 1997, *Astronomical Society of the Pacific Conference Series*, Vol. 125, *Difmap: an Interactive Program for Synthesis Imaging*, eds. G. Hunt & H. Payne, 77
- Shields, G. A. 1999, *PASP*, 111, 661
- Sironi, L., Petropoulou, M., & Giannios, D. 2015, *MNRAS*, 450, 183
- Sironi, L. & Spitkovsky, A. 2014, *ApJ*, 783, L21
- Sądowski, A., Narayan, R., Penna, R., & Zhu, Y. 2013, *MNRAS*, 436, 3856
- Sądowski, A., Wielgus, M., Narayan, R., et al. 2017, *MNRAS*, 466, 705
- Smith, F. G. 1951, *Nature*, 168, 555
- Spitkovsky, A. 2005, *Astrophysical Sources of High Energy Particles and Radiation*, 801, 345
- Spitkovsky, A. 2008, *ApJ*, 682, L5
- Spruit, H. C., Daigne, F., & Drenkhahn, G. 2001, *A&A*, 369, 694
- Sądowski, A., Narayan, R., Tchekhovskoy, A., & Zhu, Y. 2013, *Monthly Notices of the Royal Astronomical Society*, 429, 3533

## BIBLIOGRAPHY

- T. Bronzwaer, Z. Younsi, J. D. e. a. in prep
- Tchekhovskoy, A. & Bromberg, O. 2016, MNRAS, 461, L46
- Tchekhovskoy, A., McKinney, J. C., & Narayan, R. 2012, Journal of Physics: Conference Series, 372, 012040
- Tchekhovskoy, A., Narayan, R., & McKinney, J. C. 2011, MNRAS, 418, L79
- Thompson, C. 1994, MNRAS, 270, 480
- Tóth, G. 2000, Journal of Computational Physics, 161, 605
- Tsallis, C. 1988, Journal of Statistical Physics, 52, 479
- Tsuchiya, K., Enomoto, R., Ksenofontov, L. T., et al. 2004, ApJ, 606, L115
- Turland, B. D. 1975, MNRAS, 170, 281
- van der Walt, S., Colbert, S. C., & Varoquaux, G. 2011, Computing in Science and Engineering, 13, 22
- Vasyliunas, V. M. 1968, J. Geophys. Res., 73, 2839
- Viergutz, S. U. 1993, A&A, 272, 355
- Vincent, F. H., Paumard, T., Gourgoulhon, E., & Perrin, G. 2011, Classical and Quantum Gravity, 28, 225011
- Walker, R. C., Hardee, P. E., Davies, F. B., Ly, C., & Junor, W. 2018, ApJ, 855, 128
- Walker, R. C., Ly, C., Junor, W., & Hardee, P. J. 2008, in Journal of Physics Conference Series, Vol. 131, Journal of Physics Conference Series, 012053
- Walsh, J. L., Barth, A. J., Ho, L. C., & Sarzi, M. 2013, ApJ, 770, 86
- Watson, M. & Nishikawa, K.-I. 2010, Computer Physics Communications, 181, 1750
- Webster, B. L. & Murdin, P. 1972, Nature, 235, 37
- Weisberg, J. M. & Huang, Y. 2016, The Astrophysical Journal, 829, 55
- Weizsäcker, C. F. 1948, Zeitschrift Naturforschung Teil A, 3, 524
- Weizsäcker, C. F. V. 1943, ZAp, 22, 319
- Werner, G. R. & Uzdensky, D. A. 2017, ApJ, 843, L27
- Werner, G. R., Uzdensky, D. A., Begelman, M. C., Cerutti, B., & Nalewajko, K. 2018, MNRAS, 473, 4840
- Werner, G. R., Uzdensky, D. A., Cerutti, B., Nalewajko, K., & Begelman, M. C. 2016, ApJ, 816, L8
- White, C. J., Stone, J. M., & Gammie, C. F. 2016, ApJS, 225, 22
- Wilson, J. R. 1977, in 1st Marcel Grossmann Meeting on General Relativity, Vol. 1, 393–413
- Wilson, S. & Yang, Y. 2001, Astrophysical Journal, 568
- Woltjer, L. 1966, ApJ, 146, 597
- Xia, C., Teunissen, J., Mellah, I. E., Chané, E., & Keppens, R. 2018, The Astrophysical Journal Supplement Series, 234, 30
- Xiao, F. 2006, Plasma Physics and Controlled Fusion, 48, 203
- Yee, K. 1966, IEEE Transactions on Antennas and Propagation, 14, 302
- Yokosawa, M. 1993, PASJ, 45, 207
- Younsi, Z. 2016, Falling into a black hole (Realistic Ultra HD 360 VR movie) [8K], [https://www.youtube.com/watch?v=S6qw5\\_YA8iE](https://www.youtube.com/watch?v=S6qw5_YA8iE), accessed: 2018-05-20
- Younsi, Z. & Wu, K. 2015, Mon. Not. R. Astron. Soc., 454, 3283

- Younsi, Z., Wu, K., & Fuerst, S. V. 2012, *Astron. Astrophys.*, 545, A13
- Younsi, Z., Zhidenko, A., Rezzolla, L., Konoplya, R., & Mizuno, Y. 2016, *Phys. Rev. D*, 94, 084025
- Yuan, F., Quataert, E., & Narayan, R. 2003, *ApJ*, 598, 301
- Zeldovich, Y. B. 1964, *Doklady Akademii Nauk SSSR*, 155, 67
- Zenitani, S. & Hoshino, M. 2001, *ApJ*, 562, L63
- Zhao, J.-H., Bower, G. C., & Goss, W. M. 2001, *ApJ*, 547, L29
- Zhdankin, V., Uzdensky, D. A., Perez, J. C., & Boldyrev, S. 2013, *ApJ*, 771, 124
- Zhdankin, V., Werner, G. R., Uzdensky, D. A., & Begelman, M. C. 2017, *Physical Review Letters*, 118, 055103
- Zylka, R., Mezger, P. G., Ward-Thompson, D., Duschl, W. J., & Lesch, H. 1995, *A&A*, 297, 83



# SUMMARY

In this thesis, I studied black hole accretion flows and jets with various numerical tools. The main research question was how to connect the micro to macrophysics in accreting black hole systems. I studied how electron acceleration affects the appearance of supermassive black holes, studied how electrons are accelerated in kink-unstable jets and developed virtual reality visualizations of our models.

**In chapter 2**, I studied Sgr A\* by performing 2D general relativistic magnetohydrodynamics simulations. I used a grid that contained higher resolution in the locations where the jet and the disk reside. The simulation was then post-processed with the general relativistic ray-tracing code **RAPTOR**, which solves the radiative transfer equations in curved spacetime. One of the fundamental model parameters is the shape of the distribution function, which is often assumed to be a thermal Maxwellian. In this chapter, I deviated from this by also considering  $\kappa$  distributions and hybrid distributions. The non-thermal electrons are only present in the jet. This new class of  $\kappa$ -jet models shows that the radio and NIR is enhanced when non-thermal electrons are present. When compared to observations of Sgr A\*, I find that for the near-infrared quiescence state less than 1% of the electrons are accelerated, while in the flaring state, this is of the order of 10%. The underlying distribution function is a hybrid consisting of a thermal and  $\kappa$ -distribution with a power-law index of  $p = 2.5$ .

**In chapter 3**, I studied M87\*. I performed 3D Cartesian GRMHD simulations of the accretion flow. To ensure that the simulation is resolved, I used adaptive mesh refinement (AMR), this allows the code during runtime to add resolution based on user-defined criteria, such as gradients of local plasma variables. The GRMHD data was then post-processed with a Cartesian AMR version of **RAPTOR** that I developed. Similar to chapter 2, I considered both thermal and  $\kappa$ -jet models and compared their spectral energy distributions, synthetic images, and core shifts to historical data. The  $\kappa$  parameter that sets the slope of the high energy tail of the distribution function was set by PIC simulations of trans-relativistic reconnection, performed by Ball et al. (2018). The  $\kappa$ -jet model recovers the SED from radio up to optical, predicts correct core sizes at mm wavelengths, and recovers the right dependency of the core position as a function of frequency.

**In chapter 4**, I studied the kink-instability with first-principle particle-in-cell simulations. This instability is thought to be an important mechanism to dissipate magnetic energy at jet nozzles in AGNs and GRBs. At the jet nozzle, the toroidal and poloidal magnetic field components are comparable in strength, which makes them prone to current-driven instabilities such as the kink instability. I studied three non-rotating force-free setups with varying pitch profiles. I discovered that the initial electron acceleration is mediated by non-ideal electric fields, which are generated by strong guide field reconnection. At later times the instability generates turbulence, which leads to an ideal acceleration phase. I show that the PIC simulation recovers the same overall behavior as our MHD simulations, and are in agreement with linear analysis studies.

**In chapter 5**, I developed a virtual reality visualization of the accretion flow around Sgr A\*. I extended the GRRT code `RAPTOR` such that it can generate full steradian images of the viewpoint of an observer moving in curved spacetime. This method includes all relativistic effects such as Doppler boosting. I used a 3D GRMHD simulation as input for the accretion flow; the trajectory of the camera was set by a particle that is advected in a 2D simulation. The resulting movie consists of a multi-wavelength view, where I combined multiple astronomical relevant frequencies, 22 GHz, 43 GHz, 86 GHz, and 230 GHz, and a starry background. VR visualizations open a new way to show the complexity of black holes to the general public.

# SAMENVATTING

In deze thesis, heb ik accretie stromen en relativistische jets rondom zwarte gaten bestudeerd met verschillende numerieke methoden. De onderzoeksvraag die centraal stond is hoe elektron acceleratie in relativistische jets de observationele kenmerken beïnvloed.

**In hoofdstuk 2**, bestudeerde ik Sagittarius A\* (Sgr A\*). Ik heb 2D algemeen relativistische magnetohydrodynamische simulaties gemaakt. Ik gebruikte hierbij een speciaal numeriek grid met een hoog oplossend vermogen in de jet en de schijf. Ik heb deze simulaties daarna gebruikt als input voor de algemeen relativistische ray tracing code **RAPTOR**. Een van de belangrijkste aannames in straling transport is de vorm van de elektron distributie functie. De aanname die vaak wordt gebruikt is een thermische Maxwell-Jütner distributie. In dit hoofdstuk liet ik deze aanname los en bestudeerde ik hoe een  $\kappa$  distributie of een hybride distributie functie de eigenschappen van de modellen veranderd. De niet thermische elektronen zijn in deze modellen alleen aanwezig in de jet. Dit nieuwe type van  $\kappa$ -jet modellen laat zien dat de radio en NIR emissie toeneemt als de niet thermische elektronen aanwezig zijn. Uiteindelijk vergeleek ik de  $\kappa$ -jet modellen met observaties van Sgr A\*. Ik ontdekte dat voor de quiescence state minder dan 1% van de elektronen geaccelereerd zijn, terwijl in de flaring state ongeveer 10% van de elektronen geaccelereerd is. In dit geval zitten de elektronen in een hybride distributie, een combinatie van een thermisch en een  $\kappa$  distributie functie met een machtswet index van  $p = 2.5$ .

**In hoofdstuk 3**, bestudeerde ik M87\*. Ik heb 3D Cartesische GRMHD simulaties gemaakt. Om ervoor te zorgen dat het oplossend vermogen van de simulatie voldoende is gebruik ik adaptieve mesh refinement (AMR), dit zorgt ervoor dat de code tijdens de simulatie extra resolutie kan toevoegen gebaseerd op criteria die vooraf meegegeven worden, bijvoorbeeld gebaseerd op de gradient van een plasma variabele. De GRMHD data is dan als input gebruikt voor een Cartesische AMR versie van **RAPTOR** die ik heb ontwikkeld. Vergelijkbaar aan hoofdstuk 2 heb ik de aanname van een thermische distributie functie voor de elektronen los gelaten. Ik overwoog thermische en een  $\kappa$ -jet modellen en vergeleek hun spectrale energie distributies, synthetische afbeeldingen, en kern verschuiving met historische observaties van M87\*. De  $\kappa$  parameter zet de helling van de hoog energetische staart van de distributie functie. Deze heb ik gekoppeld aan een parametrisatie

die gevonden is met PIC simulaties van trans-relativistische reconnectie, uitgevoerd door Ball et al. (2018). Het  $\kappa$ -jet model verklaart de SED van radio to optische golflengtes, heeft de juist kern grootte voor mm golflengtes, en komt overeen met de geobserveerde verschuiving van de kern positie als functie van frequentie.

**In hoofdstuk 4**, bestudeerde ik de kink instabiliteit met fundamentele particle-in-cell simulaties. De instabiliteit is een mogelijke veroorzaker van magnetische energie dissipatie bij jet nozzles in AGNs and GRBs. Bij de jet nozzle zijn de toroidale en poloidale magneetvelden van vergelijkbare sterkte, dit maakt de jet instabiel voor stroom gedreven instabiliteiten zoals de kink instabiliteit. Ik bestudeerde drie niet roterende force-free opstellingen met variërende pitch profielen. Ik ontdekte dat de elektronen in eerste instantie geaccelereerd worden via niet-ideale elektrische velden gegenereerd door reconnectie met een sterk veld parallel aan het gegenereerde elektrische veld. In een later stadium wordt de versnelling van de elektronen veroorzaakt door ideale elektrische velden die gegenereerd worden door zwakke turbulentie. Ik liet zien dat de resultaten globale evolutie van de PIC simulaties in overeenstemming zijn met MHD simulaties en met lineaire analyse van de instabiliteit.

**In hoofdstuk 5**, ontwikkelde ik een virtual reality visualisatie van de accretie stromen rondom Sgr A\*. Ik breidde de GRRT code RAPTOR uit zodat het 360° afbeeldingen kan maken vanuit het oogpunt van een waarnemer die beweegt in gekromde ruimtetijd. Deze methode omvat alle relativistische effecten zoals Doppler verschuivingen. Ik gebruikte 3D GRMHD simulaties als model voor de accretie stromen; en het pad die camera volgde werd gegeven door een deeltje in de accretie stroom. De uiteindelijke visualisatie bestaat uit afbeeldingen gemaakt op verschillende astronomisch relevante frequenties van 22 GHz, 43 GHz, 86 GHz en 230 GHz, en een sterren achtergrond. Mijn VR visualisaties zijn een eerste stap naar een nieuwe manier van data visualisatie van modellen van zwarte gaten voor wetenschappers, en daarnaast dragen ze ook bij aan een nieuwe manier om onderzoek naar zwarte gaten onder de aandacht te brengen bij het brede publiek.

# CURRICULUM VITÆ

I was born on the 18th of September 1991 in Wageningen, The Netherlands. I lived my entire childhood in De Klomp, a typical Dutch village, with more animals than inhabitants. My first clear memory of astronomy was in Austria, gazing at the night sky in the Alps. This sparked a flame that over the years started to burn brighter and brighter.

After completing my high school in 2010, I started studying “Natuur- en Sterrenkunde” (Physics and Astronomy) at Radboud University Nijmegen. I completed my Bachelor program cum laude in 2013. My thesis project was under the supervision of prof. dr. A. Achterberg. During this project, I studied the propagation of cosmic rays in the galactic magnetic field.

My master’s program was also conducted at Radboud University, which I finished cum laude in 2016. My thesis was supervised by prof. dr. H. Falcke and dr. M. Mościbrodzka. During my thesis project, I modeled the black hole in the galaxy Messier 81 with a tilted accretion disk. During this project, I found that the jet that is launched by the black hole follows the precession of the tilted accretion disk. During my studies at Radboud, I was awarded the student award for combining excellent study results with contributions to academia via student politics.

After finish my master’s program, I started a Ph.D. in the group of prof. dr. H. Falcke at Radboud University. I studied non-thermal electron acceleration models for Sagittarius A\* and M87\*. I became a part of the Event Horizon Telescope Collaboration, where I am involved in the theory working group. I developed Virtual Reality visualizations of black hole accretion. The science paper that came out of this work got worldwide press coverage, and the movies have been more than one million times. In 2018 I was elected as a face of science by the Royal Dutch Academy of Arts and Sciences.

During my Ph.D. I visited the Flatirons Institutes Center for Computational Astrophysics in New York during a half year predoctoral program, where I worked with dr. A. Philippov on the particle acceleration in relativistic jets with first-principle plasma simulations.

## CURRICULUM VITÆ

After completing my Ph.D. program, I will move to New York. I will start a four-year post-doctoral fellowship at Columbia University and Flatirons Institutes Center for Computational Astrophysics.

# PUBLICATION LIST

## First-author papers

**Davelaar, J.**, Philippov, A.A., Bromberg, O., Singh, C.B., 2020, The Astrophysical Journal Letters, Volume 896, Issue 2, id. L31 , *Particle acceleration in kink-unstable jets*.

**Davelaar, J.**, Olivares, H., Porth, O., Bronzwaer, T., Janssen, M., Roelofs, F., Mizuno, Y., Fromm, C.M., Falcke, H., Rezzolla, L., 2019, Astronomy & Astrophysics, Volume 632, id. A2, *Modeling non-thermal emission from the jet-launching region of M 87 with adaptive mesh refinement*.

**Davelaar, J.**, Bronzwaer, T., Kok, D., Younsi, Z., Mościbrodzka, M., Falcke, H., 2018, Computational Astrophysics and Cosmology, Volume 5, id. 1, *Observing supermassive black holes in virtual reality*.

**Davelaar, J.**, Mościbrodzka, M., Bronzwaer, T., Falcke, H., 2018, Astronomy & Astrophysics, Volume 612, id. A34, *General relativistic magnetohydrodynamical  $\kappa$ -jet models for Sagittarius A\**.

## Papers

Kim, J-Y., Krichbaum, T.P., Broderick A.E., Wielgus, M., Blackburn, L., Gomez, J., Johnson, M.D., Bouman, K.L., Chael, A., Akiyama, K., Jorstad, S., Marscher, A.P., Issaoun, S., Janssen, M., Chan, C-K., Savolainen, T., Ozel, F., and the Event Horizon Telescope Collaboration, 2020, Astronomy & Astrophysics, forth coming, *Event Horizon Telescope imaging of the archetypal blazar 3C 279 at an extreme 20 microarcsecond resolution*

Roelofs, F., Janssen, M., Natarajan, I., Deane, R., **Davelaar, J.**, Olivares, H., Porth, O., Paine, S. N., Bouman, K. L., Tilanus, R. P. J., van Bemmell, I. M., Falcke, H., and the Event Horizon Telescope Collaboration, 2020, Astronomy & Astrophysics, Volume 636, id. A5, *SYMBA: An end-*

PUBLICATION LIST

*to-end VLBI synthetic data generation pipeline. Simulating Event Horizon Telescope observations of M 87*

van der Gucht, J., **Davelaar, J.**, Hendriks, L., Porth, O., Olivares, H., Mizuno, Y., Fromm, C.M., Falcke, H., 2020, *Astronomy & Astrophysics*, Volume 636, id. A94, *Deep Horizon, a machine learning network that recovers accreting black hole parameters*

Bromberg, Omer, Singh, Chandra B., **Davelaar, Jordy**, Philippov, Alexander A., 2019, *The Astrophysical Journal*, Volume 884, Issue 1, id. 39, *Kink Instability: Evolution and Energy Dissipation in Relativistic Force-free Nonrotating Jets*

Olivares, H., Porth, O., **Davelaar, J.**, Most, E.R., Fromm, C.M., Mizuno, Y., Younsi, Z., Rezzolla, L., 2019, *Astronomy & Astrophysics*, Volume 629, id. A61, *Constrained transport and adaptive mesh refinement in the Black Hole Accretion Code*

Porth, O., Chatterjee, K., Narayan, R., Gammie, C.F., Mizuno, Y., Anninos, P., Baker, J.G., Bugli, M., Chan, C-K., **Davelaar, J.**, Del Zanna, L., Etienne, Z.B., Fragile, P.C., Kelly, B.J., Liska, M., Markoff, S., McKinney, J.C., Mishra, B., Noble, S.C., Olivares, H. Prather, B., Rezzolla, L., Ryan, B.R., Stone, J.M., Tomei, N., White, C.J., Younsi, Z., and the Event Horizon Telescope Collaboration, 2019, *The Astrophysical Journal Supplement Series*, Volume 243, Issue 2, id. 26, *The Event Horizon General Relativistic Magnetohydrodynamic Code Comparison Project*

Event Horizon Telescope Collaboration, 2019, *The Astrophysical Journal Letters*, Volume 875, Issue 1, id. L6, *First M87 Event Horizon Telescope Results. VI. The Shadow and Mass of the Central Black Hole*

Event Horizon Telescope Collaboration, 2019, *The Astrophysical Journal Letters*, Volume 875, Issue 1, id. L5, *First M87 Event Horizon Telescope Results. V. Physical Origin of the Asymmetric Ring*

Event Horizon Telescope Collaboration, 2019, *The Astrophysical Journal Letters*, Volume 875, Issue 1, id. L4, *First M87 Event Horizon Telescope Results. IV. Imaging the Central Supermassive Black Hole*

Event Horizon Telescope Collaboration, 2019, *The Astrophysical Journal Letters*, Volume 875, Issue 1, id. L3, *First M87 Event Horizon Telescope Results. III. Data Processing and Calibration*

Event Horizon Telescope Collaboration, 2019, *The Astrophysical Journal Letters*, Volume 875, Issue 1, id. L2, *First M87 Event Horizon Telescope Results. II. Array and Instrumentation*

Event Horizon Telescope Collaboration, 2019, *The Astrophysical Journal Letters*, Volume 875, Issue 1, id. L1, *First M87 Event Horizon Telescope Results. I. The Shadow of the Supermassive*

*Black Hole*

Bronzwaer, T., **Davelaar, J.**, Younsi, Z., Mościbrodzka, M., Falcke, H., Kramer, M., Rezzolla, L., 2018, *Astronomy & Astrophysics*, volume 613, id. A2, *RAPTOR. I. Time-dependent radiative transfer in arbitrary spacetimes*.

Mościbrodzka, M., Dexter, J., **Davelaar, J.**, Falcke, H., 2017, *Monthly Notices of the Royal Astronomical Society*, Volume 468, Issue 2, id. 2214-2221, *Faraday rotation in GRMHD simulations of the jet launching zone of M87*.

Goddi, C., Falcke, H., Kramer, M., Rezzolla, L., Brinkerink, C., Bronzwaer, T., **Davelaar, J.**, Deane, R., de Laurentis, M., Desvignes, G., Eatough, R. P., Eisenhauer, F., Fraga-Encinas, R., Fromm, C. M., Gillessen, S., Grenzebach, A., Issaoun, S., Janßen, M., Konoplya, R., Krichbaum, T. P., Laing, R., Liu, K., Lu, R. -S., Mizuno, Y., Moscibrodzka, M., Müller, C., Olivares, H., Pfuhl, O., Porth, O., Roelofs, F., Ros, E., Schuster, K., Tilanus, R., Torne, P., van Bemmell, I., van Langevelde, H. J., Wex, N., Younsi, Z., Zhidenko, A., 2017, *International Journal of Modern Physics D*, Volume 26, id. 2, *BlackHoleCam: Fundamental physics of the galactic center*

**White papers**

Gurvits, L.I., Paragi, Z., Casasola, V., Conway, J., **Davelaar, J.**, Falcke, H., Fender, R., Fromm, C.M., Garcia Miro, C., Garrett, M.A., Giroletti, M., Goddi, C., Gaomez, J-L., van der Gucht, J., Guirado, J.C., Haiman, Z., Helmich, F., Humphreys, E., Impellizzeri, V., Kramer, M., Lindqvist, M., Linz, H., Liuzzo, E., Lobanov, A.P., Mizuno, Y., Rezzolla, L., Roelofs, F., Ros, E., Rygl, K.L.J., Savolainen, T., Schuster, K., Venturi, T., Wiedner, M., Zensus, J.A., 2019, arXiv:1908.10767, *TeraHertz Exploration and Zooming-in for Astrophysics (THEZA): ESA Voyage 2050 White Paper*.



## ACKNOWLEDGMENTS

This thesis completes a long journey, and during this journey I never felt alone. I received so much support and love from many people over the years, and for that I thank you all, and some of them I would like to highlight here.

My parents, for being a beacon of support and love in my life. You always believed in me, even when I did not. You helped me make the right choices and staying focussed when I was younger. You always supported my choice to pursue a science career even when that will bring me to places far from home. You taught me so much and made me who I am. You were always there when I needed you. To my sisters, Pascale and Daphne, and my brother-in-law Kevin, for all your care and love and unconditional support in my life.

To my supervisors, Heino and Monika. Heino, you always challenged me to make the most out of these four years. I thank you for all the time you took for me and the many things you thought me that made me a more complete scientist. I am really grateful to be a part of your group allowing me to study black holes within the Event Horizon Telescope. We had many great and deep talks, although you are a busy man (especially after April 10th 2019), I never felt that you were unreachable, we even had many WhatsApp conversations. To Monika, you taught me so much during these years, from the first moment I walked into your office as a Master student you helped me understand the numerical tools we used and explained the physics behind them. I thank you for passing on that knowledge to me, for that I will always be grateful, that shaped my future. Thank you both for these amazing years, and hope I will be able to visit you often in Nijmegen in the future.

To Sasha, thank you for sparking my interest in first-principle plasma simulations during the Astrosoma summerschool in Dolgoprudny. We stayed in contact and I visited you in Berkeley which resulted in me joining CCA during a predoctoral program. Thanks for all the things you taught me during those years, and your support and faith in me. I am eager to see what we can achieve in the future, and look forward to work with you when I move to New York.

## ACKNOWLEDGMENTS

To the members of the Event Horizon Telescope Collaboration. I started in the EHT at the beginning of my PhD program, which was just before the first science run where we collected the already historical data that resulted in the first picture of a black hole. Being part of the EHT, brought me in contact great people, I had many valuable interactions during conferences and meetings. Actually being on the for front of science, enhancing human knowledge is a dream come true, and I am really grateful for all the people in the Collaboration (Figure 1) that made this possible.

To my dearest friends, Jaap-Hille, Jochem, Jorim, Luc, Laura, Mike, David and Katarina, for their support, company, welcome distractions, many rounds of drinks and klaverjassen, during the past years (or even decades). To my friends at work, Thomas, Christiaan, Sara, Freek, Michael, Hamid, and Hector, for all the fun we had and the coffees we drank, and the support we gave to each other. To my office mates, Arjen, Nadia, Shan-Shan, Joris, for the the fun conversations and company. To my students, Daniël, Jeffrey, Joost, Micaela and Jesse, it was great to be involved in your projects. To David Spergel and Sasha and the Simons Foundation, who made it possible for me to join their organisation in New York. To my colleagues in New York, Bart, Lorenzo, James, Yuri, and Phil, for making me feel at home away from home. I would like to thank Luciano for my productive visits to Frankfurt, and to the people there, Oliver, Ziri, Christian, Yosuke and Mariafelicia, for the great conversations we had. To everyone at the departement, for the great atmosphere, great science, and fun conversations. To Marja, Monique, Merijn, Amanda, and Katharina, for their support and helping me out with every administrative task I struggled with. And to the reading committee for their time and constructive feedback.

And to you, Nastia, you truly mean everything to me. The last year of my Ph.D. was stressfull, applying for jobs and finishing my thesis was not always easy. The uncountable deadlines and stressed out weekends, you endured them all and helped me get through them. Thank you so much for your support, love and laughter. You are very dear to me.



FIGURE 1: The Event Horizon Telescope Collaboration at the EHTC meeting at Radboud University in October 2018.

**[jordydavelaar.com](http://jordydavelaar.com)**



[jordydavelaar.com](http://jordydavelaar.com)